IMAGING EMERGENT CORRELATED PHASES IN THE STRONTIUM RUTHENATES

Carolina De Almeida Marques

A Thesis Submitted for the Degree of PhD
at the
University of St Andrews

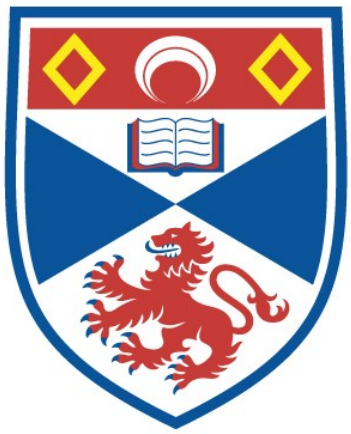

2022

Imaging emergent correlated phases in the strontium ruthenates

Carolina De Almeida Marques

University of
St Andrews

This thesis is submitted in partial fulfilment for the degree of

Doctor of Philosophy (PhD)

at the University of St Andrews

September 2021

Candidate's declaration

I, Carolina De Almeida Marques, do hereby certify that this thesis, submitted for the degree of PhD, which is approximately 65,000 words in length, has been written by me, and that it is the record of work carried out by me, or principally by myself in collaboration with others as acknowledged, and that it has not been submitted in any previous application for any degree. I confirm that any appendices included in my thesis contain only material permitted by the 'Assessment of Postgraduate Research Students' policy.

I was admitted as a research student at the University of St Andrews in August 2017.

I received funding from an organisation or institution and have acknowledged the funder(s) in the full text of my thesis.

Date 10.1.2022 Signature of candidate

Supervisor's declaration

I hereby certify that the candidate has fulfilled the conditions of the Resolution and Regulations appropriate for the degree of PhD in the University of St Andrews and that the candidate is qualified to submit this thesis in application for that degree. I confirm that any appendices included in the thesis contain only material permitted by the 'Assessment of Postgraduate Research Students' policy.

Date 10.1.2022 Signature of supervisor

Permission for publication

In submitting this thesis to the University of St Andrews we understand that we are giving permission for it to be made available for use in accordance with the regulations of the University Library for the time being in force, subject to any copyright vested in the work not being affected thereby. We also understand, unless exempt by an award of an embargo as requested below, that the title and the abstract will be published, and that a copy of the work may be made and supplied to any bona fide library or research worker, that this thesis will be electronically accessible for personal or research use and that the library has the right to migrate this thesis into new electronic forms as required to ensure continued access to the thesis.

I, Carolina De Almeida Marques, have obtained, or am in the process of obtaining, third-party copyright permissions that are required or have requested the appropriate embargo below.

The following is an agreed request by candidate and supervisor regarding the publication of this thesis:

Printed copy

Embargo on all of print copy for a period of 2 years on the following ground(s):

- Publication would preclude future publication

Supporting statement for printed embargo request

I have manuscripts in preparation for publication that uses the data and dicussions presented in this thesis.

Electronic copy

Embargo on all of electronic copy for a period of 2 years on the following ground(s):

- Publication would preclude future publication

Supporting statement for electronic embargo request

I have manuscripts in preparation for publication that use the data and discussions presented in this thesis.

Title and Abstract

- I agree to the title and abstract being published.

Date 10.1.2022 Signature of candidate

Date 10.1.2022 Signature of supervisor

Underpinning Research Data or Digital Outputs

Candidate's declaration

I, Carolina De Almeida Marques, understand that by declaring that I have original research data or digital outputs, I should make every effort in meeting the University's and research funders' requirements on the deposit and sharing of research data or research digital outputs.

Date 10.1.2022 Signature of candidate

Permission for publication of underpinning research data or digital outputs

We understand that for any original research data or digital outputs which are deposited, we are giving permission for them to be made available for use in accordance with the requirements of the University and research funders, for the time being in force.

We also understand that the title and the description will be published, and that the underpinning research data or digital outputs will be electronically accessible for use in accordance with the license specified at the point of deposit, unless exempt by award of an embargo as requested below.

The following is an agreed request by candidate and supervisor regarding the publication of underpinning research data or digital outputs:

Embargo on all of electronic files for a period of 2 years on the following ground(s):

- Publication would preclude future publication

Supporting statement for embargo request

The data used in this thesis will be used in future publications.

Title and Description

- I require an embargo on the title and description

Date 10.1.2022 Signature of candidate

Date 10.1.2022 Signature of supervisor

To my family and João

Acknowledgments

There are many people who I need to thank for making my time in St Andrews so enjoyable and without whom this thesis would not have been possible.

I want to thank my supervisor, Prof Peter Wahl, for accepting me into his group, allowing me to work in a very exciting field of physics and with an amazing group of people. I would also like to thank you for all the help, support, and encouragement to challenge myself, allowing me to grow as a researcher and person in general.

I want to thank Luke Rhodes, for being my partner on STM2, but mostly for the constant friendship, patience, support, and fruitful discussions, without which I would not have learned as much as I did.

I want to thank all my colleagues from the Wahl group. To Matt Neat, for showing me the tricks of STM2 and support when I first started. To Chi Ming, for being my mentor and teaching me the technical skills I needed to be able to perform high-quality STM measurements and to fix the instrument with precision and elegance, as well as for the encouragement and friendship. To Dibya, for the insights into physics and new perspectives on the world that made me grow as a person. To Chris, for the help, support, late days in the lab, and spontaneous dinners. To Izidor, Olivia, Masahiro, and Liam, who always made me feel welcome. To Martin, for all the help in the lab.

To everyone in the CM-CDT, especially Kaycee, Dom G., Dom R., Roberta, Cheng, James, Gordon, Mari, and Gerald, for sharing this experience with me. I would also like to thank Julie Massey and Debra Thompson, who were always available to solve any question or problem I would have regarding my PhD. I also want to thank Dr Chris Hooley for making any CM-CDT activity enjoyable and for fruitful discussions. To Prof Phil King, Prof Steve Lee, Dr Santiago Grigera, and Prof Andrew Mackenzie for being the reviewers of my PhD progress assessment over the years.

I want to thank Dr Andreas Rost, whose visits to the lab to get coffee always turned into

insightful discussions about whatever I was working on. I want to thank Craig for all the help and conversations on the bus to Dundee.

None of my PhD work would have been possible without the constant supply of liquid Helium and Nitrogen. I want to thank the cryogenics team, Callum Smith, Chris Watson, Jack Bremner, and Graeme Beaton for always doing everything in their power to get me liquid Helium in moments of despair and for helping me fixing any problem with the pumps.

I want to thank everyone with whom I had the opportunity to collaborate over the years on different projects. To Dr Timur Kim and Dr Matt Watson for helping me in my first project on Sn_4As_3. To Dr Saeed Bahramy and Dr Igor Marković for the work on PbS. To Dr Rosalba Fittipaldi, Dr Veronica Granata, and Dr Antonio Vecchione for the large supply of Sr_2RuO_4 crystals and Andrea Gerbi, and Renato Buzio for hosting me for a week in their lab in Genoa. To Dr Andreas Kreisel and Prof Peter Hirschfeld for theoretical calculations on Sr_2RuO_4 and fruitful discussions over Zoom. To Dr Alexander Komarek and Prof Andrew Mackenzie for the $Sr_3Ru_2O_7$ crystals and characterization.

I also want to thank my Master's thesis supervisor, Prof Olinda Conde, who believed in me when I was an undergraduate student, and for every recommendation letter.

To thank everyone back home, I will switch to Portuguese. Quero agradecer aos meus pais, Jorge e Leonor, por todo o suporte, carinho, paciência e por sempre acreditarem em mim. À minha irmã Catarina, por estar sempre presente, por ouvir-me ao telefone e pelos fins de semanas no sofá. Ao Zé Miguel, pelos conselhos que me ajudam sempre quando as coisas começam a ficar mais difíceis. Às minhas avós pelo constante suporte, e aos meus avôs que sempre acreditaram em mim.

Sem o apoio incondicional da Isabel, da Patrícia e do Bífidos todo este caminho seria bem mais difícil e menos divertido. Queria agradecer ao Vitorino por me passar o gosto por scanning probe microscopy, cujo tempo que passei no AFM lab foi essencial para chegar até aqui. Queria agradecer ao resto do pessoal, que me recebe sempre com um sorriso e um abraço quando volto a Lisboa. Queria também agradecer ao pessoal do Barreiro, Tiago, Bernardo, Patrícia M., Patrícia F. e Cláudio por me receberem sempre de braços abertos quando volto a casa e, mesmo longe, me apoiarem nesta jornada.

Finalmente, ao João, por tudo e mais alguma coisa, cujo encorajamento levou-me até aqui.

The research presented in this thesis was funded and supported by the Engineering and Physical Sciences Research Council [grant number EP/L015110/1].

Abstract

In strongly correlated electron materials, charge, spin and orbital degrees of freedom exhibit an intimate relationship, leading to new emergent phases that seemingly break the symmetries of the underlying crystal and are highly sensitive to external stimuli. This is well illustrated in the Ruddlesden-Popper series of the strontium ruthenates, $Sr_{n+1}Ru_n O_{3n+1}$, where a wide range of properties attributed to such physics can be found, including unconventional superconductivity, quantum criticality, metamagnetic transitions and ferromagnetism. In this thesis, using ultra-low temperature scanning tunneling microscopy, I show a detailed study of the low-energy electronic states at the surface of Sr_2RuO_4, an unconventional superconductor, and $Sr_3Ru_2O_7$, an itinerant metamagnet associated with quantum criticality. I demonstrate that the increased structural distortions in the surface layer lead to considerable changes in the Fermi surface, allowing the stabilization of new emergent phases beyond those accessible in the bulk.

At the surface of Sr_2RuO_4, we find that the surface reconstruction leads to checkerboard charge order intertwined with nematicity, intimately linked with four van Hove singularities within 5 meV of the Fermi level. Including these orders in a tight-binding model gives excellent agreement with the experiment. By applying a magnetic field, one of the van Hove singularities splits, with one branch extrapolated to reach the Fermi energy at $\sim$ 32 T, providing a textbook example of tuning towards a Zeeman-driven Lifshitz transition.

Measurements at the surface of $Sr_3Ru_2O_7$ reveal a magnetic ground state, with substantial anisotropy of the electronic states. With increasing magnetic field, we observe the formation of a stripe order and were able to track a van Hove singularity shift across the Fermi energy. Our measurements establish the surface layer as having a distinct ground state from the bulk, undergoing a magnetic field induced Lifshitz transition at a magnetic field of $\sim$ 11 T.

Keywords: Scanning tunneling microscopy, scanning tunneling spectroscopy, quasiparticle interference, Sr_2RuO_4, $Sr_3Ru_2O_7$, Ruddlesden-Popper series, van Hove singularity, magnetic field-driven Lifshitz transition

Contents

Chapter 1

Introduction

Current technology relies on controlling electron charges in metals and semiconductors to transport, store and process information. The underlying physical processes can be understood by considering the electrons as essentially moving independently of each other on a crystal, giving a surprisingly accurate description of the observed properties of these materials.

When electronic correlations become significant, the non-interacting electron description breaks down and entirely new physics becomes accessible. In strongly correlated electron systems, strong Coulomb repulsion between the electrons results in the interplay between charge, spin and orbital degrees of freedom, leading to rich phase diagrams with a variety of emergent orders, such as unconventional superconductivity, Mott insulator, metamagnetism and colossal magnetoresistance [1, 2]. These phase diagrams often show different emergent phases in close proximity to each other, being highly sensitive to external stimuli such as doping, pressure/strain and magnetic field. The suppression of the transition temperature to absolute zero of one of the ordered phases by an external parameter can result in a quantum critical point. In the vicinity of the quantum critical point, the phase transitions cease to be driven by thermal fluctuations and quantum fluctuations become dominant, at which the system tends to adopt newly ordered ground states [3]. The above illustrates two important features of strongly correlated electron systems: high tunability with applied external stimuli, and a platform to stabilize new emergent phases, both relevant for the development of new concepts that not only use charge but also spin for technological applications.

High tunability of emergent phases and evidence for quantum criticality can be found in the members of the Ruddlesden-Popper series of the strontium ruthenates, $Sr_{1+n}Ru_nO_{3n+1}$. Their ground states range from an isotropic ferromagnet, passing through an itinerant metamagnet associated with quantum criticality, to an unconventional superconductor, where the main difference between the members of this series is the number of RuO_6 units within a layer and the

presence/absence of distortions to the RuO_6 octahedra. The physics found in these systems are influenced by the proximity of a van Hove singularity (vHs), that is, a divergent peak in the density of states, to the Fermi energy [4, 5]. The details of the electronic structure, in particular the position of the vHs relative to the Fermi level, is intimately linked to the underlying crystal structure, being highly sensitive to tiny structural distortions induced either by doping [6] or strain [7]. By gaining insight into how these tiny structural distortions affect the physics observed in the Strontium ruthenate materials, it will be possible to disentangle the role of quantum criticality and that of the van Hove singularity in the stabilization of different emergent phases.

The unconventional superconductor Sr_2RuO_4, the single-layer $n = 1$ compound, provides one of the cleanest systems to study the emergence and tuning of new phases. Starting from a textbook-like Fermi liquid state, one of the most enigmatic superconducting states appears [8, 9], whose symmetry of the order parameter is still under intense debate [10, 11]. The superconducting state is quickly suppressed by introducing disorder [12] and the system can be pushed towards different magnetic phases by doping [13, 14] and uniaxial strain [11], linked to distortions of the RuO_6 cage and showing that strong magnetic fluctuations play an important role. In the bilayer $n = 2$ compound, $Sr_3Ru_2O_7$, the RuO_6 octahedra have in-plane rotations. Superconductivity is not observed, instead, there is evidence for a metamagnetic quantum critical end point and the emergence of exotic phases, such as nematicity of the electronic states [15–18]. The effect of quantum fluctuations is detected throughout the phase diagram at higher temperatures above the quantum critical end point, and $Sr_3Ru_2O_7$ provides one of the cleanest systems to study the tuning towards a quantum critical end point by magnetic field. The ground state of $Sr_3Ru_2O_7$ is also highly sensitive to tiny structural distortions of the RuO_6 octahedra, with antiferromagnetic and ferromagnetic phases stabilized by doping [19–21] or strain [22].

To understand the effects of tiny distortions to the electronic structure of these materials, it is instructive to consider a single layer of Sr_2RuO_4, where one can show that a small octahedral rotation is sufficient to move a vHs across the Fermi level from positive to negative energies [23]. Fortunately, this system already exists at the surface of single crystals of Sr_2RuO_4, in which upon cleaving, the surface layer undergoes a surface reconstruction with the octahedra rotating in-plane, doubling the unit cell and drastically changing the electronic structure [24–27]. In $Sr_3Ru_2O_7$, the surface layer does not reconstruct but undergoes a relaxation [28], however, even tiny changes can have a high impact on the ground state of the system [21, 22, 29, 30]. Due to the low-energy scales involved, the changes to the band structure will occur within less than 5 meV around the Fermi level (E_F), thus, high-energy resolution spectroscopic measurements are necessary. Scanning tun-

neling microscopy (STM) is the ideal technique to detect such a vHs close to E_F : the energy resolution is limited only by the measurement temperature, which means that at mK temperatures, energy resolutions on the order of 10 μeV can be achieved; it can probe both occupied and unoccupied states, and can be used under high magnetic fields. It allows us to image quantum critical matter when tuning through a metamagnetic critical point and to disentangle the surface electronic structure, giving insights into how tiny distortions drastically change the electronic properties of the strontium ruthenates.

In this thesis, I investigated the low-energy electronic structure of the surfaces of Sr_2RuO_4 and $Sr_3Ru_2O_7$ using scanning tunneling microscopy and spectroscopy, at ultra low-temperatures (< 100 mK) and under magnetic fields up to 14 T. Combining high-energy resolution spectroscopy with quasiparticle interference measurements, we were able to identify the position of the van Hove singularities at the surfaces of Sr_2RuO_4 and $Sr_3Ru_2O_7$. Our measurements show the stabilization of new emergent orders that are not present in the bulk, definitely establishing the surface layers of these two Strontium ruthenate compounds as distinct strongly correlated electron systems from the bulk.

This thesis is organized as follows. In Chapter 2, the concepts of superconductivity, itinerant metamagnetism and quantum criticality are introduced, followed by a discussion on the current knowledge of the properties of both Sr_2RuO_4 and $Sr_3Ru_2O_7$. In Chapter 3, the principles behind STM are presented, together with a description of the STM and dilution fridge system used in this work, as well as the characterization of the samples that were measured. In Chapter 4, two methods to model the electronic structure will be presented, followed by the description of how to model quasiparticle interference from the Green's function formalism. The low energy electronic states at the surface of Sr_2RuO_4 are explored in Chapter 5, with the description of how to tune the system towards a Lifshitz transition by magnetic field. The detailed study of the surface electronic structure of the metamagnetic $Sr_3Ru_2O_7$ is presented in Chapter 6, where a magnetic-field driven Lifshitz transition is demonstrated. Final conclusions and outlook are presented in Chapter 7.

Chapter 2

Strongly correlated electron systems

Strongly correlated electron systems are technologically relevant materials that promise the opportunity to exploit the entanglement of spin, charge and orbital degrees of freedom. They have properties that are highly sensitive to external stimuli and rich phase diagrams where magnetically ordered phases appear in close proximity, or even coexist, with unconventional superconductivity [1, 31]. Many of these materials show evidence of quantum criticality, where quantum fluctuations dominate thermal fluctuations close to absolute zero temperature, opening up the opportunity to find newly ordered phases [3]. These materials include the cuprate high-temperature superconductors, iron-based superconductors, heavy fermion systems and the family members of the Ruddlesden-Popper series of the strontium ruthenates, $Sr_{1+n}Ru_nO_{3n+1}$, which are the object of study in this thesis.

In this chapter, the unconventional phases found in these materials will be discussed, namely superconductivity and itinerant metamagnetism, as well as quantum criticality and some of the mechanisms used to explain their properties. Then, a review of the current knowledge of the properties of Sr_2RuO_4 and $Sr_3Ru_2O_7$ will be given, the single layer and bilayer members of the Ruddlesden-Popper series of the strontium ruthenates.

2.1 Unconventional electronic phases in correlated electron materials

2.1.1 Fermi liquid theory

When correlations are introduced in a system of electrons, the description given by the free Fermi gas can break down. The electrons can no longer be described as independent particles that move freely through a material, in which the physical properties are derived from the Pauli exclusion principle and Fermi-Dirac statistics alone, as in the Sommerfeld model. The correlations

arise primarily from the Coulomb interactions. Once interactions are included, the eigenstates of the system can no longer be the single-electron states and have to correspond to stationary states of the whole system. At sufficiently low temperatures, we can consider only the low-energy excited states of the system, close to the ground state, that is, within an energy range of $k_B T$ around the Fermi level. These low energy excited states can be written as a linear combination of elementary excitations, which L. D. Landau called *quasiparticles* [32]. The quasiparticles have well-defined energies ε and carry the quantum numbers of a bare electron, momenta $\mathbf{k}$ and spin σ, with an energy dispersion $\varepsilon(\mathbf{k})$ that has a similar structure as the one of the Fermi gas, in the sense that a Fermi surface is well defined. As a consequence, the quasiparticle properties are related to those of the free electron gas such that: their mass is renormalized, $m^* = Cm$, with C a constant and m the electron band mass; they carry only a fraction of the spectral weight associated with all single-particle excitations, $Z_\mathbf{k}$, defined via the real part of the self-energy [33]; and have a finite lifetime, $\tau_\mathbf{k} = \hbar/\Gamma_\mathbf{k}$, at finite temperature but infinite lifetime at the Fermi surface and at $T = 0$ (as required for a well-defined Fermi surface). The strength of the interactions in a material can thus be characterized by the values acquired by m^* , $Z_\mathbf{k}^{-1}$ and $\Gamma_\mathbf{k}$, with larger values corresponding to stronger interactions [34, 35]. The thermodynamic properties will follow the same behavior as the Fermi gas but replacing m with m^*, with the specific heat maintaining a linear temperature dependence and the magnetic susceptibility remaining constant, both at low temperatures ($T \to 0$). The resistivity shows a $\rho(T) \propto T^\alpha$ behavior with $\alpha = 2$ at low temperatures due to the electron interactions, which is qualitatively different compared to the Fermi gas [36]. This is one of the hallmarks of a Fermi liquid.

2.1.2 Phase diagram of strongly correlated electron systems

To identify regions on a phase diagram that correspond to Fermi liquid (FL) and non-Fermi liquid (N-FL) behavior, deviations from the expected FL response of the specific heat, magnetic susceptibility, and resistivity can be used. In the case of the exponent α of the temperature dependence of the resistivity, these regions are identified by deviations from the expected $\alpha = 2$ of FL theory, with linear T resistivity indicating N-FL behavior. Regions of Fermi liquid and Non-Fermi liquid behavior are found on the phase diagram of many strongly correlated electron systems such as the cuprate high-temperature superconductors, Figure 2.1(a), and the heavy-fermion systems, Figure 2.1(b), at low temperatures and under applied external stimuli. These materials show rich phase diagrams, with seemingly mutually exclusive phases appearing close to each other (Figure 2.1(a)) or even coexisting (Figure 2.1(b)), such as antiferromagnetic order and superconduct-

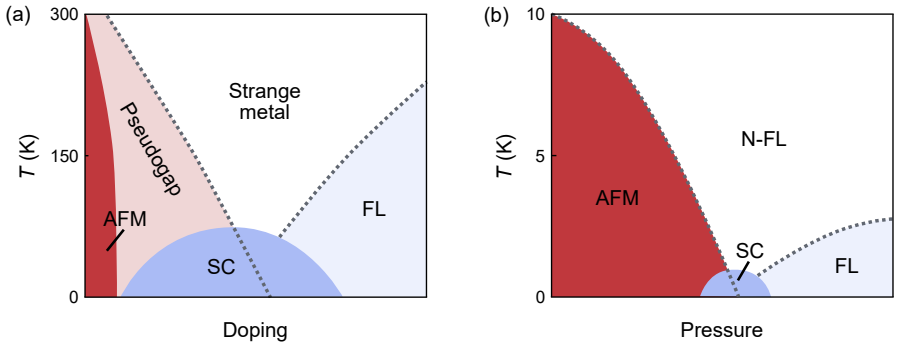

Figure 2.1: **Illustration of the phase diagrams of two families of strongly correlated electron materials.** (a) Simplified sketch of the typical phase diagram of the cuprate high-T_c superconductors, with hole-doping, based on ref. [38, 39]. (b) Sketch of the low-temperature phase diagram of heavy-fermion superconductors, based on ref. [1]. The dashed lines indicate the not so strict boundaries between phases (FL: Fermi liquid, N-FL: non-Fermi liquid, AFM: antiferromagnet, SC: superconductor). Non-Fermi liquid behavior is identified by a deviation of the temperature dependence of the resistivity from $\rho(T) \propto T^2$.

ivity. The closeness of these orders opens up the unique opportunity to study their interplay and find new mechanisms with which new phases emerge. Moreover, there is evidence that quantum fluctuations, due to the proximity to a quantum critical point [37], play an important role in the stabilization of these phases [38]. By understanding how to tune between them and the role of quantum fluctuations in the physical mechanisms behind their stabilization, we can expect that it will become possible to design materials with emergent phases with specific properties, which is highly desirable for technological applications.

2.1.3 Superconductivity

A superconductor is a material in which the electrical resistivity drops to zero below a critical temperature T_c, due to the pairing of electrons. This means that electrical current passes through without energy dissipation. Superconductors are also perfect diamagnets, with their magnetic susceptibility dropping to -1 at T_c, causing the Meissner effect. Superconductivity was first observed by H. Kamerlingh Onnes in 1911 while cooling down Mercury (Hg) to liquid Helium temperatures [40], and since then a large range of materials have been found to be superconductors.

To form the electron pairs, a pairing interaction is required which is attractive between the electrons. It results in an energy gap around the Fermi level that is the order parameter of the superconducting transition. The pairing interaction and symmetry of the order parameter can be used to classify the known superconductors, dividing them into two groups: the conventional superconductors, where the pairing of electrons is mediated by weak electron-phonon interactions as described by the Bardeen-Cooper-Schrieffer (BCS) theory, resulting in an isotropic order parameter (s-wave symmetry); and the unconventional superconductors, where the pairing interaction

cannot be accounted for by weak electron-phonon coupling, exhibiting an order parameter that has different signs on different parts or sheets of the Fermi surface (e.g. $s\pm$- and d-wave symmetries).

Conventional superconductors

In BCS theory [41] to describe conventional superconductivity, the Fermi liquid has an instability due to attractive interactions, that pair up quasiparticles with equal and opposite momenta and anti-parallel spins, $|\mathbf{k},\uparrow\rangle$ and $|-\mathbf{k},\downarrow\rangle$, into bound states. These pairs of quasiparticles are called Cooper pairs due to an attractive interaction mediated by lattice vibrations, that is, they occur via an electron-phonon coupling mechanism. As a consequence of pairing, an energy gap appears around the Fermi energy and the energy dispersion becomes

$$E_{\pm}(\mathbf{k}) = \pm\sqrt{\varepsilon(\mathbf{k})^2 + \Delta(\mathbf{k})^2}, \tag{2.1}$$

where $\varepsilon(\mathbf{k})$ is the energy dispersion of the quasiparticles relative to the Fermi energy in the normal state and $|\Delta(\mathbf{k})|$ is the superconducting order parameter, given by the magnitude of the energy gap. The Cooper pairs are made up of two spin-$1/2$ quasiparticles, which means that the Cooper pair will have integer spin, in general either 0 or 1. In the case of conventional superconductivity, the Cooper pair is in a state of total spin $S = 0$, a spin singlet state, and the order parameter is isotropic in k-space, $\Delta(\mathbf{k}) = \Delta = 1.76 k_{\mathrm{B}} T_c$, so that the whole Fermi surface is gapped out, Figure 2.2(a). This is refered to as the order parameter having s-wave symmetry, in analogy with the symmetry of an s-orbital. Examples of conventional superconductors include the elemental superconductors, e.g. Al, Hg, Sr, Pb, Nb, and composite materials, e.g. Nb_3Ge and Nb_3Sn, all with a crystal structure with high symmetry, and non-magnetic and metallic normal states. Their transition temperatures are typically low, with Al having $T_c \sim 1.2$ K [42] and Nb_3Sn a $T_c \sim 18$ K [43]. Recently, it was found that some materials show superconductivity with $T_c > 200$ K under extremely high pressures ($P \sim 200$ GPa), such as H_2S [44] and LaH_{10} [45], which are well described by BCS theory.

Unconventional superconductors

Despite the success of describing conventional superconductivity, the BCS theory described above fails to explain the properties of unconventional superconductivity found in many strongly correlated electron materials. The electron-phonon coupling pairing mechanism does not accurately predict the transition temperature T_c, predicting a lower T_c than observed experimentally, and the order parameter $\Delta(\mathbf{k})$ in these materials can have a complex structure, changing sign between

different parts of the Fermi surface, contrary to the s-wave case. While in conventional superconductors, the superconducting state arises from a normal metallic state, the normal state of a strongly correlated superconductor can be a bad metal or even an insulator. This is the case of the cuprate high-T_c superconductors, iron-based superconductors and heavy fermion materials.

Cuprate high-T_c superconductors: In the cuprate high-T_c superconductors the undoped material is an antiferromagnetic Mott insulator, with Néel type order with characteristic vector $\mathbf{q} = (\pi, \pi)$, due to strong Coulomb interactions [38]. These materials have a layered-perovskite crystal structure, characterized by planes of CuO_2, and a Fermi surface consisting of a hole-like pocket centered around the corner of the Brillouin zone. Upon doping, the antiferromagnetic order is quickly suppressed, and a superconducting dome appears, as illustrated in Figure 2.1(a), with T_c reaching a maximum at optimal doping. In the superconducting phase, the quasiparticles form Cooper pairs, however, the order parameter, while still singlet, becomes modulated in k-space, $\Delta(\mathbf{k}) = (\Delta_0/2)(\cos(k_x a) - \cos(k_y a))$, having d-wave symmetry [46, 47], Figure 2.2(b). It means that there are points on the Fermi surface whereby symmetry the gap has to be zero and hence they are gapless at the lowest temperatures, rendering the thermodynamic properties of the high-T_c superconductors completely distinct from those of conventional superconductors. The three main characteristics of high-T_c superconductors are an antiferromagnetically ordered Mott insulating ground state in the undoped material, a superconducting dome upon doping and a d-wave superconducting gap, which suggest a distinct pairing mechanism from the simple electron-phonon

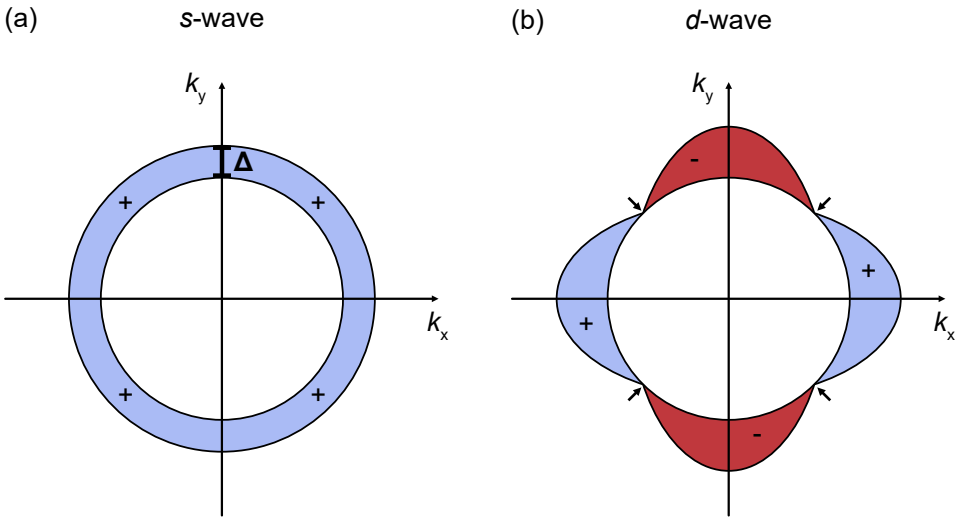

Figure 2.2: **Illustration of the s-wave and d-wave gap symmetries for a circular Fermi surface.** (a) Superconducting gap with s-wave symmetry. The shaded region shows an isotropic superconducting gap, with its width indicating the magnitude of Δ. (b) Superconducting gap with d-wave symmetry. The width of the shaded regions indicate $|\Delta(\mathbf{k})|$. The red $(-)$ and blue $(+)$ colors represent the sign of $\Delta(\mathbf{k})$. The arrows indicate the position of the nodes, where $\Delta(\mathbf{k}) = 0$.

coupling. Currently, the prevalent theories are either based on spin fluctuation pairing [48, 49] or by electron correlations [50]. In these materials, the superconducting critical temperatures T_c are much larger than in conventional superconductors, with examples such as $YBa_2Cu_3O_{7-\delta}$ with $T_c = 93$ K [51] and $HgBa_2Ca_2Cu_3O_{6+x}$ with $T_c = 133.5$ K [52]. Their phase diagrams also show the presence of a strange phase, the *pseudogap* phase, characterized by strong suppression of the density of states (DOS) at the Fermi level (E_F), but whose physics is not currently fully understood. The suppression of the onset temperature of this phase is thought to be related to a quantum critical point, which is hidden inside the superconducting dome [37, 53].

Iron-based superconductors: The iron-based family of superconductors are also layered materials, but the Fermi surface typically consists of localized hole and electron pockets around the center and corners of the Brillouin zone. For several of the pnictide superconductors, e.g. the $BaFe_2As_2$ and NaFeAs families, the undoped members show a static spin-density wave (SDW) with characteristic wave vector $\mathbf{q} = (0, \pi)$ whose onset temperature decreases with doping, giving rise to a superconducting dome. In this case, there is a region of the phase space where both SDW and superconductivity coexist. Superconductivity in the iron pnictides is fairly well described by spin-fluctuation pairing between the hole and electron pockets in the Fermi surface, within which different order parameters seem to compete with each other, namely $s_\pm$ state (sign of the order parameter changes between Fermi surface sheets) and d-wave pairing [54], both singlet states. In the iron-pnictides and chalcogenides there is an unexpectedly strong symmetry breaking in the orthorhombic phase indicating the emergence of a nematic order [55], which terminates above the superconducting dome and is thought to be connected to a quantum critical point [56]. The maximum superconducting transition temperatures found in this family of superconductors is somewhat lower than those of cuprate superconductors but higher than conventional superconductors, with examples such as $La[O_{1-x}F_x]FeAs$ with $T_c = 26$ K [57] and $BaFe_2(As_{1-x}P_x)_2$ with $T_c = 30$ K [58].

Heavy fermion superconductors: The heavy fermion systems are materials in which, at low temperatures, the quasiparticles have very large effective masses that can go up to $1000m_e$, and large electronic specific heat coefficients 100 to 1000 times larger than in usual metals [59–61]. These materials show an antiferromagnetic state at low temperatures, Figure 2.1(b), that can be suppressed by applied pressure, inducing superconductivity. The line of phase transitions between the antiferromagnetic state and the non-Fermi liquid state ends on top of the superconducting dome, suggesting that a magnetic quantum critical point is hidden by the superconducting phase. Moreover, the presence of non-Fermi liquid behavior in the phase space above the superconducting

dome is believed to indicate the presence of quantum critical fluctuations, and it is thought that in these materials they play a crucial role in the superconducting pairing mechanism [62]. The superconducting transition temperatures is these materials are typically low, with examples such as $CeRhIn_5$ with $T_c = 2.1$ K [63] and $CePd_2Si_2$ with $T_c \sim 0.4$ K [64, 65], both under pressure.

There are a number of features that are common for the superconducting states of strongly correlated electron materials [66]: (a) phase diagrams with magnetic order (antiferromagnetic or SDW) close or coexisting with superconductivity; (b) unconventional superconductivity; and (c) potential proximity to a quantum critical point.

All of the symmetries of superconducting gaps described above were derived from a spin-singlet state. However, in theory, Cooper pairs could also form from electrons with equal spins resulting in spin-triplet pairs, in an analog way to the superfluid state of ^{3}He [67, 68]. Here, the pairing results in a spin-triplet state, which means that due to the Pauli exclusion principle the spatial part of the pairing wave function must be asymmetric, for example of p-wave symmetry. Such pairs could form due to ferromagnetic spin fluctuations. This type of order parameter has a large technological interest because its symmetry can correspond to doubly-degenerate chiral states, which can serve as qubit base states for quantum computing [69]. One of the key experiments to demonstrate the presence of triplet pairing is the absence of a Knight shift in nuclear magnetic resonance (NMR) experiments when entering the superconducting state. It corresponds to the spin susceptibility not changing between the normal and superconducting states as a consequence of the components with equal spins of the spin-triplet pairs being unaffected by a small magnetic field [70]. This behavior was previously observed in Sr_2RuO_4 [71], propelling a wide interest in the superconducting state of this material [72]. However, recent NMR experiments show a considerable Knight shift upon entering the superconducting state [9, 73], excluding the p-wave scenario for Sr_2RuO_4. Currently, one of the strongest candidates for p-wave superconductivity is the heavy-fermion material UPt_3, where no Knight shift has been detected so far [74, 75].

2.1.4 Itinerant metamagnetism

Metamagnetism is defined as a sharp increase in magnetization M under the application of an external magnetic field H, that is, a transition from a low magnetization state into a high magnetization state driven by magnetic field. This transition can be described in two different extremes: from a localized and from an itinerant picture. The first case can be described by a Heisenberg model where the transition occurs from an antiferromagnetic state into a ferromagnetic state, via a spin-flip mechanism [76]. In the second case, the properties of the itinerant system depend strongly

on the characteristics of the electronic band structure and the transition usually occurs between a paramagnetic state and a state with high net magnetic moment (not necessarily with static magnetic order) and its magnetism can be described within the framework of Stoner's model [77].

Itinerant metamagnetism was first observed as a transition from a paramagnetic phase to a ferromagnetic phase in YCo_2 [78], under high magnetic fields ≤ 94 T. Since then, metamagnetic transitions have been found in several materials such as MnSi [79, 80], UPt_3 [81], $CeRu_2Si_2$ [82, 83] and $Sr_3Ru_2O_7$ [15–17].

In the Stoner's model of itinerant ferromagnetism, the finite magnetization appears due to the spontaneous spin-splitting of the bands at zero external magnetic field. Spontaneous ferromagnetism becomes possible if the condition $Un(E_F) \geq 1$ is satisfied, that is, if both Coulomb energy U and the density of states at the Fermi level $n(E_F)$ are both large [84]. Consider a paramagnet on the verge of satisfying the Stoner criterion, for example by having a peak in the density of states in the vicinity of E_F. As an external magnetic field H is applied, the bands spin-split and the peak in the density of states of one of the spin species is pushed towards the Fermi level, giving rise to a super-linear increase of the magnetization M, so that there is a crossover to metamagnetism. However, a simple peak is not enough to push the system into a metamagnetic phase transition. For a metamagnetic phase transition to occur, there has to be a discontinuity in the magnetization M with increasing magnetic field, resulting in a 1^{st} order phase transition. This transition is of first-order because it does not involve any spontaneous symmetry breaking since the application of the magnetic field already broke the rotational symmetry of the paramagnetic state.

The metamagnetic transition can be derived from Ginzburg-Landau theory [85], mean-field theory [86], from the presence of a singularity in the density of states in the vicinity of E_F [4] or from Fermi liquid theory via a Pomeranchuk instability that results in spin-dependent Fermi-surface distortions [87]. In $Sr_3Ru_2O_7$, one of the materials studied in this thesis, the metamagnetic transition occurs at temperatures below 1 K and at ~ 5 T, for an in-plane magnetic field. The transition is seen through a jump in magnetization, indicating a rapid change from a paramagnetic state at low fields to a more polarized state at high fields. It demonstrates that the system has strong ferromagnetic coupling [15]. Microscopic theories developed to describe the metamagnetic transition in $Sr_3Ru_2O_7$ are presented in section 2.2.2.

2.1.5 Quantum criticality

The emergence of both superconductivity and metamagnetic phases in strongly correlated electron systems have been associated with quantum criticality [3].

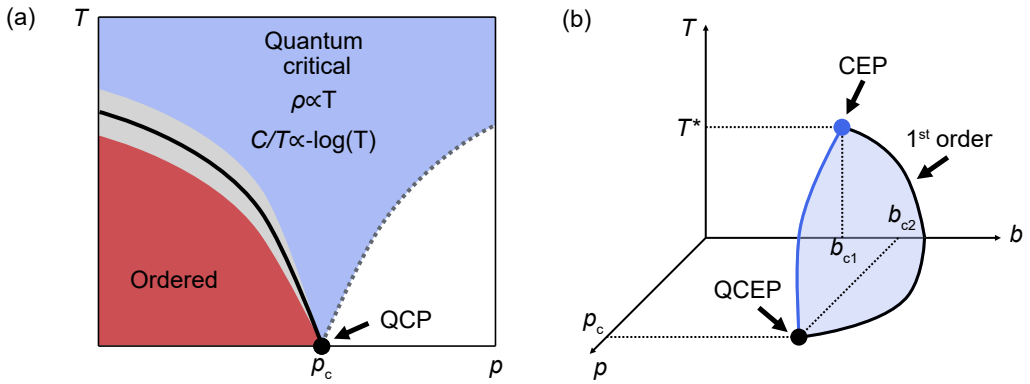

Figure 2.3: **Illustration of a quantum critical point and a quantum critical end point.** (a) A QCP (circle) appears when a line of second-order phase transitions ends at absolute zero, by an external parameter p. Effects of quantum fluctuations on the properties of the system are observed in a fan-like shaped area of the phase diagram above the QCP (blue shaded area). The gray shaded area indicates classical critical behavior. (b) The system is tuned to a QCEP when the temperature of a CEP, T^*, in the phase space (b,T) is pushed to $T=0$ by the aplication of an external parameter p. Illustrations based on ref. [90].

A quantum phase transition occurs when the critical temperature of an ordered phase, that is, the characteristic temperature of a second order phase transition, is suppressed towards absolute zero by an external parameter p, such as doping, pressure or magnetic field (Figure 2.3(a)), giving rise to a quantum critical point (QCP) at a critical value p_c. This quantum phase transition is driven by quantum fluctuations associated with Heisenberg's uncertainty principle, instead of thermal fluctuations [88]. Contrary to thermally-driven critical phase transitions, where the critical nature of the transition can only be observed very close to the critical point, the effects of quantum criticality can be detected far away from the QCP (blue area in Figure 2.3(a)), observed as a breakdown of Fermi liquid theory [3]. The non-Fermi liquid behavior is reflected in the properties of the system as a linear dependence of resistivity with temperature, $\rho(T) \propto T$, and a logarithmic divergence in the specific heat, $C/T \propto -\log(T)$ [89], corresponding to a divergence in the effective mass of the quasiparticles. To avoid this mass divergence, quasiparticles tend to organize themselves into new stable electronic configurations. The importance of quantum criticality is because it becomes a promoter for the creation of new states of matter. This is observed in cuprate high-T_c superconductors [53], iron-based superconductors [56] and heavy fermion systems [64], where the appearance of unconventional superconductivity within a dome in the phase diagram is thought of as a way to avoid a QCP.

Quantum criticality can also be induced by suppressing a line of first-order phase transitions in the phase space (b,T) by a second external parameter p, Figure 2.3(b). The onset temperature, T^*, of the critical end point (CEP) at b_{c1} of the line of first-order phase transitions is pushed towards absolute zero, creating a quantum critical end point (QCEP) at (b_{c2}, p_c). This type of

quantum criticality, since it involves a first-order phase transition, occurs between a phase of low density and a phase of high density without involving spontaneous symmetry breaking, as for example a metamagnetic transition (between a low and a high magnetization state). In this case, evidence for quantum fluctuations is also detected in a large range of the phase diagram, like in the case of a quantum critical point. From a renormalization group formalism [91] to describe a QCEP driven by magnetic field, $b = H$, once p is tuned to p_c and at low temperatures ($T \to 0$), as one approaches $b_{c2} = H_c$ (from either side), the specific heat is proportional to $C/T \propto \log h^{-1}$ for a three-dimensional system, or to $C/T \propto h^{-1/3}$ for a two-dimensional system, with $h = (H - H_c)/H_c$. The resistivity will have a Fermi-liquid like behavior, $\rho(T = 0) = AT^2$, with $A \propto h^{-1/3}$, in three-dimensions, and $A \propto h^{-2/3}$, in two-dimensions.

One of the materials that is famously known for having a metamagnetic critical point is $Sr_3Ru_2O_7$. In this material, a QCEP can be induced in two ways: (1) in less pure samples, T^* is suppressed by rotating an external magnetic field from in-plane to out of plane [16] ($b = H$ and $p = \theta$ in Figure 2.3(b)); (2) or in high-purity samples by applied pressure [92] ($b = H$ and $p = P$ in Figure 2.3(b)).

2.1.6 Van Hove singularities and Lifshitz transitions

Defined by van Hove for the elastic vibrations of a crystal [93], a van Hove singularity (vHs) is an analytic singularity in the frequency distribution function. This is also valid for the electronic structure $E(\mathbf{k})$, where now it corresponds to a singularity in the density of states $n(E)$. Singularities in $n(E)$ appear due to points in the energy dispersion $E(\mathbf{k})$ with $\nabla E(\mathbf{k}) = 0$, thus including saddle points (Figure 2.4) and band maxima and minima. They appear as a consequence of the periodicity of the crystal lattice, from Morse's theorem, and the number of vHs present in a system depends on its dimensionality, crystal symmetry and interaction strength between the electrons. Figure 2.4(a) and (b) show the case of a saddle-point vHs in the energy dispersion of a one-band model on a square lattice. In this case, the vHs in the DOS diverges logarithmically, $n(E) \propto \log(E)$, resulting in a peak with the shape shown in Figure 2.4(c).

A van Hove singularity is associated with a Lifshitz transition [94]. Lifshitz transitions correspond to changes in the topology of the Fermi surface, either by changing from a closed-loop into an open contour (saddle point), appearance or disappearance of a Fermi pocket (band minima/maxima), or merging of existing Fermi surfaces. An example of a Lifshitz transition is shown in Figure 2.4(c), where the constant energy contour below the vHs (ii) is a closed pocket around the center of the Brillouin zone (BZ), whereas above the vHs (i) it is an open loop forming a closed

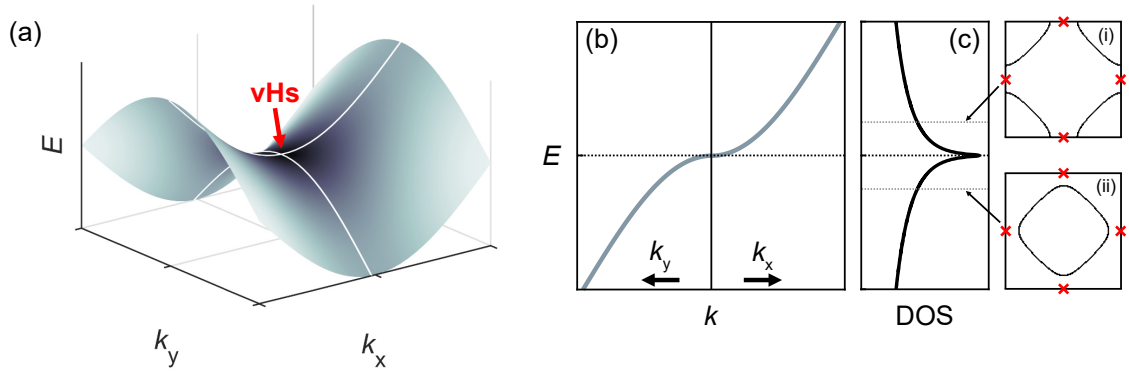

Figure 2.4: **Saddle point van Hove singularity.** (a) Three-dimensional representation of a saddlepoint, where the black shaded region indicates the position of the van Hove singularity. (b) Energy cut along k_y and k_x, with the saddle point at the center of the panel. (c) Density of states corresponding to the van Hove singularity. Constant energy contours above (i) and below (ii) the van Hove singularity. The red crosses indicate the position of the van Hove singularity in the Brillouin zone.

pocket around the corner of the BZ.

The case shown in Figure 2.4 corresponds to a vHs where two sheets of the Fermi surface connect at the Brillouin zone boundary, resulting in the $n(E) \propto \log(E)$ shape of the vHs peak in the DOS. This is what happens in bulk Sr_2RuO_4. However, the divergence of the vHs depends on where in the Brillouin zone it occurs, as well as on the crystal symmetry. In the case of $Sr_3Ru_2O_7$, four Fermi pockets join together at the Brillouin zone corner, resulting in $n \propto E^{-1/2}$. The type of divergence of the vHs will determine the physical properties of the system, especially when the vHs is tuned towards the Fermi level [95].

The presence of a vHs sufficiently close to E_F will satisfy the Stoner criterion and can be responsible for the stabilization of ferromagnetism. In addition, pushing a vHs across the Fermi level is the kind of mechanism that could lead to a metamagnetic phase transition, as briefly mentioned in section 2.1.4, as well as promoting superconductivity since in the BCS framework T_c is directly dependent on the density of states. Many strongly correlated materials have one or multiple vHs in the vicinity of the Fermi level, which seem to have strong influence on their physical properties. Examples include the metamagnetic phase transition in UPt_3 [81], enhanced superconductivity on Sr_2RuO_4 under uniaxial strain [96], and the engeneering of vHs in twisted bilayer graphene leading to superconducting/Mott insulating states [97–100].

2.1.7 Zeeman-driven Lifshitz transitions

Consider a vHs below E_F. Upon the application of a magnetic field, this vHs will Zeeman-split, Figure 2.5, with the vHs from the minority spin species moving towards the Fermi level (down, blue), and the one from the majority spin species moving away (up, red). If the vHs from

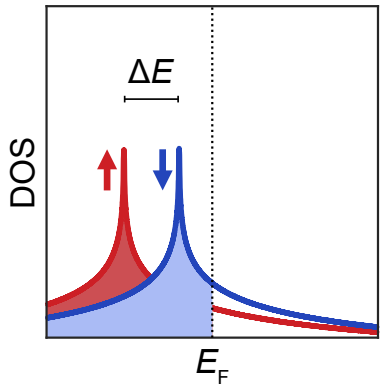

Figure 2.5: **Zeeman-splitting of a van Hove singularity.** A vHs is Zeeman-split by an external magnetic field, with energy splitting $\Delta E = g^* \mu_B B$. Red and blue indicate spin up and down, respectively.

the minority spin crosses the Fermi level, it will induce a Lifshitz transition.

In heavy-fermion systems, the bands at the Fermi level are quite flat and usually harbour several vHs, so that a magnetic field can easily Zeeman split the bands, inducing one or more Lifshitz transitions within a small range of fields, usually accompanied by jumps in the magnetization [101]. This has been shown to be the case for materials such as $CeIrIn_5$ [102], $CeRu_2Si_2$ [103], UPt_3 [81] and $YbRh_2Si_2$ [104], where their metamagnetic phase transitions seem to be related to multiple Lifshitz transitions induced by Zeeman-splitting. These metamagnetic phase transitions are associated with quantum critical end points (see section 2.1.5). The Zeeman-driven Lifshitz transition mechanism can explain several of the key features of these QCEP, such as Fermi liquid behavior at low temperatures at magnetic fields below and above the critical field H_c and non-Fermi liquid behavior at high temperatures above the QCEP [105]. Such a mechanism has been proposed to describe the metamagnetic phase transition and QCEP in $Sr_3Ru_2O_7$ [95], where the Zeeman-splitting of the vHs plus charge conservation considerations are able to reproduce the specific heat divergence observed in the experiment without the need to invoke quantum fluctuations.

2.2 Strontium ruthenates as a playground for strong electron correlations

A family of materials in which all the above phenomena can be found is the Ruddlesden-Popper series of strontium ruthenates, $Sr_{1+n}Ru_nO_{3n+1}$. These materials have layered-perovskite crystal structures, where n is the number of RuO_2 planes in a layer. Figure 2.6 shows four of its family members: Sr_2RuO_4 ($n = 1$), is an unconventional superconductor [8]; $Sr_3Ru_2O_7$ ($n = 2$), has a metamagnetic phase transition intimately linked with quantum criticality and nematicity [16–

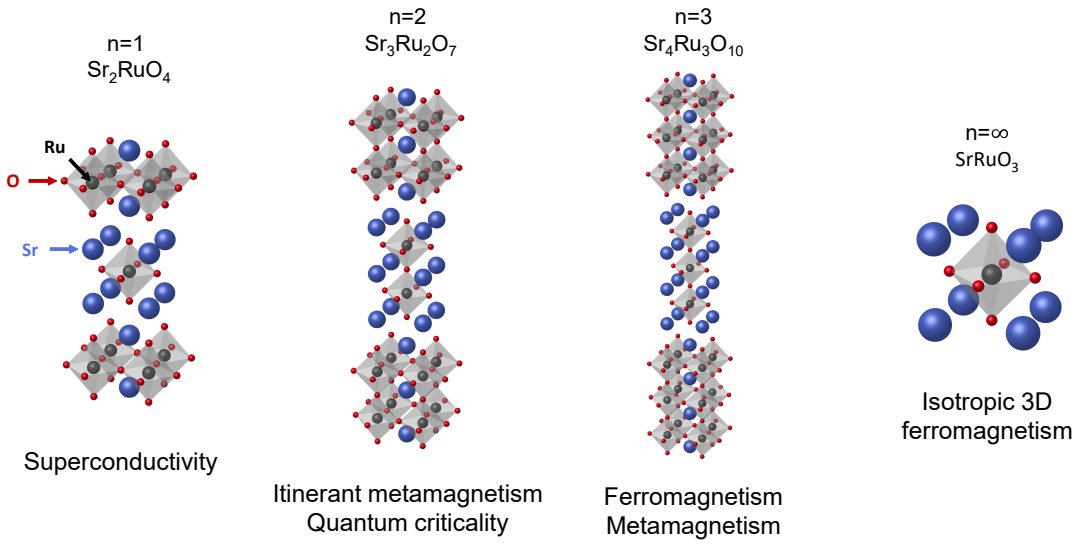

Figure 2.6: **The Ruddlesden-Popper series $Sr_{n+1}Ru_nO_{3n+1}$.** Members of the Ruddlesden-Popper series of the strontium ruthenates displayed in increasing number n, where n is the number of RuO_6 octahedra at the center of the unit cell. The superconductivity observed in Sr_2RuO_4 is suppressed and gives way to increasing tendency towards ferromagnetism.

18]; $Sr_4Ru_3O_{10}$ ($n = 3$), has a rich phase diagram with different metamagnetic and ferromagnetic phases [106]; and $SrRuO_3$ ($n = \infty$), is an isotropic ferromagnet [107].

Essentially, the main structural difference between each member of this series is the number of RuO_6 octahedra coupled via the apical oxygen and the octahedral distortions. While in $n = 1$ the crystal structure is undistorted, in $n = 2,3$ the RuO_6 octahedra are rotated in-plane and in $n = \infty$ the octahedra tilt away from the c-axis below room temperature [108]. The electronic structures of these materials show van Hove singularities in the proximity of the Fermi level, whose position relative to E_F is intimately related to the observed ground states [4] and is extremely sensitive to tiny structural distortions [7]. This diversity of emergent electronic and magnetic phases appear from a Fermi liquid ground state [109–112] and since its properties are well known, it should be possible to understand the emergence of such strongly correlated electron phenomena. Insight into how tiny distortions are responsible for the stabilization of different emergent electronic states will allow the control and optimization of the properties of these materials, opening up the opportunity for the development of novel devices.

2.2.1 The unconventional superconductor Sr_2RuO_4

Crystal structure

Sr_2RuO_4 has a layered perovskite crystal structure with a tetragonal unit cell (*I4/mmm* symmetry) [113, 114], Figure 2.7(a), isostructural to the high-T_c superconductor La_2CuO_4. Due to

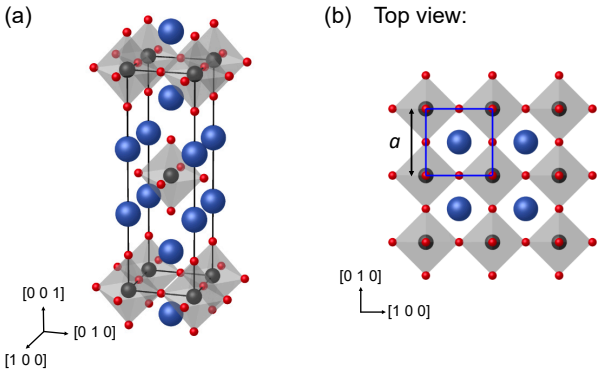

Figure 2.7: **Crystal structure of Sr_2RuO_4.** (a) Structural model of Sr_2RuO_4, showing the tetragonal unit cell (black: Ru, red: O, blue: Sr atoms). (b) Top view. The blue square indicates the two-dimensional unit cell, with lattice constant $a = 3.87$ Å.

the weak coupling between adjacent SrO layers, evidenced by highly anisotropic transport properties [115], Sr_2RuO_4 is a quasi-two-dimensional material, where the RuO_6 octahedra form a two-dimensional square lattice with a lattice constant of $a = 3.87$ Å, Figure 2.7(b). As a consequence, the prefered cleaving plane occurs between adjacent SrO-SrO layers [116].

Fermi surface and electronic structure

The Fermi surface of Sr_2RuO_4 has been well established by both quantum oscillations [119] and angle-resolved photoemission spectroscopy (ARPES) [24,117]. Figure 2.8(a) shows the Fermi surface of Sr_2RuO_4 measured in ARPES by Tamai *et al.* [117]. It is composed of three bands, due to the crystal field created by the octahedral configuration of the oxygen atoms that splits the $4d$ orbitals of the Ru atom into the lower energy t_{2g} (d_{xz}, d_{yz} and d_{xy}) and the higher energy e_g ($d_{x^2-y^2}$,

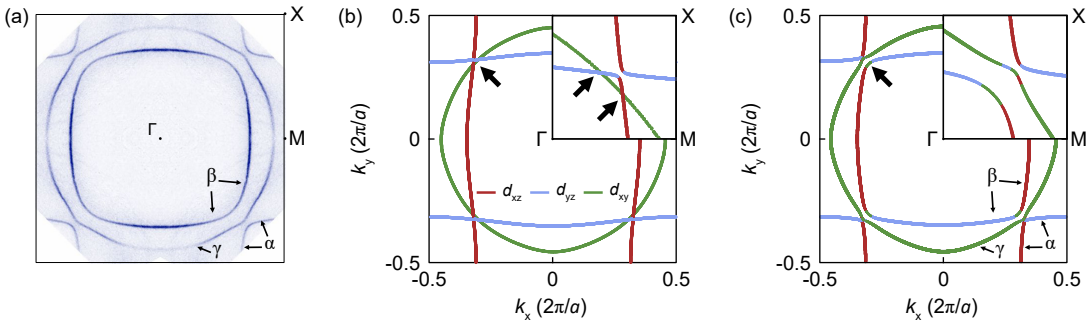

Figure 2.8: **Fermi surface of Sr_2RuO_4 and the effect of spin-orbit coupling.** (a) ARPES Fermi surface map, reproduced from A. Tamai *et al.* [117]. (b) Fermi surface of Sr_2RuO_4 calculated using the tight-binding model developed by Scaffidi *et al.* in ref. [118], without including SOC. The arrow indicates the ΓX direction and the region where the bands cross. The inset shows a close-up of that region, with the arrows indicating the crossing points between the γ and β bands. (c) Same, but including SOC. The inset shows a close-up of the region indicated by the arrow, where the hybridization between the bands is visible. The Fermi surfaces were calculated on a 2048×2048 k-grid, with energy broadening $\gamma = 0.5$ meV.

d_{z^2}) states, where the four electrons of the Ru^{4+} ion partially fill the t_{2g} orbitals. The Fermi sheets are designated as: α and β, the quasi-1D bands of d_{xz}/d_{yz} orbital character, and γ, the quasi-2D band of d_{xy} character. Thus, the Fermi surface can be well described by a tight-binding model containing only the t_{2g} states [118, 120–122].

The Fermi surface and band structure of Sr_2RuO_4 are reasonably well reproduced by Density functional theory (DFT) calculations, both within the local density approximation (LDA) [123–125] and the generalized gradient approximation (GGA) [126]. Both ARPES and quantum oscillations measurements show that the electronic structure of Sr_2RuO_4 is strongly correlated, with a large enhancement of the quasiparticle effective masses, resulting in the need of renormalization of the DFT calculated electronic structure [26] to get good agreement with experiment. The γ-band is more correlated than the α and β bands, as evidenced by an effective mass of $17m_e$ for the γ-band compared to $6m_e$ for the β band along the ΓM direction [70, 117], a consequence of its vHs being close to E_F, where increased correlations are more likely to occur. Calculations within dynamical mean-field theory (DMFT), reveal that the electronic correlations in Sr_2RuO_4 are driven by Hund's coupling [35], evidenced by the large difference in mass enhancement between the out-of-plane d_{xz}/d_{yz} and the in-plane d_{xy} states.

The agreement between calculations and experiments is further improved by considering spin-orbit coupling (SOC). Experimentally, the effects of SOC in the electronic structure of the ruthenates was first demonstrated in the insulating ruthenate Ca_2RuO_4 by spin-resolved circularly polarized photoemission [127], and later on also in Sr_2RuO_4 [117, 128–130]. The effects of SOC are strong and k-momentum dependent. To illustrate its effects, Figure 2.8(b) and (c) show the Fermi surface of Sr_2RuO_4 calculated using the tight-binding model developed by Scaffidi *et al.* in ref. [118], without and including SOC, respectively. Without SOC, the γ band of d_{xy} orbital character has crossing points with the β band of d_{xz}, d_{yz} character close to the symmetry line $\Gamma - X$, as indicated by the arrows in the inset in Figure 2.8(b). When SOC is included, these bands hybridize and the crossing points are removed, Figure 2.8(c), reproducing the experimental Fermi surface shown in Figure 2.8(a). As a consequence, the orbital character of the β and γ bands switches around the $\Gamma - X$ direction. In addition, without SOC, LDA calculations show that the γ band crosses the α and β bands along k_z, having a considerable k_z dispersion. By including SOC, these crossings are removed, rendering the k_z dispersion negligible [128], in agreement with quantum oscillations experiments [131].

The electronic structure of Sr_2RuO_4 calculated from the tight-binding model developed by Scaffidi *et al.* [118] including SOC is shown in Figure 2.9(a). It shows that the γ-band has a vHs

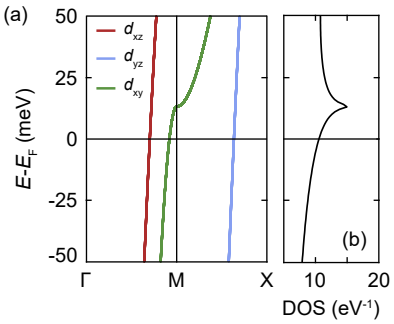

Figure 2.9: **Band structure and density of states of Sr_2RuO_4.** (a) Band structure along the path $\Gamma - M - X$ close to the Fermi level. (b) Total density of states, calculated on a 2048×2048 k-grid, with energy broadening $\gamma = 0.5$ meV.

at the M-point of the Brillouin zone above the Fermi level, which has been measured by ARPES to be at ~ 14 meV above E_F [6], corresponding to a peak in the density of states (Figure 2.9(b)). This vHs has two-fold symmetry, where two pockets join together at the BZ edge and it has been shown that its proximity to the Fermi level strongly influences the properties of its superconducting state [7, 96].

Normal state transport and magnetic properties

In the normal state, Sr_2RuO_4 is a paramagnetic metal with textbook-like Fermi liquid behavior below $T < 25$ K [109, 132], providing one of the cleanest oxide systems. Its transport properties are highly anisotropic, with the resistivity along the c-axis approximately three orders of magnitude larger than the resistivity along the RuO_2 plane ($\rho_c/\rho_{ab} \sim 10^3$) [115, 133]. In addition, the out-of-plane resistivity shows a maximum at ~ 130 K, decreasing with increasing temperature, while the resistivity in-plane remains metallic. It has strongly correlated behavior as indicated by a Wilson ratio larger than 1, the expected value for a normal metal, with $R_W = 1.5$ [131], which can be related to the Landé g-factor by $R_W = g^*/g$ [134], giving $g^* = 3$, assuming spin $1/2$.

The low-temperature Fermi liquid state of Sr_2RuO_4 is known to have strong magnetic fluctuations at specific wavevectors. Evidence for ferromagnetic fluctuations in the Fermi liquid regime was found early on in nuclear magnetic resonance (NMR) experiments [135] coming from the γ-band. In addition, inelastic neutron scattering (INS) measurements found incommensurate spin fluctuations below 200 K with characteristic wavevector $\mathbf{q}_0 = (0.3, 0.3, 0)$, in units of $2\pi/a$, which persist in the superconducting state [136, 137], due to nesting between the β-bands across the BZ corner. However, although Sr_2RuO_4 is close to ferromagnetic instabilities, due to proximity to an isotropic ferromagnetic state in $SrRuO_3$, polarized INS measurements found that the incommensurate spin fluctuations dominate the spin fluctuation spectrum of Sr_2RuO_4 [138].

The superconducting state

Sr_2RuO_4 was the first material isostructural to the cuprate high-T_c superconductors of the family $La_{2-x}Sr_xCuO_4$ to be found to have a superconducting transition without copper [8]. Contrary to the cuprates, Sr_2RuO_4 provides a very clean system without structural distortions, with a well-defined Fermi liquid ground state at low temperatures from which superconductivity emerges. It was thus thought that the mechanism behind its superconducting state could be easily characterized and help in understanding the mechanism behind high-temperature superconductivity. However, as further measurements of its superconducting state were being done the complexity of its order parameter became evident, making it a subject of intense research in its own right.

The superconducting state in Sr_2RuO_4 is highly sensitive to disorder being quickly suppressed by the presence of non-magnetic impurities [12, 139, 140]. Only samples with an in-plane residual resistivity of $\rho_{\text{res}} < 1.1\ \mu\Omega$cm [12] show a superconducting transition, with the highest transition temperature of $T_c = 1.5$ K found in the purest crystals. This is in contrast with the cuprate superconductors, where the superconducting transition occurs at optimal doping. The proximity to ferromagnetic fluctuations [135] suggested that these could drive superconductivity, allowing the formation of Cooper pairs from electrons with aligned spins, originating an order parameter with p-wave symmetry. Three pieces of evidence supported such an order parameter: no change in Knight shift upon entering the superconducting phase from NMR spectroscopy measurements [71, 141], time-reversal symmetry breaking (TRSB) below T_c, from zero-field muon spin relaxation [142] and non-zero Kerr rotation [143]. However, other experiments were reporting results inconsistent with the p-wave scenario. Ultrasound [144], thermal conductivity [145] and specific heat [146, 147] measurements indicated the presence of line nodes in the superconducting gap, either vertical protected by symmetry, or horizontal. Furthermore, chiral edge currents were never found [148–150] and the behavior of T_c under uniaxial pressure [96, 151] showed a single transition with a maximum in T_c, instead of a split transition as expected for a superconducting gap with p-wave symmetry.

The triplet scenario has become all but excluded when a substantial Knight shift was observed in NMR experiments at zero and under uniaxial strain [9], in disagreement with the original reports [71]. These experiments have been reproduced [73], and the drop in spin polarization upon entering the superconducting state compared to the normal state is large enough to be inconsistent with any purely odd-parity order parameter, also shown from field dependent measurements [152]. The most recent experiments constraint the order parameter to fulfil even parity, chirality and have two components that are degenerate on the tetragonal lattice [11, 153–157]. Recent muon spin re-

laxation and heat capacity measurements under uniaxial stress show a split of the onset temperature of superconductivity and that of time-reversal symmetry breaking, supporting a two-component superconducting order parameter that breaks time-reversal symmetry [11].

Spectroscopic information promises to allow the determination of the symmetry of the superconducting order parameter in Sr_2RuO_4. This could be attempted in scanning tunneling microscopy (STM), which can access low enough temperatures and has the necessary energy resolution. Such measurements have been attempted, with sometimes contradictory results. Most works report a SrO surface that is non superconducting [158–161]. The superconducting gap was detected either on a different surface reconstruction [162] or on surfaces cleaved in air [163,164]. Recently, an STM work on the SrO-terminated surface reports the detection of a gap consistent with the expected superconducting gap width of Sr_2RuO_4 and Bogoliubov quasiparticle interference imaging measurements, revealing a single component order parameter of $d_{x^2-y^2}$ symmetry [165], inconsistent with the previous chiral two-component scenario. The reason why it has been so difficult to detect the superconducting gap at the SrO-terminated surface of Sr_2RuO_4 by STM rests in the presence of a surface reconstruction [25], which appears to suppress superconductivity.

Effects of doping and lattice distortions

The electronic structure of Sr_2RuO_4, and consequently its ground state, is extremely sensitive to disorder. The substitution of Sr^{2+} with La^{3+} leaves the RuO_6 cage largely unaffected, inducing a rigid-band shift of the Fermi level across the vHs, followed by non-Fermi liquid behavior and enhancement of ferromagnetic fluctuations [6, 140, 170]. The isoelectronic substitution of Sr^{2+} by Ca^{2+} induces distortions to the RuO_6 octahedra due to the smaller ionic radius of Ca. This is

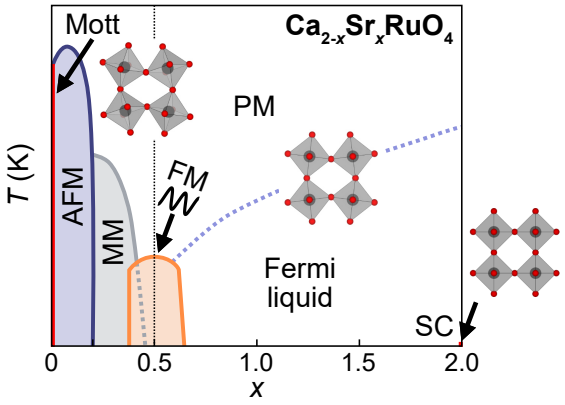

Figure 2.10: **Illustration of the phase diagram of the system $Ca_{2-x}Sr_xRuO_4$.** Phase diagram of $Ca_{2-x}Sr_xRuO_4$, based on ref. [13, 166–169]. The structural models show the structural distortions induced with increasing Ca content (SC: superconductivity, PM: paramagnetic metal, FM: Ferromagnetic fluctuations (wiggly line represents fluctuations), MM: glassy magnetic metallic, AFM: antiferromagnetic).

illustrated in Figure 2.10, which shows a sketch of the phase diagram of $Ca_{2-x}Sr_xRuO_4$. Upon the introduction of Ca, the RuO_6 octahedra rotate in-plane and superconductivity (SC) is suppressed. The system is still a paramagnetic metal (PM) with Fermi liquid behavior at low temperatures. With increasing x, the octahedral rotation angle increases until it reaches $\sim 12^\circ$ at $x \sim 0.5$, where strong ferromagnetic (FM) fluctuations are detected. Increasing x further results in the tilting of the RuO_6 octahedra about the c-axis, with a glassy magnetic metallic (MM) state appearing. As the concentration of Ca is increased, the tilting angle increases and an antiferromagnetic (AFM) order appears, finally stabilizing into a Mott-insulating state in the pure compound Ca_2RuO_4 when the tilting angle reaches $\sim 12^\circ$ [13, 166–169]. These are reasonably tiny distortions to the RuO_6 cage (rotation and tilting angles $\lesssim 12^\circ$) that drive the system through a large diversity of ground states. Another example is the structural distortion at half doping observed upon the substitution of Ru for Ir, which changes the symmetry of the lattice and induces an incommensurate antiferromagnetic order, also driven by the lattice degrees of freedom [14].

The disorder introduced by doping poses challenges when trying to understand the microscopic physics of these phase transitions, making it difficult to separate the effects of chemical inhomogeneity from the effect of the lattice distortions. One way to create lattice distortions without introducing disorder is by applying strain. Measurements of the resistivity of Sr_2RuO_4 crystals under uniaxial strain applied along the [100] crystallographic directions have shown an increase in the superconducting T_c for both compressive and tensile strains [151, 171]. Upon compressing the crystal further, the T_c is observed to have a maximum at $T_c = 3.5$ K [96]. In the same strain range, the resistivity of the normal state is seen to change to a non-Fermi liquid behavior, with a decrease in the exponent α of the temperature dependence T^α from 2 to 1.5 [172]. This change in the transport properties corresponds to a Lifshitz transition of the γ band, where the vHs in the direction perpendicular to the applied strain is moved across the Fermi level, as demonstrated by ARPES [7]. Epitaxial strain measurements on thin films [173] have shown an enhancement of the mass of the quasiparticles as the vHs is moving across E_F, with non-Fermi liquid behavior when the vHs is in the close vicinity of E_F. Recent experiments on single crystals, where higher strain values were reached, show not only the separation of the superconducting T_c with the onset energy of TRSB but also the stabilization of a static magnetic order [11].

To understand how these tiny distortions of the RuO_6 octahedra control the stabilization of such a diversity of ground states, we should ideally start by understanding how the ground state of a single layer of Sr_2RuO_4 changes upon the introduction of octahedral rotations. Such a system can be found at the surface of Sr_2RuO_4.

The surface layer of Sr_2RuO_4

In Sr_2RuO_4, adjacent SrO layers are weakly coupled, resulting in a preferable cleaving plane along the [100] direction, exposing a SrO-terminated surface. The bulk crystal of Sr_2RuO_4 has a structural instability towards formation of octahedral rotations evidenced by a phonon mode that corresponds to the in-plane rotational mode of the RuO_6 octahedra and softens at the Brillouin zone corner [174,175]. Upon cleaving, this phonon mode freezes at the surface layer, with adjacent RuO_6 octahedra rotated in opposite orientations (Fig. 2.11(a)) resulting in a doubling of the unit cell (Fig. 2.11(b)). The angle of rotation has been estimated by IV/LEED to be between 6°-9° [25,176], mimicking the octahedral rotation that appears upon Ca-doping and of $Sr_3Ru_2O_7$.

This surface reconstruction dramatically changes the electronic structure as revealed by ARPES measurements [24,26,27]. Figure 2.12 shows the ARPES Fermi surface map measured by Veenstra *et al.* [27], showing a Fermi surface that is consistent with the folding of the bands due to the doubling of the unit cell, with the d_{xy} band displaying a change in its topology due to the vHs being pushed below E_F. This is supported by the observation that the dispersion of the γ-band changes from electron-like in the bulk to hole-like at the surface. In ARPES, these surface states are seen superimposed with the bulk bands and can be suppressed either by cleaving in air [7], degrading the surface through temperature cycles [24] or adsorption of CO molecules [117].

Laser ARPES measurements [177,178] show that the surface is an extremely correlated Hund's metal, which is well isolated from the bulk and can thus be treated as a distinct system. The bandwidth of the γ-band of the surface system is found to be 3 times narrower than the bulk, being more correlated, a consequence of the vHs being closer to E_F than in the bulk.

DFT calculations of Sr_2RuO_4 within the local density approximation, with different angles of octahedral rotations, show that increasing the angle of rotation pushes the vHs down in energy,

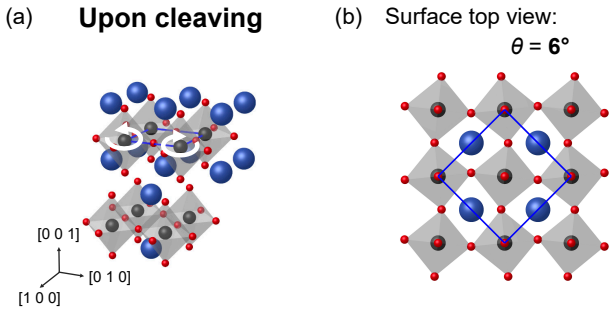

Figure 2.11: **Sketch of the surface reconstruction in Sr_2RuO_4.** (a) When a crystal of Sr_2RuO_4 is cleaved, the topmost layer undergoes a reconstruction where the RuO_6 octahedra rotate in-plane, as indicated by the arrows. (b) Top view of the surface crystal structure, showing the octahedral rotation. The blue square indicates the surface unit cell.

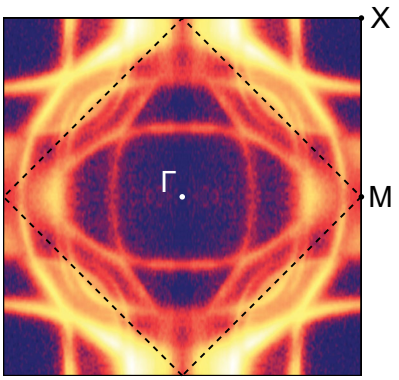

Figure 2.12: **Fermi surface of the surface layer of Sr_2RuO_4.** ARPES Fermi surface map showing the bands from the surface layer of Sr_2RuO_4, superimposed on the bulk bands. Reproduced with permission from Veenstra *et al.* [27].

being below the Fermi level for $\theta > 6^\circ$ and reproducing the Fermi surface observed by ARPES [23]. It also shows that the rotation promotes mixing between the t_{2g} and e_g states, with the vHs at the M-point gaining a small d_{z^2} contribution.

The consequences of this vHs shift to the ground state of the surface layer are not trivial. STM measurements [25,116] show a checkerboard intensity pattern on top of the Sr atoms, which is not captured in the I/V LEED [25,176]. Using DFT calculations to compare possible magnetic ground states with the non-magnetic case, Matzdorf *et al.* [25] showed that a ferromagnetic configuration becomes energetically favourable at the octahedral rotation angle observed at the surface layer. However, this is inconsistent with ARPES measurements, where evidence for ferromagnetism was never found [26]. Scanning tunneling spectroscopy shows the opening of a partial gap around the Fermi level [179] instead of a clear peak in the local density of states, in disagreement with the presence of a single vHs. In addition, it is not clear whether the rotation suppresses superconductivity. Most STM measurements report the absence of a superconducting gap in high-resolution STS on the SrO-terminated surface [158–161], whereas the detection of a superconducting gap at this surface has been recently reported [165].

The Fermi surface of the surface layer of Sr_2RuO_4 shows similarities with the Fermi surface of $Sr_3Ru_2O_7$ (see below Figure 2.14). First, the symmetry of the vHs at the M-point changes from two-fold in the bulk Sr_2RuO_4 to four-fold at the surface layer, with four pockets joining together at the vHs point, as in $Sr_3Ru_2O_7$ when ignoring orthorhombicity and considering a tetragonal unit cell. Second, the energy of the vHs in the surface layer of Sr_2RuO_4 appears at a similar energy as in $Sr_3Ru_2O_7$. This brings up the question of whether the surface of Sr_2RuO_4 has a ground state similar to that of $Sr_3Ru_2O_7$, becoming quantum critical. The studies of the surface reconstruction in the $Ca_{2-x}Sr_xRuO_4$ system show that the surface layer of crystals with increasing

Ca doping stabilize the structural distortion observed in the bulk at higher doping concentration, as for example, the surface layer of Sr_2RuO_4 shows rotations, which is only stabilized in the bulk upon Ca doping.

Unveiling the low-energy electronic states of the surface layer of Sr_2RuO_4 provides an ideal model system to understand how the proximity to a vHs in strongly correlated systems stabilizes different emergent orders. In particular, how in the ruthenates system the distortions of the RuO_6 octahedra control the appearance of such a large diversity of states. The surface layer of Sr_2RuO_4 provides an ultra-clean two-dimensional system to test this. In Chapter 5, I study the low-energy electronic structure of this system, revealing the presence of emergent orders distinct from the bulk.

2.2.2 The metamagnetic $Sr_3Ru_2O_7$

Crystal structure

$Sr_3Ru_2O_7$ crystallizes in an orthorhombic unit cell (space group *Bbcb*) [180], Figure 2.13(a). It is a layered perovskite, where each layer consists of two RuO_2 planes (or two RuO_6 octahedra connected by the same apical oxygen), defining a bilayer of strontium ruthenate. It has in-plane octahedral rotations by $\sim 7.85°$, where the direction of rotation is opposite between adjacent Ru atoms in the same RuO_2 plane and between RuO_2 planes in the same bilayer (arrows in Figure 2.13(a)). The orthorhombicity is a consequence of the stacking of the bilayers because there are two different ways in which the rotations of the next bilayer can be oriented: either the top bilayer is shifted by $(\sqrt{2}/2, \sqrt{2}/2)$ or by $(-\sqrt{2}/2, \sqrt{2}/2)$ in relation to the bottom bilayer. These two orientations are energetically identical, but define a symmetry breaking axis. To first order, we can estimate the effect of the orthorhombicity to be energetically of the same order as the interlayer coupling.

Despite the orthorhombicity, the distance between the Ru atoms along x and y are the same within experimental uncertainty [181] with a Ru-Ru distance of $a = 3.89$ Å. To describe some of the properties of this material, a pseudo-tetragonal unit cell is used, with the a and b axis defined as the in-plane lattice vectors that connect adjacent Ru atoms, Figure 2.13(b), and the c-axis parallel to the $[001]$ direction.

The two RuO_6 octahedra in a bilayer couple strongly via the apical oxygen, but the coupling between bilayers is weak, evidenced by anisotropic transport properties [110]. The preferable cleaving plane is along the $[100]$ plane, between adjacent SrO layers, as in Sr_2RuO_4. Figure 2.13(b) shows a top view of the crystal structure of $Sr_3Ru_2O_7$, where the in-plane octahed-

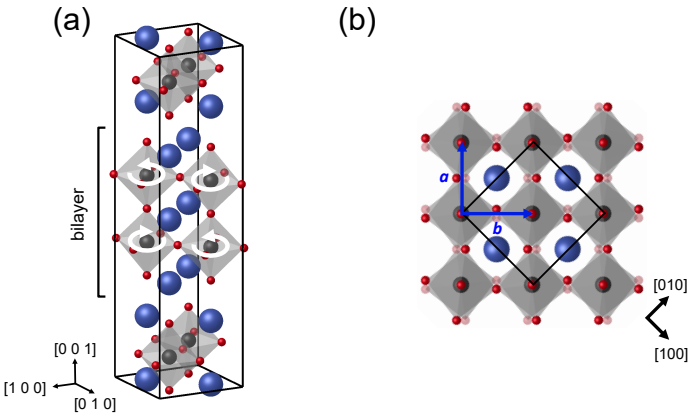

Figure 2.13: **Crystal structure of $Sr_3Ru_2O_7$.** (a) The orthorhombic unit cell of $Sr_3Ru_2O_7$. (b) Top view of a bilayer, showing opposite rotation between the top and bottom RuO_6 octahedra. The bottom layer is shown with transparency. The black square indicates the 2D unit cell and the blue arrows the pseudo-tetragonal axes a and b.

ral rotation is visible. The square shows the 2D unit cell for a single bilayer, with the pseudo-tetragonal lattice vectors shown as a and b.

Fermi surface and electronic structure

The Fermi surface of $Sr_3Ru_2O_7$ can be constructed from that of Sr_2RuO_4 by including the doubling of the unit cell, due to the octahedral rotation, and bilayer splitting due to the presence of the second RuO_2 layer in a single bilayer unit of $Sr_3Ru_2O_7$. The unit cell of the bilayer in $Sr_3Ru_2O_7$ has 4 Ru^{4+} ions, each with four electrons partially filling the three t_{2g} orbitals of each atom, resulting in a total of 12 orbitals per unit cell [182]. However, according to ARPES [183] and quantum oscillations measurements [182, 184], the Fermi surface of $Sr_3Ru_2O_7$ has six bands, half of the expected bands.

Figure 2.14 shows the Fermi surface of $Sr_3Ru_2O_7$ measured by ARPES, from Tamai *et al.* [183] showing the six Fermi pockets: δ, a circular pocket centered around the Γ-point of $d_{x^2-y^2}$ orbital character; α_1 and α_2, of d_{xz}/d_{yz} character; γ_1 and β centered around the M-point, due to the mixing of d_{xz}/d_{yz} with d_{xy} orbitals, with the β band with stronger d_{xz}/d_{yz} orbital character; and the small γ_2 pockets around the X-point of d_{xy} character. Both ARPES and quantum oscillations show quasiparticle mass enhancement, with effective masses between $5.6 - 10.1\ m_e$, where the lighter band corresponds to the β pocket and the heavier band to the α_2 pocket. The energy-momentum cuts of the bands from ARPES show a vHs at -4 meV [183, 185] around the X-point of the Brillouin zone, from the dispersion of the γ_2 pocket.

DFT calculations within the local density approximation using the orthorhombic unit cell of $Sr_3Ru_2O_7$ fairly reproduce the Fermi surface from ARPES [186]. The renormalization factor to

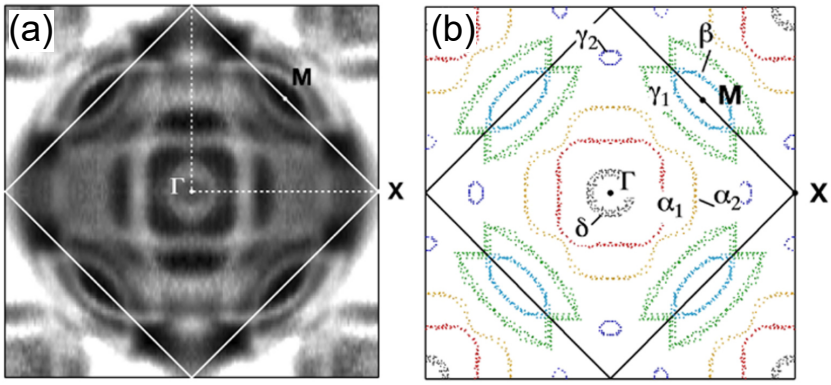

Figure 2.14: **Experimental Fermi surface of $Sr_3Ru_2O_7$.** (a) Fermi surface of $Sr_3Ru_2O_7$ measured by ARPES. (b) Pockets extracted from (a). The lines indicate the two-atom unit cell. The bands are label in agreement with quantum oscillatons nomenculature. Reproduced with permission from Tamai *et al.* [183].

correct for the Fermi velocities found in ARPES is larger than in Sr_2RuO_4, and to achieve good agreement requires band-dependent renormalizations to be applied [187]. The bandwidth of the δ band around the Γ-point is ~ 20 times lower than the one predicted by DFT. The band structure in $Sr_3Ru_2O_7$ shows a slight k_z-dispersion due to the interlayer coupling that makes the planes $k_z = 0$ and $k_z = \pi$ slightly different from each other [183, 186].

The effective masses from ARPES are consistent with the ones obtained in quantum oscillation measurements, indicating that the Fermi surface is representative of the bulk. However, the surface layer of $Sr_3Ru_2O_7$ undergoes a slight surface relaxation, with the increase of the octahedral rotation ($\sim 12^\circ$) and possibly a small tilt ($\lesssim 2.5^\circ$) at low temperatures [28]. It preserves the bulk unit cell, which, compared to Sr_2RuO_4, makes it more difficult to distinguish between surface and bulk bands in ARPES, where small changes to the band structure cannot be excluded.

Metamagnetism and quantum criticality

$Sr_3Ru_2O_7$ is a paramagnetic metal with a strongly correlated Fermi-liquid ground state at low temperatures. Its transport properties are highly anisotropic, with the resistivity along the c-axis two orders of magnitude larger than the in-plane resistivity with $\rho_c/\rho_{ab} \sim 300$ at 0.3 K [110]. It has a large Wilson ratio, $R_W > 10$, implying that $Sr_3Ru_2O_7$ is close to a ferromagnetic instability [110]. As a function of magnetic field H, it shows a sharp increase in magnetization, undergoing a metamagnetic phase transition associated with nematicity of the electronic states and a quantum critical end point [15, 17, 18].

The details of the metamagnetic transition in $Sr_3Ru_2O_7$ are extremely sensitive to disorder. Single crystals of $Sr_3Ru_2O_7$ with residual resistivity of $\rho_{res} = 2.3 - 5\ \mu\Omega$cm, show a metamagnetic

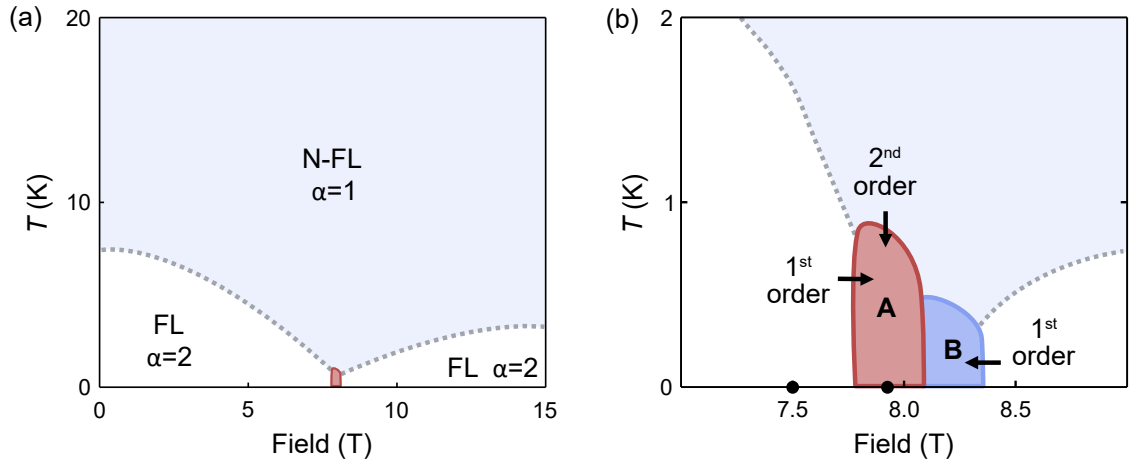

Figure 2.15: **Phase diagram of $Sr_3Ru_2O_7$.** (a) Sketch of the phase diagram of $Sr_3Ru_2O_7$ for $\mathbf{H}||c$-axis, based on the coefficient of the resistivity measurements from Ref. [16]. The dotted lines indicate the smooth boundaries between Fermi liquid (FL) and non-Fermi liquid (N-FL) behaviors. The metamagnetic phase seen in high-purity samples ($\rho_{res} < 1$ $\mu\Omega$cm) is shown in red. For lower-purity samples ($\rho_{res} = 2.3-5$ $\mu\Omega$cm), instead of this phase, there is a QCEP at ~ 8 T. (b) Low-temperature phase diagram of high purity single crystals of $Sr_3Ru_2O_7$, focusing on the metamagnetic phases. The black circles indicate the two QCEP. Sketch based on Ref. [17, 190, 192].

transition below 1.3 K at ~ 5 T, for $\mathbf{H}||ab$ plane [15, 188], corresponding to a first-order phase transition. Tilting the field out of plane towards the c-axis pushes the metamagnetic field to ~ 8 T and suppresses the transition temperature to < 100 mK, ending in a quantum critical end point (QCEP) [16]. The presence of quantum fluctuations in the vicinity of the QCEP is indicated by a change from Fermi liquid behavior ($\rho(T) = \rho_{res} + AT^{\alpha}$, with $\alpha = 2$) at low T and low fields to non-Fermi liquid behavior ($\alpha \sim 1$) in the field range of the transition, recovering FL behavior at higher fields [16], as illustrated in Figure 2.15(a). In samples of higher purity, $\rho_{res} < 1$ $\mu\Omega$ cm, a metamagnetic phase (A phase) appears below 1 K for $\mathbf{H}||c$ in the field range $7.8-8.1$ T, enclosing the quantum critical end point [17, 18, 189], red region in Figure 2.15(a). This phase has well-defined phase boundaries, Figure 2.15(b), with two lines of first-order phase transitions on each side of the field range and a line of second-order phase transitions with decreasing temperature. The purest samples of $Sr_3Ru_2O_7$ show a second phase (B phase) in the high field range of $8.1-8.5$ T [190] with a lower onset temperature of 0.6 K, and a second metamagnetic QCEP at ~ 7.5 T [191, 192].

The metamagnetic phase in $Sr_3Ru_2O_7$ is characterized by anomalies in transport and thermodynamic measurements. In a.c. magnetic susceptibility measurements, two peaks are observed at the field boundaries of the metamagnetic transition, consistent with first-order phase transitions [17]. When the magnetic field is applied parallel to the c-axis, the electrical resistivity shows anomalous behavior at 100 mK characterized by a step-like increase as it enters the meta-

magnetic phase at ~ 7.8 T, approximately doubling in value, and a sudden decrease as it leaves it at ~ 8.1 T for current $\mathbf{I}$ applied along the a and b axes [17](see axes definition in Figure 2.13(b)). However, if the field is rotated towards one of the in-plane axes by a small angle, say the a-axis, the resistivity becomes anisotropic. If the current is applied along the a-axis, similar behavior to when the field is out-of-plane is observed, whereas if the current is applied along the b axis the high resistivity regime is not observed, giving rise to an easy direction for conduction [18]. The easy direction is determined by the in-plane component of the magnetic field, if the magnetic field is oriented along the b-axis, then the a-axis becomes the easy direction for conduction. This occurs at both the A and B phases [193] in Figure 2.15(b), and for a small range of angles from the c-axis, $0 < \theta < 40°$. Elastic neutron scattering measurements for $\mathbf{H}||c$ puts an upper bound of 4×10^{-5} Å to any structural difference between the a and b lattice constants in the anomalous resistivity region [18]. This behavior is consistent with the formation of a novel quantum phase, an electron nematic phase that breaks rotational symmetry, in the vicinity of the quantum critical end point. Linear magnetostriction measurements under $\mathbf{H}||c$ show three step-like increases along the c-axis at 7.5 T, 7.8 T and 8 T, corresponding to the fields of the second QCEP and the boundaries of the metamagnetic A phase, indicating a strong magnetoelastic coupling along the c-axis [194], whereas along the ab-plane the observed jump in linear magnetostriction is five times smaller [195].

The specific heat at zero field shows a broad maximum below 20 K, attributed to an increase of spin fluctuations near a field-driven quantum phase transition [196]. The temperature T^* of this broad maximum is suppressed towards $T = 0$ K with increasing magnetic field, resulting in the divergence of the specific heat at low temperatures as the metamagnetic phase is approached. The divergence of the specific heat [197] is of the form $C/T \propto h^{-1}$, with $h = (H - H_c)/H_c$ where H_c is the critical field, in disagreement with the predicted trend from the renormalization group description of QCEP [91], discussed in section 2.1.5. Upon crossing the metamagnetic phase at higher fields (> 8.1 T), T^* reemerges and moves towards higher temperatures. Approaching the metamagnetic phase at constant field by decreasing the temperature shows $C/T \propto \log(T)$ [198]. Magnetocaloric measurements identify jumps in the entropy at the boundaries of the metamagnetic phase transition, suggesting that the formation of the metamagnetic phase is a way for the system to avoid a singularity in the entropy near the quantum critical end point. In addition, at 1.5 K, above the phase transition, the entropy shows a peak at the critical field of 8 T, in agreement with an approach to quantum criticality [197].

Inelastic neutron scattering measurements indicate a strong competition between ferromag-

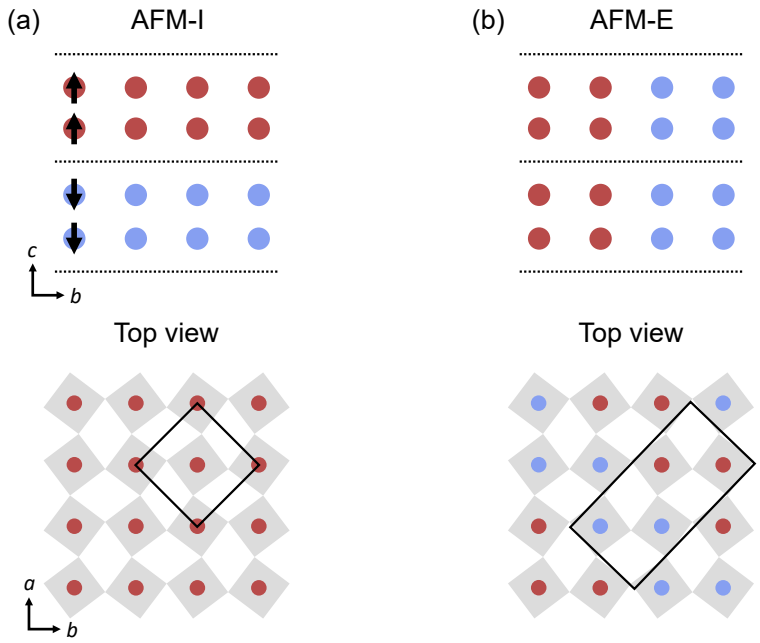

Figure 2.16: **Metastable AFM orders in $Sr_3Ru_2O_7$.** (a) Illustration of the AFM-I order. The top shows a side view, where two bilayers are visible. The magnetic moments align ferromagnetically along the bilayer, but antiferromagnetically between adjacent bilayers. The bottom shows a top view. The black square shows the unit cell. (b) Illustration of the E-type AFM order. The orientation of the spins is the same between adjacent bilayers. The bottom shows a top view, where the zigzag patterns of the spins is visible. The black rectangle shows the unit cell. Red and blue circles indicate up and down spins, respectively.

netic (FM) and antiferromagnetic (AFM) fluctuations throughout its phase diagram. FM fluctuations are observed to dominate at $T \gtrsim 20$ K [199], and incommensurate AFM fluctuations prevail at lower temperatures in a wide range of applied magnetic fields [200]. This competition between ferromagnetic and antiferromagnetic ordering is visible in DFT calculations [186, 201, 202]. Both LDA and Perdew-Burke-Ernzerhof (PBE) predict a ferromagnetic ground state for $Sr_3Ru_2O_7$, however, calculations considering different magnetic orders show that some are almost degenerate to the FM order. These include the AFM-I order [201], Figure 2.16(a), with FM in individual bilayers but AFM between adjacent bilayers, and E-type AFM order, Figure 2.16(b), which is the lowest energy AFM-ordered metastable state [202]. While the AFM-I order retains the surface unit cell, in the E-type order, since the spins are aligned in a zigzag pattern, the unit cell changes, drastically modifying the electronic structure. For the E-type order, the Fermi surface will appear with C_2-symmetry due to the new symmetry of the unit cell.

Magnetic neutron scattering measurements [190] show the appearance of ordered spin-density waves (SDW) in the A and B phases. In the A phase, at $B = 7.95$ T and $T < 1$ K, a magnetic Bragg peak at $\mathbf{q}^A_{\mathrm{SDW}} = (0.233, 0, 0)$, in units of $2\pi/a$, is observed, which changes to $\mathbf{q}^A_{\mathrm{SDW}} = (0.218, 0, 0)$ at $B = 8.15$ T, in the B phase. These q-vectors are consistent with a linear transverse SDW aligned with one of the in-plane axes a, b. When the magnetic field is applied parallel to the c-axis, at

the A phase, two sets of magnetic Bragg peaks are detected, at $(\pm 0.233, 0, 0)$ and $(0, \pm 0.233, 0)$, indicating the presence of domains of SDW propagating along the a and b axis, respectively. When the field is tilted to have a component parallel to a, entering the regime of anisotropic resistivity, the peaks at $(0, \pm 0.233, 0)$ are completely suppressed, indicating that the SDW domains align along the in-plane component of the field. Rotating the field towards the b-axis suppresses the domains along the a-axis, showing that the domain populations can be tuned with an in-plane magnetic field. The tuning of the orientation of the SDW with an in-plane magnetic field can thus be associated with the anisotropic behavior found in resistivity, where the easy direction for conduction occurs in the direction perpendicular to the SDW.

Microscopic theories for metamagnetism and quantum criticality

Several interpretations for the emergence of the nematic ordering at the metamagnetic phases have been proposed. One proposal considers that the nematic phase is a spatially modulated magnetic state analogous to a Fulde-Ferrell-Larkin-Ovchinnikov (FFLO) phase proposed for superconductivity under magnetic field [203, 204]. Another interpretation follows an analogy with itinerant ferromagnetism where the itinerant metamagnetism appears due to a polarization of the spin-up and spin-down Fermi surfaces at the critical field so that the fluctuations can be thought of as fluctuations of the Fermi surface itself [15]. Electron nematicity could then appear via a Pomeranchuk instability, where the electronic interactions result in a sudden distortion of the Fermi surface for one spin species, inducing a different symmetry than the Fermi surface of the other spin species [18]. Indeed, in a metal, it has been shown that electron nematic order can drive metamagnetic transitions via topological changes to a spin-up Fermi surface close to a vHs, in an increasing magnetic field, while the spin-down Fermi surface changes continuously [87].

Different microscopic theories have been proposed to describe the emergence of nematicity at the metamagnetic phases and its relationship to the quantum critical end point in $Sr_3Ru_2O_7$, from the point of view of Fermi surface distortions. There are two different approaches for metamagnetic and nematic phase transitions driven by the proximity of the vHs to the Fermi energy [205–208], with some theories arguing that the vHs on the γ band and of d_{xy} orbital character is the one governing the metamagnetic phase transition [205, 206] and some that it is the one due to the quasi-1D states of d_{xz}/d_{yz} character of the α_1 and α_2 bands [207, 208].

The idea behind the first approach is that the octahedral rotation in $Sr_3Ru_2O_7$ largely affects the d_{xy} states in relation to the Fermi surface of Sr_2RuO_4, pushing the d_{xy} vHs below E_F and changing its symmetry from a two-fold vHs in Sr_2RuO_4 to four-fold in $Sr_3Ru_2O_7$, due to the doubling of the

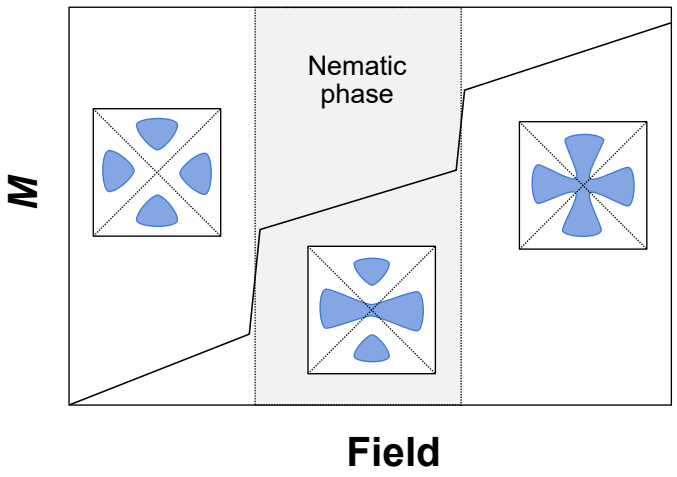

Figure 2.17: **Illustration of the Fermi surface topological changes associated with magnetization jumps.** Sketch of the magnetization as a function of magnetic field in $Sr_3Ru_2O_7$, showing the jumps in magnetizations that determine the boundaries of the metamagnetic phase. From the model developed by Puetter *et al.* [205], the first jump occurs when the vHs along one of the spatial directions is moved across E_F, becoming C_2 symmetric. Increasing the magnetic field further pushes the other vHs across E_F, restoring C_4-symmetry to the Fermi surface, suppressing the nematic phase, and a second jump in the magnetization appears. Illustration based on the phase diagram in ref. [205].

unit cell. Puetter *et al.* [205] developed a mean-field theory in which nematic order is accompanied by jumps in the magnetization, by focusing on the γ_2 band at the X-point of the Fermi surface of $Sr_3Ru_2O_7$. Starting from a tight-binding model with the three t_{2g} orbitals, spin-orbit coupling and unit cell doubling due to the octahedral rotations, they find from a mean-field theory that a finite nearest-neighbor interaction promotes the nematic state, whereas the on-site intraorbital interaction promotes ferromagnetism. The application of a magnetic field parallel to the c-axis makes the γ_2 band anisotropic, driving one of the γ_2 vHs (along one direction) close enough to E_F to induce a nematic transition, resulting in a jump in the magnetization and thus a metamagnetic transition. Increasing the field further pushes the other vHs to higher energies, restoring C_4-symmetry and suppressing the nematic state, accompanied by a second jump in magnetization (see Figure 2.17). This implies that the nematic order is sensitive to the location of the vHs and the balance between competing instabilities, which are controlled via the octahedral rotation and spin-orbit coupling.

In the second approach, the idea is that the major difference between Sr_2RuO_4 and $Sr_3Ru_2O_7$ rests in a large bilayer splitting in $Sr_3Ru_2O_7$, which strongly affects the d_{xz}/d_{yz} states. In this picture, the nematic and metamagnetic phase transitions arise as a consequence of orbital ordering between the quasi-1D bands, α_1 and α_2. Lee *et al.* [207], extend the Pomeranchuk instabilities into multiorbital systems, describing the nematic order as arising from the orbital ordering of the quasi-1D bands, where the magnetic field pushes the majority-spin van Hove singularity of the d_{xz}/d_{yz} states closer to the Fermi energy, which triggers the nematic distortion in the majority-

spin Fermi surfaces. Raghu *et al.* [208] start from a tight-binding model on a bilayer (one layer of $Sr_3Ru_2O_7$) to take into account bilayer splitting and construct a mean-field theory considering only the d_{xz}/d_{yz} states. They find that when the on-site Coulomb repulsion between two electrons on the same orbital (U) dominates the on-site Coulomb repulsion between two electrons in different orbitals (V), ferromagnetism is promoted. However, if $U \approx V$, then the application of an increasing magnetic field induces a metamagnetic transition where nematic order develops, and by increasing the field further, a second metamagnetic transition occurs, destroying the nematic phase, as observed in the resistivity experiments. By introducing a spin-orbit coupling term that depends on the angle θ between the magnetic field $\mathbf{H}$ and the c-axis while treating the d_{xy} band as a free-electron system, the model was able to account for the angle-dependent metamagnetic transitions with increasing θ. The nematic phase arises due to distortions to the α_1 and α_2 Fermi pockets around the Γ-point, where the contribution from the bilayer splitting is largest.

Both approaches appear complementary to each other. While one neglects bilayer splitting [205, 206], the other overlooks the effects of octahedral rotation [207, 208], when both are necessary to understand the differences between the bilayer, $Sr_3Ru_2O_7$, and the single layer, Sr_2RuO_4, ruthenates. It has been shown that the change in symmetry of the d_{xy} vHs between Sr_2RuO_4 and $Sr_3Ru_2O_7$, which results in a different divergence law of the peak in the DOS, can accurately capture the divergence in the specific heat without needing to invoke quantum fluctuations on approaching the metamagnetic phase [95], thus indicating that the shape of the γ_2 vHs and its proximity to E_F are important to describe the low-energy states of $Sr_3Ru_2O_7$. One way to distinguish between these two scenarios is via spectroscopic measurements. Quasiparticle interference (QPI) simulations [209] on a tight-binding model of $Sr_3Ru_2O_7$ taking into account bilayer splitting, octahedral rotations and on-site spin-orbit coupling, suggest that the QPI from the d_{xy} band should be suppressed at the surface due to its in-plane nature and that the scattering due to the d_{xz}/ d_{yz} bands should dominate. The resulting QPI is C_4-symmetric, and by including a nematic order parameter on the d_{xz}/ d_{yz} states, the scattering patterns become C_2-symmetric along the a and b directions. Using a scanning tunneling microscope to measure QPI across the critical magnetic field would allow distinguishing between the two cases. STM QPI measurements at 4 K on a Ti-doped $Sr_3Ru_2O_7$ sample show patterns consistent with dominant scattering vectors coming from the α_2 band [210].

Another way to distinguish between both scenarios is by performing first principle calculations including the effects of magnetic field. DFT calculations with LDA including spin-orbit coupling (SOC) and electron correlations by Behrmann *et al.* [211], on the orthorhombic unit cell, show

a Fermi surface that is C_2-symmetric along the [010] direction, mainly affecting the α_1 and α_2 pockets, with an avoided band crossing along one of the $\langle 010 \rangle$ directions, leaving a crossing point in the opposite direction, but still consistent with ARPES. This results in two inequivalent M and M' symmetry points in the Brillouin zone. In addition, the γ_2 band also shows a slight anisotropy along the $\langle 110 \rangle$ directions, rendering the symmetry points X and X' along each direction inequivalent. Upon applying a magnetic field along the c-axis, metamagnetism is observed if both SOC and correlations are included in the calculations. They observe an interorbital charge transfer from d_{xy} to d_{xz}/d_{yz} with magnetic field. While the dominant d_{xy} part shows substantial paramagnetic response with field, the generally much smaller d_{xz}, d_{yz} terms exhibit paramagnetic/diamagnetic orbital response, which appears as a key microscopic building block for the metamagnetic behavior. With increasing field the vHss at the X-point are shifted up in energy, crossing the Fermi level and changing the topology of the γ_2 band in an anisotropic way between X and X'. The α_2 band also becomes distorted, shrinking and deforming along [100]. The density of states runs through several peaks at the Fermi energy, but not the same as just moving the Fermi level of the $H = 0$ band structure. The pockets of the γ_2 band become C_2-symmetric upon application of magnetic field in the metamagnetic region, recovering C_4-symmetry at larger fields, similar to the microscopic model of Puetter *et al.* [205].

To disentangle the role of quantum fluctuations near the quantum critical point in $Sr_3Ru_2O_7$, high-energy resolution spectroscopic data is necessary, to follow the density of states as the metamagnetic phase is approached. STM measurements [212] on $Sr_3Ru_2O_7$, for samples with a residual resistivity of $\rho_{res} \sim 7\ \mu\Omega$cm, show a partial gap around E_F, with a two-peak structure within ± 5 meV of the Fermi level. The topographies show a checkerboard intensity pattern similar to the one found at the surface of Sr_2RuO_4. The evolution of tunneling spectra from 0 T to 11 T shows a complex behavior, with shifts of the spectral density towards lower energies and the filling of states at the Fermi level with increasing field, not allowing a definite determination of the role of quantum fluctuations in the phases observed in $Sr_3Ru_2O_7$, calling for more detailed studies.

Effects of doping and lattice distortions

The ground state of $Sr_3Ru_2O_7$ can be tuned towards different magnetic orders by doping and lattice distortions. The substitution of Sr by Ca, $(Sr_{1-x}Ca_x)_3Ru_2O_7$, increases the octahedra distortions similar to Sr_2RuO_4, increasing the susceptibility towards ferromagnetism with an increased rotation and ultimately stabilising long-range antiferromagnetic order accompanied by tilting [19, 29]. On the other hand, Ru substitution by Mn, $Sr_3(Ru_{1-x}Mn_x)_2O_7$, reduces the oc-

tahedral rotations and shrinks the unit cell volume, with the octahedra rotation angle suddenly dropping to zero for $x > 0.16$ [213], resulting in a metal-to-insulator transition and E-type antiferromagnetic order (Figure 2.16(b)) [20, 214, 215]. Introducing magnetic impurities via doping with Fe, $Sr_3(Ru_{1-x}Fe_x)_2O_7$, also induces E-type antiferromagnetic order for concentrations $x \geqslant 0.03$ [21].

Cleaner ways to induce distortions to the lattice without disorder include hydrostatic pressure and uniaxial strain. Via hydrostatic pressure, the metamagnetic critical field for $\mathbf{H}||ab$, is tuned to higher fields, reaching ~ 10 T at a pressure of ~ 16 kbar, followed by the decrease in transition temperature, giving rise to another quantum critical end point [92]. Uniaxial strain applied along the c-axis induces ferromagnetism [22], while when applied in-plane, it enhances the metamagnetism and nematic behavior [30].

Chapter 3

Experimental technique and methodology

To fully comprehend the properties of strongly correlated electron systems, it is necessary to obtain information about both localized and delocalized states in real and momentum space, with high energy, spatial and k-resolution. This can be achieved in scanning tunneling microscopy (STM), where the local density of states of both occupied and unoccupied states of a sample can be directly measured in real-space, and momentum space information can be obtained via the Fourier transform of such images. The possibility of measuring at ultra-low temperatures (< 100 mK) and under high magnetic fields makes STM a powerful technique, where a large phase space can be probed, with extremely high-precision.

This chapter contains a brief introduction to the principles behind Scanning Tunneling Microscopy, based on the detailed descriptions found in references [216, 217]. Different types of STM measurements will be discussed, such as topography, spectroscopy and quasiparticle interference. The experimental setup used in this work is described in detail. Characterization of the properties and quality of the single crystals measured as part of this thesis is given.

3.1 Scanning tunneling microscopy

The concept behind scanning probe microscopy is simple: put a sharp tip very close to a surface and measure the interaction between them. In scanning tunneling microscopy, the quantity that is measured is the current $I_{\text{tip}-\text{s}}$ due to quantum tunneling of electrons through the vacuum barrier between a metallic tip and a sample when a voltage difference $V_{\text{set}}$is applied between them

[218, 219], as illustrated in Figure 3.1. This current is proportional to

$$I_{\text{tip}-\text{s}} \propto e^{-2\kappa d}, \qquad \text{with} \quad \kappa = \sqrt{\frac{2m_e\phi_{\text{eff}}}{\hbar^2}}, \tag{3.1}$$

where d is the tip-sample distance, ϕ_{eff} is a combination of the work functions of the tip and sample, m_e is the mass of the electron and $\hbar$ is the reduced Planck constant. Thus, the current is highly sensitive to changes in tip-sample distance d. The typical work function of a metal is ~ 5 eV, resulting in a decrease of one order of magnitude in the current when the tip-sample distance d is increased by only 1Å. By attaching the tip to a piezoelectric scanner, the tip can be scanned over the sample surface, where its topographic features will result in changes in the distance d, and consequently, to measurable changes in $I_{\text{tip}-\text{s}}$. Comparing the tip-sample current with a preset current via a feedback loop, the height profile of the topography of the surface is obtained. As it will be discussed in the following sections, STM is not only sensitive to topographic changes, but it can probe the local density of states of the sample, having access to its electronic properties for both occupied and unoccupied states.

The first prototype of using quantum tunneling current has a probe was developed by Young *et al.* [220], but it was Binnig, Rohrer and coworkers [218] that first measured the dependence of Eq. 3.1 between a Tungsten tip and a Platinum sample and were able to achieve atomic resolution for the first time [221, 222] (winning the Nobel prize in Physics in 1986). Since then, STM has become one of the most important experimental techniques in the study of strongly correlated electron materials. From atomic manipulation [223, 224], observation of quantum confinement [225], standing waves due to quasiparticle interference at defects [226–228], STM has played a

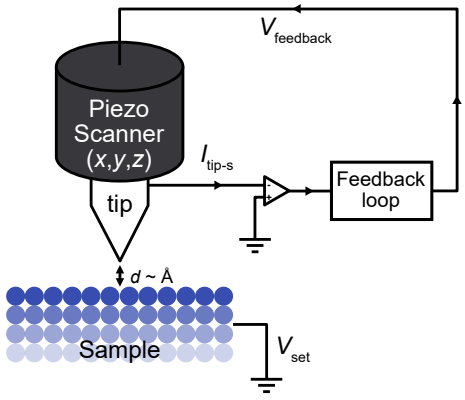

Figure 3.1: **Illustration of STM.** A sharp metallic tip is put a few ångström away from a sample surface. When a bias voltage V_{set} is applied between tip and sample, a current $I_{\text{tip}-\text{s}}$ flows through the vacuum between the two. The tip is scanned over the surface along (x,y) by a piezoelectric scanner which also controls the tip-sample distance, d, due to a feedback loop that applies V_{feedback} to the scan piezo to keep the current at a preset value I_{set} .

crucial role in shedding light on problems such as the symmetry of the order parameter of High-Tc [47] and iron-based superconductors [229], Kondo systems [230, 231], magnetic textures [232, 233] and magic angle graphene [98, 100], just to name a few examples.

3.1.1 Measurement modes

Topography

There are two ways of obtaining a topographic image of the surface of a sample using STM: either the tip height z is kept constant and the changes in current are measured as the tip is scanned (constant-height imaging, Figure 3.2(a)) or the current is kept constant and the height z of the tip is changed to maintain a constant current while scanning (constant-current imaging, Figure 3.2(b)).

In constant-height imaging, Figure 3.2(a), the tip is scanned at a constant height z over the surface of the sample. Variations in the surface topography change the tip-sample distance d as the tip is scanned, changing the current $I(x,y)$ accordingly. Since the tunneling current depends on the local density of states (LDOS), regions of high electronic density will result in an increase in the current, exemplified by the dark circle in Figure 3.2(a). As it will be discussed in Section 3.1.2, this imaging mode provides a two-dimensional image that is a measurement of the integrated density of states in the plane above the surface in which the tip is moving.

In constant-current imaging, Figure 3.2(b), a feedback loop is used to extend/contract the piezo scanner, decreasing/increasing the tip-sample distance, in order to maintain the current at a constant value I_{set}. By knowing the calibration of the piezo scanner, the exact amount z by which the tip-sample distance is adjusted is known, and a real-space image of the surface topography is

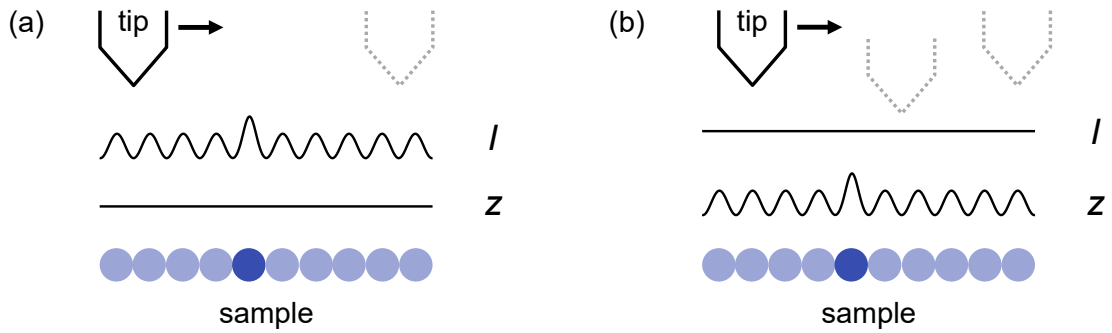

Figure 3.2: **Illustration of imaging modes.** (a) Constant-height imaging mode. The tip height z is kept constant while it is scanned over the surface (constant z-channel). All the topographic information will appear on the current I channel. An impurity with high DOS (dark circle) will show as an increase in current at its position. (b) Constant-current imaging mode. The tip height z is changed due to a feedback loop to keep the current constant at a setpoint value, I_{set}. The current I channel is now ideally a constant line, while all the topographic information is in the z-channel. On top of an impurity with high DOS, the tip will retract to keep the current constant, which could otherwise increase due to the increased density of states.

obtained, $z(x,y)$. Figure 3.2(b) shows the ideal case of a constant-current scan, where the current channel shows a straight line, whereas the z channel contains all the topographic information. In this case, an impurity with high DOS will appear with a larger apparent height despite being at a lower or at the same height as the atomic lattice, because the feedback loop will retract the tip to keep the current constant. This has to be taken into account in the interpretation of STM constant-current images, in order to distinguish true topographic features from local changes in the DOS.

Both methods have their advantages and disadvantages. On one hand, in constant-current imaging, the feedback loop can accommodate abrupt topographic changes, such as step edges, and counter-acts on the effect of thermal drift, keeping the tip always at about the same distance above the surface and therefore preserving the tip shape and properties. On the other hand, in the constant-height imaging mode, the tip can slowly drift towards or away from the sample, possibly touching the surface or loose tunneling after long periods of time. In this mode, the tip is not able to react to rapid changes in the topography, risking destroying not only its apex but also the surface itself. Therefore, constant-current imaging is more suitable for large area scans, and constant-height mode is usually used in areas of just a few nm. The advantage of constant-height imaging is that it is in principle faster than the constant-current mode because the scanning speed is only limited by how fast one can record the current, whereas in constant-height mode it is limited by how fast the feedback loop is. In this work, the topographies shown were measured using the constant-current mode, unless stated otherwise.

Spectroscopy

In scanning tunneling spectroscopy (STS), the local density of states is measured at a fixed position on the surface of the sample by sweeping the tip-sample bias V and recording the response of the current I. This is a consequence of the differential conductance, $g(V) = \mathrm{d}I(V)/\mathrm{d}V$, being proportional to the density of states of the sample, as it will be shown in Section 3.1.2.

To measure $g(V)$ directly, a lock-in amplifier is used to overlap an AC-voltage of frequency ω, $V_{AC} = V_L \cos(\omega t)$, with the tip-sample bias V. As a consequence, the tunneling current I will now have a modulation with the same frequency. Its amplitude can be determined from the first order term in the Taylor expansion,

$$I = I(V) + \frac{dI}{dV}(V) V_L \cos(\omega t) + O(V_{ac}^2), \tag{3.2}$$

where one sees that the component at frequency ω is proportional to $g(V)$. The amplitude V_L

will act as an averaging window on the measurement of $g(V)$, and so this approximation will be valid if $g(V)$ is a slowly varying function, that is, if it does not vary over smaller voltage scales than V_L. In addition, to resolve sharp features in the LDOS, V_L should not exceed the thermal energy k_BT, to ensure enough energy resolution, otherwise, the modulation will dominate and the true $g(V)$ will not be resolved.

Differential conductance maps

Since the tip is a local probe, a $g(V)$ spectrum can be taken at every point of an image of the surface, while simultaneously recording the topography. At each point, a V_{set} is applied to the sample, the feedback loop adjusts the tip position to keep the current at I_{set}, and its displacement z is recorded. After stabilising for a few ms, the feedback loop is switched off, the voltage is swept over a chosen energy range and both $I(V)$ and $g(V)$ are recorded. As it will be discussed in Section 3.1.2, one effectively gets two-dimensional real-space images that are proportional to the LDOS of the sample, at each bias voltage, where any spatial changes will be mapped.

3.1.2 Principles

Tunneling current

Consider a positive bias voltage V applied to the sample. The Fermi level of the sample, E_{F}^{s}, is lowered by an energy eV with respect to the Fermi level of the tip, E_{F}^{t}, as illustrated in Figure 3.3. Electrons can now tunnel through the vacuum barrier over an energy window of width $eV + k_{\text{B}}T$, with k_{B} the Boltzmann constant. The total tunneling current will be dominated by the current $I_{t\to s}$

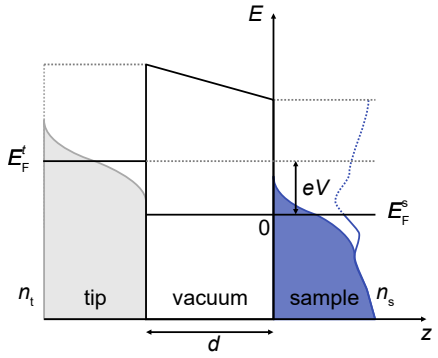

Figure 3.3: **Sketch of the tunneling process.** Diagram of a tip with constant DOS, n_t, at a distance d from a sample with DOS n_s. The applied bias V shifts the Fermi level of the sample, E_{F}^{s}, by an energy eV below the Fermi level of the tip, E_{F}^{t}. The tunneling current will be dominated by the flow of electrons from the occupied states of the tip (gray shaded area) through the vacuum potential barrier to the unoccupied states of the sample. Due to thermal excitations, there will be a small contribution to the current from electrons tunneling from the sample occupied states (shaded blue area) above E_{F}^{s} to the tip.

due to the flow of electrons from occupied states on the tip to unoccupied states on the sample. However, for finite temperatures, the probability of electrons flowing from sample to tip is non-zero and a current $I_{s\to t}$ will also contribute. Setting $E_{\mathrm{F}}^{\mathrm{s}}$ as the origin of the energy scale, and considering only elastic tunneling, the total tunneling current will be given by [216, 217]

$$I = \int_{-\infty}^{+\infty} \left[I_{t\to s}(\varepsilon) - I_{s\to t}(\varepsilon) \right] d\varepsilon = -\frac{4\pi e}{\hbar} \int_{-\infty}^{+\infty} |M|^2 n_s(\varepsilon) n_t(\varepsilon - eV) [f(\varepsilon - eV) - f(\varepsilon)] d\varepsilon. \quad (3.3)$$

where $-e$ is the electron charge, $|M|^2$ is the matrix element for the tunneling barrier, $n_s(\varepsilon)$ is the density of states (DOS) of the sample, $n_t(\varepsilon)$ is the DOS of the tip and $f(\varepsilon)$ is the Fermi-Dirac distribution. By doing measurements at low temperatures, the Fermi-Dirac distribution approximates a step function and the integral in the previous equation will only have non-negligible terms in an energy window $\varepsilon \in [0, eV]$, so that

$$I \approx -\frac{4\pi e}{\hbar} \int_0^{eV} |M|^2 n_s(\varepsilon) n_t(\varepsilon - eV) d\varepsilon. \quad (3.4)$$

Bardeen [234] showed that the tunneling matrix element, M, only depends on the properties of the wavefunction inside the barrier. For a one dimensional potential barrier of energy ϕ_{eff}, the modulus squared of M reduces to the transmission factor of the traveling wavefunction [217], such that $|M|^2 = T(\phi_{\mathrm{eff}}, d) \propto e^{-2\kappa d}$, recovering the behavior in Eq. (3.1). For low bias voltages, $|M|^2$ can be assumed to be constant in energy, and thus can be taken outside the integral. In addition, Eq. (3.4) shows that the total tunneling current is a convolution of both the tip and sample DOS. By using a tip with a featureless DOS in the relevant energy range of ± 200 meV (e.g. W or Pt-Ir), n_t is constant in energy and the total current becomes

$$I \approx C \int_0^{eV} n_s(\varepsilon) d\varepsilon, \qquad \text{with} \quad C = -\frac{4\pi e}{\hbar} |M|^2 n_t(0). \quad (3.5)$$

However, in STM the two electrodes (tip and sample) do not have the same surface area, with the tip being, ideally, atomically sharp. This implies that the tunneling current is highly localized at the sample surface. Tersoff and Hamann [235] showed that for a tip with a spherical apex, the current for low bias voltages ($V \sim 0$ V) becomes proportional to the LDOS of the surface at its Fermi level at the position of the tip $\mathbf{r}_t$, $n_s(\mathbf{r}_t, E_{\mathrm{F}}^{\mathrm{s}})$

$$I \propto \sum_n |\psi_n(\mathbf{r}_t)|^2 \delta(E_{\mathrm{F}}^{\mathrm{s}} - \varepsilon_n) \equiv n_s(\mathbf{r}_t, E_{\mathrm{F}}^{\mathrm{s}}), \quad (3.6)$$

where $\psi_n(\mathbf{r}_t)$ is the wavefunction of an electron in the sample of energy ε_n at position $\mathbf{r}_t$. Thus, by scanning the tip over the sample and measuring the current as a function of position $\mathbf{r}_t$, one obtains a real-space image of the local density of states at the Fermi level.

Differential conductance

From Eq. (3.5), the tunneling current is proportional to the integrated DOS of the sample. The differential conductance,

$$g(V) = C\frac{d}{dV}\left\{\int_0^{eV} n_s(\varepsilon)d\varepsilon\right\} \tag{3.7}$$

$$\propto n_s(eV), \tag{3.8}$$

is, therefore, directly proportional to the DOS of the sample at the energy eV, defined by the sample bias V. This is also valid for applied negative bias ($E_{\mathrm{F}}^{\mathrm{t}}$ lowered in relation to $E_{\mathrm{F}}^{\mathrm{s}}$), switching the energy range of interest to $-|eV| < \varepsilon < 0$. Thus, by sweeping the sample bias voltage V, the DOS of a sample for both occupied (negative bias) and empty (positive bias) states can be obtained as a function of energy. This is the principle of scanning tunneling spectroscopy.

The above equation is valid when the tunneling matrix element $|M|^2$ is constant in energy, which is obtained in the limit of small bias V. However, for many systems, the energy range of interest is not confined to a few meV around the Fermi level, and the energy dependence of $|M|^2$ becomes relevant. The tunneling matrix element is proportional to [236],

$$|M|^2 \propto \exp\left(-2\sqrt{\frac{2m\phi_{\mathrm{eff}}}{\hbar^2}}d\right). \tag{3.9}$$

For large voltages V, the effective tunneling barrier ϕ_{eff} becomes bias dependent. For a positive bias voltage applied to the sample, Figure 3.4, the Fermi level of the sample, $E_{\mathrm{F}}^{\mathrm{s}}$, lowers down in energy by an amount $eV/2$, whereas the tip Fermi level, $E_{\mathrm{F}}^{\mathrm{t}}$, is increased by the same amount. The effective tunneling barrier becomes

$$\phi_{\mathrm{eff}} = \frac{\phi_{\mathrm{t}} + \phi_{\mathrm{s}}}{2} + \frac{eV}{2} - \varepsilon, \tag{3.10}$$

where ϕ_{t} and ϕ_{s} are the work functions of the tip and the sample, respectively. This equation shows that for states at the Fermi level of the tip, $\varepsilon = eV$, the tunneling barrier is smaller (red arrow in Figure 3.4), resulting in a large tunneling matrix element $|M|^2$. On the other hand, for states with energy $\varepsilon = 0$, the tunneling barrier is higher, and $|M|^2$ is small (gray arrow in Figure 3.4).

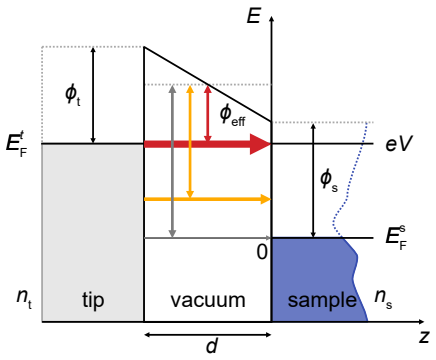

Figure 3.4: **Bias dependence of the tunneling matrix element $|M|^2$.** For a positive bias V applied to the sample, the electrons with energy eV at the tip see a potential barrier with lower height (red arrow) than the electrons with energy 0 (gray arrow). The tunneling matrix element is thus larger for electrons with energy eV, and these are the states which will dominate the integration in Eq. (3.4).

Thus, the terms which will dominate in the integral in Eq. (3.4) are the DOS of the tip at its Fermi level and the DOS of the sample at eV. It shows that for positive bias voltages, mainly the Fermi level of the tip probes the DOS of the sample, and thus the tunneling spectrum will show the features corresponding to the DOS of the sample. Since $|M|^2$ increases exponentially with the bias voltage, the tunneling spectrum will have an exponentially increasing background overlapping the sample DOS. For negative bias voltage, this scenario is flipped: the Fermi level of the tip is an energy eV below the Fermi level of the sample. The magnitude of $|M|^2$ will be larger for states at the sample Fermi level, which is now probing the DOS of the tip. It is thus necessary to have a tip with a constant DOS at the desired energy range, to guarantee that the features that appear in the tunneling spectrum are dominated by the sample density of states.

The stabilization of the tip height z by the feedback loop at a setpoint (V_{set}, I_{set}) introduces a constant background in the differential conductance $g(V)$ spectrum. To keep the current I constant means keeping the integral in Eq. (3.5) in the range 0 to V_{set}, at a constant value. If the LDOS of the sample n_s is not uniform along the surface, this integral will have different values at different tip positions (x,y). Therefore, the differential conductance $g(V)$ spectra taken at different tip positions (x,y) over the surface will have different backgrounds, which will be proportional to $\int_0^{eV_{\text{set}}} n_s(\varepsilon)d\varepsilon$. This is responsible for the well-known setpoint effect.

At low bias, the effects from the background due to the bias dependence of $|M(\varepsilon,V)|^2$ can be canceled out by dividing the differential conductance by the total conductance, $(\mathrm{d}I/\mathrm{d}V)/(I/V)$. Using Eq. (3.5) and Eq. (3.7),

$$\frac{\mathrm{d}I/\mathrm{d}V}{I/V} = \frac{C\frac{\mathrm{d}}{\mathrm{d}V}\{\int_0^{eV} n_s(\varepsilon)d\varepsilon\}}{\frac{C}{V}\int_0^{eV} n_s(\varepsilon)d\varepsilon} \propto \frac{Vn_s(eV)}{\int_0^{eV} n_s(\varepsilon)d\varepsilon}, \tag{3.11}$$

which is often called the Feenstra function [237]. Furthermore, since the denominator is given

by the integral of Eq. (3.5), it will also remove the effects due to the stabilizing setpoint conditions.

Inelastic tunneling

In addition to the elastic tunneling processes described above, the tunneling electrons can interact with bosonic excitations, such as phonons and magnons, at the sample surface. Consider a vibrational mode of energy $h\nu$, with ν its frequency, at the surface of the sample. For a tunneling electron of energy $e|V|$ lower than $h\nu$, only elastic tunneling channels are available. However, for $e|V| \geqslant h\nu$, the tunneling electron can give up some of its energy to excite the vibrational mode and still tunnel to empty states on the sample, opening up an inelastic tunneling channel. This additional tunneling channel increases the slope of the $I(V)$ curve, resulting in kinks in the differential conductance spectrum at $V = \pm h\nu$. The derivative of $g(V)$ as a function of voltage, $\mathrm{d}^2I/\mathrm{d}^2V$, will have sharp peaks at $\pm h\nu$ and their shape and intensity will depend on the details of the electron-phonon interaction. [238]

Energy resolution in STS

There are two main sources of energy broadening in STS. The first one is due to finite temperature, where the Fermi-Dirac distribution function in Eq. (3.3) will not be step-like and the integral has to be taken over infinity. As a consequence, rather than the approximation used in Eq. (3.7), the DOS of the sample has to be convoluted by the derivative of $f(\varepsilon, T)$, [239]

$$g(V,T) \propto \int_{-\infty}^{\infty} n_s(\varepsilon) \left[-\frac{\partial f(\varepsilon + eV, T)}{\partial V} \right] d\varepsilon. \tag{3.12}$$

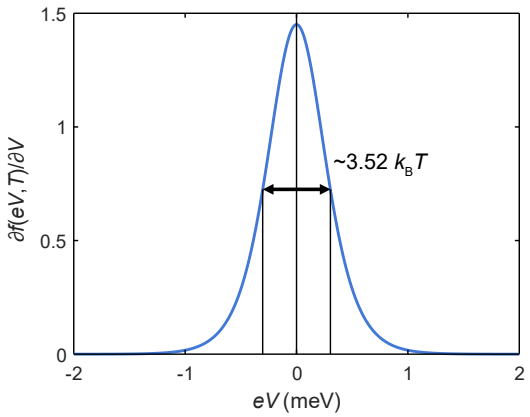

Figure 3.5: **Plot of the derivative of the Fermi-Dirac distribution at $T = 2$ K.**

At zero energy, the partial derivative of $f(eV,T)$ with respect to V is given by

$$\frac{1}{e}\frac{\partial f(eV,T)}{\partial V} = -\frac{e^{eV/(k_B T)}}{k_B T[1+e^{eV/(k_B T)}]^2}. \tag{3.13}$$

This function is plotted in Figure 3.5 as a function of energy, at a temperature of $T = 2$ K. Its full width at half maximum is $\sim 3.52 k_B T$, which will determine the energy broadening. The energy resolution at $T = 2$ K is 608 μV, being reduced to 15 μV by measuring at $T = 50$ mK.

The second source of energy broadening comes from the lock-in modulation. It induces an energy broadening that can be taken into account by convoluting Eq. (3.12) with a half-circle [239]

$$g'(V,T) \propto \int_{-\sqrt{2}V_L}^{\sqrt{2}V_L} g(V+\varepsilon,T)\sqrt{2V_L^2-\varepsilon^2}\,d\varepsilon. \tag{3.14}$$

Quasiparticle interference

The quasiparticles will interact with inhomogeneities at the surface, such as impurities and step edges. For a quasiparticle that scatters off an impurity, the wavefunction of the incoming quasiparticle will interfere with the wavefunction of the scattered quasiparticle, giving rise to standing wave patterns in the LDOS, which can be detected in differential conductance maps. An example of an $g(x,y,V)$ image is shown in Figure 3.6(a), taken at the surface of a PbS sample. Several impurities can be identified with clear modulations emanating from them. The wavevectors of these oscillations will carry information about the underlying electronic structure, and so will change with energy accordingly. Their dispersions can be obtained by taking the Fourier transform of a set of real-space $g(x,y,V)$ images taken at different bias voltages. Figure 3.6(b) shows a three-dimensional stack of the Fourier transforms of real space images from QPI measurements on PbS

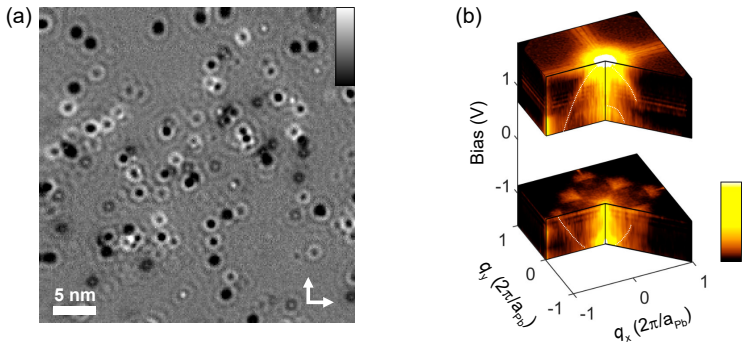

Figure 3.6: **Example of a $g(V)$ real-space image.** (a) A real space image of $\left(\mathrm{d}I/\mathrm{d}V\right)/(I/V)$ of the surface of PbS at 1.44 V. Clear oscillations are visible around the defects due to quasiparticle interference. (b) Three-dimentional stack of the Fourier transforms of real space $\left(\mathrm{d}I/\mathrm{d}V\right)/(I/V)$ images of PbS in the bias range ± 1.6 V. Cuts along the high symmetry directions [10] and [11] reveal the energy dispersion of the scattering vectors, highlighted by the dashed lines.

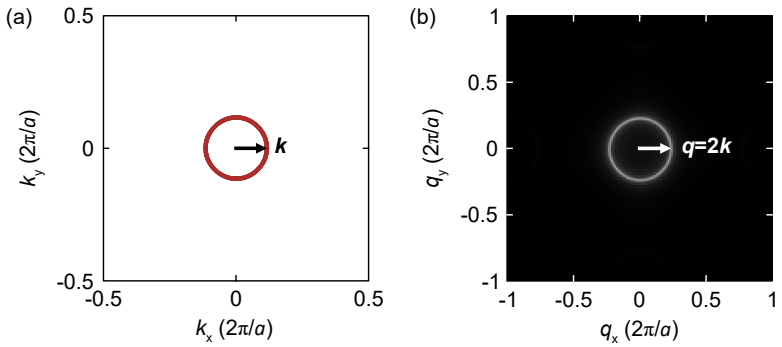

Figure 3.7: **QPI from a circular constant energy contour.** (a) Constant energy contour consisting of a parabolic band with momentum $\mathbf{k}$. (b) Scattering pattern with momentum $\mathbf{q} = 2\mathbf{k}$ resulting from the interference between states with $\mathbf{k}_i = -\mathbf{k}$ and $\mathbf{k}_f = \mathbf{k}$.

in the range ± 1.6 V, where the cuts along the high symmetry directions [10] and [11] reveal clear energy dispersions.

To get a better description, one can go back to the definition of LDOS in Eq. (3.6). The weighting factor in the LDOS is the square-modulus of the quasiparticle eigenstates $\psi_k(\mathbf{r})$. In the simple case where these eigenstates can be written as Bloch wavefunctions, $\psi_k(\mathbf{r}) = u(\mathbf{r})e^{i\mathbf{k}.\mathbf{r}}$, the modulus becomes $|\psi_k(\mathbf{r})|^2 = |u(\mathbf{r})|^2$, and the LDOS is sensitive only to modulations in real space. By definition of the Bloch wavefunction, $u(\mathbf{r})$ has the periodicity of the crystal lattice, and so the only modulation that will appear in the real space image is the atomic corrugation. However, the breaking of the translational symmetry by any inhomogeneity in the atomic lattice may induce coherent scattering between quasiparticle states with the same energy ε_n, but different momenta $\mathbf{k}_n$. As a result, an additional $\mathbf{k}$-dependent term appears in the quasiparticle eigenstates, resulting in energy-dependent standing waves [240]. This scattering leads to quasiparticle interference (QPI) patterns with wavevector $\mathbf{q}(\varepsilon) = \mathbf{k}_f(\varepsilon) - \mathbf{k}_i(\varepsilon)$ and wavelength $\lambda = 2\pi/q$, where $\mathbf{k}_i$ and $\mathbf{k}_f$ are the wavevectors of the initial and final states. These patterns appear as modulations in the LDOS and can thus be detected in the constant energy $g(x,y,V)$ real-space images obtained by STM [241], as seen in Figure 3.6(a). By calculating the Fourier transform of such images, one has access to the scattering vectors $\mathbf{q}$, obtaining information about the dominant scattering processes. This is illustrated in Figure 3.7(a) for the simplest case of a circular constant energy contour, where scattering occurs between states with $\mathbf{k}_i = -\mathbf{k}$ and $\mathbf{k}_f = \mathbf{k}$. The resulting pattern in q-space, the space of the scattering vectors, is thus a circle with a radius of $\mathbf{q} = 2\mathbf{k}$, retaining the shape of the original contour. Although QPI measurements are not directly sensitive to k-space, the underlying bandstructure may still be extracted from the energy dispersion of the detected q-vectors.

The setpoint effect discussed previously has to be taken into account in the analysis of QPI

measurements. Since the feedback loop is switched on each time the tip moves onto the next pixel, adjusting its z position according to $(V_{\text{set}}, I_{\text{set}})$, the $g(V)$ layers will have a background which depends on the bias setpoint. This effect can induce non-dispersive features in QPI measurements [242], which can sometimes be confused with real energy dispersions.

k_z scattering in QPI

At the surface, because there is no translational symmetry in the direction of the surface normal, k_z is not a good quantum number anymore, and only k_x and k_y are well-defined. As a consequence, QPI measurements are two-dimensional in nature and have been successful in unveiling the electronic properties of highly anisotropic materials, such as layered materials [47, 243, 244] where the band structure can be approximated as 2D, and of surface states, which by definition are two-dimensional [226, 227, 245, 246]. In these cases, considering only the $k_z = 0$ plane of the bulk band structure is enough to have a full description of the measurements.

However, if the band structure has some degree of k_z dispersion, considering the $k_z = 0$ plane alone will not allow to fully describe QPI measurements. In cubic systems, such as Cu and Au, besides the signatures from surface states, scattering due to the three-dimensional Fermi surface is also detected [247]. Scattering from subsurface defects is detected at the surface, which can only originate from a 3D electronic structure, where scattering between different k_z planes is possible [248]. Here, the k_z planes relevant for scattering are the ones where parts of the Fermi surface have group velocities with the same direction as the tip-defect distance vector [249]. This constrains the number of k_z planes needed to describe the QPI and implies that for surface defects, where the tip-defect distance vector is parallel to the surface, only the k_z planes with zero group velocity along z will contribute to scattering. This has been observed in iron-based superconductors, where the Fermi pockets have a slight k_z-dispersion, and considering only the $k_z = 0$ plane fails, but including the scattering from planes with zero Fermi velocity along z is needed to describe the observed QPI dispersion [250, 251]. For truly isotropic systems, such as the cubic PbS, Figure 3.6, the evolution of the constant energy surfaces is such that the relevant k_z planes for scattering change with energy, having energies with no states at $k_z = 0$, but strong QPI is detected [252]. This clearly shows that a naive description by only the $k_z = 0$ plane of the electronic structure fails in this case.

3.1.3 Surface preparation - possibility of surface reconstruction

When analyzing STM data, care has to be taken when interpreting the observations at the surface in terms of the properties of the bulk crystal. One of the limitations is the possibility of

surface reconstruction, in which the surface of a sample undergoes a structural distortion due to the breaking of translational symmetry in the z-direction. Origins of such distortions include stress between a relaxed surface layer and the bulk layers, freezing of a soft phonon mode at the surface layer or surface polarity. In these cases, the surface is not representative of the bulk system, and the properties being measured cannot usually be extended to the bulk properties. Early examples of the observation of such reconstructions by STM include the 7×7 reconstruction of the Si(111) surface [222] and the herringbone reconstruction of the Au(111) surface [253].

Certain strongly correlated electron systems, such as the ruthenates materials, are known to have surface reconstructions [24, 28, 254] that dramatically change their properties, potentially stabilizing new orders not present in the bulk material. In addition, since the vacuum interface is not a small perturbation and considering the extreme sensitivity of the electronic structure of strongly correlated electron systems to external stimuli, one should expect the electronic states at the surface to be different than the bulk even without reconstruction.

3.1.4 Milli-Kelvin STM instrumental setup

The STM used in this work operates at temperatures from 10 K to 20 mK, by means of a dilution refrigeration system, and in magnetic fields up to 14 T generated by a superconducting magnet. The dilution refrigerator, a Kelvinox 400MX, cryostat and superconducting magnet are from Oxford Instruments. There are three key aspects of the insert to which the STM is attached, described by Enayat *et al.* [232, 239]: (1) a clear shot tube from room temperature to the STM to allow for sample transfer/exchange without warming up, (2) *in-situ* cleavage mechanism, and (3) a pre-cool system to allow cooling down without the need for exchange gas.

The essential components of an STM are the tip, the piezo scanner, voltage contacts, walker, and sample holder, which makes the STM head, Figure 3.8(a). In this work, the tip was made of a Pt-Ir wire. It is attached to a piezoelectric scan tube composed of four quadrants responsible for movements in the (x, y) plane with one interior electrode for movements along z. The scanner is inside a triangular sapphire prism clamped between six piezo stacks that walk the tip macroscopically closer or farther away from the sample. This is mounted inside a sapphire body, to provide high mechanical stiffness and good thermal conductivity to the system. The sample holder will be clamped between the sapphire body and an aluminum oxide plate with the voltage contacts, Figure 3.8(b), which is placed over the sapphire body. I built a contact plate with four independent electrical contacts [255], where the outer tungsten contacts are used to apply the bias voltage, while the inner contacts can be used to perform different experiments on the sample or to allow

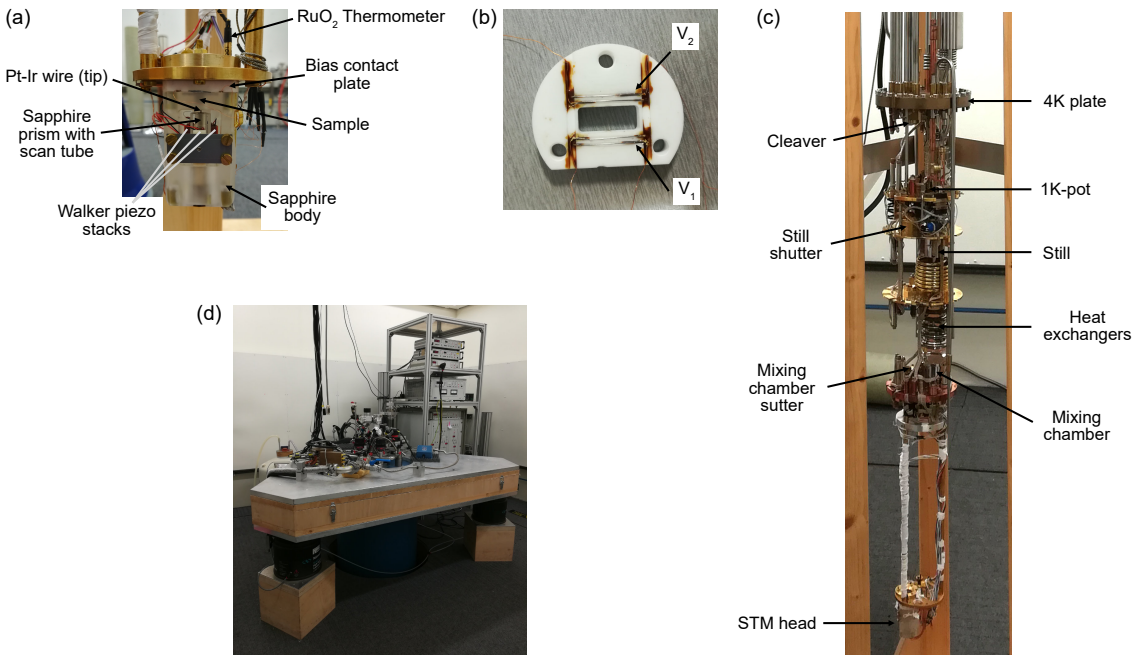

Figure 3.8: **STM insert and vibration isolation system.** (a) Photo of the STM head, with the essential parts labeled. (b) Four-contact plate. The outer contacts V_1 and V_2 are used to apply the bias voltage to the sample, the inner ones can be used for additional functionalities. (c) Dilution refrigerator insert. The different stages of the dilution fridge unit are indicated. The STM head is clamped to the bottom copper plate. (d) Photo of the vibration isolation table, which makes the system mechanically twice-decoupled from the environment.

the use of more complex devices [256]. A brass sample holder is used, with the sample glued on top with Epotek H20E conductive epoxy. For the *in-situ* cleaving of the sample, a rod is glued on top of it, which is knocked out by the cleaver mounted on the 4K-plate of the dilution fridge (see Figure 3.8(c)).

The STM head is attached to a copper plate, suspended by three gold-coated copper rods from a dilution refrigerator, Figure 3.8(c). The STM position in the copper plate is such that it is aligned with the line of sight for the sample transfer, making it 2 cm off-centered from the magnet main axis. However, this does not pose a major source of uncertainty, since it leads to a deviation from the desired applied magnetic field of less than 1% [239]. During ramping up and down of the magnetic field, a residual magnetic field of approximately 30 mT usually remains on the superconducting magnet. A Hall-probe is used to accurately measure the applied field, with an uncertainty of ± 1 mT.

The dilution refrigerator is composed of three stages: 1K-pot, still, and mixing chamber, shown in Figure 3.8(c). With the 1K-pot shut down, the STM operates at 10 K. When the 1K-pot system is running, the system is able to cool down to 1.2 K. Here, liquid He (LHe) flows from the main bath at 4.2 K through a small capillary into the 1K-pot where the vapor above the liquid

is pumped, cooling the system [257]. To reach temperatures down to 20 mK, a mixture of ^{4}He and ^{3}He is circulated through the insert. Firstly, the mixture passes through liquid nitrogen and LHe cold traps to trap any dirt which might have leaked from air. Then, the mixture enters the insert, goes through the 1K-pot where the ^{3}He and ^{4}He condensate, until it reaches the mixing chamber where a phase separation into concentrated and diluted phases occurs. The concentrated phase is rich in ^{3}He, whereas the diluted phase is rich in ^{4}He. When the concentration of ^{3}He is 6.6% in the diluted phase, the cooling power at the phase separation is at its maximum. Inside the mixing chamber, ^{3}He diffuses through the phase boundary from the concentrated phase to the diluted phase, while the ^{4}He acts as a superfluid background. ^{3}He flows to the still due to the pressure difference between the still and the mixing chamber. The still temperature ($\sim$ 800 mK) is such that ^{3}He is evaporated, while ^{4}He stays liquid. A roots pump is used to pump the ^{3}He out of the still line, through pipes installed outside of the cryostat at room temperature (RT). ^{3}He passes through a gas handling system, which controls the flow of the mixture. As the mixture circulates through the system, the cooling of the system increases, cooling it down to mK temperatures. The mixing chamber will be the coldest part of the insert, reaching 10 mK, and the STM head will be at $\sim$ 20 mK, cooling through good thermal coupling [232].

The only way in and out of the insert is through the sample transfer line of sight. To minimize thermal radiation from room temperature along the transfer path to the STM head, mechanic shutters are placed at each important stage of the dilution refrigerator: mixing chamber, still, and 4K-plate, where the cleaver also acts as a radiation shield. In addition, two radiation shields are used. The first shield is closed on top of the mixing chamber stage and the second one is fixed to the 4K-plate. Before putting the insert into the LHe cryostat, the inside of the shields is pumped to pressures $3.4 - 8 \times 10^{-6}$ mbar with a turbopump. This results in a cryogenic ultra-high vacuum when the system is cooled down.

To isolate the whole system as much as possible from external mechanical noise, the cryostat is mounted on a lead-filled table suspended on three pressurized air springs, Figure 3.8(d). This rests on a 17 t concrete slab which is also supported by pressurized air springs, making the instrument twice decoupled from the outside environment. The whole setup is inside an individual measurement box, which is also twice separated from the outside environment by two sets of soundproofed walls. All the vacuum and circulation pumps are outside the measuring box to minimize mechanical noise.

The energy resolution of the instrument was characterized by measuring the superconducting gap of Sn_4As_3 at a base temperature of $T = 50$ mK [258], Figure 3.9. A fully formed supercon-

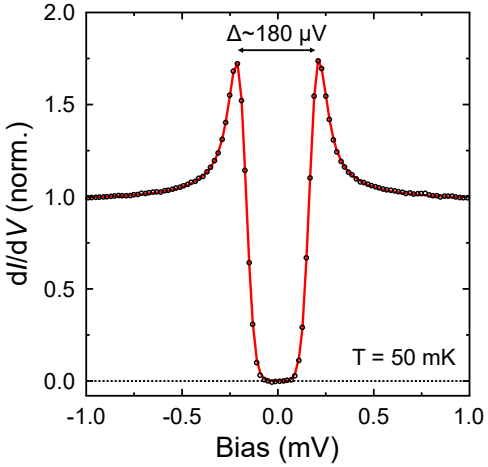

Figure 3.9: **Energy resolution at base temperature.** Tunneling spectrum measured at $T = 50$ mK, showing the superconducting gap of Sn_4As_3. The red line shows the fit of a Dynes function, taking into account both thermal and lock-in broadening. The fit gives a superconducting gap of width $\Delta \sim 180$ μV and an electronic temperature of $T_{\text{elec}} \sim 223$ mK (V_{set}= 0.8 mV, I_{set}= 400 pA, V_{L}= 25 μV).

ducting gap can be observed, with sharp coherence peaks. Fitting a Dynes function including both thermal and lock-in broadening using Eq. (3.12) and Eq.(3.14) [239] gives a superconducting gap of width $\Delta \sim 180$ μ V and an electronic temperature of 223 mK. Here, the electronic temperature is dominated by the lock-in modulation, V_{L}= 25 μV, whose contribution to broadening is larger than the temperature. This measurement puts an upper bound of 60 μeV of energy resolution, given by the width of the coherence peaks, which are the narrower features that can be resolved in Figure 3.9.

3.1.5 STM data analysis

While taking a topography, the hysteresis and thermal drift of the scanner will induce a small distortion in the image, so that the atomic lattice will appear slightly distorted. Due to the hysteresis, the tip will also drift slightly between scans, such that images taken in the same area will not appear fully aligned. To correct these imaging artifacts in topographies, I use two procedures. Firstly, the image distortions are corrected by a Lock-in algorithm (Appendix D). Secondly, the images are aligned via a translation transformation estimated using the phase correlation between the two images, from the Registration Estimator of the image processing toolbox in Matlab.

The time of data acquisition for a differential conductance map can take up to ~ 96 hours, depending on the lateral size of the image, pixel number, number of layers, and averaging time. To minimize the effects of the hysteresis of the scanner, we scan the same area for ~ 6 hours with the chosen setpoint conditions (V_{set}, I_{set}) before starting a map, but there is always going to be some residual piezo creep. As a result, and due to the long measurement time, the tip will drift over time

and the maps will show a distortion in the real-space images. To correct for this distortion, we use a geometrical transformation to map the atomic peaks of the map onto the atomic peaks of a perfect lattice, so that they are all at the same distance from $\mathbf{q} = (0,0)$ and with 90° between them, assuming a perfect square lattice, which is the case for Sr_2RuO_4 and, within experimental precision, for $Sr_3Ru_2O_7$.

To probe large area maps of lateral size ~ 90 nm, the maps were taken with undersampling, that is, with a pixel size lower than the one required for the atomic resolution. As a result, the atomic peaks appear aliased, that is, folded to a lower q-value. To recover the original position of the atomic peaks, an anti-aliasing algorithm is applied, shown in Appendix E. This is followed by the distortion correction described in the previous paragraph. Before setting up the maps, we made sure that the aliased atomic peaks do not interfere with the QPI signals we were interested in.

3.2 Sample preparation and characterization

To give the reader a complete picture of the samples measured in this work by STM, a short description of their growth and characterization will be given in this section. These were not performed by myself, and acknowledgment of those who have grown the samples and characterized them is given.

3.2.1 Sr_2RuO_4 single crystals

Crystal growth

The Sr_2RuO_4 single crystals used in this thesis were provided by Rosalba Fittipaldi, Veronica Granata and Antonio Vecchione, from CNR-SPIN, Italy. The crystals were grown using a commercial image furnace with double-elliptical mirrors and two 2.0 kW halogen lamps, by the floating-zone technique with Ru self-flux.

Characterization

At low temperatures, the electrical resistivity of a metal is dominated by quasiparticle collisions with lattice imperfections and impurities. The purer the crystal, the lower its residual resistivity will be, therefore, the residual resistivity can be used to determine the quality of a crystal. The resistance of the Sr_2RuO_4 single crystals was measured by a four-probe technique in a ^{3}He refrigerator, from room temperature to 500 mK. The resistance curve is shown in Figure 3.10(a),

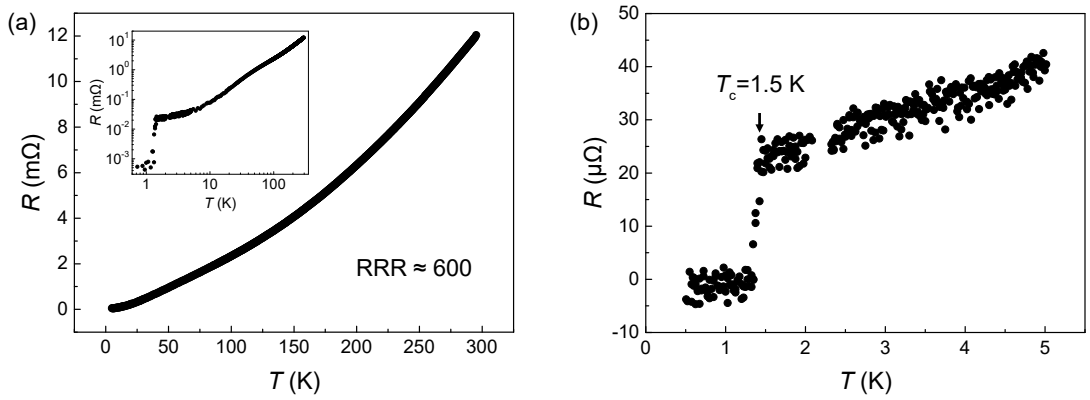

Figure 3.10: **Resistivity measurements.** (a) Resistance curve from room temperature to 500 mK. The inset shows a close-up at low temperatures, where the superconducting transition can be observed. (b) Resistance curve at temperatures below 5 K. The superconducting transition occurs at $T_c = 1.5$ K. These curves were provided by Rosalba Fittipaldi, Veronica Granata and Antonio Vecchione.

showing metallic behavior. The sample is observed to undergo a superconducting transition, as seen in the inset of Figure 3.10(a). Extrapolating the resistance to $T = 0$ K by fitting a Fermi liquid behaviour $R(T) = R_0 + AT^2$ to the curve in the normal state, the residual-resistance ratio (RRR) obtained is ~ 666, defined as $\lim_{T\to 0\mathrm{K}} R_{300\mathrm{K}}/R(T)$. This is within the values reported for high-purity single crystals [12]. Figure 3.10(b) shows a close-up at low temperatures, focusing on the superconducting transition. The transition occurs at $T_c = 1.5$ K, with a width of ~ 0.14 K. Due to the extreme sensitivity of T_c to disorder, such high critical temperature confirms the high-quality of the Sr_2RuO_4 samples.

To check the orientation of the Sr_2RuO_4 single crystal and to exclude the presence of inclusions of $Sr_3Ru_2O_7$ or $Sr_4Ru_3O_{10}$, electron back-scattered diffraction (EBSD) and transmission

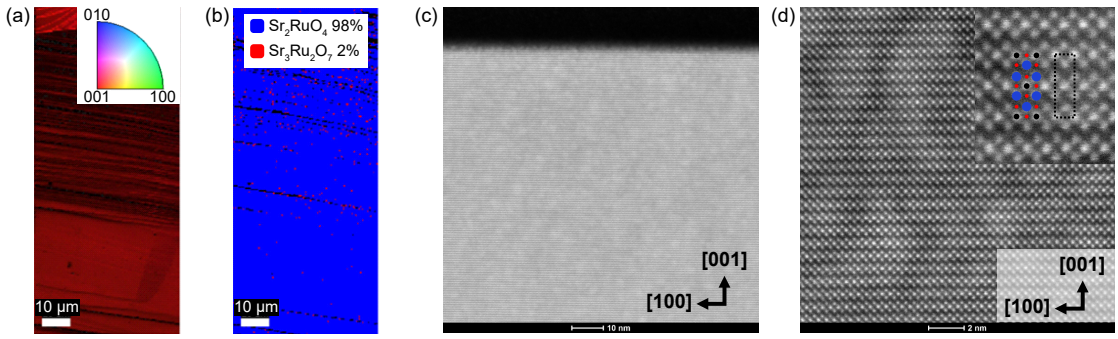

Figure 3.11: **Electron back-scattered diffraction and transmission electron microscopy images.** (a) EBSD Image quality (IQ) and inverse pole figure (IPF) map on a single crystal of Sr_2RuO_4, showing that the surface has the preferential orientation [001] (b) EBSD phase image, showing that the surface is Sr_2RuO_4. (c) TEM image along the *b*-axis. (d) High-resolution TEM image, showing atomic resolution and confirming the structural purity of the sample with no evidence for layers with different stoichiometry. The inset shows a close-up image with the Sr_2RuO_4 crystal structure superimposed by circles (black: Ru, red: oxygen and blue: Sr). The dotted lines indicate the bulk unit cell. These measurements were performed by David Miller and were taken on a Sr_2RuO_4 crystal after STM measurements.

electron microscopy (TEM) measurements were performed on a sample after it had been measured in STM, by David Miller, University of St Andrews. The EBSD was performed on a FEI Scios focused beam scanning electron microscope (FIBSEM) equipped with an EDAX Hikari Super EBSD detector. Figure 3.11(a) shows a map of EBSD image quality (IQ) plus inverse pole figure (IPF) of the surface of a single crystal of Sr_2RuO_4 after cleaving on the STM and exposure to air. It shows that the surface orientation is homogeneous and oriented perpendicular to the $[001]$ direction, as expected of a single crystal. The EBSD phase image, Figure 3.11(b), which determines the structure of the surface, shows that the surface is Sr_2RuO_4 and is homogeneous, with the 2% of $Sr_3Ru_2O_7$ detected within the measurement uncertainty and due to the diffraction spots not being well defined at the step edges.

After determining the orientation with the EBSD, the sample for STEM analysis was prepared by conventional gallium focused ion beam (FIB) milling using the FIBSEM. TEM high angle annular dark-field (HAADF) images were recorded using a probe corrected FEI Themis 200 scanning/transmission electron microscope operated at 200 kV. Figure 3.11(c) shows an image of the cross-section of the sample, cut along the *b*-axis. It shows that the sample is homogeneous along the *c*-axis on the scale of ~ 80 nm up to the surface, and no inclusions of other members of the Ruddlesden-Popper series are found. Figure 3.11(d) shows a zoom in, where the atomic stacking is visible. Superimposing the crystal structure of Sr_2RuO_4 on top of the atomic stacking (inset) shows good agreement, with both Ru and Sr atoms visible.

3.2.2 $Sr_3Ru_2O_7$ single crystals

Crystal growth

The $Sr_3Ru_2O_7$ single crystals used in this thesis were provided by the group of Andrew Mackenzie, Max Planck Institute for Chemical Physics of Solids, Dresden, Germany. The crystals were grown in an image furnace by the floating-zone technique.

Characterization

The resistivity of the $Sr_3Ru_2O_7$ single crystals was measured by a four-probe method from room temperature to 2K. Figure 3.12(a) shows the resistivity curve at 0 T, revealing a residual-resistivity ratio of RRR $= \rho_{300K}/\rho_{2K} = 102$. It has a residual resistivity of $\rho_{res} = 1.3$ $\mu\Omega$cm, obtained from fitting $\rho(T) = \rho_{res} + AT^{\alpha}$ to the low temperature regime (inset of Figure 3.12(a)). This residual resistivity is slightly higher than the residual resistivity of the samples that show

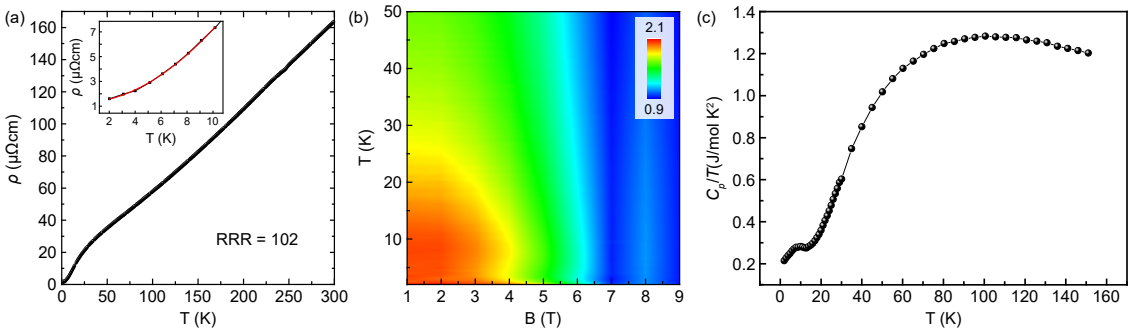

Figure 3.12: **Transport and specific heat measurements of $Sr_3Ru_2O_7$ single crystals.** (a) Resistivity curve. The inset shows a close up at low temperatures, where the red line is the fit to the function $\rho(T) = \rho_{res} + AT^{\alpha}$. (b) High temperature phase diagram of the exponent α of resistivity $\rho(T,B)$ as a function of temperature T and magnetic field B, at temperatures down to 2 K. Magnetic field applied parallel to the c-axis. (c) Specific heat at zero applied magnetic field. Data provided by Alexander Komarek.

the formation of the itinerant metamagnetic region in the proximity of the quantum critical end point ($\rho_{res} < 1$ $\mu\Omega$cm) [17, 18, 189, 190], but of higher quality than the samples where evidence for the quantum critical end point was first found ($\rho_{res} = 3$ $\mu\Omega$cm) [15, 16]. These are the highest purity single crystals of $Sr_3Ru_2O_7$ ever reported to be measured in STM. Figure 3.12(b) shows the evolution of the resistivity exponent α, from the previous expression, as a function of temperature and applied magnetic field, for $\mathbf{B}||c$-axis. It shows the typical region of Fermi liquid behavior at low temperatures and fields ($\alpha = 2$), whose value decreases to $\alpha \sim 1$ near the metamagnetic transition, having the typical signatures found in $Sr_3Ru_2O_7$ near the quantum critical point [16]. Thermodynamic measurements, Figure 3.12(c), at 0 T, also show the typical behavior for good quality single crystals of $Sr_3Ru_2O_7$.

To access the homogeneity of the sample and in particular the quality of the cleaved surface, EBSD was measured on a sample after it was measured by STM. The SEM image, Figure 3.13(a), shows a flat surface with few step edges visible close to the edges of the sample. The phase map measured by EBSD, Figure 3.13(b), shows a homogeneous phase of $Sr_3Ru_2O_7$, represented

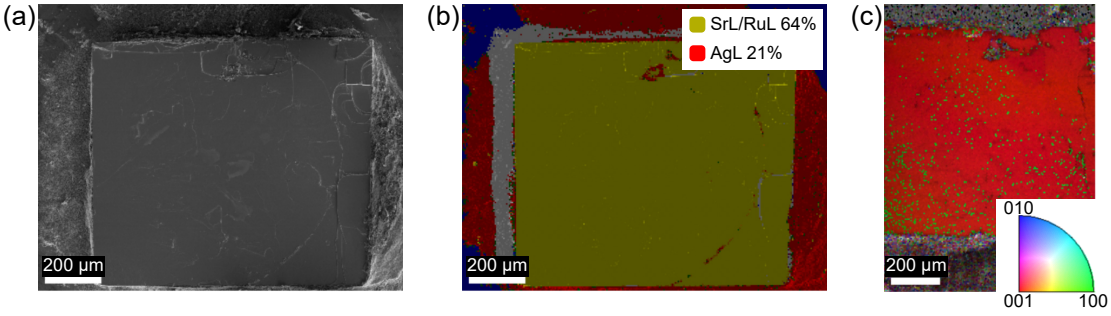

Figure 3.13: **EBSD on a $Sr_3Ru_2O_7$ single crystal.** (a) SEM image. (b) Phase map. Yellow indicates the presence of Sr and Ru and red the presence of Ag. (c) IQ + IPF image. Measurements done by David Miller.

by yellow. Red patches indicate traces left by the silver epoxy glue, after cleaving with a brass rod. The IQ+IPF map, Figure 3.13(c), shows that the exposed surface is perpendicular to the [001] plane, as expected and identical to the case of Sr_2RuO_4, consistent with cleaving between adjacent SrO-SrO layers. The random distribution of green dots indicating [100] are within the experimental noise/error.

Chapter 4

Modeling electronic structure and quasiparticle interference

QPI measurements allow indirect access to the electronic structure at the surface of a material. As discussed in the previous chapter, it gives information about the dominant electronic scattering processes with wavevector $\mathbf{q} = \mathbf{k}_f(\varepsilon) - \mathbf{k}_i(\varepsilon)$. While in one-band systems [226] the interpretation of QPI measurements is rather straight-forward, in multi-band systems the difficulty of disentangling the original band structure from $\mathbf{q}$ dispersions increases rapidly with N, the number of bands in the system, due to the possibility of both intra- and inter-band scattering. Additional complexity comes in once charge, orbital and spin degrees of freedom are introduced into the system [259], especially when these are momentum dependent. In these cases, it is imperative to have an accurate model of the band structure of the system in question, as well as account for the matrix element effects between the tip and the sample, to be able to do realistic model calculations enabling a correct interpretation of the QPI and reveal the physical properties of the system.

In this chapter, I will describe *ab-initio* calculations using DFT and how to use tight-binding models of the electronic structure to qualitatively model QPI using a continuum LDOS calculation.

4.1 Density-functional theory

In a material containing N electrons, its electronic structure is described by the many-body Schrödinger equation

$$\hat{H}\Psi(\mathbf{r}_1,...,\mathbf{r}_N) = E\Psi(\mathbf{r}_1,...,\mathbf{r}_N), \quad \text{with} \tag{4.1}$$

$$\hat{H} = -\frac{\hbar^2}{2m_e}\sum_i \nabla_i^2 + \sum_i V(\mathbf{r}_i) + \frac{1}{2}\sum_{i\neq j}\frac{e^2}{|\mathbf{r}_i - \mathbf{r}_j|}, \tag{4.2}$$

where $\mathbf{r}_i$ is the position of electron i, Ψ is the many-electron wave function and E is the energy eigenvalue of the system. The first term of the Hamiltonian $\hat{H}$ describes the kinetic energy of the system, the second term contains the potential due to electron-nucleus and nucleus-nucleus interactions, and the third term the Coulomb repulsion. The problem with this equation is that, even in the simplest case where only the positions of the electrons are considered, the number of parameters needed to get an accurate solution scales as 3^{3N}. The number of atoms in a crystal is of the order of the Avogadro's number ($N_A = 6.02 \times 10^{23}$), and so, there is no hope in solving Eq. (4.2) for a given crystal in any modern computer.

To get around this limitation, Density-functional theory was developed. The basic principle behind DFT is given by the Hohenberg-Kohn theorem [260], which states that an external potential $V_{\text{ext}}(r)$ is uniquely defined by the ground-state electron density $n(r)$ of a system of interacting electrons in that potential, such that the total energy of the system is the functional of the electronic density

$$E[n] = T[n] + \int n(\mathbf{r})V_{\text{ext}}(\mathbf{r})\mathrm{d}\mathbf{r} + E_{\text{H}}[n] + E_{\text{xc}}[n], \tag{4.3}$$

where $T[n]$ is the kinetic energy of the non-interacting electron system, V_{ext} is the external potential felt by the electrons (e.g., the potential created by the atomic nuclei), $E_{\text{H}}[n]$ is the Hartree energy (Coulomb interaction energy due to $n(\mathbf{r})$) and $E_{\text{xc}}[n]$ is the exchange-correlation energy (contains all correlation effects due to interacting electrons).

The Kohn-Sham equations [261] are derived by mapping the many-body wavefunction into the one-electron wavefunctions, $\phi_i(\mathbf{r}_i)$, such that the many-body states are written as

$$\Psi(\mathbf{r}_1, ..., \mathbf{r}_N) = \frac{1}{\sqrt{N!}}\begin{vmatrix} \phi_1(\mathbf{r}_1) & \phi_2(\mathbf{r}_1) & \cdots & \phi_N(\mathbf{r}_1) \\ \phi_1(\mathbf{r}_2) & \phi_2(\mathbf{r}_2) & \cdots & \phi_N(\mathbf{r}_2) \\ \vdots & \vdots & \ddots & \vdots \\ \phi_1(\mathbf{r}_N) & \phi_2(\mathbf{r}_N) & \cdots & \phi_N(\mathbf{r}_N) \end{vmatrix}, \tag{4.4}$$

so that the electron density can be written via the one-electron wave functions as

$$n(\mathbf{r}) = \sum_{i=1}^{N} |\phi_i(\mathbf{r})|^2. \tag{4.5}$$

The minimization of Eq. (4.3) using this mapping results in the Kohn-Sham equations

$$\left(-\frac{1}{2}\Delta + V_{\text{ext}}(\mathbf{r}) + V_H[\rho](\mathbf{r}) + V_{\text{xc}}[\rho](\mathbf{r})\right)\phi_i(\mathbf{r}) = \varepsilon_i\phi_i(\mathbf{r}), \tag{4.6}$$

which are solved self consistently to get the eigenvalues ε_i and corresponding eigenfunctions $\phi_i(\mathrm{r})$. This is achieved by calculating the density via Eq. (4.5), inputting the result onto Eq. (4.6) to get the eigenfunctions $\phi_i(\mathrm{r})$ which are then used to calculate the density again through Eq. (4.6). Self-consistency is achieved when the input density $n(\mathrm{r})$ is equal (within a set tolerance) to the output density calculated through Eq.(4.5).

The functional in Eq. (4.3) is exact if the exchange correlation functional, $E_{\text{xc}}[n]$, was known exactly. However, this is not the case and therefore approximations are needed to estimate $E_{\text{xc}}[n]$. Currently, there is a large variety of exchange-correlation functionals, but in the following chapters, the two that will be used are the local density approximation (LDA) and the Generalized Gradient approximation (GGA). In LDA [261], $E_{\text{xc}}[n]$ is approximated to that of an uniform electron gas with the same electron density as the local electron density of the real system, so that $E_{\text{xc}}[n]$ is a functional only of $n(\mathbf{r})$,

$$E_{\text{xc}}[n(\mathbf{r})] = \int n(\mathbf{r})E^0_{\text{xc}}(n(\mathbf{r}))d\mathbf{r}, \tag{4.7}$$

where E^0_{xc} is the functional of a homogeneous electron gas. Since it is exact for a uniform electron gas, it is a good approximation for systems with slowly varying electron densities.

On the other hand, in GGA, $E_{\text{xc}}[n]$ is now a functional of both $n(\mathbf{r})$ and its gradient $|\nabla n(\mathbf{r})|$. Here, care has to be given to how the functional is defined because $|\nabla n(\mathbf{r})|$ can be very large in real materials resulting in the break down of the expansion. It is thus defined in a generalized form, through the echange-correlation functional of the uniform electron gas times an enhancement factor $F_{\text{xc}}(n(\mathrm{r}), |\nabla n(\mathrm{r})|)$,

$$E_{\text{xc}}[n(\mathbf{r})] = \int E^0_{\text{xc}}(n(\mathbf{r}))F_{\text{xc}}(n(\mathbf{r}), |\nabla n(\mathbf{r})|)d\mathbf{r}. \tag{4.8}$$

The definition of F_{xc} is what distinguishes the different GGA exchange-correlation functionals. Here, the Perdew–Burke–Ernzerhof (PBE) exchange-correlation functional [262] will be used.

In addition, solving Eq. (4.6) depends on an initial choice for the eigenfunctions ϕ_i to calculate the initial density in Eq. (4.5). This choice is determined by the basis set in which to expand the wavefunctions ϕ_i. Two different basis sets will be used in the following chapters, the linear

combination of atomic orbitals (LCAO) and plane waves (PW). In LCAO, the wavefunctions, ϕ_i, are expanded in the basis set defined by atomic-like orbitals $\psi_m(\mathbf{r})$,

$$\phi_i(\mathbf{r}) = \sum_m c_{mi}\psi_m(\mathbf{r}), \tag{4.9}$$

with c_{mi} the transformation coefficients and

$$\psi_{nml}(\mathrm{r}) = \varphi_{nl}(r_\alpha)Y_{lm}(\hat{r}_\alpha), \tag{4.10}$$

constructed as products of numerical radial functions, $\varphi_{nl}(r_\alpha)$, and spherical harmonics, $Y_{lm}(\hat{r}_\alpha)$, with $r_\alpha = r - R_\alpha$, where R_α is the position of the nucleus α.

On the other hand, in PW, the basis set is composed of plane-waves

$$\phi_{n\mathbf{k}}(\mathbf{r}) = \frac{1}{\Omega^{1/2}}\sum_{\mathbf{G}} C_{\mathbf{G}n\mathbf{k}}e^{i(\mathbf{G}+\mathbf{k})\mathbf{r}}, \tag{4.11}$$

with Ω the volume of the unit cell and $\mathbf{G}$ a reciprocal lattice vector. Since there is an infinite number of possible plane waves, a cut-off energy, E_{cutoff}, is defined so that the basis set only includes all the plane waves with kinetic energy lower than E_{cutoff}, $(\hbar^2/2m_e)|\mathbf{G}+\mathbf{k}|^2 < E_{\text{cutoff}}$.

In practice, solving Eq. (4.6), even with the above approximations, is still computationally expensive. The reason for this is because the number of wavefunctions one needs to solve the Kohn-Sham equations scales with the number of electrons in the system, such that the wavefunctions close to the nucleus become highly oscillatory, and one would need incredibly high E_{cutoff} to account for them in the calculation. To solve this issue, two more approximations can be done. The first one is the frozen core approximation, which stems from the fact that the core electrons do not contribute actively to the chemical and physical properties of the system. Therefore, the potential due to the core electrons can be pre-calculated in an atomic environment and kept frozen during the rest of the calculations. The second one is replacing the exact potentials of the non-core electrons with pseudopotentials. Here, the general idea is that it is only necessary to reproduce the potential correctly at a certain distance from the center of the atom, after which it becomes relevant to determine the physical and chemical properties. One of the methods to construct these pseudopotentials is the projector augmented-wave (PAW) method. The PAW method is formally an all-electron method that provides an exact transformation between the smooth pseudo-wavefunctions and the all-electron wavefunctions.

DFT is an *ab-initio* method, where the band structure of a system is obtained by using as input only the atomic positions in the unit cell and the type of elements in the system. This

method can reproduce well the properties of weakly interacting systems, however, it has some difficulties in getting good agreement for materials with strong electron correlations, where large band renormalizations are needed and some bands are not well captured. This is because the exchange-correlation functional includes only local correlation effects and because only one Slater determinant is used, rather than a series of Slater determinants including higher excited states.

In this work, the DFT calculations will be performed using the GPAW code[1], which implements the PAW method [263, 264] and the atomic simulation environment (ASE)[2] [265, 266].

4.2 Tight-binding model

While DFT provides an *ab-initio* description of the electronic structure, it does not allow to easily track the mechanisms that drive changes on a microscopic level. Using a tight-binding model to describe the system provides an easier way to constrain the electronic structure, more flexibility to include different order parameters (e. g. superconducting order parameter), and the possibility to use it in a Green's function formalism to calculate the local density of states and quasiparticle interference patterns.

Here we consider the tight-binding approximation for a system of atoms rigidly placed in a periodic lattice. The orbitals are assumed to be well-described by atomic-like localized wavefunctions, and the overlap between the wavefunctions on neighboring sites is described by a hopping term t. In this picture, the electrons are allowed to hop between neighboring atoms and the Hamiltonian is written in the form

$$\hat{H}_0 = \sum_{\mathbf{R},\mathbf{R}'} \sum_{\alpha,\beta} t^{\alpha\beta}_{\mathbf{R}\mathbf{R}'} \hat{c}^{\dagger}_{\mathbf{R}\alpha} \hat{c}_{\mathbf{R}'\beta} - \mu_0 \sum_{\mathbf{R}\alpha} \hat{n}_{\mathbf{R}\alpha}, \tag{4.12}$$

where $\hat{c}^{\dagger}_{\mathbf{R}\alpha}$ is the creation operator that creates an electron at the lattice vector $\mathbf{R}$ on orbital α and $\hat{c}_{\mathbf{R}'\beta}$ is the anihilation operator that removes a particle from the lattice vector $\mathbf{R}'$ and orbital β. The $t^{\alpha\beta}_{\mathbf{R}\mathbf{R}'}$ elements are the hopping parameters between orbitals α and β in unit cells $\mathbf{R}$ and $\mathbf{R}'$. The chemical potential is μ_0 and enters as diagonal terms in the Hamiltonian. From Bloch's theorem, the wavefunctions are periodic in space, with the periodicity of the underlying crystal lattice. The Fourier transform is thus well defined, and the following relation holds for the matrix

[1] https://wiki.fysik.dtu.dk/gpaw

[2] https://wiki.fysik.dtu.dk/ase

elements that connect orbital α to orbital β

$$H_{\alpha\beta}(\mathbf{k}') = \sum_{\mathbf{R}} e^{i\mathbf{k}'.\mathbf{R}} H_{\alpha\beta}(\mathbf{R}). \tag{4.13}$$

This can be diagonalized to obtain the eigenvectors, $\mathbf{u}_n(\mathbf{k})$, and eigenvalues, $\varepsilon_n(\mathbf{k})$, and thus the electronic structure of the system.

4.2.1 Green's function of a homogeneous system

The Green's function, often called the propagator, describes how electrons propagate through the system between two distinct states $\mathbf{k}$ and $\mathbf{k}'$. The homogeneous retarded Green's function can be obtained from the eigenvectors and eigenvalues of the previous tight-binding model by [267]

$$G^0_{\mathbf{k}}(\omega) = \sum_n \frac{\mathbf{u}_n(\mathbf{k})\mathbf{u}^*_n(\mathbf{k})}{\omega + i\Gamma - \varepsilon_n(\mathbf{k})}, \tag{4.14}$$

where n denominates the band index and Γ ensures the analyticity of the function and effectively acts as an energy broadening. The density of states (DOS) in k-space is given by

$$n^0(\omega) = -\frac{1}{\pi}\mathrm{Tr}\left[\mathrm{Im}\left(\sum_{\mathbf{k}} G^0_{\mathbf{k}}(\omega)\right)\right]. \tag{4.15}$$

The retarded lattice Green's function describing propagation of an electron from lattice site $\mathbf{R}$ to lattice site $\mathbf{R}'$ is given by the Fourier transformation of 4.14

$$G^0_{\mathbf{R}-\mathbf{R}'}(\omega) = \sum_{\mathbf{k}} G^0_{\mathbf{k}}(\omega) e^{i(\mathbf{R}-\mathbf{R}').\mathbf{k}}. \tag{4.16}$$

For a homogeneous system (no impurity) we have

$$G_{\mathbf{R},\mathbf{R}'}(\omega) = G^0_{\mathbf{R}-\mathbf{R}'}(\omega). \tag{4.17}$$

4.2.2 Green's function of a system with an impurity

Let us introduce a single impurity in the system at lattice site $\mathbf{R}_n$. The Hamiltonian will be given by

$$\hat{H}(\mathbf{R}) = \hat{H}_0(\mathbf{R}) + \hat{V}_{\mathrm{imp}}\delta(\mathbf{R}_n). \tag{4.18}$$

The retarded Green's function, $G_{\mathbf{R},\mathbf{R}'}$, corresponding to the impurity problem, can be written in terms of the Green's function of the unperturbed system, $G^0_{\mathbf{R}-\mathbf{R}'}$ using

$$G_{\mathbf{R},\mathbf{R}'}(\omega) = G^0_{\mathbf{R}-\mathbf{R}'}(\omega) + G^0_{\mathbf{R}-\mathbf{R}_n}(\omega)\hat{V}_{\text{imp}}G_{\mathbf{R}_n,\mathbf{R}'}(\omega). \tag{4.19}$$

For simplicity let's put the impurity at the origin, $\mathbf{R}_n = (0,0,0)$. After expanding it into an infinite series, the previous equation can be written in the form

$$G_{\mathbf{R},\mathbf{R}'}(\omega) = G^0_{\mathbf{R}-\mathbf{R}'}(\omega) + G^0_{\mathbf{R}}(\omega)\hat{T}(\omega)G^0_{-\mathbf{R}'}(\omega), \tag{4.20}$$

where the *T-matrix* is defined by the geometrical series

$$\hat{T}(\omega) = \hat{V}_{\text{imp}}\left[1 + G^0(\mathbf{R}=0,\omega)\hat{V}_{\text{imp}} + (G^0(\mathbf{R}=0,\omega)\hat{V}_{\text{imp}})^2 + ...\right], \tag{4.21}$$

which can be rewritten in closed form as

$$\hat{T}(\omega) = \frac{\hat{V}_{\text{imp}}}{\hat{\mathbb{I}} - \hat{V}_{\text{imp}}G^0(\mathbf{R}=0,\omega)} = \frac{\hat{V}_{\text{imp}}}{\hat{\mathbb{I}} - \hat{V}_{\text{imp}}\sum_{\mathbf{k}}G^0_{\mathbf{k}}(\omega)}, \tag{4.22}$$

where $G^0(\mathbf{R}=0,\omega)$ is the zeroth component of the Fourier transform of $G^0_{\mathbf{k}}(\omega)$, which follow form equation 4.16.

4.2.3 Continuum Green's function and continuum LDOS calculation

In the above description, the Green's function is calculated on a discrete lattice where each point corresponds to the center of a unit cell. However, in reality, the space in which the atomic lattice exists is not discrete and there is a continuous space which is occupied by the atoms in each unit cell, over which the DOS changes. An STM, although it measures on a discrete grid of pixels, probes the density of states in continuous real space coordinates. To be able to simulate STM measurements, it is necessary to calculate the local DOS in the continuum. This section follows the description given in references [268–272].

The transformation from the discrete space consisting only of the lattice vectors $\mathbf{R}$ into the continuum space is done via a basis transformation

$$\Psi_\sigma = \sum_{\mathbf{R},\alpha}\hat{c}_{\mathbf{R}\alpha}w_{\mathbf{R}\alpha}(\mathbf{r}), \tag{4.23}$$

where $w_{\mathbf{R}\alpha}$ are the Wannier functions at the position $\mathbf{R}$ and of the orbital α. They contain spatial information of the shape of the orbitals, and can be calculated in *ab-initio* calculations.

The continuum Green's function can thus be written as

$$G(\mathbf{r},\mathbf{r}';\omega) = \sum_{\mathbf{R}\mathbf{R}'}\sum_{\alpha\beta} G^{\alpha\beta}_{\mathbf{R},\mathbf{R}'}(\omega) w_{\mathbf{R}\alpha}(\mathbf{r}) w_{\mathbf{R}'\beta}(\mathbf{r}'), \tag{4.24}$$

where $\mathbf{r}$ and $\mathbf{r}'$ are the continuum coordinates of real space. The continuum local density of states (cLDOS) can be obtained from equation 4.24 by

$$n(\mathbf{r},\omega) = -\frac{1}{\pi}\mathrm{Im}\left[G(\mathbf{r},\mathbf{r};\omega)\right]. \tag{4.25}$$

Substituting eq. 4.20 into the continuum Green's function, Eq. (4.24), allows the calculation of the cLDOS in the presence of an impurity, obtaining a simulated image in real space, effectively providing a simulated topographic image. The Fourier transform of such an image will give information about the scattered vectors, equivalent to a QPI measurement. In addition, calculating the cLDOS for a series of energies allows simulating tunneling spectra of the clean and perturbed surface.

4.2.4 Choice of Wannier functions

There are multiple choices for the Wannier functions, $w_{\mathbf{R}\alpha}$, used in the continuum transformation of equation 4.23. Wannier functions are functions that play the role of the atomic wave functions [273]. These can be obtained from *ab-initio* slab calculations, where the correct orbital spread and vacuum tail of the orbitals are taken into account. In the case where the vacuum tail of the Wannier functions looks essentially identical to atomic-like orbitals [272], a simple way to approximate these Wannier functions is by using gaussian-like orbitals with the correct symmetries.

In this work, we chose as $w_{\mathbf{R}\alpha}$ gaussian-type orbitals with the symmetry of the orbitals present in the system. For a tight-binding model which describes the strontium ruthenates, three orbitals are necessary: d_{xz}, d_{yz} and d_{xy}. The following gaussian based functions are used

$$w_{\mathbf{R},\mathrm{xz}}(\mathbf{r}) = (x-R_x)(z-R_z)e^{-\frac{1}{2}\pi\phi\left[(x-R_x)^2+(y-R_y)^2+(z-R_z)^2\right]}, \tag{4.26}$$

$$w_{\mathbf{R},\mathrm{yz}}(\mathbf{r}) = (y-R_y)(z-R_z)e^{-\frac{1}{2}\pi\phi\left[(x-R_x)^2+(y-R_y)^2+(z-R_z)^2\right]}, \tag{4.27}$$

$$w_{\mathbf{R},\mathrm{xy}}(\mathbf{r}) = (x-R_x)(y-R_y)e^{-\frac{1}{2}\pi\phi\left[(x-R_x)^2+(y-R_y)^2+(z-R_z)^2\right]}. \tag{4.28}$$

with $\mathbf{R} = (R_x, R_y, R_z)$, $\mathbf{r} = (x, y, z)$ and $\phi = a/\sigma$ which is the ratio of the lattice spacing to the gaussian spread [274].

4.2.5 One-band model on a square lattice

To illustrate the Green's function formalism described above for the calculation of the continuum LDOS in real space as means to simulate QPI measurements, it is instructive to first consider a one-orbital tight-binding model on a square lattice, Figure 4.1(a), where each atom has an s-orbital and hopping is allowed between nearest-neighbors. The Hamiltonian in the form of Eq. (4.12) is given by

$$\hat{H} = \sum_{\mathbf{R}} t(\hat{c}^{\dagger}_{\mathbf{R}+\mathbf{a}}\hat{c}_{\mathbf{R}} + \hat{c}^{\dagger}_{\mathbf{R}}\hat{c}_{\mathbf{R}+\mathbf{a}} + \hat{c}^{\dagger}_{\mathbf{R}+\mathbf{b}}\hat{c}_{\mathbf{R}} + \hat{c}^{\dagger}_{\mathbf{R}}\hat{c}_{\mathbf{R}+\mathbf{b}}),$$

for $\mathbf{a},\mathbf{b}$ defined in Figure 4.1(a) and we choose the hopping amplitude $t = -0.1$ eV and on-site energy of 0 eV. The band structure (Figure 4.1(b)) consists of an electron-pocket centered at the Γ-point of the Brillouin zone at energies below the Fermi level. The Fermi surface (inset of Figure 4.1(b)) has a saddle point at the M-point and marks the energy across which the constant energy contours change from an electron pocket around the Γ-point to a hole-pocket around the X-point, corresponding to a van Hove singularity. The density of states of this model is shown in Figure 4.1(c), where a logarithmic peak is observed.

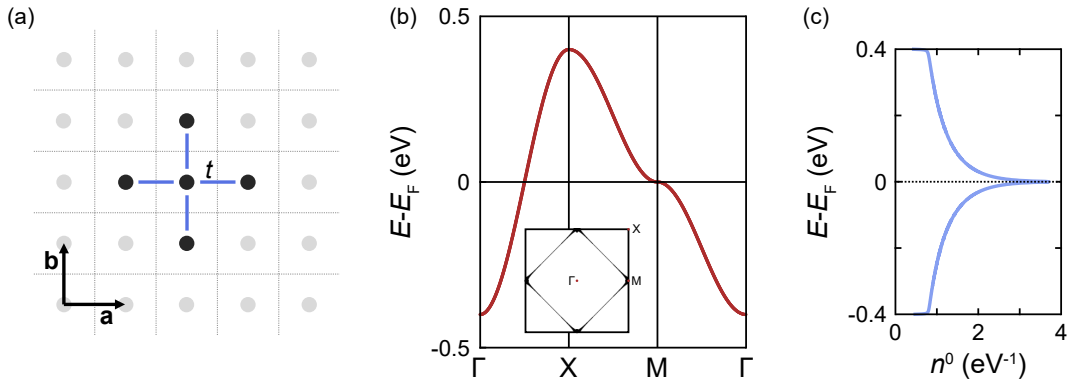

Figure 4.1: **Square lattice tight-binding model.** (a) Sketch of a square lattice with nearest-neighbor hopping t. (b) Bandstructure along the path $\Gamma - \mathrm{X} - \mathrm{M} - \Gamma$, for a hopping term of $t = -0.1$ eV. There is a saddle point (van Hove singularity) at E_{F} at the M-point, across which the system undergoes a Lifshitz transition. The inset shows the Fermi surface. (c) Total density of states $n(E)$, with a peak corresponding to the van Hove singularity at E_{F} with logarithmic divergence. The Fermi surface and density of states were calculated on a 640×640 k-grid, with energy broadenings of $\gamma = 4$ meV and $\gamma = 1$ meV, respectively. The band structure was calculated in 10001 points along the path shown.

We can now follow the procedure described in the previous subsections and calculate the continuum LDOS, using spherical gaussian-type orbitals as an approximation for the s-orbitals and including an impurity with impurity potential $V_{\mathrm{imp}} = 0.05$ eV. Figure 4.2(a) shows the real space cLDOS, $n(\mathbf{r},E)$, for $E = -20$ meV, capturing the square lattice of the s-orbitals and the impurity

at the center of the image. Clear oscillation patterns are seen around the impurity, which originate from scattering between k-states on the same constant energy contour. Possible scattering vectors are shown in Figure 4.2(b) for $E = -20$ meV: one intra-pocket vector ($\mathbf{q}_1$), and two inter-Brillouin zone scattering vectors ($\mathbf{q}_2$ and $\mathbf{q}_3$). The Fourier transform of $n(\mathbf{r},E)$ reveals which $\mathbf{q}$-vectors contribute to the scattering events. Figure 4.2(c) and (d) show the Fourier transform of $n(\mathbf{r},E)$ at -20 meV and 20 meV, respectively. At -20 meV, a pocket corresponding to $\mathbf{q}_1$ is visible, with increasing intensity at $\mathbf{q} = (\pm 0.5, \pm 0.5)$ due to strong nesting in this direction (parallel sections of the pocket) as indicated by the orange arrow. Two additional scattering patterns are visible, although with weaker intensity. The inter-pocket $\mathbf{q}$-vector $\mathbf{q}_2$ is observed around $\mathbf{q} = (0,0)$, while $\mathbf{q}_3$ appears around the Bragg peaks ($\mathbf{q}_3 = \mathbf{q}_2 + 2\pi$). A different situation occurs at 20 meV. The strongest $\mathbf{q}$-vector still corresponds to $\mathbf{q}_1$ but now it connects pockets centered around opposite X-points in the Brillouin zone. The vector $\mathbf{q}_2$ is visible around $\mathbf{q} = (0,0)$, however, $\mathbf{q}_3$ is no longer visible along the $\Gamma - \mathrm{M}$ direction since the constant energy contour now consists of a hole-pocket around the X-point.

To illustrate how the dispersion of a band with a van Hove singularity is expected to appear in differential conductance maps measured in STM, $n(\mathbf{r},E)$ was calculated for energies between ± 0.10 eV. The dispersion of the van Hove singularity is captured in a cut-through $\mathbf{q} = (0,0)$ along the $\mathrm{M} - \Gamma - \mathrm{M}$ direction, Figure 4.2(e), and across the Bragg peaks at $\mathbf{q}_{\mathrm{at}} = 1$, Figure 4.2(f). It can be observed in two ways: via $\mathbf{q}_2$ with scattering around $\mathbf{q} = (0,0)$ and via $\mathbf{q}_3$ around $\mathbf{q}_{\mathrm{at}} = (\pm 1, 0), (0, \pm 1)$. The scattering from $\mathbf{q}_2$ allows access to the dispersion at both negative and positive energies in a single cut, whereas the full dispersion from $\mathbf{q}_3$ around the Bragg peaks can only be obtained from the analysis of the $\mathrm{M} - \Gamma - \mathrm{M}$ line cut and a line cut through $\mathbf{q}_{\mathrm{at}}$ in the perpendicular direction. However, in QPI measurements from STM, access to low-q scattering is often difficult, because not only large area images are necessary to have good q-resolution to be able to resolve the patterns (requiring long measuring times), the presence of randomly distributed defects over the surface contribute to increasing noise around $\mathbf{q} = (0,0)$ in the Fourier transform of real space dI/dV images. On the other hand, it is easier to resolve features around the Bragg peaks, where only the atomic lattice will contribute to the intensity. Moreover, since the dispersion of the van Hove singularity collapses onto $\mathbf{q} = (\pm 1, 0), (0, \pm 1)$, the intensity at the Bragg peaks will show a maximum at the energy of the vHs, as is shown in the left panel of Figure 4.2(f), giving us another way to determine the energy of vHs. In the following chapters, we will identify the presence of van Hove singularities in the band structure of the studied materials and determine their energies by detecting QPI dispersions around the Bragg peaks.

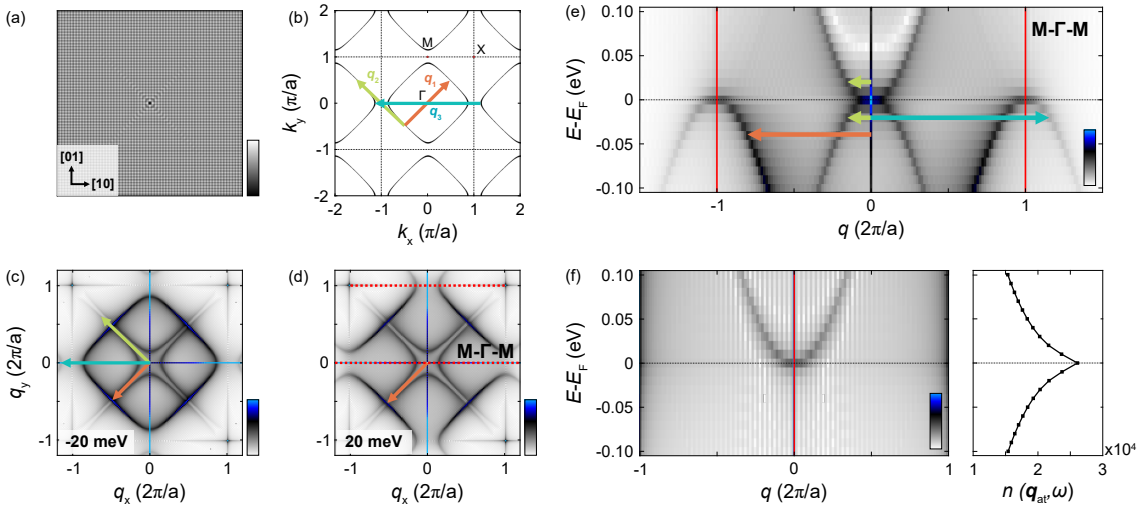

Figure 4.2: **Continuum LDOS of a one-band model.** (a) Real space cLDOS at -20 meV. The impurity is at the center of the image, with an impurity potential of $V_{\text{imp}} = 0.05$ eV. (b) Constant energy contour at -20 meV, shown in the extended Brillouin zone. Possible scattering vectors are shown: orange arrow indicates the intra-pocket $\mathbf{q}_1$ vector, the green and blue arrows indicate inter-Brillouin zone vectors $\mathbf{q}_2$ and $\mathbf{q}_3$. (c) and (d) show the Fourier transform of cLDOS layers at -20 meV and +20 meV respectively. Both intra and inter-pocket scattering vectors are observed, as indicated by the orange, green and blue arrows. The red dotted lines indicate the path of the linecuts in (e) and (f). The Green's functions were calculated on a 640×640 grid with energy broadening $\gamma = 5$ meV. The transformation into the continuum was performed using gaussian-like orbitals with s-symmetry at the center of the unit cells with a width of $\phi = 1$. The real space images were calculated with 5 pixels per unit cell, with 64 unit cells in the field of view, and considering only contributions up to two next-nearest neighbor unit cells. (e) Energy linecuts along the $\text{M} - \Gamma - \text{M}$ direction. The dominant scattering occurs around the M-point between inter-Brillouin zone q-vectors, $\mathbf{q}_2$ and $\mathbf{q}_3$. The $\mathbf{q}_2$ vector collapses onto $\mathbf{q} = (0,0)$ at the energy of the vHs (Fermi level), changing from inter-pocket to intra-pocket scattering. The $\mathbf{q}_3$ scattering vector collapses onto $\mathbf{q}_{\text{at}} = (1,0)$ at the vHs energy and disappears at positive energies (in units of $2\pi/a$). Red vertical lines indicate the position of the Bragg peaks. Due to the perfect lattice arrangement, the Bragg peaks fall onto a single pixel. To avoid the intensity contribution from the Bragg peaks, the linecut was taken one pixel above the center of the image. (b) Linecut across $\mathbf{q}_{\text{at}}$, as indicated by the dashed red line in (d). The dispersion of the equivalent vector to $\mathbf{q}_3$ at positive energies is seen. The left panel shows the intensity at $\mathbf{q}_{\text{at}}$ as a function of energy, revealing a peak at the vHs energy when the magnitude of the $\mathbf{q}_3$ vector equals 1. The intensities shown are the square root of the calculated values to increase the image contrast. Both color bars are scaled to the same intensity values.

Chapter 5

Unveiling the low-energy states of the surface layer of Sr_2RuO_4

The electronic properties of strontium ruthenates are highly sensitive to tiny distortions of the RuO_6 octahedra. In Sr_2RuO_4, superconductivity is enhanced by uniaxial strain [96], while it is suppressed by doping and structural distortions, giving rise to different magnetic phases [13, 14]. Understanding how the shape of the RuO_6 octahedra influences the electronic structure and stabilizes distinct electronic phases in this material will allow us to gain insight into the fluctuations that drive the different phase transitions. In return, it will ultimately result in a controlled tuning of the properties of the ruthenates, imperative for the development of new electronic devices. The first step towards this goal is to establish the relationship between structural distortions and electronic structure in the most simple system: a single layer of Sr_2RuO_4 with a tiny octahedral distortion. Such system is present in the surface layer of single crystals of Sr_2RuO_4, where the surface reconstruction results in an in-plane rotation of the RuO_6 octahedra [25]. The goal of this chapter is to study and establish the low-energy electronic structure of this system using low-temperature Scanning tunneling microscopy.

STM/STS measurements on the reconstructed surface of Sr_2RuO_4 were taken in the temperature range 56 mK to 35 K and in magnetic fields up to 14 T. A phenomenological tight-binding model is presented and used in continuum LDOS calculations to describe the experimental results. Possible origins of the observed low-energy states are presented, including DFT calculations for single layer and three-layer slabs of Sr_2RuO_4 with different lattice distortions. The detection of the d_{xy} band with STM, limitations of the use of gaussian-type orbitals for cLDOS calculations, absence of the superconducting gap and the possibility of quantum criticality in the surface layer

of Sr_2RuO_4 are discussed. The experimental data shown in this chapter was collected together with Luke C. Rhodes, who also developed the tight-binding model used in section 5.8.

5.1 The surface layer of S_2RuO_4

The bulk of Sr_2RuO_4 has a lattice instability towards in-plane octahedral rotation due to the softening of the corresponding phonon mode at the zone corner at $(0.5,0.5)$ [174, 175], in units of $2\pi/a$. While the bulk structure itself does not show octahedral distortions, having a tetragonal unit cell of side $a = 3.87$ Å (black square in Figure 5.1(a)), the surface layer suffers a structural reconstruction due to the freezing of this soft phonon mode. The octahedra at the surface layer are locked into rotated positions in opposite directions on adjacent lattice sites, Figure 5.1(a), resulting in the doubling of the unit cell (blue square). As a consequence, the Brillouin zone (BZ) corresponding to the surface structure is halved in size and is rotated 45° relative to the bulk BZ, Figure 5.1(b).

Despite the doubling of the unit cell, this octahedral distortion does not result in additional periodicities by itself. Adjacent Sr atoms are still equivalent by symmetry, via 90° rotation or a mirror plus a glide plane. This is in agreement with IV/LEED measurements on Sr_2RuO_4 [25,176], where no additional spots besides the ones due to the rotation at the surface were found.

To allow for a clear comparison between the bulk and surface electronic structures and with the literature, the results presented in this chapter will be discussed within the BZ of the bulk unit cell. All values corresponding to the reciprocal space will be given in units of $2\pi/a$.

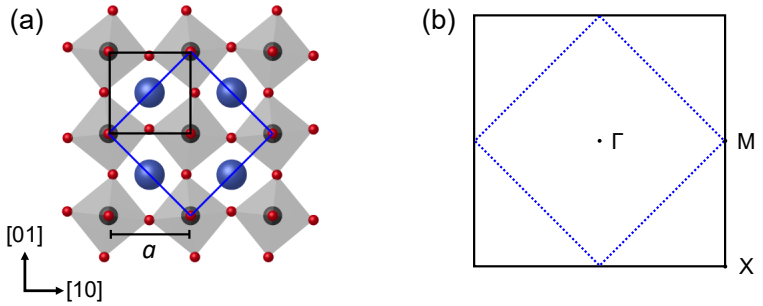

Figure 5.1: **Surface reconstruction of Sr_2RuO_4 and Brillouin zone.** (a) Crystal structure of the reconstructed surface layer of Sr_2RuO_4 with rotation of the RuO_6 octahedra . The black and blue squares indicate the unit cells of the bulk and surface structures, respectively. The bulk in-plane lattice constant is $a = 3.87$ Å. (b) Sketch of the Brillouin zone corresponding to the bulk (black) and surface (dotted blue) unit cells.

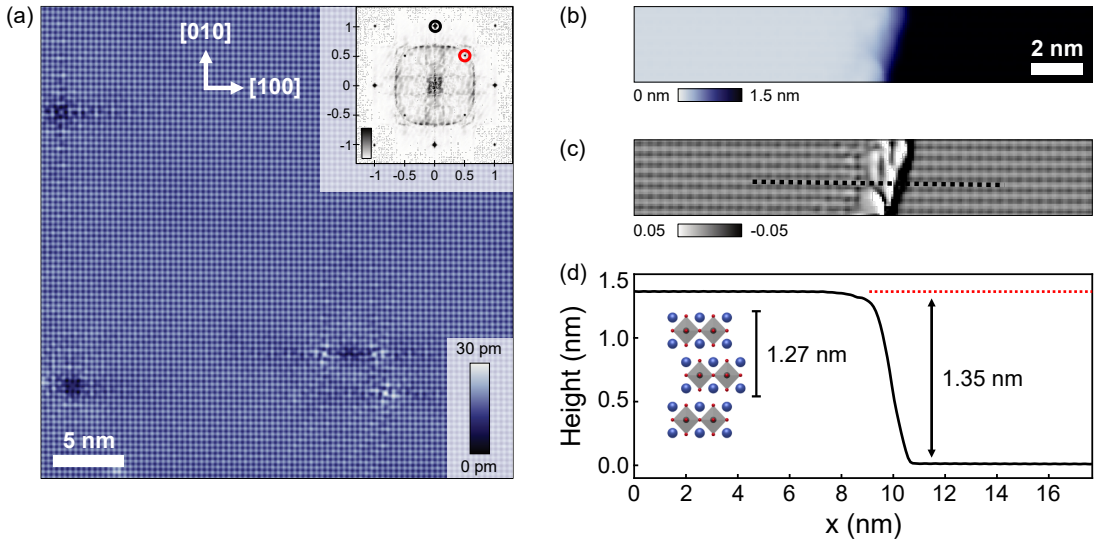

Figure 5.2: **Topography of the surface of Sr_2RuO_4**(a) Typical topography of the reconstructed surface of Sr_2RuO_4 showing a SrO-terminated cleave (V_{set}= 5 mV, I_{set}= 50 pA, T = 76 mK). The upper inset shows the Fourier transform. Atomic peaks are visible at $(0,1)$ (black circle) and at $(0.5,0.5)$ (red circle), corresponding to the Sr lattice and the surface reconstruction periodicity, respectively (units of $2\pi/a$). (b) Topography of a step edge on the same surface as (a). (c) Laplacian of the image in (b) after Gaussian filtering, showing the Sr lattice on both terraces. The dotted line is a guide to the eye. (d) Line profile obtained from averaging (b) along the y-axis, to extract the step height. The inset shows a three-layer stack of Sr_2RuO_4 along the $[010]$-axis, with the height of two layers indicated.

5.2 Topography of the reconstructed surface of Sr_2RuO_4

Cleaving results in atomically flat terraces of sizes larger than 100 nm. A typical topography with atomic resolution taken at the surface of a single crystal of Sr_2RuO_4 is presented in Figure 5.2(a). It shows a square lattice with an atomic distance of ~ 3.9 Å, consistent with the lattice constant of bulk Sr_2RuO_4 (see Figure 5.1(a)).

There are two possible cleaving planes in Sr_2RuO_4: between perovskite layers, exposing a SrO-terminated surface, or at the RuO_2 layer, breaking the RuO_6 octahedra . To determine which termination is measured, step edges found on the surface were investigated. A topography with a step edge is shown in Figure 5.2(b) imaged with an atomically sharp tip. From the relative phase between the atomic lattices on the two terraces, one can determine whether the step edge is an even or odd number of layers high. Figure 5.2(c) shows the Laplacian of Figure 5.2(b) after Gaussian filtering, which enhances the atomic contrast, showing no phase shift between the atomic lattices on the two terraces (dotted line) indicating a step height of an even number of perovskite layers. This is confirmed by measuring its height. The line profile obtained by averaging the topography in Figure 5.2(b) along the y-axis shows a step height of ≈ 1.35 nm, consistent with a bilayer step within 5% error. Additionally, if the step edge separated terraces of two different terminations, one would expect them to look considerably different. However, the two terraces look identical.

This confirms that the imaged surface corresponds to an SrO layer.

Having established that the cleaved surface corresponds to SrO, it is now necessary to determine which atomic lattice is being imaged. To do so, a simulated STM image from DFT slab calculations was performed and is shown in Appendix A, Figure A.1(a). It reveals that the charge density has maxima on top of the Sr atoms when the tip is 5 Å away from the surface. Therefore, the atomic lattice seen in Figure 5.2(a) corresponds to the Sr atoms, in agreement with previous reports [116, 158, 179, 275].

Besides the Sr atomic lattice, Figure 5.2(a) shows the presence of point defects that occupy positions in between Sr atoms, corresponding to the Ru sites. The analysis of large area topographies reveals that they cover about 0.1% of the surface. These defects are surrounded by clear QPI modulations whose characteristic wavevectors are captured in the Fourier transform (FT), inset of Figure 5.2(a). Additionally, the FT reveals the presence of two sets of atomic peaks: at $(0, \pm 1)$, $(\pm 1, 0)$ and $(\pm 0.5, \pm 0.5)$,$(\pm 0.5, \mp 0.5)$ corresponding to the Sr square lattice and to the periodicity of the surface reconstruction, respectively, consistent with previous reports [179].

5.2.1 Chiral defects at the Ru sites

The defects on Ru sites have two distinct orientations, reflecting the two directions of rotation of the RuO_6 octahedra in the surface reconstruction. Two of the defects in Figure 5.2(a) with opposite orientations are shown in more detail in Figure 5.3(a). The sketch below the topography confirms that the two defects are at two inequivalent Ru lattice sites, corresponding to the two sites in the unit cell with opposite rotations, Ru(A) and Ru(B). The QPI patterns coming from each defect have opposite chiralities: for the defect on the left the closest Sr atoms have a change in intensity which follows the direction of rotation (clockwise), whereas on the defect on the right the intensity modulation of the closest Sr has the opposite direction (couterclockwise), as indicated in the sketch in Figure 5.3(a) as red circles with different sizes. This is more clearly seen when these defects are sufficiently separated in space. Figure 5.3(b) and (c) show topographies centered at defects with each rotation. The long-range QPI patterns that emanate from them have the chirality of the defect encoded in them. The Fourier transformation of such topographies contains information about this chirality, shown in Figure 5.3(d) and (e), where the intensity of the QPI patterns reflects the chirality of the defects in real space, as shown by the red lines. Subtracting (e) from (d) shows this point more clearly (Figure 5.3(f)), where the high intensity points (red) follow the chirality of $d_{Ru(A)}$ and the low intensity points (blue) the chirality of $d_{Ru(B)}$. This means that the overall QPI from a large area topography will have contributions from both chiralities.

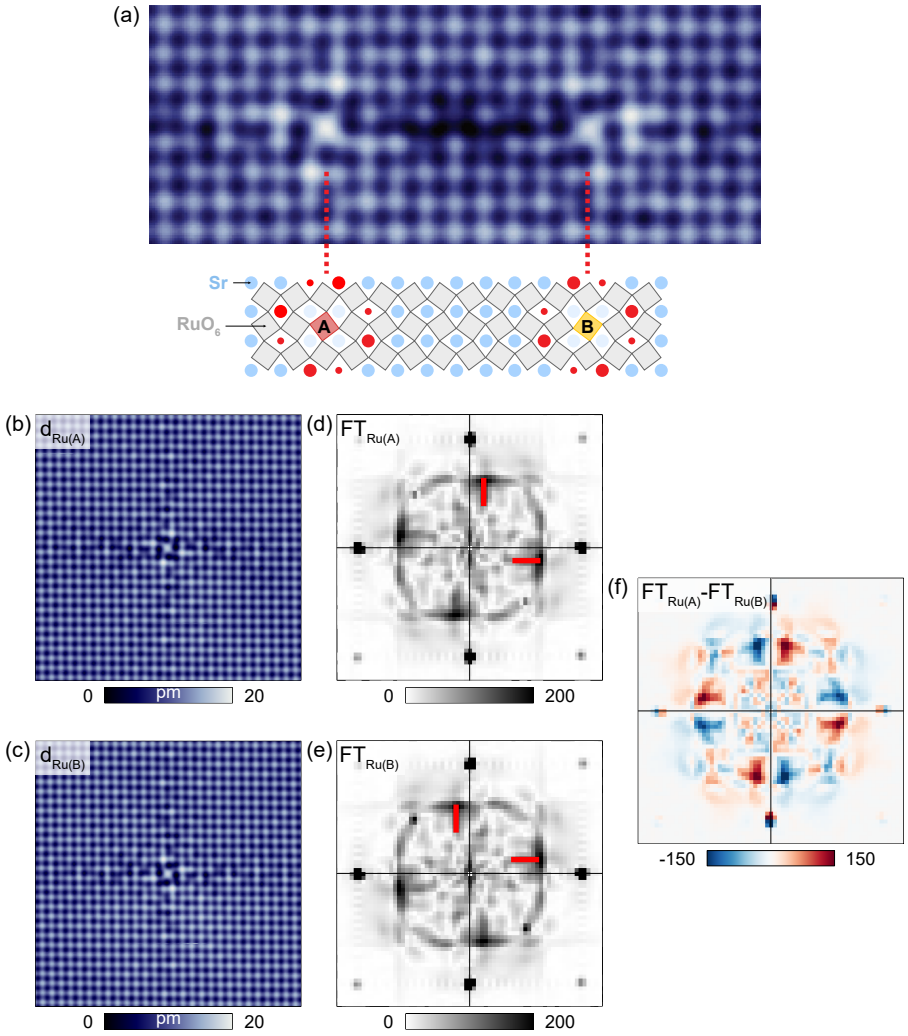

Figure 5.3: **Chiral defects at the Ru sites.**(a) Magnified image of two defects present in Figure 5.2(a). The two defects occur at two inequivalent Ru sites, Ru(A) and Ru(B), in the surface unit cell, as shown on the sketch below: the defect on the left corresponds to a RuO_6 octahedron rotated clockwise (red), whereas the defect on the right resides in an octahedron with counterclockwise rotation (yellow). The octahedral rotation results in a change of the intensity of the closest Sr atoms in a chiral way, as sketched by the bright red circles, the size of which reflects their intensity. (b) and (c) show topographies centered at defects at sites Ru(A) and Ru(B) ($d_{Ru(A)}$ and $d_{Ru(B)}$), respectively ($V_{set} = 5$mV, $I_{set} = 100$pA, $T = 500$ mK). (d) and (e) show the absolute value of the Fourier transformations of (b) and (c). The intensity of the QPI patterns follows the chirality seen in the topography, evidenced by the red lines. (f) Difference of (d) and (e). The brightest red spot is 10° rotated in relation to the $[100]$ direction.

The position of the maximum intensity spots in Figure 5.3(f) can be used to determine the angle from the high-symmetry directions. It gives an angle of $\theta \approx 10^\circ$. While it suggests a very good agreement with the angle of rotation of the RuO_6 octahedra as determined by IV-LEED [25], it is not clear whether the maximum intensity spots are directly connected to the angle of octahedral rotation.

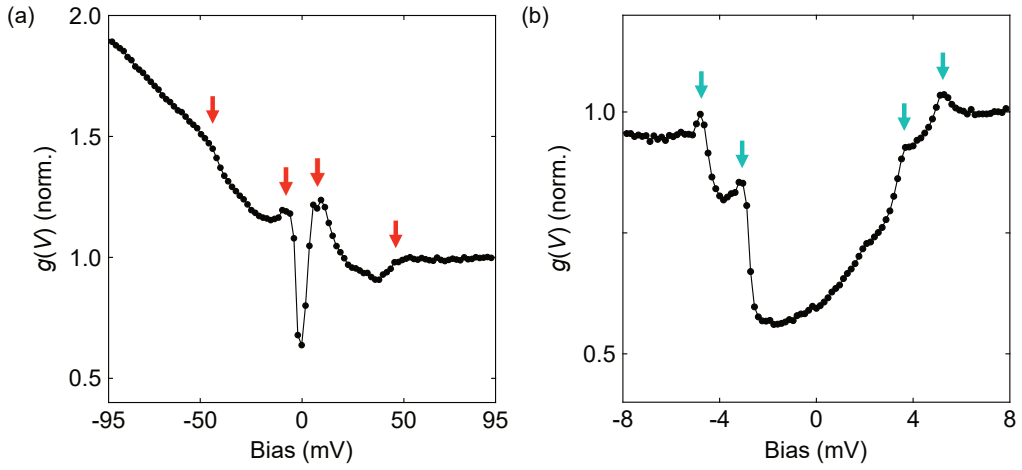

Figure 5.4: **Tunneling spectroscopy at the surface of Sr_2RuO_4** (a) Typical tunneling spectrum $g(V)$ of the SrO-terminated surface, measured at $T = 76$ mK ($V_{set} = 100$ mV, $I_{set} = 265.2$ pA, $V_L = 1.75$ mV). Four distinct features are observed, indicated by the red arrows. (e) High energy resolution $g(V)$ spectrum ($V_{set} = 8$ mV, $I_{set} = 500.2$ pA, $V_L = 155$ μV, $T = 56$ mK). Four peaks are indicated by the blue arrows.

5.3 Spectroscopy

A typical differential conductance spectrum, $g(V)$, measured at $T = 76$ mK on the clean surface of Sr_2RuO_4 is shown in Figure 5.4(a). Four distinct features are visible (red arrows) in agreement with previous reports [158–160, 179]. The outer arrows indicate kinks at ± 40 mV, whose particle-hole symmetry suggests that they are due to inelastic tunneling and have been attributed to the coupling of the β-band with a surface phonon [179]. The energy at which these kinks occur is close to the energy of vibrational modes where the oxygen octahedron moves opposite to the Ru core, which has been measured by high-resolution electron energy loss spectroscopy (HREELS) to have an energy of 50 meV [276].

The inner arrows in Figure 5.4(a) indicate the edges of a partial gap around E_F, with a width of 5 mV. In Figure 5.4(b), a $g(V)$ spectrum in a narrower energy range is shown. It reveals the presence of at least four sharp peaks in the vicinity of the Fermi level at energies -4.8 mV, -3.2 mV, 3.7 mV and 5.2 mV, approximately, indicated by the arrows. The partial gap is asymmetric in relation to E_F and represents a suppression of differential conductance by about 40% relative to the value at 8 mV.

The $g(V)$ spectrum shown in Figure 5.4(b) was taken at a temperature well below the superconducting temperature of our samples, as obtained by resistivity measurements. Although the measurement was taken with sufficient energy resolution to see signs of a superconducting gap of width $\Delta \sim 350$ μV, no signs of such a feature can be observed. To confirm the absence of a

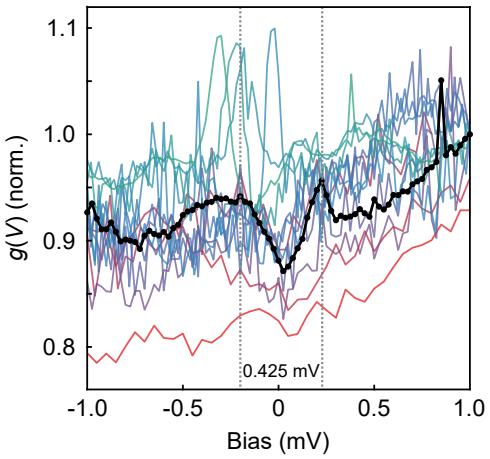

Figure 5.5: **Point spectra below** 100 **mK and in the range** ± 1 **mV.** The different curves were taken at different positions on the surface and with different setpoint parameters. The curve in black shows an example of a curve where a gap-like feature of width $\Delta = 212.5$ μV can be observed ($V_{\text{set}} = 8.0$ mV, $I_{\text{set}} = 800.25$ pA, $V_{\text{L}} = 30$ μV).

superconducting gap, several point spectra were taken with higher energy resolution. Figure 5.5 shows a set of spectra taken at different places on the sample surface with different setpoint parameters ($V_{\text{set}} = 5-8$ mV, $I_{\text{set}} = 200-1000$ pA and $V_{\text{L}} = 80-25$ μV). No consistent feature can be observed, with gap-like and peak shaped features appearing around E_{F} depending on the characteristics of the tip. Occasionally, a gap-like feature with a width similar to the one expected is seen (black curve in Figure 5.5), which however was not reproducible when moving the tip by a few nm. These results suggest that the surface reconstruction on a SrO-terminated surface suppresses superconductivity.

5.3.1 Temperature dependence

If the partial gap observed in the tunneling spectrum was a BCS-type gap of width $\Delta_{\text{g}} = 5$ meV, it should disappear at a temperature of about $\Delta/1.76k_{\text{B}} \sim 33$ K (as for a charge density wave in mean field theory). To investigate its temperature dependence, measurements were performed at temperatures between 76 mK and 35 K, where the higher temperature was limited by the instrumental setup[1]. The curves at the different temperatures are shown in Figure 5.6(a), where the depth of the gap is seen to reduce with increasing temperature, followed by a slight increase in width. At 35 K, signs of the partial gap are still visible. The change in the spectrum background between 10 K and 20 K is due to a tip change between measurements, a result of an increasingly

[1]The warming up of the radiation shield of the dilution fridge insert and its large surface area implies that the amount of particles which evaporate from its walls as the temperature is increased becomes too large above 35 K to allow for a stable tunneling junction between the tip and sample

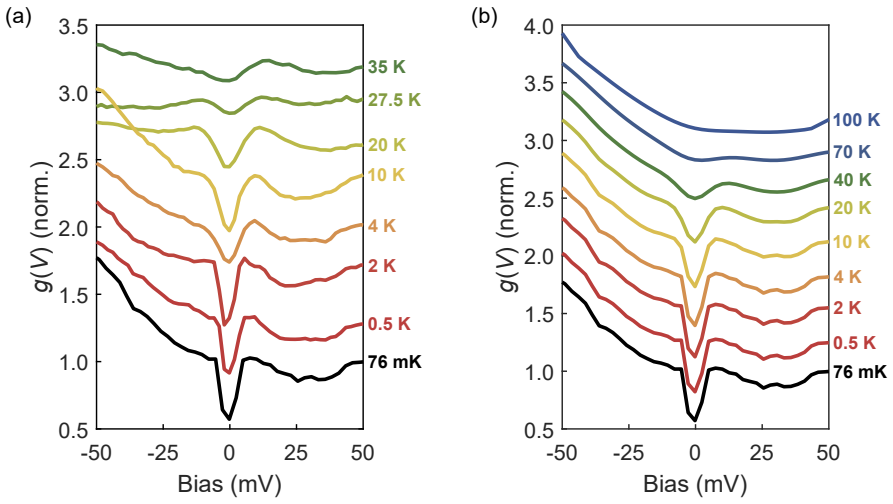

Figure 5.6: **Temperature dependence of tunneling spectroscopy.** (a) Measured point spectra at increasing temperatures, from 76 mK to 35 K. (V_{set}= 100 mV for all curves; 35 K: I_{set}= 2 nA, V_{L}= 3 mV; 27.5 K: I_{set}= 1 nA, V_{L}= 2.5 mV; 20 K: I_{set}= 265 pA, V_{L}= 2 mV; 10 K - 76 mK: I_{set}= 265 pA, V_{L}= 1.75 mV). The curves are vertically displaced by a constant for clarity. (b) Point spectra at 76 mK convoluted with the derivative of the Fermi function to account for thermal broadening for increasing temperatures.

unstable tunneling junction, with the tip becoming blunt at temperatures higher than 10 K.

To investigate the effects of energy broadening due to the increase in temperature alone, the density of states in Eq. (3.12) can be approximated by the tunneling spectrum taken at 76 mK, $g_{\text{data}}(V, T = 0.076)$, where the thermal broadening is minimized and of the order of 23 μV, and the energy broadening is dominated by the lock-in modulation, as discussed in section 3.1.2. By convoluting $g_{\text{data}}(V, T = 0.076)$ with the derivative of the Fermi-Dirac function, $f(\varepsilon, T)$, as given by the expression

$$g_{\text{calc}}(V,T) = \int_{-\infty}^{\infty} g_{\text{data}}(V, T = 0.076) \left[-\frac{\mathrm{d}f(\varepsilon - eV, T)}{\mathrm{d}\varepsilon} \right] d\varepsilon, \tag{5.1}$$

it is possible to calculate how the tunneling spectrum at 76 mK would evolve with increasing temperature if the only change is the increased thermal energy broadening.

Figure 5.6(b) shows the calculated $g_{\text{calc}}(V,T)$ curves for temperatures from 0.5 to 100 K. For an effect due purely to thermal broadening, the gap depth should decrease and its edges should appear broader, with its full disappearance at 100 K. Comparing Figures 5.6(a) and (b), the measured spectra seem consistent with the calculated curves, suggesting that the observed suppression of the gap in the tunneling spectra with increasing temperature comes predominantly from thermal broadening. It can not be clearly attributed to the closing of a gap.

5.4 Line defects

In addition to point defects, some of the surfaces show line defects aligned with the $\langle 110 \rangle$ directions with different widths and depths, see Figure 5.7(a) and (b). These look identical to the line defect chains observed by Pennec *et al.* [116] for samples cleaved at 20 K. Similar defects have also been observed by Kambara *et al.* [160] on a sample that exhibits the 3K-phase of Sr_2RuO_4 and were attributed to Ru-lamella inclusions.

The line defects could be a consequence of domains of the surface reconstruction, however, the Laplacian of Figure 5.7(b), presented in Figure 5.7(c), shows that there is no phase shift between the atomic lattices on either side of the defect (dotted black line). The line profile perpendicular to the direction of the defect (dotted black line) gives a width of $\sim 8a\sqrt{2}$ and a depth of ~ 214 pm, significantly less than the full step height of 640 pm. Figure 5.7(c) also reveals an atomic lattice at the bottom of the defect. A line profile taken parallel to the direction of the defect along its center (red dotted line), Figure 5.7(e), shows an atomic corrugation with a distance between maxima of $\sim a\sqrt{2}$, consistent with a Sr lattice. The rather small depth of the line defects suggests that it is a consequence of missing rows of Sr atoms at the surface than a full step, where locally a full layer is removed.

To test this hypothesis, I have simulated STM constant current topographic images from DFT calculations. Figure 5.7(f) shows a simulated STM image showing the charge density 5 Å above the top-most Sr layer of a slab with a $3 \times 3 \times 1$ supercell, where a row of Sr atoms has been removed along the $[110]$ direction (open blue circles). It shows that a missing row of Sr atoms gives rise to dark rows in the topography of width $a\sqrt{2}$, consistent with the experiment. A line profile perpendicular to the missing row of Sr atoms (red dotted line in Figure 5.7(f)), Figure 5.7(g), shows a height difference of ~ 122 pm between the rows with and without Sr, which has reasonably comparable size with the one observed experimentally.

The TEM and EDX analysis of our sample shows that the sample is homogeneous along the c-axis, see section 3.2.1. Stacking faults and Ru-inclusions were not observed, suggesting that these line defects are induced by the cleaving of the crystal. Our results are thus consistent with missing rows of Sr atoms.

5.4.1 Point spectra across a line defect

The presence of the line defects shown in section 5.4 provides an opportunity to investigate how the tunneling spectrum changes across a discontinuity in the lattice, which could give further

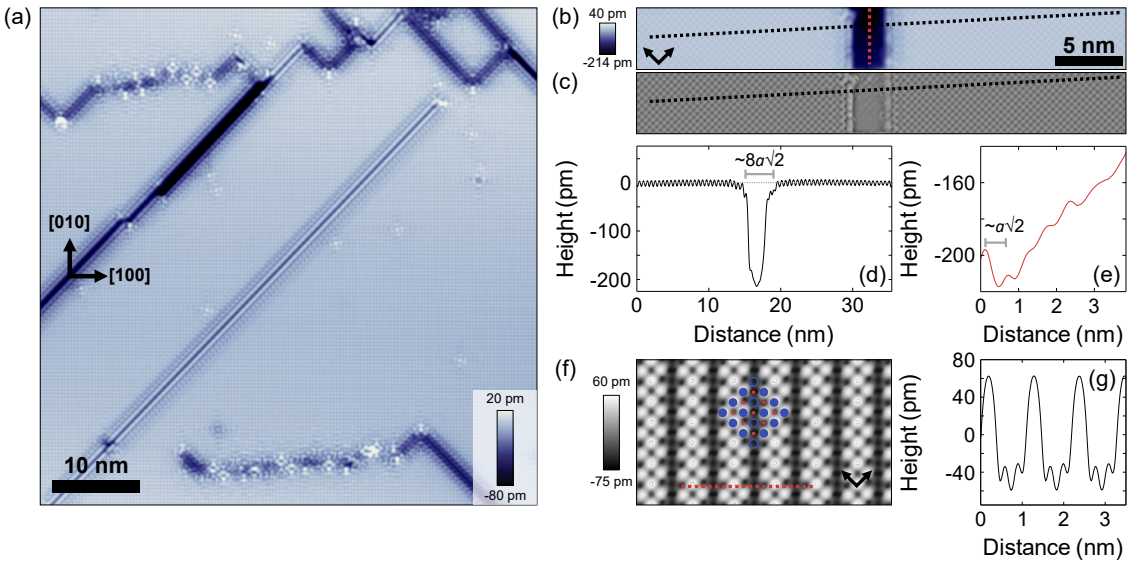

Figure 5.7: **Line defects.** (a) Topography of an area with several line defects, which occur along the $\langle 110 \rangle$ directions with different widths and depths (V_{set}= 20 mV, I_{set}= 50 pA). (b) Topography showing a section of a wide line defect at the center (V_{set}= 20 mV, I_{set}= 200 pA). The arrows indicate the crystallographic directions [100] and [010] as in (a). (c) Laplacian of the image in (b) after Gaussian filtering. It reveals atomic structure inside the line defect. Following the dotted line shows that there is no phase shift between the two sides of the defect, as might be expected if it was a boundary between different domains of the surface reconstruction. (d) Line profile along the black dotted line in (b). (e) Line profile of the red dotted line in (b). (f) Simulated STM topography at 100 meV and 5 Å above the surface obtained from a DFT calculation of a single layer slab with a $3 \times 3 \times 1$ supercell, where a row of Sr atoms was removed along the [110] direction. The colored circles show the top SrO layer of the supercell, with the full blue circles representing the Sr positions, empty blue circles the removed Sr atoms and red the position of the O atoms. The arrows indicate the spatial directions as in (a). The DFT calculation was performed with GPAW, using atomic orbitals as basis functions (LCAO, double-zeta polarized basis set) and the local density approximation, in a $8 \times 8 \times 1$ k-grid. (g) Line profile along the red dotted line in (f), showing a corrugation of magnitude $\sim$ 122 pm.

insights into its origin. Figure 5.8(a) shows a point spectrum at the bare surface (black) and inside the line defect (red), as indicated by the circles in the inset topography. The kinks at $\pm$40 mV seem to be broadened and the partial gap is suppressed. Individual spectra in a narrower energy range, Figure 5.8(b), show that both the width and depth of the partial gap decrease at the center of the line defect, without it being fully suppressed.

To investigate the evolution of the width and depth of the partial gap, the differential conductance has been mapped over the topography shown in Figure 5.8(c), which contains a section of a line defect at the center. The gap width is extracted by subtracting the peak positions of two Lorentzian functions fitted to the derivative of each curve. The obtained values were then averaged along the vertical direction of the topography and plotted in Figure 5.8(d). The width of the gap decreases continuously when approaching the line defect, with a maximum reduction of $\sim$ 2.7 mV at its center. The change in gap depth across the line defect is shown in Figure 5.8(e), where the values indicate the reduction in differential conductance at its minimum relative to the value at

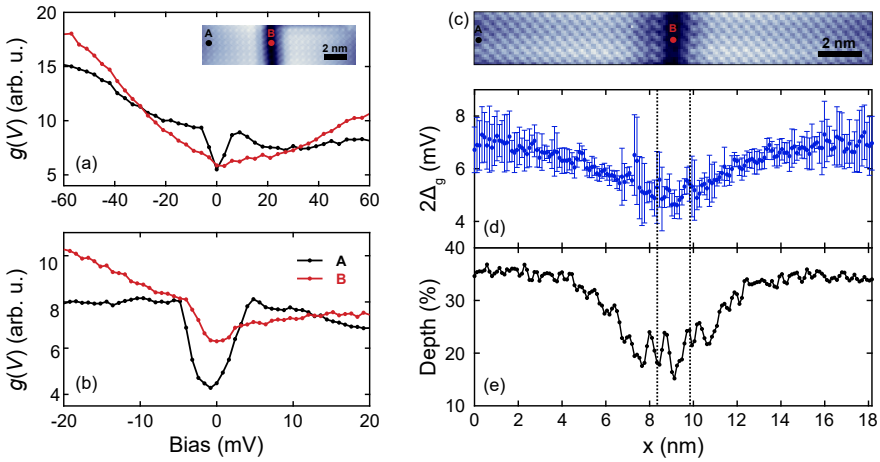

Figure 5.8: **Point spectra across line defects.** (a) Point spectra on the bare surface (black) and at the center of the line defect (red), at the positions indicated on the topography in the inset (V_{set}= 60 mV, I_{set}= 250 pA, V_{L}= 2.8 mV, T = 2 K). (b) Same, in a narrower energy range and at the positions indicated in (c)(V_{set}= 20 mV, I_{set}= 225 pA, V_{L}= 0.9 mV, T = 2 K). (c) Topography taken at the same time as the $g(V)$ map from where the curves in (b) were extracted. (d) The full width $2\Delta_g$ of the gap-like feature as a function of position x. The width is defined as the difference between the center of two Lorentzian peaks fitted to the first derivative of each curve of the map. Each point is the mean of this difference along each column of the topographic image and the error bars are the corresponding standard deviations. (e) Relative depth of the gap as a function of x, normalized to the value at 20 mV.

20 mV. The gap starts to become shallower at about 5 nm away from the edges of the line defect, filling up to a reduction of only 16% at its center. It suggests that a band that is gapped out at the clean surface is not gapped at the center of the defects.

5.5 Checkerboard order

The Fourier transform of the topography shown in Figure 5.2(a) shows faint peaks at $(\pm 0.5, \pm 0.5)$ and $(\pm 0.5, \mp 0.5)$, coinciding with the periodicity of the surface unit cell. Bias dependent imaging showed that the intensity of these peaks is highly dependent on the bias setpoint, corresponding to a checkerboard modulation on top of the Sr atoms. This is demonstrated in Figure 5.9(a), where topographies taken with increasing bias voltages in the same area are shown, with a quarter of the respective FT shown as insets. At V_{set}= -70 mV, the Sr square lattice is visible with adjacent Sr atoms appearing with the same intensity, corresponding to strong atomic peaks at $(0,1)$ and $(1,0)$. The peak at $(0.5, 0.5)$ is barely visible. Closer to E_{F}, at $V_{set} = -5$ mV, the topography shows a clear checkerboard modulation on top of the Sr lattice. This modulation has the periodicity of the doubled unit cell due to the octahedral rotations at the surface, resulting in the increase of the peak intensity at $(0.5, 0.5)$. With increasing bias setpoint towards more positive voltages (20 mV and 100 mV), the checkerboard modulation is seen to fade away, with a decrease in the $(0.5, 0.5)$ peak intensity.

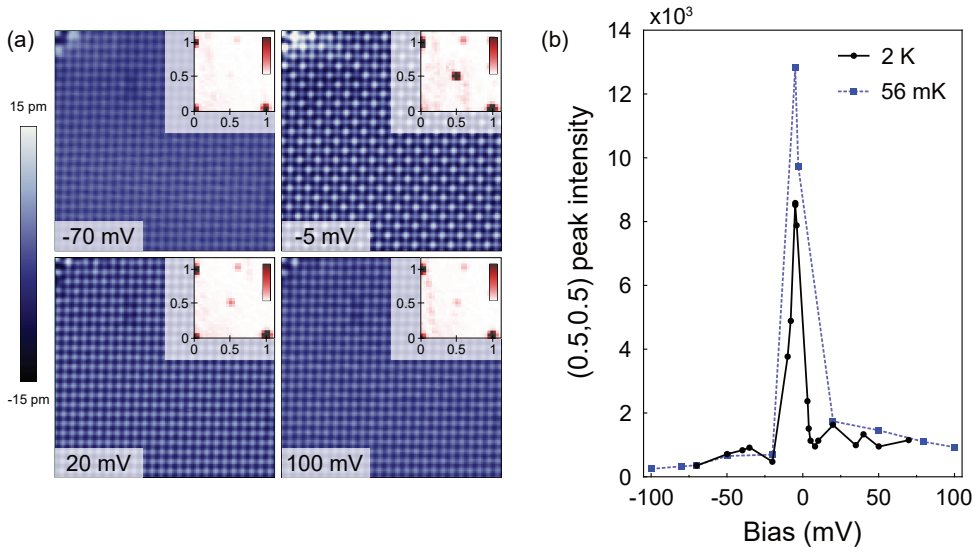

Figure 5.9: **Bias dependence of topography.** (a) Topographies measured with bias setpoints of -70, -5, 20 and 100 mV ($T = 56$ mK, $I_{\text{set}} = 100$ pA). The insets show a quarter of the Fourier transform, where the atomic peaks are aligned with the x and y directions. At -70 mV, the $(0.5, 0.5)$ peak is almost invisible. At -5 mV, the $(0.5, 0.5)$ peak has a strong intensity, which decreases as the bias voltage is increased, as seen in the panels for 20 and 100 mV. (b) $(0.5, 0.5)$ peak intensity as a function of setpoint bias at 2 K and 56 mK. There is a peak around -5 mV at both temperatures.

The bias dependence of the checkerboard modulation can be obtained by taking a series of topographies at different setpoint bias and plotting the intensity of the $(0.5, 0.5)$ peak as a function of bias, as shown in Figure 5.9(b), for $T = 2$ K and $T = 56$ mK. The intensity of the $(0.5, 0.5)$ peak increases by a factor of 1000 close to E_{F}. A fitting of a Lorentzian to the curves gives a peak centered at -4.3 mV with a width of 6.7 mV at 2 K and of 4.0 mV at 56 mK. It shows that the checkerboard modulation of adjacent Sr atoms is pinned to very low energies close to the Fermi level. If the checkerboard modulation was due to a structural reconstruction of the surface Sr atoms, with a staggered vertical displacement of the Sr atoms, this should show up as a corrugation in topographic images which is largely bias independent. By extracting the height difference between adjacent Sr atoms as a function of bias, see Appendix B Figure B.1, an upper bound for the vertical displacement of the Sr atoms can be obtained. For bias voltages $|V| > 20$ mV, the contrast of the checkerboard becomes largely bias independent, so can be expected to be most representative of the actual atomic displacements if there are any. At 100 mV, the height difference between adjacent Sr atoms is ~ 130 fm, providing an upper bound for the vertical displacement of the Sr atoms. In addition, the topographies taken in STM have contributions from the local DOS at energies between 0 and eV_{set}, as discussed in section 3.1.2. Since the Sr states only contribute to the density of states at energies far away from the Fermi level ($E > 1$ eV) [124], if the Sr atoms were physically displaced in a checkerboard pattern, this should become more visible at higher

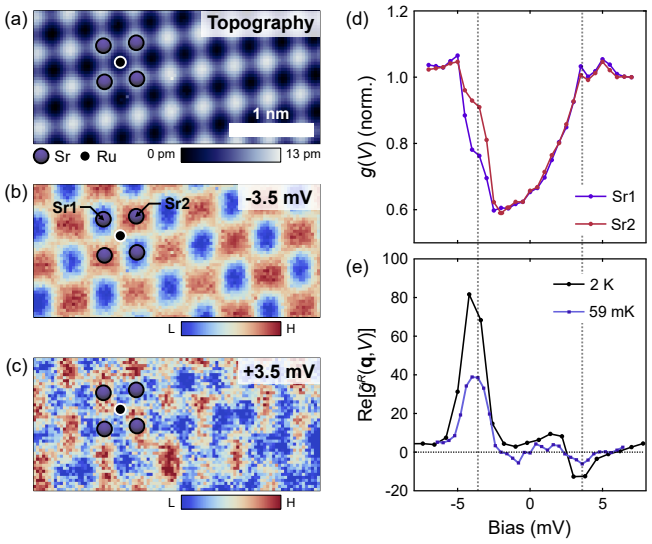

Figure 5.10: **Checkerboard charge order.** (a) Atomically resolved topography, measured simultaneouly as a $g(V)$ map, with $V_{set} = 7$ mV. The positions of Sr and Ru atoms are indicated by purple and black circles, respectively. (b), (c) Differential conductance layers at energies -3.5 and 3.5 mV, respectively. Both show a checkerboard modulation on top of the Sr atoms, with opposite phase between them ($T = 59$ mK, $V_{\text{set}} = 7.0$ mV, $I_{\text{set}} = 250$ pA, $V_{\text{L}} = 495$ μV). (d) $g(V)$ spectra on top of adjacent Sr atoms (Sr1 and Sr2 in (b)). (e) Phase-referenced FT, Re $\left[\tilde{g}^{\text{R}}(\mathbf{q},V)\right]$, as a function of energy at the $(0.5,0.5)$ peak in the Fourier transform for $g(V)$ maps taken at 2 K and 59 mK. The dotted lines indicate the energy of the peaks in the PR-FT.

bias voltages, contrary to what is observed.

To investigate the characteristic energy scale of the checkerboard modulation, a differential conductance map with atomic resolution is shown in Figure 5.10. While the Sr lattice is seen with uniform intensity in the topography taken simultaneously with the map (V_{set}= 7 mV, Figure 5.10(a)), the checkerboard dominates over the atomic contrast at -3.5 mV (Figure 5.10(b)). At 3.5 mV, Figure 5.10(c), a checkerboard with opposite phase is observed. The $g(V)$ spectrum on top of each inequivalent Sr site, Sr1 and Sr2, shows that the two checkerboard modulations correspond to a modulation in the intensity of the peaks at -3.5 and 3.5 mV in the spectroscopy (Figure 5.10(d)).

In order to obtain information on both the intensity and phase of the checkerboard modulation as a function of energy, a phase-referenced Fourier transform (PR-FT) [277] can be performed on the energy layers of the $g(V)$ map. Here, to remove the intrinsic global phase factor present in each energy layer, the phase at each energy is referenced to the phase $\phi(\mathbf{q},V_0)$ such that

$$\tilde{g}^{\text{R}}(\mathbf{q},V) = \frac{\tilde{g}(\mathbf{q},V)}{e^{i\phi(\mathbf{q},V_0)}} = \sqrt{\frac{\Delta x \Delta y}{N_x N_y}} \mid \tilde{g}(\mathbf{q},V) \mid e^{i(\phi(\mathbf{q},V)-\phi(\mathbf{q},V_0))}. \tag{5.2}$$

where Δx and Δy are the size of the map along the x and y directions and N_x and N_y are the

number of pixels in each direction. The real part of $\tilde{g}^{\mathrm{R}}(\mathbf{q},V)$ is then given by

$$\mathrm{Re}\left[\tilde{g}^{\mathrm{R}}(\mathbf{q},V)\right] = \sqrt{\frac{\Delta x \Delta y}{N_x N_y}} \mid \tilde{g}(\mathbf{q},V) \mid \cos\left(\phi(\mathbf{q},V) - \phi(\mathbf{q},V_0)\right), \tag{5.3}$$

where the cosine will take positive values if the phase at V is equal to the referenced phase at V_0 and negative values if it has the opposite phase. Since we are interested on the energy evolution of the checkerboard modulation, we reference the phase of all energy layers to the phase at $V_0 = -3.5$ mV, where the checkerboard is strongest and plot the quantity $\mathrm{Re}\left[\tilde{g}^{\mathrm{R}}(\mathbf{q},V)\right]$ at $\mathbf{q} = (0.5, 0.5)$ as a function of energy, Figure 5.10(e). At both $T = 2$ K and $T = 59$ mK, the PR-FT shows a sharp peak with positive intensity centered at -3.5 mV, with a width of 1 mV. A second peak with similar width but with negative intensity is seen centered at 3.5 mV, representing the phase reversal as seen by comparing Figure 5.10(b) and (c). In the 1D model of a charge density wave with a gap opening close to or at the Brillouin zone boundary, the LDOS at the gap boundaries at positive and negative energies have a phase change of π [278]. As a result, in STM, this is expected to be detected as a contrast inversion of the modulation between occupied and unoccupied states, as the one observed here. Thus, the phase reversal of the checkerboard modulation between ± 3.5 mV and the partial gap observed in the spectroscopy seem to be consistent with what is expected from a charge density wave [279–281].

5.6 C_4-symmetry breaking and nematicity

In addition to the characteristic energy scale of the checkerboard order, the $g(V)$ maps reveal more intriguing patterns at the atomic scale. In Figure 5.11(a), like in Figure 5.10(a), the topography at $V_{\mathrm{set}} = 7.8$ mV shows the square Sr lattice, which we can use to pinpoint the position of the Sr atoms in the $g(V)$ layers as purple circles. The position of the Ru atom is shown as a black circle. The $g(V)$ layer at 7.8 mV, outside the partial gap in the spectrum, Figure 5.11(b), shows a square lattice sitting on top of the Ru positions. However, as the energy approaches the Fermi level, the electronic states align along the [10] direction, Figure 5.11(c) at 4.6 mV. At 3.4 mV, less than 2 mV lower, the electron density switches direction, aligning along the [01] direction, Figure 5.11(d). It shows that the low energy electronic states break C_4-symmetry, as expected for a nematic order. This modulation at the atomic scale will reveal itself as an anisotropy in the intensity of the atomic peaks at $(0,1)$ and $(1,0)$ as a function of energy in the Fourier transform of such $g(V)$ maps.

Another way in which this C_4-symmetry breaking can be observed is in the QPI patterns

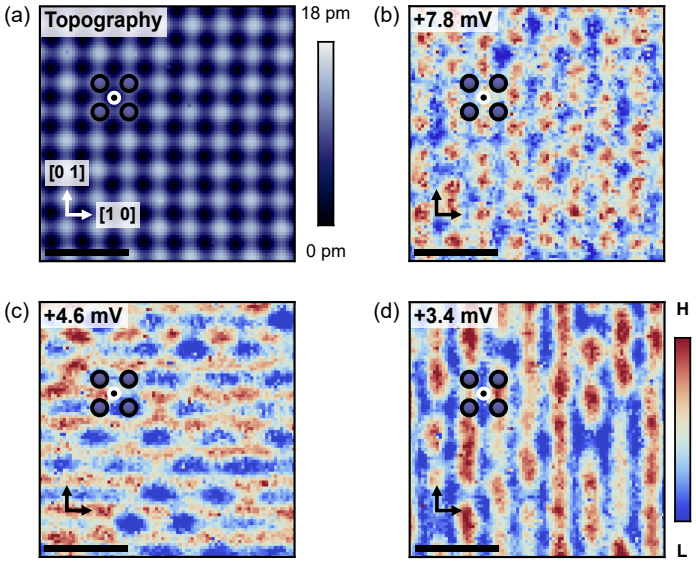

Figure 5.11: C_4**-symmetry breaking of the atomic scale modulations.** (a) Topography with V_{set}= 7.8 mV. (b)-(d) Energy layers of a $g(V)$ map taken simultaneously as (a), at 7.8, 4.6 and 3.4 mV, respectively ($T = 1.8$ K, $V_{\text{set}} = 7.8$ mV, $I_{\text{set}} = 500$ pA, $V_{\text{L}} = 370$ μV).

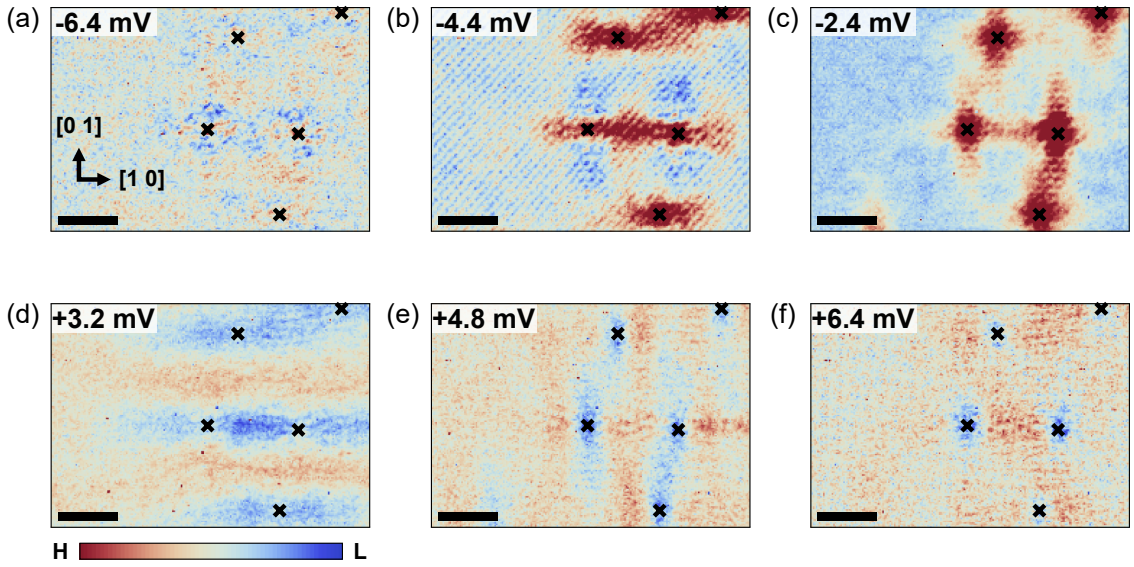

Figure 5.12: C_4**-symmetry breaking of the quasiparticle interference patterns.** (a)-(f) Energy layers of a $g(V)$ map in an area containing point defects at energies -6.4, -4.4, -2.4, 3.2, 4.8, 6.4 mV, respectively ($T = 56$mK, $V_{\text{set}} = 6.4$ mV, $I_{\text{set}} = 225$ pA, $V_{\text{L}} = 398$ μV). The positions of the point defects are indicated by crosses.

around point defects, shown in Figure 5.12. At -6.4 mV, Figure 5.12(a), the QPI patterns around the defects look four-fold symmetric. This energy is outside the partial gap observed in the $g(V)$ spectrum. With decreasing energy, entering the ± 5 mV of the gap, the QPI patterns become unidirectional, aligning with the $[01]$ direction at -4.4 mV (Figure 5.12(b)) then with the $[10]$ direction at -2.4 mV (Figure 5.12(c)), switching back to horizontal at 3.2 mV (Figure 5.12(d)) and then to vertical at 4.8 mV (Figure 5.12(e)), and becoming C_4-symmetric again at 6.4 mV (Fig-

ure 5.12(f)). Both these results demonstrate that the underlying electronic structure of the surface layer of Sr_2RuO_4 has states that break C_4-symmetry at certain energies. This C_4-symmetry breaking is not consistent with the crystal structure shown in Figure 5.1(a), which remains four-fold symmetric despite the octahedral rotations, suggesting additional mechanisms for its origin, such as a magnetic order, electronic correlations or additional structural distortions.

5.7 DFT calculations

5.7.1 Single layer

To understand how the band structure of Sr_2RuO_4 changes with the RuO_6 octahedral rotation, a series of DFT calculations were performed on a single perovskite layer of Sr_2RuO_4 with increasing angle of rotation. The calculations were performed using the linear combination of atomic orbitals (LCAO) representation of the wavefunctions, using local-density approximation (LDA) as the exchange-correlation functional. The unit cell used in the calculations was the surface unit cell shown in Figure 5.1(a). Spin-orbit coupling was not included, as a result, the band hybridizations along the ΓX direction are not captured (see Chapter 2, section 2.2.1). Although the overall shape of the bands is well captured by DFT, the Fermi velocity is considerably higher when compared to experiment [27]. In order to put the vHs at the M point at 14 meV, as measured experimentally [6], the energy of the bands was renormalized by a factor of 2.3. After renormalization, the band structure for $\theta = 0°$, Figure 5.13(a), compares well to the dispersion of the bulk bands measured by ARPES from ref. [117], and while the dispersion of the d_{xz}/d_{yz} bands is in good agreement for binding energies lower than 40 meV, the dispersion of the d_{xy} band is considerably heavier in the experiment, highlighting the highly correlated nature of this band.

Figure 5.13 shows the Fermi surface, band structure and total DOS for calculations with in-plane octahedral rotation angles from 0° to 8°. The vHs at the M point is pushed below E_F with increasing angle of rotation: for $\theta = 0°$ the vHs is above E_F, resulting in a peak in the total DOS above but close to E_F, and as θ is increased, the vHs touches E_F for $\theta = 4°$, being pushed to lower energies for $\theta = 6°$ and $\theta = 8°$. This occurs as a consequence of hybridization between d_{xy} and d_{z^2} states which is allowed due to the octahedral rotations. As the vHs is pushed below E_F, its saddle point becomes more flat resulting in the increase in the intensity of the peak in the DOS. Additionally, for angles $\theta > 5°$, an electron pocket at the Γ point crosses the Fermi level, also moving down in energy, as a result of the hybridization between the d_{xy} and the $d_{x^2-y^2}$ states. These calculations reproduce previous reports [23, 27, 282].

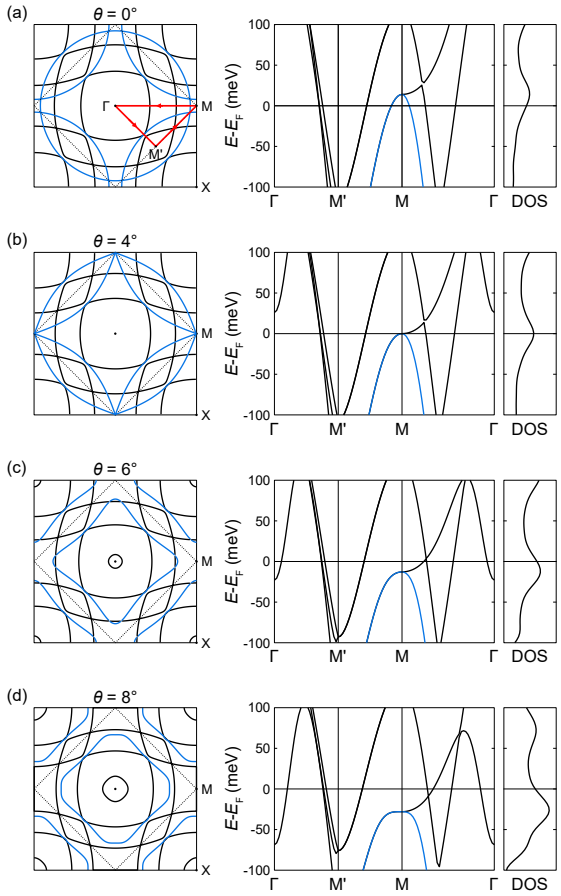

Figure 5.13: **DFT calculations on a single layer of Sr_2RuO_4 with increasing angle of rotation.** (a) - (d) Fermi Surface, band structure and total DOS for angles of rotation of the RuO_6 octahedra of 0°, 4°, 6° and 8°, respectively. The band of d_{xy} character which has the relevant vHs is shown in blue. The path along which the band structure was calculated is indicated by red lines in (a), with M' the middle point of the edge of the reconstructed BZ. The DFT calculations were performed using GPAW, using atomic orbitals as basis functions (LCAO, double-zeta polarized basis set) and the local density approximation. The band structure plot was calculated in a $40 \times 40 \times 1$ k-grid, and the Fermi surface plots were obtained from a calculation with a $151 \times 151 \times 1$ k-grid. The total DOS was calculated with a broadening of 19.6 meV and the x-axis goes from 2.5 to 6.5 states/eV. The energy of the bands was renormalized by a factor of 2.3 such that the vHs at 0° angle is at 14 meV, as estimated from experiment [6].

The Fermi surfaces for $\theta = 6°, 8°$ show overall agreement with the Fermi surface measured by ARPES [24, 26, 27, 117], where the Fermi pockets corresponding to the d_{xz}/d_{yz} and d_{xy} bands have the correct shape, despite differences in k_F. The circular pocket at the Γ and X points is overestimated, with its minimum below E_F, while ARPES measurements reveal that it should be a few meV above the Fermi level [26]. However, the band structure is not in agreement with the STM measurements presented in this chapter: it does not reproduce the partial gap around E_F, the four peaks in LDOS, C_4-symmetry breaking nor the checkerboard on top of the Sr lattice.

5.7.2 Three-layer slab

To study what kind of structural distortions could lead to the appearance of four peaks in the DOS and a partial gap around E_F, DFT calculations on a three-layer slab of Sr_2RuO_4 were performed. The following distortions of the surface layer were investigated here: (i) octahedral rotation plus the tilt characteristic of Ca_2RuO_4; (ii) vertical displacement of the topmost Sr atoms in a checkerboard pattern; (iii) displacement of the surface layer along the [100] direction; and (iv) checkerboard AFM order on the Ru atoms in the surface layer. These distortions were chosen to either create a checkerboard pattern (i,ii and iv) or to induce C_4-symmetry breaking (iii). The calculations were performed using a plane-wave basis set, with an energy cut-off of 650 eV and the generalized gradient approximation (PBE) for the exchange-correlation functional, on a $8 \times 8 \times 1$ k-grid (unless otherwise stated). The results are summarised in Table 5.1, with the respective total energies.

	θ (°)	Δd (pm)	E_T (eV)
Slab†	0.00	0.0	-286.512 (-265.530^*)
Rotation 1st layer†	5.02	0.0	-286.517
Rotation + Tilt 1st layer	5.00 2.00	0.0	-286.493
Staggered Sr	5.00	± 5.0	-286.505
[100] shift 1st	5.00	7.0	-286.509
Ru AFM	5.00	0.0	-265.462^*

Table 5.1: Summary of DFT calculations on a three-layer slab of Sr_2RuO_4, with θ the angle of octahedral rotation, Δd the displacement magnitude and E_T the total energy. All calculations had a vacuum layer of 21 Å, were performed in a $8 \times 8 \times 1$ k-grid, and using a plane-wave basis with an energy cut-off of 650 eV, and PBE. The relaxations were done with the bottom layer fixed. * Calculations performed with a cut-off energy of 450 eV and in a $6 \times 6 \times 1$ k-grid. † Calculations after relaxation with bottom layer fixed.

First, the slab representative of the bulk of Sr_2RuO_4 was relaxed, fixing the positions of the bottom layer. The resulting band structure is shown in Figure 5.14(a), showing three vHss corresponding to each layer, with the bands from the top layer shown in blue. The vHss appear at different energies for each layer due to an increasing elongation of the RuO_6 octahedra along the c-axis between the top and middle layers. Second, the RuO_6 octahedra of the first layer were rotated by 5° and relaxed, with the bottom layer fixed. This resulted in a slightly larger rotation angle of 5.02°, and a total energy 5 meV lower than the undistorted slab, suggesting that this configuration is more stable, reproducing the reconstruction of the surface layer. The band structure,

Figure 5.14(b), shows the expected shift of the vHs to lower energies. The following calculations with different distortions were done using this relaxed structure as a basis.

The first distortion was to induce a staggered tilt of the RuO_6 octahedra, in the same way as observed at the surface of $Ca_{2-x}Sr_xRuO_4$ samples [254]. The total energy of the system is 24 meV higher than the slab with rotation on the top layer. The band structure, Figure 5.14(c), shows the vHs at the same energy as before, with a hybridization gap between the d_{xy} and d_{xz}/ d_{yz} bands appearing at slightly higher energies.

The second distortion was to move the Sr atoms along the z axis in a checkerboard-like fashion, by ± 5 pm, as represented in Figure 5.14(d). The total energy of the system is 12 meV higher than the slab with only rotation of the oxygen octahedra on the top layer. The band structure in Figure 5.14(d) shows that the vHs of the top layer splits into two and that it breaks C_4-symmetry. However, our measurements provide an upper bound of ~ 130 fm for a vertical displacement of the Sr atoms, far smaller than what is necessary to obtain a sizeable symmetry breaking.

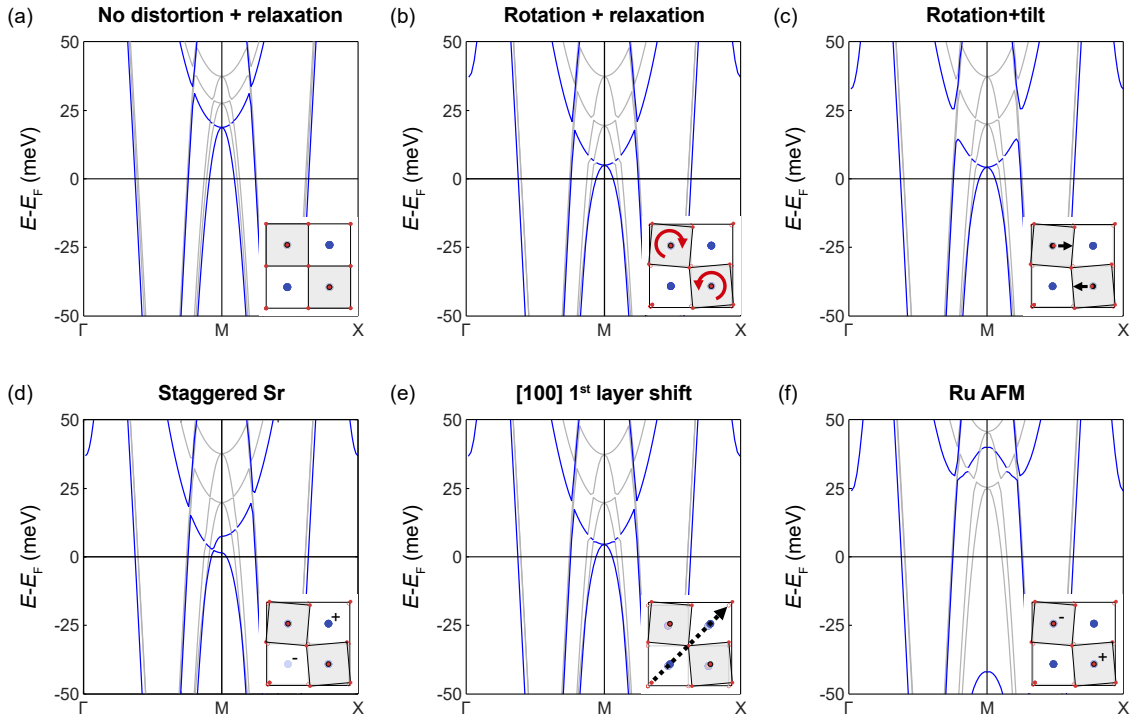

Figure 5.14: **Slab calculations with different distortions.** (a) Bandstructure calculated from DFT of a non-reconstructed three-layer slab of Sr_2RuO_4 after the relaxation of the two top layers. The bands of the surface layer are shown in blue. (b) Same, but with a 5° octahedral rotation on the topmost layer followed by the relaxation of the two top layers. (c) including tilt, (d) staggered vertical displacement of Sr atoms by ± 5 pm (indicated by the plus and minus signs in the inset), (e) horizontal displacement of the top layer along the [100] direction by 7 pm and (f) with AFM order on the Ru atoms (local magnetic moments of 0.195 μ_B/Ru and -0.190 μ_B/Ru, indicated by the plus and minus signs in the inset). The insets show a sketch of the unit cell, with red, black and blue circles as O, Ru and Sr atoms. The calculations were performed over 144 k-points along the path shown and the energies of the bands were renormalized by a factor of 2.3.

The third distortion was shifting the top layer laterally along the [100] direction by 7 pm relative to the second layer in the slab, as illustrated in Figure 5.14(e), giving rise to an increase of 8 meV of total energy in relation to the slab with rotation on the top layer. This breaks C_4-symmetry due to the inequivalent positions between the first and second layer, however, the band structure does not show such symmetry breaking at the van Hove point, showing a dispersion almost identical to Figure 5.14(b).

The last attempt was to include antiferromagnetic order on the Ru atoms at the top layer, as illustrated by the plus and minus signs in Figure 5.14(f). The local magnetic moments of the Ru atoms were initialized as $\pm 1\ \mu_B/\text{Ru}$, and the calculations stabilized in local magnetic moments of $0.195\ \mu_B/\text{Ru}$ and $-0.190\ \mu_B/\text{Ru}$. The bandstructure in Figure 5.14(f) shows the splitting of the vHs at the surface layer, opening a gap at the Fermi level. However, the antiferromagnetic order does not lead to a breaking of C_4-symmetry alone.

None of the above cases seems to capture all the changes to the band structure needed to explain the STM measurements. On one hand, there are cases where a gap is opened but C_4-symmetry breaking occurs along a different direction than that observed experimentally, such as the rotation plus tilt distortion and the AFM order at the surface layer. On the other hand, the staggered displacement of the Sr atoms captures the C_4-symmetry breaking in the correct direction but, to obtain a considerable gap, a much larger distortion than that observed exprimentally is needed.

5.8 Tight-binding model

The DFT calculations presented in the previous section show that the octahedral rotations alone are not enough to describe the STM measurements. To gain insight into how the checkerboard charge order and nematicity modify the band structure of the surface, we will include them phenomenologically into a tight-binding model.

To describe the surface of Sr_2RuO_4, a model with a two-atom unit cell is necessary due to the octahedral rotation. Consider the lattice shown in Figure 5.15, where the unit cell has two Ru atoms, Ru(A) and Ru(B), at the positions $(-0.25, 0.25)$ and $(0.25, -0.25)$ in relation to the center of the unit cell (size 1×1). We will use a tight-binding model with lattice Hamiltonian of the form of Eq. 4.12, described in section 4.2. As a minimal model to describe the surface layer, and in agreement with previous models developed to describe the physical properties of Sr_2RuO_4 [118] and also $Sr_3Ru_2O_7$ [205–208] (where octahedral rotations are present), we will only account for

the $4d$ t_{2g} orbitals of the Ru atoms. This results in a 6-band tight-binding model with orbital basis $\{d^A_{xz}, d^A_{yz}d^A_{xy}, d^B_{xz}, d^B_{yz}d^B_{xy}\}$.

The hopping parameters are illustrated in Figure 5.15. The nearest-neighbor (NN) d_{xz}/d_{yz} hopping terms are given by t_1 in the plane of the lobes of the orbitals and t_2 in the perpendicular direction, Figure 5.15(a). Hopping between d_{xz} and d_{yz} orbitals between next-nearest-neighbors (NNN) is given by t_{inter}, Figure 5.15(b). For the d_{xy} channel, we include hopping up to the third nearest neighbor, Figure 5.15(c), with t_3 as NN hopping, t_4 as NNN hopping, and t_5 as the third NN hopping term. The chemical potential of the degenerate d_{xz} and d_{yz} orbitals is given by μ. To account for the octahedral rotation, which from the DFT shifts the d_{xy} band down in energy, the chemical potential of the d_{xy} orbital was set to μ_c. Spin-orbit coupling is included as off-diagonal terms in the 3×3 diagonal blocks, with strength η. The values of the parameters are shown in Table 5.2 in eV and were given by Luke C. Rhodes in Ref. [161]. The value of μ_c places the d_{xy} vHs within

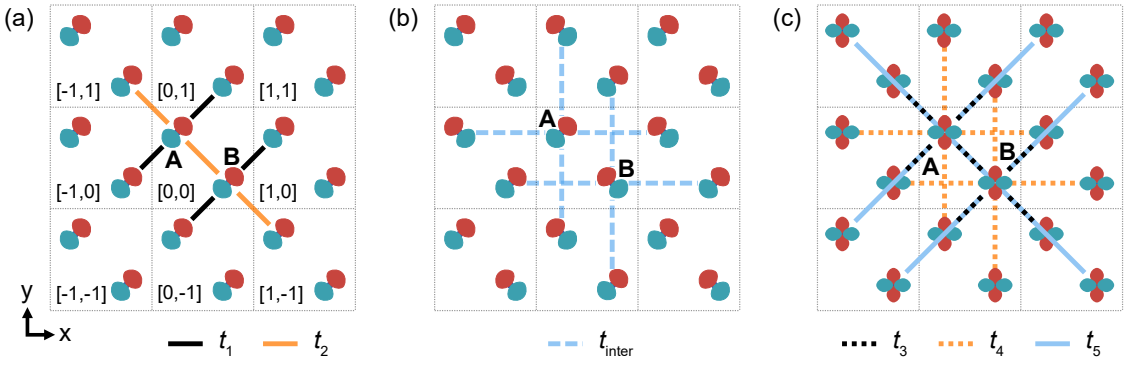

Figure 5.15: **Sketch of hopping parameters.** (a) Sketch of a square lattice with a two-atom unit cell. A and B indicate the atomic positions at $(-0.25, 0.25)$ and $(0.25, -0.25)$, in relation to a unit cell of size 1×1. The nearest-neighbor hopping between d_{xz} orbitals on Ru(A) and Ru(B) is illustrated by the colored lines. The hopping in the direction of the orbital lobes is t_1 (black line) and in the perpendicular direction is t_2 (orange line). The same picture can be drawn for the d_{yz} orbitals, with t_1 and t_2 swapped. The unit cells are labeled relative to the unit cell at the center. (b) Next-neighbor inter-orbital hopping between the d_{xz} and d_{yz} orbitals on Ru(A) on adjacent unit cells, and on Ru(B). (c) Hopping parameters for hopping between d_{xy} orbitals. The nearest-neighbor hopping is t_3 (black dashed line), next-nearest neighbor is t_4 (dashed orange line) and third nearest neighbor hopping is t_5 (solid blue line).

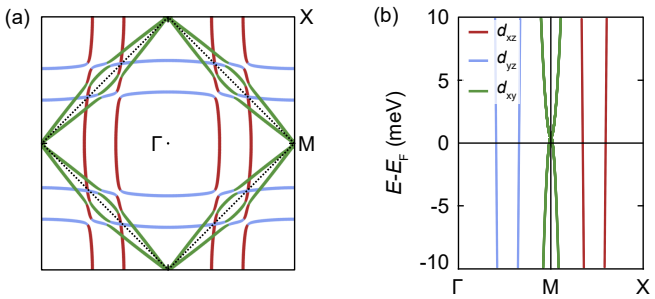

Figure 5.16: **Tight-binding model Fermi surface and band structure.** (a) Fermi surface from the tight-binding model using the hopping parameters of Table 5.2. (b) Corresponding band structure.

less than 1 meV above the Fermi level. Figure 5.16(a) shows the Fermi surface obtained from this tight-binding model. The Fermi wave vector of the d_{xz} and d_{yz} bands are in agreement with the ARPES measurements of the surface bands [27]. While the d_{xy} pockets are slightly narrower than the pockets observed in ARPES and DFT (see Figure 2.12 and Figure 5.13, respectively), this does not affect the comparison with the experiment. The band structure, Figure 5.16(b), shows the correct hole-like behavior of the d_{xy} band, in agreement with the ARPES dispersion of the surface d_{xy} band.

t_1	t_2	t_{inter}	t_3	t_4	t_5	η	μ	μ_c
0.150	0.015	0.0015	0.120	0.045	0.01425	0.015	0.1125	0.1218

Table 5.2: Hopping parameters for the two-atom unit cell tight-binding model of the surface of Sr_2RuO_4, optimized by Luke C. Rhodes in ref. [161]. The values are given as absolute values and in eV.

5.8.1 Staggered bond order and nematic order parameter

The checkerboard order can be phenomenologically included in this tight-binding model by adding a t_{bond} term to the NNN hopping terms of the d_{xy} orbitals, with opposite signs on Ru(A) and Ru(B), as illustrated by the blue and red lines in Figure 5.17(a), realizing a staggered bond order [272]. The nematic order parameter is included by making the NN hopping between d_{xy} orbitals inequivalent in the x and y-directions by an amount t_{nem}, Figure 5.17(b).

Choosing $t_{\text{bond}} = t_{\text{nem}} = 3.5$ meV, results in the Fermi surface shown in Figure 5.17(c), presented in the extended Brillouin zone. The sheets of the Fermi surface of d_{xy} character show an anisotropy around the M-point, where the vector that connects the tips of the two d_{xy} Fermi sheets along the k_x-direction is shorter than the connecting vector along the k_y-direction. The M-points along k_x and k_y are now inequivalent and will be defined as M_x and M_y. The 3D band dispersion around the M_x point, shown in Figure 5.17(d), reveals the appearance of four van Hove singularities: three saddle points $S1$, $S2$, and $S3$ and a maximum M, labelled according to van Hove's notation [93]. The band structure plot along the path $\Gamma - M_x - X$, Figure 5.17(e), shows that the d_{xy} band is gapped at the M_x and M_y points, with two vHss below ($S1$ and M) and above ($S2$ and $S3$) the Fermi level. The total DOS from this model is shown in Figure 5.17(f) for ± 10 mV, and shows strinking similarities with the measured $g(V)$ spectrum of Figure 5.4(b), with an anisotropic partial gap around the Fermi level and four sharp peaks.

The band structure obtained from this tight-binding model bears similarity with the band structure observed for the slab calculation including a displacement of the Sr atoms along the z-direction

in a checkerboard pattern, Figure 5.14(d). Both show the splitting of the d_{xy} vHs at the M-point, resulting in C_4-symmetry breaking along the same direction, as well as the gapping of this band (although almost negligible in the case of the slab calculation). It illustrates the equivalence between checkerboard and nematic orders in this system.

5.8.2 Continuum local density of states calculations

This model can now be used to calculate the continuum local density of states following the formalism described in section 4.2. The calculations presented in this chapter were performed using the parameters summarized in Table 5.3. A k-grid of 2560×2560 was chosen so that a sub-meV energy broadening, γ, can be used and the effects of the scattering involving the four vHs can be resolved. The calculation was performed over 64 unit cells in real space, corresponding

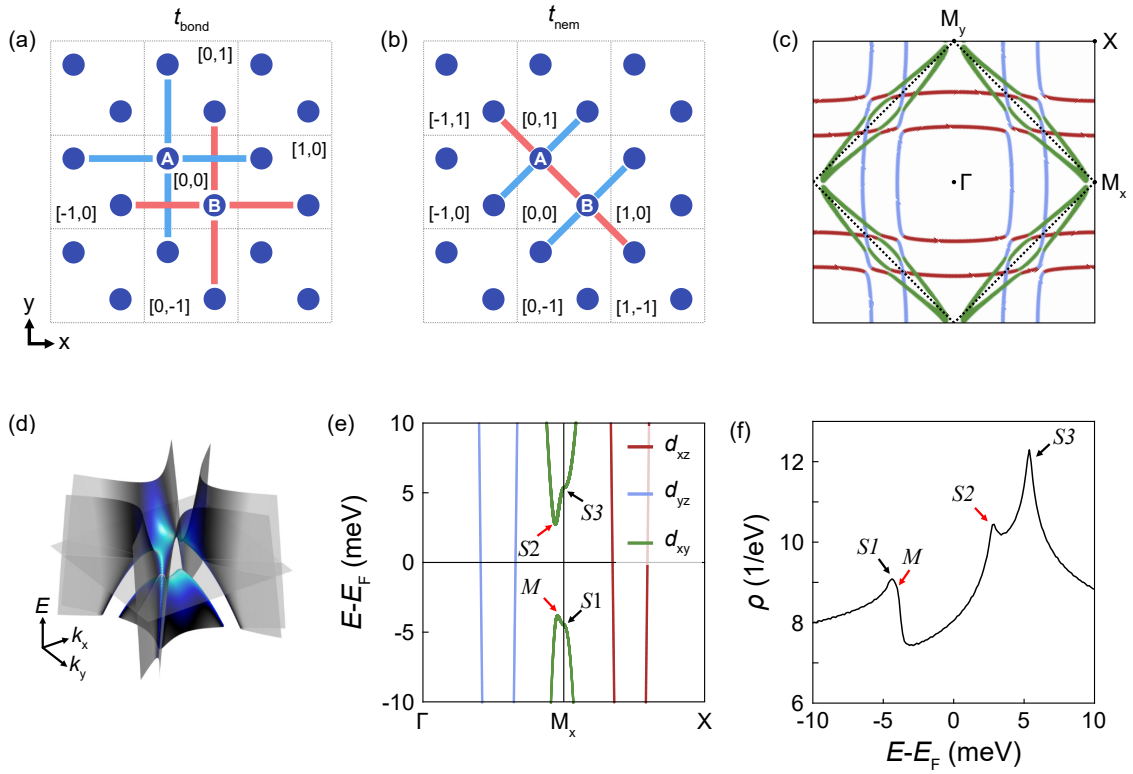

Figure 5.17: **Tight-binding model with a staggered bond order and a nematic order parameter.** (a) The staggered bond order is introduced by adding a term t_{bond} to the NNN hopping of the d_{xy} orbitals with opposite sign on the A and B sites, as indicated by the blue and red lines. (b) Illustration of the nematic order parameter realized by an additional term, t_{nem}, to the d_{xy} NN hopping, with opposite signs along the two spatial directions. (c) Fermi surface in the extended Brillouin zone, with the dashed lines representing the BZ of the two-atom unit cell. (d) Three-dimensional band dispersion around the M_x-point within 15 meV of E_F. The plane indicates E_F. (e) Band structure along the path $\Gamma - M_x - X$ (with a k-resolution of 1×10^{-4}). The vHs are labelled according to van Hove's notation, with the three saddle points and maximum labelled $S1$, $S2$, $S3$ and M, respectively. (f) Density of states. The calculations were performed with $t_{nem} = 3.5$ meV and $t_{bond} = 3.5$ meV. The Fermi surface and DOS were calculated over a 2560×2560 k-grid, with energy broadenings of 2.5 meV and 1.50 μV, respectively.

k grid	γ (μeV)	n_{pixel}	N_{cells}	ϕ	V_{imp} (eV)	$C_{xz/yz}$	C_{xy}	θ_{rot} (°)
2560	150	6	64	2	0.1	1	4	6

Table 5.3: Parameters for continuum LDOS calculations.

to a q-resolution of 0.003 Å^{-1} for a lattice constant of $a = 3.87$ Å . To do the continuum transformation, gaussian-type orbitals with the symmetries of the d_{xz}, d_{yz} and d_{xy} orbitals were used (Figure C.1 in Appendix C). The spread of the gaussian-type orbitals, ϕ, was chosen such that no artifacts appeared in the homogeneous cLDOS calculation over two unit cells (see Figure C.2 in Appendix C). With this spread, the gaussian-type orbitals extend to the neighboring and next-neighboring unit cells (see Figure C.1 in Appendix C), but its effect is barely seen in unit cells further away. Therefore, the calculation was performed such that the sum in Eq. (4.24) only goes over up to the next-neighboring unit cells of the unit cell at $[0,0]$. To enhance the contribution from the d_{xy} channel to the cLDOS calculations, the d_{xy} gaussian-type orbital was multiplied by a constant $C_{xy} = 4$, while the d_{xz}/ d_{yz} gaussian-type orbitals constant was $C_{xz/yz} = 1$. To simulate the rotation of the RuO_6 octahedra at the surface, the gaussian-type orbitals were rotated in opposite directions at the two Ru sites by an angle $\theta = 6°$. The impurity potential is then put on site A or B in the unit cell at the center of the field of view. An example of the outcome of such a calculation is shown in Figure 5.18(a), with a close-up on the impurity. The high intensity spots building the atomic lattice occur in between the Ru positions, reproducing the Sr lattice observed in the experiment.

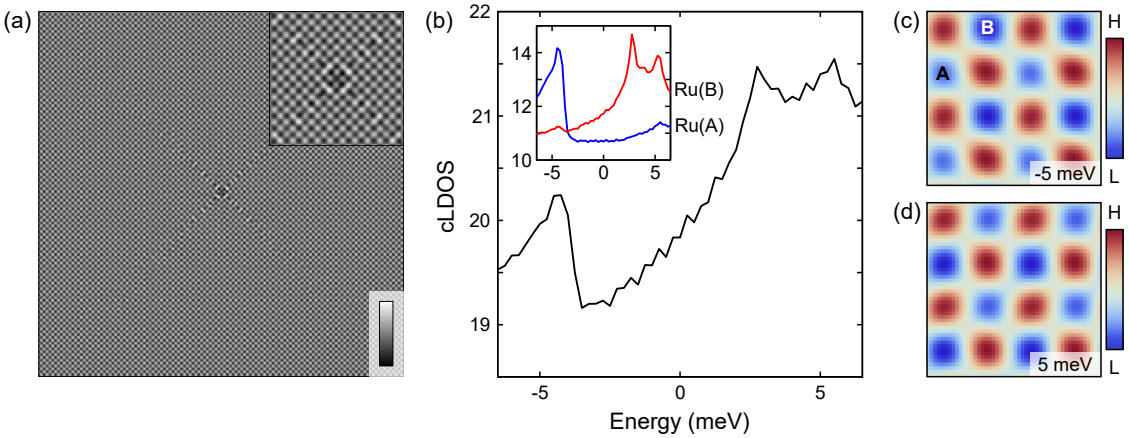

Figure 5.18: **cLDOS calculations.** (a) Real space cLDOS at 1.75 meV. The impurity is located at site Ru(A) in the unit cell at the center of the field of view. Inset shows a close up on the impurity, also showing the atomic lattice in detail. The maxima that make up the atomic lattice occur at the positions of the Sr atoms. (b) cLDOS as a function of energy averaged over a unit cell. The inset shows the cLDOS on top of a Ru(A) site (Blue) and a Ru(B) site (red). (c) and (d) Homogeneous cLDOS over four unit cells at -5 meV and 5 meV. The checkerboard modulations is more clearly observed at the Ru positions.

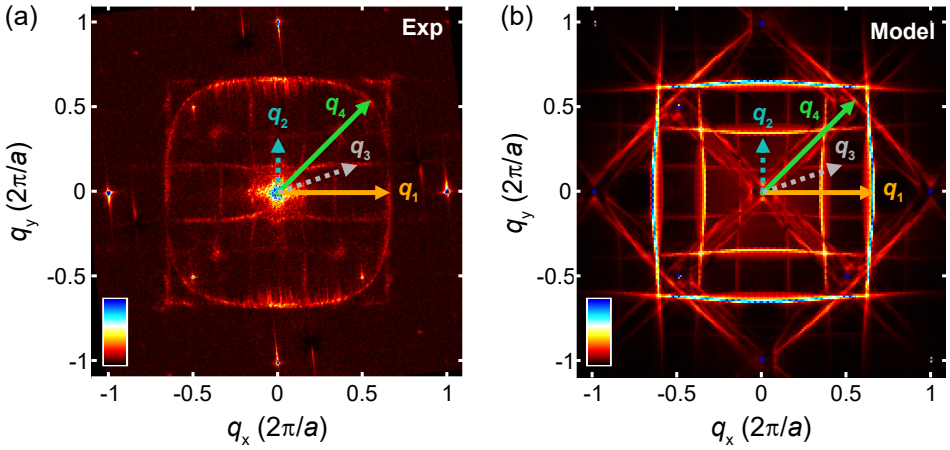

Figure 5.19: **QPI comparison between experiment and model.** (a) Experimental QPI layer at 1.87 mV where four characteristic vectors $\mathbf{q}_1$, $\mathbf{q}_2$, $\mathbf{q}_3$ and $\mathbf{q}_4$ are identified ($V_{\text{set}} = 5.8$ mV, $I_{\text{set}} = 200$ pA, $T = 600$ mK, $B = 12$ T). The map was performed in a field of view of 85×85 nm^2 with a pixel number lower than necessary to resolve the atomic lattice, therefore the atomic peaks were aliased. To recover the full QPI pattern, an antialiasing algorithm was performed and the intensity of the aliased peaks was suppressed by the subtraction of a gaussian at the positions of the aliased atomic peaks. (b) Calculated QPI layer at 1.75 meV, averaging over impurity patterns from both types of Ru impurities. The same **q**-vectors as in (a) are shown.

The simulated cLDOS spectrum, obtained from averaging over a unit cell far from the impurity (top left corner of Figure 5.18 (a)) is shown in Figure 5.18(b). It shows good agreement with the experimental $g(V)$ spectrum in Figure 5.4(b). The cLDOS spectra on top of the two inequivalent Ru sites in the unit cell, Ru(A) and Ru(B), are shown in the inset of Figure 5.18(b). There is a modulation in the intensity of the vHs peaks, where the vHss at negative energies appear more intense on top of Ru(A) sites, whereas the vHss at positive energies are more intense on Ru(B). This results in a checkerboard intensity modulation at the energies of the vHss on top of the Ru sites, with the phase changing across E_{F}. Comparing with experiment, while it reproduces a stronger checkerboard at the energy of the vHs and the phase reversal, the checkerboard appears more clearly on top of Ru sites instead on top of the Sr lattice, see Figure 5.18(c) and (d).

Due to the rotation of the gaussian-like orbitals, placing the impurity on site A or B results in chiral QPI patterns, as in the experiment (Figure 5.3). Since the experimental QPI will have contributions from defects with both chiralities, the cLDOS was calculated individually for impurities placed on site A and site B. Then, the absolute value of the FT of the cLDOS was taken for both calculations and averaged to obtain a QPI pattern with contributions from both types of impurities.

5.9 Quasiparticle interference

As shown in Figure 5.12, clear quasiparticle interference patterns are observed around defects at the surface of Sr_2RuO_4. In order to identify the scattering processes responsible for the observed QPI patterns, in this section the QPI from experimental measurements is presented together with the cLDOS calculations described above.

Figure 5.19(a) shows a QPI map layer taken at 1.87 mV over a field of view of lateral size 85 nm. It shows a QPI pattern consistent with the literature [165, 179]. Four specific shapes can be distinguished, characterized by the $\mathbf{q}$-vectors indicated by the colored arrows, labeled $\mathbf{q}_1$, $\mathbf{q}_2$, $\mathbf{q}_3$ and $\mathbf{q}_4$. The magnitude of $\mathbf{q}_1$, if it is an interband scattering vector, gives $k_F = 0.53 \pm 0.18$ Å^{-1} and its energy dispersion gives a Fermi velocity of $v_F = 0.55 \pm 0.32$ eV Å, in agreement with the Fermi velocity extracted from ARPES for the surface β band [27]. This confirms that the observed QPI patterns originate from the surface bands due to the surface reconstruction, as probed by ARPES. The Fourier transform of the cLDOS calculation shown in Figure 5.18 at energy 1.75 meV is presented in Figure 5.19(b). The same $\mathbf{q}$-vectors are indicated, showing good agreement with the experimental data in Figure 5.19(a), where the overall patterns seem to be captured. Differences in shape are observed due to the details of the underlying tight-binding model.

To disentangle the contributions from the d_{xz}/ d_{yz} and the d_{xy} channels, a cLDOS calculation can be performed where the amplitude of the gaussian-type orbitals of the unwanted channels is put to zero. Figure 5.20(a) shows a cLDOS calculation with the same parameters as before, but with $C_{xy} = 0$ so that only the contributions from the d_{xz} and d_{yz} channels enter into the continuum Green's function. The three $\mathbf{q}$-vectors $\mathbf{q}_1$, $\mathbf{q}_2$ and $\mathbf{q}_3$ are captured. On the other hand, Figure 5.20(b) shows a calculation with $C_{xz/yz} = 0$, so that only the d_{xy} channel contributes to the continuum Green's function, capturing $\mathbf{q}_4$. Looking at the extended Fermi surface shown in Figure 5.20(c), the outer ring comes from intraband scattering between the β band around the zone center with $\mathbf{q}$-vector $\mathbf{q}_1$, whereas both $\mathbf{q}_2$ and $\mathbf{q}_3$ are due to intraband scattering across the boundaries of the Brillouin zone of the two-atom unit cell. The $\mathbf{q}$-vector $\mathbf{q}_4$ is due to the scattering between the Fermi sheets with d_{xy} character.

Note also that only the d_{xy} channel has significant spectral weight around $\mathbf{q} = (0,0)$ and around the atomic peaks $(\pm 1, 0)$ and $(0, \pm 1)$. Comparing with the experimental data in Figure 5.19(a), $\mathbf{q}_4$ is well visible, as well as low-q scattering. The scattering close to the atomic peaks is quite weak and only visible at certain energies. In these calculations, the intensity of the d_{xy} gaussian-like orbitals was exaggerated so that the signal coming from the d_{xy} channel is clearly visible. To

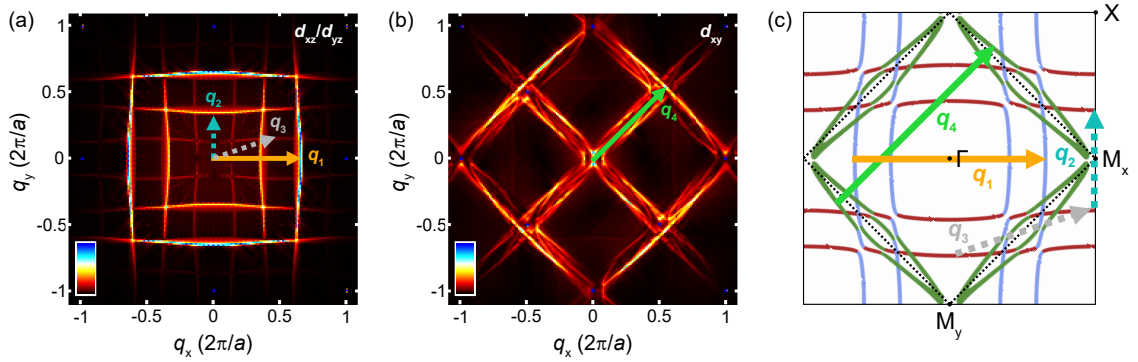

Figure 5.20: **Contribution from different orbital channels to QPI.** (a) cLDOS calculation with $C_{xy} = 0$. The **q**-vectors $\mathbf{q}_1$, $\mathbf{q}_2$ and $\mathbf{q}_3$ are identified. (b) cLDOS calculation with $C_{xz/yz} = 0$. The **q**-vector $\mathbf{q}_4$ is identified. Both calculations are at 1.75 meV. (c) Fermi surface with the previous **q**-vectors identified.

model the relative intensities more realistically requires independent determination of the relative weights of the band with different orbital character, as it is achieved when using Wannier functions as obtained from an *ab-initio* calculation [272].

5.9.1 QPI from the van Hove points

Since the vHss are saddle points in the energy dispersion corresponding to high DOS, strong scattering with a **q**-vector connecting van Hove points is expected. This scattering can occur in two ways: across the M-points with small **q**-vector which collapses onto $\mathbf{q} = (0,0)$ or across the Γ-point with large **q**-vector that becomes $|\mathbf{q}| = 1$ at the energy of the vHs, collapsing onto the atomic peaks in QPI measurements.

QPI scattering patterns with small **q**-vectors correspond to long wavelength modulations in real space. This means that in order to have sufficiently high q-resolution to be able to capture the small **q**-vectors, the surface area to perform a $g(V)$ map has to be large. In Figure 5.21 eight energy

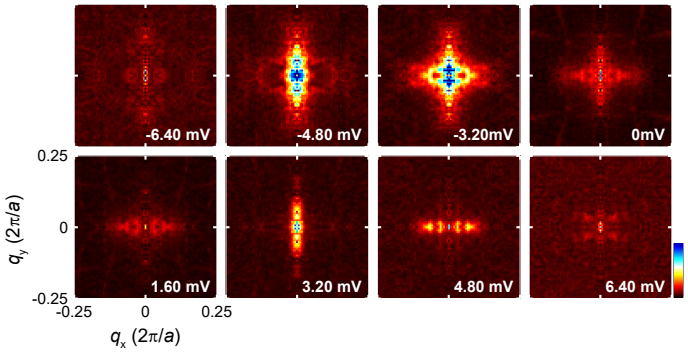

Figure 5.21: **Low-q scattering from d_{xy} band.** QPI patterns around $\mathbf{q} = (0,0)$ from a $g(V)$ map measured in an area of 63×63 nm^2 ($V_{set} = 8$ mV, $I_{set} = 350$ pA, $V_L = 800$ μV, $T = 56$ mK).

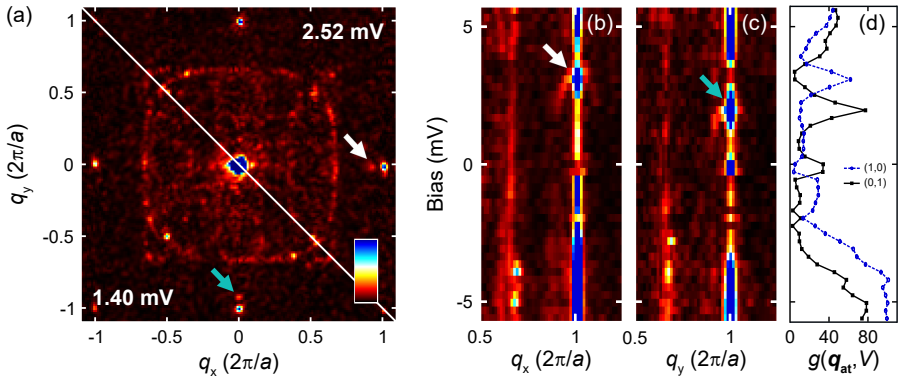

Figure 5.22: **QPI dispersion from vHs at the atomic peaks.** (a) Two QPI layers at 1.40 mV and 2.52 mV. The arrows indicate QPI features close to the atomic peaks along different spatial directions at the different energies. (b) QPI energy dispersion along q_x around the $(1,0)$ atomic peak. A dispersion collapses onto the atomic peak, as indicated by the arrow. (c) QPI dispersion along q_y around the $(1,0)$ atomic peak, where a clear dispersion is observed, which collapses onto the atomic peak at a lower energy than along q_x ($V_{\text{set}} = 5.6$ mV, $I_{\text{set}} = 225$ pA, $V_{\text{L}} = 300$ μV, $T = 76$ mK, $B = 6.5$ T). (d) Differential conductance $\tilde{g}(\mathbf{q}_{\text{at}},V)$ at the atomic peaks $\mathbf{q}_{\text{at}} = (1,0)$ and $(0,1)$.

layers of the FT of a $g(V)$ map with 63 nm lateral size are shown, focusing on the low-q patterns. For energies $|\varepsilon| > 5$ mV, outside the partial gap, almost no weight is observed. Approaching the energies of the vHss, the intensity of the QPI around $\mathbf{q} = (0,0)$ gets stronger and becomes C_2-symmetric, switching between the two high symmetry directions. This is expected from the vHss reaching the M_x and M_y points at different energies. Althought the breaking of C_4-symmetry is clearly detected in these measurements, it is difficult to measure the energy dispersion around $\mathbf{q} = (0,0)$ because in order to have enough q-resolution large area $g(V)$ maps are needed, which result in long-time measurements in order to get enough energy resolution. In addition, the broad background from the random defect distribution appears as spectral weight around $\mathbf{q} = (0,0)$, possibly masking the low-q QPI.

On the other hand, scattering vectors with magnitude $\mathbf{q} \sim 1$ result in modulations with short wavelength, close to the atomic corrugation. Figure 5.22(a) shows two energy layers of a QPI map taken over an area of $(28\text{ nm})^2$ at energies 2.52 mV and 1.40 mV. While a clear feature (indicated by the arrow) is observed close to $\mathbf{q}_{\text{at}} = (1,0)$, no feature is observed close to the atomic peak at $\mathbf{q}_{\text{at}} = (0,1)$. The opposite is found at 1.40 mV, revealing the expected nematicity. The energy dispersions around the two atomic peaks are shown in Figure 5.22(b), where two clear dispersions are observed that collapse onto the atomic peaks along the q_x and q_y directions at different energies. We can determine the energy of the vHss along the different directions by looking at the intensity of the atomic peaks, $\tilde{g}(\mathbf{q}_{\text{at}},V)$, Figure 5.22(c). The vHs along q_x occurs at 3.08 mV and along q_y it is at 1.96 mV. The energy difference between the two is 1.12 mV, giving an indication of the

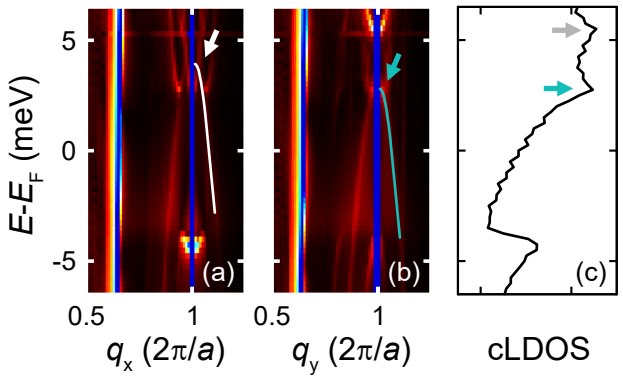

Figure 5.23: **Energy dispersion from cLDOS calculations.** (a) and (b) Show the energy dispersion of the cLDOS calculations around the atomic peaks along the q_x and q_y directions, respectively. The white and blue arrows indicate the position where the vHs dispersion collapses onto the atomic peaks. Lines serve as a guide to the eye. (c) cLDOS averaged over a unit cell. The arrows indicate the position of the vHss.

energy scale of the nematicity in this system.

Energy dispersions around the atomic peaks are also captured in the cLDOS calculations, Figure 5.23(a) and (b), where two hole-like dispersions are seen collapsing onto the atomic peaks at different energies for each spatial direction, corresponding to the energy of the vHss as observed in the cLDOS spectrum, Figure 5.23(c). However, there are important differences. First, the dispersion due to the vHs at negative energies is clearly present, whereas it is not observed in the experiment. In the experimental $g(V)$ spectrum, the vHs at ~ -3.5 mV is the most prominent one and so one would expect to see a larger contribution to QPI coming from it. However, this is not the case, and it seems to be because the signal due to the strong checkerboard order completely dominates over modulations with a wavelength similar to the atomic corrugation. Second, the hole-like dispersions from the vHss at positive energies appear weak and have other dispersions overlapping with them. These dispersions are also from scattering close to the van Hove points, but since the d_{xy} sheets have a small area and very straight edges, their dispersion is narrow compared to the experiment. Continuum LDOS calculations using the Wannier functions and tight-binding model derived from DFT calculations show the hole-like dispersions with larger intensity [272], in better agreement with the experiment.

5.10 Magnetic-field dependence - towards a Lifshitz transition

The comparison between experimental data, the phenomenological tight-binding model and cLDOs calculations establish the four peaks detected in the $g(V)$ spectrum as four vHss. Such vHss so close to E_F open up the possibility to tune the system towards a Lifshitz transition via the application of a magnetic field.

Here, magnetic fields up to 14 T were applied perpendicular to the surface plane, at a temperature of $T = 76$ mK. Figure 5.24(a) shows point spectra with increasing magnetic field, focusing on the most prominent peak at ~ -3.5 mV. As the magnitude of the magnetic field is increased from 0 T to 13.4 T, the peak splits, with one of its branches moving towards E_F, and the other branch moving away, getting washed out by the edges of the partial gap above 11.8 T. To obtain the peak positions as a function of field, first, an arctangent and a constant ($f(V) = A \cdot \arctan[(V - V_0)/\Gamma] + c$) are fitted to the background of the data at 13.4 T to describe the partial gap edge at negative energies. For the curves at other fields, V_0 and Γ are fixed at the values of the fit at 13.4 T, while A and c are fitted to the background using the same arctangent function. After subtracting the resulting function $f(V)$ at each field as a baseline, the peaks are fitted by Lorentzian functions. The peak positions as a function of applied field for both vHs branches are shown in Figure 5.24(b). For a Zeeman splitting under magnetic field, the peak positions will follow (assuming quasiparticles with spin $1/2$):

$$\varepsilon_{\pm} = \varepsilon_0 \pm \frac{1}{2} g^* \mu_B B + \Delta\mu B, \tag{5.4}$$

where g^* is the Landé g-factor, μ_B is the Bohr magneton, B is the applied magnetic field and $\Delta\mu B$ is a field-dependent chemical potential shift due to charge conservation. The positive and

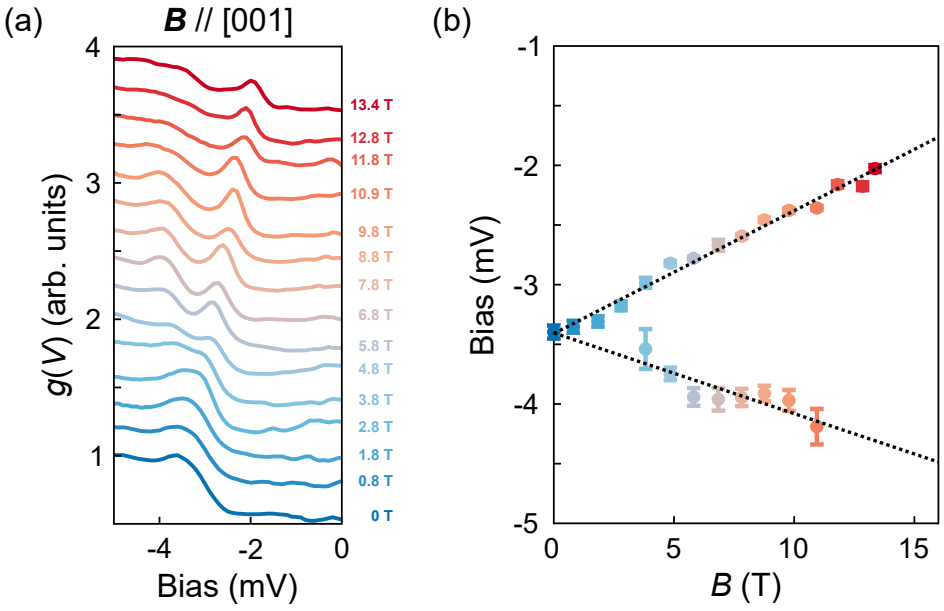

Figure 5.24: **Magnetic-field splitting of a vHs.** (a) Tunneling spectra with increasing magnetic field applied along the [001] direction, from 0 T (blue) to 13.4 T (red) ($T = 76$ mK, $V_{set} = 5$ mV, $I_{set} = 225$ pA, $V_L = 100\,\mu$V). The vHs at -3.4 mV splits into two, with one branch moving towards the Fermi energy. (b) Peak position extracted from (a) as a function of applied field (error bars: 95% confidence intervals). The splitting follows a linear field dependence, as expected from a Zeeman splitting, with $g^* \approx 3$.

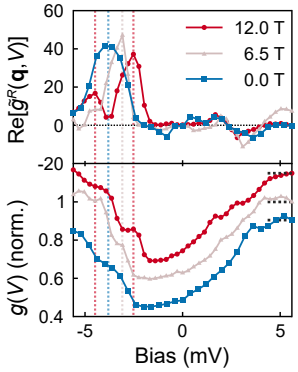

Figure 5.25: **PR-FT as a function of magnetic field.** Top panel shows the PR-FT at the $(0.5,0.5)$ peaks for maps taken at 0 T, 6.5 T and 12 T ($T = 76$ mK, $V_{\text{set}} = 5.6$ mV, $I_{\text{set}} = 225.2$ pA, $V_{\text{L}} = 300$ μV map at 6.5 T; $T = 500$ mK, $V_{\text{set}} = 5.6$ mV, $I_{\text{set}} = 200.5$ pA, $V_{\text{L}} = 280$ μV for map at 12 T). The bottom panel shows the average tunneling spectra $\langle g(r,V)\rangle_r$ for the maps at each field. The vertical dashed lines indicate the positions of the split vHs. Each spectrum is normalized and vertically shifted for clarity, the short dashed gray lines indicate $g(V) = 1$.

negative moving vHs branches are seen to follow an approximate linear trend, consistent with Zeeman splitting and Eq. (5.4). Both $\Delta\mu$ and g^* can be estimated from the slopes $a_1 = 0.10$ mV/T and $a_2 = -0.07$ mV/T of the linear fits to the positive and negative vHs branches, respectively, by

$$\Delta\mu = \frac{a_1 + a_2}{2} \approx 17\ \mu\text{V/T}, \tag{5.5}$$

and

$$g^* = \frac{a_1 - a_2}{\mu_B} \approx 3, \tag{5.6}$$

which is consistent with the Wilson ratio of the bulk material $R_W = g^*/2 = 1.5$ [131, 134]. Extrapolating the linear fit to the positive moving vHs branch predicts that this vHs will reach E_{F} at a magnetic field of 32 T. While there are high-field magnets capable of reaching magnetic fields higher than 32 T, currently, this value is not reachable by currently commercially available superconducting laboratory magnets.

The checkerboard order reported in section 6.4 is associated with the vHs which splits under field. To determine if the bias voltage at which it exhibits maximum contrast follows the peak once it is split, the PR-FT analysis was performed for maps taken at magnetic fields of 0 T, 6.5 T and 12 T, shown in Figure 5.25. The maximum intensity in the PR-FT, corresponding to the energy where the checkerboard is strongest, is seen to move with the peak in the $g(V)$ spectrum (lower panel of Figure 5.25). Therefore, the checkerboard order is intimately linked with the vHs energy and becomes spin-polarized under magnetic field.

Despite shifting the checkerboard modulation in energy according to the split vHs, the applica-

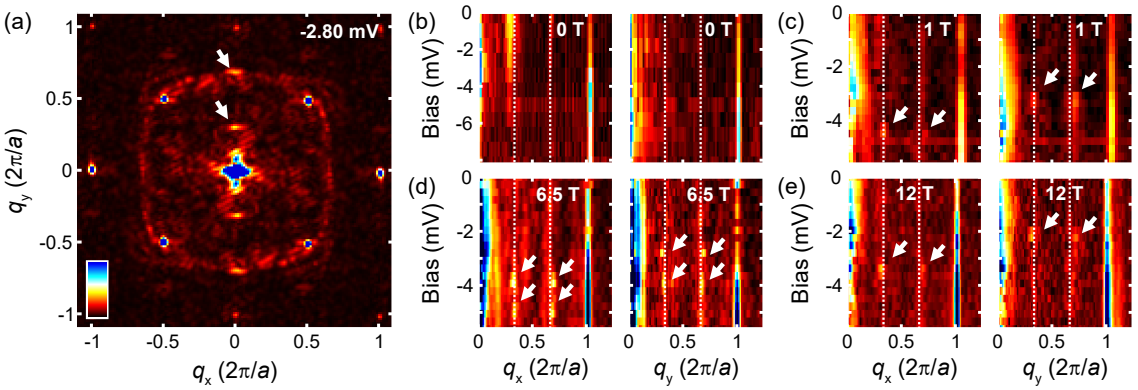

Figure 5.26: **QPI feature at $1/3$ under magnetic field.** (a) QPI layer at -2.80 mV, under 6.5 T, for negative energies. Features at $(0,1/3)$ and $(0,2/3)$ are indicated by the arrows. (b) - (e) Energy linecuts at negative energies at $q_y = 0$ (left) and $q_x = 0$ (right) for magnetic fields of 0 T, 1 T, 6.5 T and 12 T, respectively. The dotted lines correspond to $q = 1/3, 2/3$ and the arrows indicate the peaks energies.

tion of a magnetic field does not seem to change the energy dispersion of the QPI scattering vectors close to the Fermi level. However, for QPI maps taken under magnetic field, sharp features appear at $1/3$ and $2/3$ along a preferential direction at fixed energies, as highlighted in Figure 5.26(a) by the arrows. The energy linecuts of the QPI maps at different magnetic fields along q_x and q_y show at which energies these peaks appear. At 0 T, Figure 5.26(b), no peak is observed along both q_x and q_y directions. Upon applying 1 T, Figure 5.26(c), peaks appear at $q = 1/3, 2/3$ first along the q_x direction at -4.48 mV, and then along q_y direction at -3.36 mV. At 6.5 T, Figure 5.26(d), two sets of peaks appear along each q-direction, at -5.04 and -3.92 mV along q_x and at -3.92 and -2.8 mV along q_y. Increasing the field to 12 T, Figure 5.26(e), puts these peaks at -3.36 mV along q_x and at -2.24 mV along q_y. The difference between the bias voltages at which the peaks appear along each q-direction is 1.12 mV for all fields, equal to the energy difference found experimentally between the vHss above E_F as shown in section 5.9.1. It thus gives an energy scale of 1.12 meV for the C_4-symmetry breaking observed at the surface of Sr_2RuO_4.

5.11 Discussion

The STM measurements reported in this chapter uncover the low energy electronic states in the surface layer of Sr_2RuO_4 under octahedral rotation. In addition to the previously reported features of the surface reconstruction, namely the detection of a partial gap around E_F [158–160, 179] and the presence of the checkerboard modulation on the Sr lattice in STM topographies [25, 116], here we reveal that the surface exhibits its own emergent electronic states: (1) the checkerboard modulation is bias dependent and changes phase across the Fermi level, (2) the low energy elec-

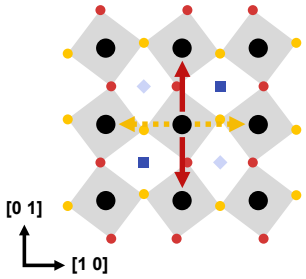

Figure 5.27: **Sketch to explain the equivalence of checkerboard order and nematicity at the surface of Sr_2RuO_4.** Structure of the surface layer of Sr_2RuO_4 at the RuO_2 plane including a checkerboard modulation on the Sr positions, represented by the light and dark blue diamonds and squares. The oxygen atoms are colored red/yellow according to the proximity to a light/dark Sr position, resulting in inequivalent hopping between the vertical and horizontal directions illustrated by the full and dashed arrows.

tronic states break C_4-symmetry at certain energies and (3) these two orders are intimately linked to four sharp peaks found within 5 mV of E_F in the $g(V)$ spectrum as well as to the partial gap.

5.11.1 Possible mechanisms for checkerboard charge order and nematicity

The appearance of the checkerboard charge order and nematicity cannot be explained from the octahedral rotation alone, since the unit cell of the reconstructed surface, Figure 5.1(a), is C_4-symmetric and preserves the equivalence of adjacent Sr positions. However, checkerboard order and nematicity become linked through the octahedral rotation: if the Sr positions are inequivalent, the oxygen atoms along the vertical and horizontal directions become inequivalent, and vice-versa. This equivalence is sketched in Figure 5.27, where the oxygen atoms along the $[10]$ direction are closer to dark Sr positions (yellow) and the oxygen atoms along the $[01]$ direction are closer to light Sr positions (red) as a consequence of the octahedral rotation, becoming inequivalent due to the inequivalence of the Sr positions. As a result, there is an anisotropy in the electron hopping between Ru atoms across yellow oxygen atoms (dashed arrow) and across red oxygen atoms (full arrow), leading to C_4-symmetry breaking, or nematicity of the low energy states.

The mechanism behind the stabilization of the checkerboard charge order and nematicity is not trivial, nor is their equivalence via the octahedral rotation. It is not clear from the measurements if one order is driving the other or if there is an additional mechanism responsible for their stabilization. Possible origins include additional structural distortions, electron correlations, or an underlying magnetic order.

For a typical charge density wave scenario, a considerable structural distortion is expected [283]. Different types of lattice distortions were explored in section 5.7.2. Slab calculations with tilting of the RuO_6 octahedra along the $\{110\}$ directions produce a hybridization gap between

the d_{xy} and d_{xz}/d_{yz} states, Figure 5.14(c). It results in a partial gap in the total density of states, where the edges of the hybridization gap together with the vHs of the d_{xy} band and the minimum of the electron-pocket at the Γ and X points would give peak-like structures in the density of states similar to what it is observed in the spectroscopy measurements in Figure 5.4(b). However, the resulting nematicity does not occur along the same direction as observed experimentally and the QPI measurements do not show evidences of a dispersion corresponding to an electron-pocket linked to the feature at the Γ and X points. By tilting the RuO_6 octahedra along the [100] direction in a staggered fashion produces the correct direction for nematicity but no gap appears, due to the d_{xy} states only hybridizing with the d_{xz} states and not the d_{yz} states which occur in the direction perpendicular to the tilting direction. Only one of the considered distortions shows the necessary changes to the band structure, corresponding to the staggered vertical displacement of Sr atoms, Figure 5.14(d), confirming the equivalence of the checkerboard order and nematicity through the octahedral rotation, as sketched in Figure 5.27. However, this distortion is not in agreement with the presented data because for a true physical displacement, the checkerboard should be visible at all bias voltages, which it is not, and the upper bound for possible height difference between adjacent Sr atoms from topographies taken at 100 mV is $\sim$ 130 fm, much smaller than what is needed as input in the calculation to produce a gap of the same size. On the other hand, it is known that in correlated materials, DFT requires significantly larger orthorhombic distortions to explain electronic-driven orders such as nematicity, compared to what is seen experimentally [284].

In the case of nematicity driven by electron correlations, additional structural distortions would also be expected, such as a transition from tetragonal to orthorhombic structure, similar to what is observed in the iron pnictides [285]. In this scenario, the checkerboard order should be observed to disappear at some temperature, however, it is still visible at room temperature [25]. Additionally, IV/LEED measurements show spots which only agree with in-plane octahedral rotation [176], not allowing the confirmation of any of these two scenarios.

Another possible mechanism is the presence of an underlying magnetic order, such as an antiferromagnetic order which results in both checkerboard charge order and nematicity and would require a much smaller structural distortion. In this case, magnetic domains are expected to be formed, which were not observed for fields of view of lateral size > 200 nm. The experimental data presented in this chapter lacks strong evidence against or in favor of this scenario.

Although the presented data does not favor a particular mechanism, it provides a characteristic energy scale for each order. The checkerboard charge order is intimately linked with the peaks in the tunneling spectrum that occur at ± 3.5 mV, while the nematicity is connected with the energy

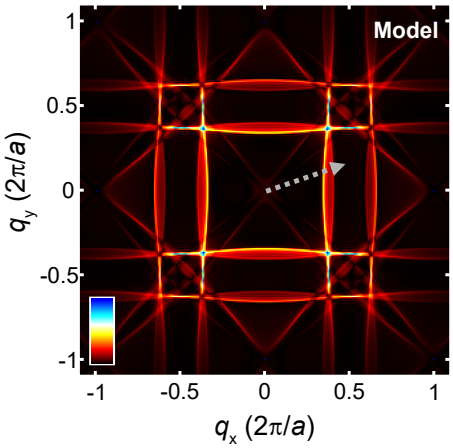

Figure 5.28: **QPI from a one-atom unit cell model.** Fourier transform of a cLDOS calculation using a one-atom unit cell tight-binding model with the hopping parameters of Table 5.2. The parameters for the cLDOS calculation are the same as in Table 5.2, with $\theta_{\text{rot}} = 0°$. The dotted arrow indicates the missing vector $\mathbf{q}_3$.

difference between the vHss found along the q_x and q_y directions, as well as to the field-induced features at $q = (0,1/3),\ (0,2/3)$, giving an energy scale of 1.12 meV.

5.11.2 Detailed comparison of the tight-binding model

The tight-binding model presented in section 5.8 includes the necessary ingredients to describe the electronic structure of the surface layer of Sr_2RuO_4, as revealed by the STM measurements: (1) doubling of the unit cell, (2) checkerboard charge order, and (3) C_4-symmetry breaking of the low energy states.

The effects of the doubling of the unit cell in the STM measurements are visible in the QPI patterns. Figure 5.28 shows the Fourier transform of a cLDOS calculation using a one-atom unit cell tight-binding model of Sr_2RuO_4, representative of the bulk. Comparison with the experimental data reveals that the parallel lines along the direction of the atomic peaks ($\mathbf{q}_3$), which are due to scattering between the folded d_{xz}/d_{yz} bands, can only be reproduced in a two-atom unit cell model.

Including the checkerboard charge order and the breaking of C_4-symmetry via a staggered bond order t_{bond} and a nematic order parameter t_{nem}, results in a density of states that is in excellent agreement with the experimental $g(V)$ spectrum. The opening of a gap on the d_{xy} band around E_F reproduces the asymmetric shape of the partial gap, and the appearance of four vHs in this band explains the four peaks observed in the tunneling spectrum. The C_4-symmetry breaking atomic-scale modulations observed in the differential conductance maps (Figure 5.11) are naturally explained by the vHs in the k_x and k_y directions becoming inequivalent, resulting in them

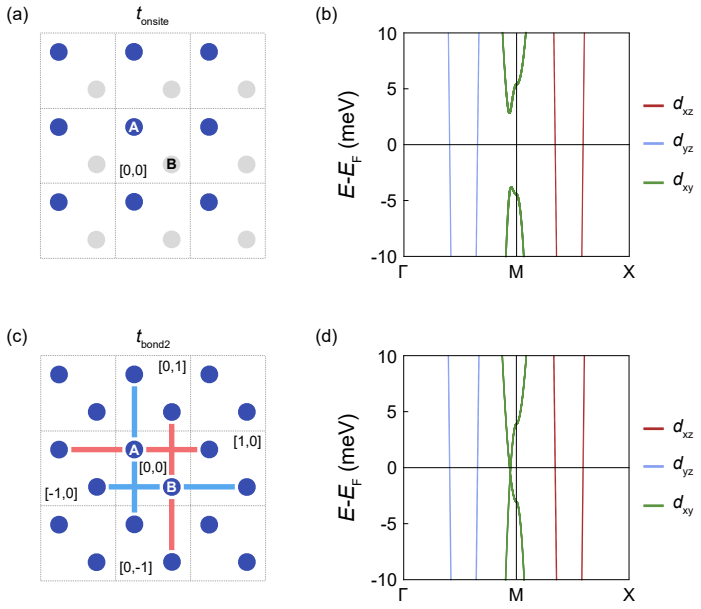

Figure 5.29: **Possible staggered orders to describe the Sr-centered checkerboard.** (a) Illustration of staggered onsite order. A and B indicate the positions of Ru(A) and Ru(B) sites in the unit cell and blue and gray colors indicate the opposite sign in onsite energy. (b) Band structure for staggered onsite energy order. The colors indicate the orbital character. (c) Illustration of staggered bond order 2, with d-wave symmetry. (d) Band structure for bond order 2. For both calculations, $t_{\text{nem}} = 3.5$ meV and $t_{\text{onsite}} = t_{\text{bond2}} = 3.5$ meV. The band structures were calculated for 30003 k-points along the shown path.

collapsing onto the Bragg peaks at $(1,0)$ and $(0,1)$ at different energies, as well as collapsing onto $(0,0)$ from the two different directions at different energies, giving rise to C_2-symmetric long-range QPI modulations (Figure 5.12).

Despite the excellent agreement between the model and the experimental data, there are striking differences between the calculated DOS and measured $g(V)$ spectrum. The right intensities and energy difference of the vHss are not captured, while in the experiment the vHss at negative energies are separated, in the calculations they are difficult to separate in energy and appear in the DOS as a peak with an anisotropic shape. In the $g(V)$ spectrum (Figure 5.4) the vHs at -3.5 mV is a peak, whereas in the calculation it is a step-like feature due to corresponding to a band maximum and not to a saddle point. The depth of the measured partial gap is considerably larger than predicted by the calculations. Additionally, the checkerboard modulation appears more clearly on top of the Ru sites, Figure 5.18(c) and (d), instead of on top of the Sr positions.

A staggered bond order of the form used in section 5.8 is not the only way of realising a checkerboard modulation on top of Sr atoms. Figure 5.29 shows two alternative orders that can produce such a modulation: staggered onsite energies (t_{onsite}) and staggered bond order with d-wave symmetry (t_{bond2}). The addition of an onsite energy with opposite signs on the d_{xy} orbital channel of the Ru(A) and Ru(B) results in the gapping of the d_{xy} band, Figure 5.29(b), identical to the band struc-

ture derived from the inclusion of the staggered bond order shown in Figure 5.17(e). These two orders indeed become equivalent at the corners of the reconstructured Brillouin zone. Transforming the Hamiltonian into k-space, the staggered bond order reduces to $f_{\text{bond}}(\mathbf{k}) = \pm t_{\text{bond}} 1/2(\cos k_x + \cos k_y)$ which results in $\mp t_{\text{bond}}$ at $\mathbf{k} = (0.5, 0.5)$, becoming equivalent to the staggered onsite energy order.

The staggered bond order 2 is illustrated in Figure 5.29(c). Here, the hopping between NNN Ru(A) atoms in the horizontal direction has an opposite sign to the hopping in the vertical direction, whereas it is inverted for the NNN hopping between Ru(B) atoms. Due to the interwoven blue and red lines, a true checkerboard appears at the top of the Sr atoms. The k-space formulation of this order parameter is $f_{\text{bond2}}(\mathbf{k}) = 1/2(-\cos k_x + \cos k_y)$, which is 0 at the corners of the reconstructed Brillouin zone. As a consequence, the band structure, Figure 5.29(d), does not show the gapping of the d_{xy} band at the Fermi level, instead, the vHs is split due to the nematic order parameter and a Dirac-like dispersion appears.

Neither of the three staggered orders suggested to describe the Sr-centered checkerboard seems to be the ideal order parameter. Although both staggered onsite t_{onsite} and bond t_{bond} orders predict the gapping of the d_{xy} band and appearance of four vHs, they can only be realized in practice if the two Ru atoms are chemically inequivalent, whether via structural distortions (e.g. tilt) or magnetic order, for which there is no experimental evidence in Sr_2RuO_4. On the other hand, in staggered bond 2 order t_{bond2}, the two Ru atoms would still be chemically identical, and a true checkerboard would appear centered at the Sr positions, but it does not result in the gapping of the d_{xy} band. Possibly, including a rotation on the staggered bond 2 directions would make the order parameter $\neq 0$ at $(0.5, 0.5)$, opening up the gap at the M-point.

5.11.3 Continuum LDOS calculations with gaussian-type orbitals

The cLDOS calculations from the tight-binding model described in section 5.8 and using gaussian-type orbitals with the correct orbital symmetries for the continuum transformation of the Green's function allowed for a good description of the experimental data, Figure 5.18 and Figure 5.19. It correctly captures several features of the STM measurements: (1) the atomic contrast exhibits maxima on the Sr sites, a consequence of the symmetry and vacuum tail of the atomic wave functions since the Sr atoms are not contained in the model, (2) the chirality of the defects, by including a rotation of the gaussian-type d-orbitals to model the octahedral rotation, (3) the QPI patterns due to the scattering from the d_{xz}/ d_{yz} bands, and (4) the QPI patterns due to the d_{xy} band around the atomic peaks.

While all observed **q**-vectors could be accounted for, the right orbital composition of $\mathbf{q}_4$ and the correct intensities of the scattering patterns is not correctly captured. Although Figure 5.20(b) clearly shows $\mathbf{q}_4$ on the d_{xy} channel, cLDOS calculations using a tight-binding model and Wannier functions from *ab-initio* calculations [272], show this **q**-vector with d_{xz}/d_{yz} character. It illustrates the differences between our phenomenological model and the tight-binding model derived from *ab-initio* calculations and may be a consequence of how spin-orbit coupling is implemented in both models. The incorrect relative intensities of the QPI patterns from different orbital channels is a consequence of the magnitude of the wavefunctions being accounted for phenomenologically when using gaussian-type orbitals. The same happens to the lateral extent of the orbital lobes, which is also a free parameter that enters in the calculation but can however be set by comparison with the Wannier functions obtained from DFT calculations.

In the case of the calculations shown in this chapter, the magnitude of the d_{xy} gaussian-type orbital was chosen so that the features corresponding to this orbital channel were visible in Figure 5.19(b). The extend of the gaussian-type orbitals was chosen such that the resulting atomic lattice looked like an atomic lattice, like the one probed by the STM (see Appendix C). Although the calculations were performed with the gaussian-type orbitals rotated by 6° degrees to model the octahedral rotation, their overall shape remained the same. From comparison with the *ab-initio* calculated Wannier functions, this appears to be a good approximation for the d_{xz}/d_{yz} orbitals, while it only seems to work partially for the d_{xy} orbitals.

To account for all these parameters, the continuum transformation can be performed using Wannier functions calculated from *ab-initio* calculations. Using such functions allows to chose the distance above the surface where the calculations will be performed, simulating the tip-sample distance. The correct vacuum tail of the orbitals is obtained, which shows the increase in vacuum overlap of the d_{xy} states [272]. The shape of the orbitals also changes slightly, going towards the NNN, increasing its extend relative to the non-rotated surface. Since the Wannier functions are obtained from the Wannierization of a DFT calculation, they will also include contributions from other states, such as the O *p*-orbitals, which do not take part in our tight-binding model description.

5.11.4 Detection of d_{xy} band by STM

The clear detection of the vHs of d_{xy} character, as well as the respective energy dispersion, is surprising due to the in-plane nature of the d_{xy} orbitals. Since their lobes rest in the plane of the surface, the vacuum tail of the corresponding wave functions is short, resulting in a small overlap with the STM tip. This can be seen by comparing the total DOS for a single layer of Sr_2RuO_4

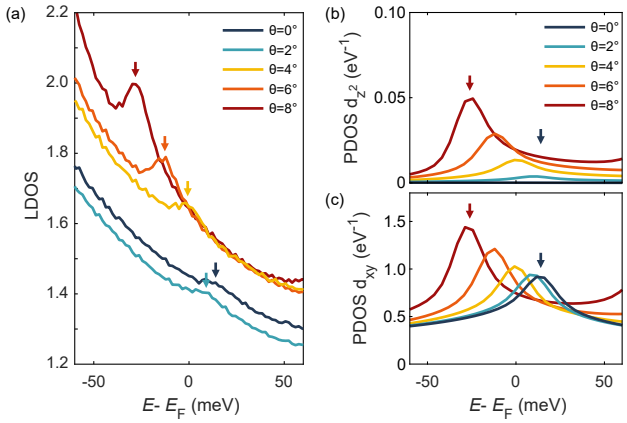

Figure 5.30: **Local density of states and projected-DOS for d_{z^2} and d_{xy} orbitals.** (a) LDOS in the vacuum 5.5Å above a single layer of Sr_2RuO_4 for different angles of rotation, from $\theta = 0°$ to $\theta = 8°$. The arrows indicate the energies of the vHs. (b) Projected-DOS (PDOS) for the d_{z^2} states of the Ru atom. (c) PDOS of the d_{xy} orbital of the Ru atom. The peaks correspond to the vHs in the d_{xy} band which moves across E_F with increasing angle of rotation. The color legend is the same as in (a). Calculations were performed on a $201 \times 201 \times 1$ k-grid in one eighth around the BZ corner to achieve high k-point sampling of the vHs. The energy broadening was 4.4 meV for the LDOS calculations and 8.7 meV for the PDOS calculations.

without octahedral rotation, Figure 5.14(a), with the LDOS calculated for the same system at 5.5 Å above the surface, dark blue line in Figure 5.30(a). While in the total DOS the peak corresponding to the d_{xy}vHs is clearly visible, in the LDOS it is almost imperceptible.

For larger octahedral rotation angles, the peak corresponding to the vHs in the LDOS becomes increasingly more pronounced as it moves below E_F, Figure 5.30(a), showing that the tunneling between d_{xy} states and the STM tip is promoted by the octahedral rotation. The projected DOS (PDOS) onto the d_{z^2} and d_{xy} orbitals of the Ru atoms are shown in Figure 5.30(b) and (c). While for $\theta = 0$ no d_{z^2} weight is observed and the vHs is only visible in the PDOS of the d_{xy} orbitals, as the angle of rotation increases, a peak appears in the d_{z^2} PDOS, at the same energy as the peak in the d_{xy} PDOS, following the movement of the vHs with rotation angle.

The PDOS calculations together with the LDOS in the vacuum with increasing angle of rotation show that the admixture of d_{z^2} orbital character at the van Hove singularity promotes the vacuum overlap with the STM tip, allowing for the detection of these states.

5.11.5 Origin of partial gap

The tight-binding model introduced in section 5.8 reproduces the four peaks due to the vHss, and the partial gap width and asymmetric shape around the Fermi level as seen in the $g(V)$ spectrum. However, the gapping of the d_{xy} band only accounts for 16% of the density of states reduction from the partial gap, while experimentally the partial gap represents a 40% reduction in

differential conductance in relation to the background differential conductance at 8 mV. The cL-DOS calculations taking into account the vacuum tail of Wannier functions [272] also encounter the same problem, suggesting that the larger depth of the gap in the experiments is not just an effect of tunneling matrix elements.

The evolution of the $g(V)$ spectra across line defects, Figure 5.7, can give hints about the origin of the partial gap. It shows that not only does the gap width decrease, but its depth reduces from $\sim 35\%$ at 8 nm away from the edge of the line to 16% at the center of the defect, suggesting the gapping of an additional band at the clean surface, which is not gapped at the center of the defects. The origin of these defects is not known, but plausible scenarios include missing rows of Sr atoms, line cracks caused by the release of local strain due to the octahedral rotation, or a combination of both. For the first scenario, the STM simulated image from the DFT calculations on a slab with a missing row of Sr atoms seems consistent with the topographic characteristics of the line defects. In this case, the suppression of the partial gap at the line defects is related to the Sr atoms. One possibility is that if one assumes that the checkerboard is linked to the displacement of the Sr atoms, and the checkerboard causes the opening of the partial gap than the partial gap would be suppressed once the Sr atoms are removed. Another possibility is that part of the partial gap is linked to the hybridization between Sr states with the p-orbitals of the apical oxygens [5]. In the second scenario, due to the strain release, the rotation of the octahedra would decrease gradually towards the edge of the defect and the decrease in gap width would be correlated with the rotation of the RuO_6 octahedra. In this picture, the gap should disappear at the center of the line defect and the vHs should be seen to merge together. However, at the center of the defect, the gap has a depth similar to what is predicted by the calculations, suggesting that another band is gapped at the clean surface which ceases to be gapped out at the line defects. A possible interpretation could be that the d_{xy}/d_{yz} band is partially gapped at the clean surface and its gap disappears at the linear defect.

Another evidence in the data that suggests that another band is gapped out is that in Figure 5.22(b), (c), the measured energies for the position of the vHss are lower than the peaks at positive energies identified in Figure 5.4(b), suggesting that the higher energy peak corresponds to another band. However, no clear evidence has been found in our QPI maps that corroborate the gapping of another band.

5.11.6 Absence of Superconducting gap

As shown in section 5.3, no superconducting gap was observed at temperatures well below the superconducting transition temperature of the samples, although the energy resolution of the instrument is sufficiently high to detect it. In agreement with previous reports [158–160], this observation suggests that the SrO-terminated surface with octahedral rotation suppresses superconductivity. Previous STM measurements that successfully detected a superconducting gap and were able to verify the assignment from temperature and magnetic-field dependence consistent with bulk Sr_2RuO_4 were obtained on surfaces cleaved in air [163, 164] or on a different surface reconstruction [162]. The common factor between these studies is the absence or suppression of the octahedral rotation at the surface, emphasizing the role of the surface reconstruction. Recently, a study [165] reported the detection of a gap attributed to superconductivity on a SrO-terminated surface, however, it is not clear what the difference is between their experimental setup and the one used here. Thus, it seems that to be able to reliably probe the superconducting gap of Sr_2RuO_4, new ways of suppressing the surface reconstruction have to be explored, such as controlled coverage of the surface with adsorbate layers [117, 286].

The absence of a superconducting gap at the reconstructed SrO-terminated surface indicates that the emergent phases detected in this study are crucial in the suppression of superconductivity, since both checkerboard and nematicity are detected at the surface at temperatures below and above the T_c of the Sr_2RuO_4 samples. In analogy to other strongly correlated materials [38, 287], it seems plausible that the checkerboard charge order and nematicity compete with superconductivity. Whether it is the gapping of the d_{xy} band at the Fermi level or freezing out of the phonon mode associated with the in-plane octahedral rotation that plays a crucial role in the superconducting pairing remains an open question.

5.11.7 Towards quantum criticality

In this work, I have established that the surface layer of Sr_2RuO_4 has vHss in the proximity of the Fermi level and that one of them clearly splits under magnetic field with one branch moving towards E_F. The extrapolated data indicates that it will reach the Fermi level at 32 T, where the system will undergo a Lifshitz transition. This study shows that if it could be reached, it would be possible to measure the whole evolution of the vHs as it crosses the Fermi level, which will allow us to determine the role of quantum fluctuations in such a phase transition.

The surface layer of Sr_2RuO_4 has many similarities with the bilayer compound $Sr_3Ru_2O_7$. Both have in-plane octahedral rotations with similar angle of rotation ($\sim 6^\circ$ for the surface of

Sr_2RuO_4 [25] and $\sim 8^\circ$ for $Sr_3Ru_2O_7$ [28]) and the energy of the dominant vHs observed in the $g(V)$ spectrum in the surface layer of Sr_2RuO_4 is close to -4 meV, the energy at which the vHs of $Sr_3Ru_2O_7$ is found in ARPES measurements [183]. The Wilson ratio, $R_W = 7.3$, of $Sr_3Ru_2O_7$ is larger than the value we found for the surface layer of Sr_2RuO_4, $R_W = 1.5$, evidencing stronger ferromagnetic correlations in the bilayer compound [110]. Due to the higher Wilson ratio in $Sr_3Ru_2O_7$, the vHs can be tuned to the Fermi level with a magnetic field of 8 T, whereas at the surface layer of Sr_2RuO_4 it only reaches E_F at 32 T.

In $Sr_3Ru_2O_7$, a metamagnetic transition is associated with a quantum critical end point (QCEP) [16] at magnetic fields applied parallel to the c-axis. For sufficiently pure samples [17], an ordered phase appears before the system reaches the QCEP, which is associated with electron nematic behavior [18, 190, 288]. The presence of nematicity in the surface layer of Sr_2RuO_4 provides an opportunity to study the influence of the symmetry breaking on what would otherwise have been a multicritical Lifshitz point in the same class as that of $Sr_3Ru_2O_7$ and which has been invoked to explain the power law behaviors of thermodynamic quantities for $Sr_3Ru_2O_7$ [95]. In addition, the surface layer of Sr_2RuO_4 is a two-dimensional system, whereas in $Sr_3Ru_2O_7$ the Fermi surface has a certain degree of three-dimensionality [186], which puts the criticality of the Lifshitz transition in these systems into different universality classes. It thus raises the questions: Is it possible to tune it to a QCEP or will an ordered phase be induced? What kind of ordered phase will it be?

Since Sr_2RuO_4 is a very clean system, where very pure samples can be grown, the surface layer of Sr_2RuO_4 provides a clean system where a clear Zeeman-driven Lifshitz transition can be studied. It has been shown previously that the vHs in bulk Sr_2RuO_4 can be tuned across the Fermi energy by uniaxial strain [7], suggesting that at the surface it would become possible to tune the vHs in a strained sample across the Fermi energy at magnetic fields currently available in low temperature STM. This would allow to map out the surface electronic structure across the expected metamagnetic phase transition.

5.12 Conclusion

The measurements presented in this chapter show that the surface layer of Sr_2RuO_4 provides a two-dimensional model system to study the effects of structural distortions on the physical properties of strongly correlated electron systems. We establish the presence of checkerboard order intertwined with nematicity and find that the surface reconstruction leads to the appearance of four vHs within 5 mV of the Fermi level. The absence of a superconducting gap in the $g(V)$ spec-

trum suggests a competition between these emergent orders and superconductivity. The Zeeman-splitting of a vHs under an applied magnetic field provides a textbook example of tuning towards a magnetic field-driven Lifshitz transition. This opens up the possibility to study, under sufficiently high magnetic fields, the effects of a vHs approaching E_F to establish the role of quantum fluctuations across a field-tuned Lifshitz transition. Our results reveal new opportunities for tailoring correlated electronic phases in two dimensions through the sensitivity of the electronic structure of ruthenates to tiny structural distortions.

Chapter 6

Imaging magnetism and nematicity at the surface layer of $Sr_3Ru_2O_7$

In the previous chapter, I have established that a small in-plane rotation of the RuO_6 octahedra in the surface layer of Sr_2RuO_4 induces new emergent orders, charge modulation and nematicity, seemingly suppressing the superconducting state of the bulk. The bilayer compound, $Sr_3Ru_2O_7$, already has in-plane octahedral rotations and, instead of superconductivity, it exhibits a series of metamagnetic transitions around a magnetic-field of 8 T, which have been associated with quantum criticality and nematic behavior [15–18]. The surface layer of the bilayer compound $Sr_3Ru_2O_7$ is also known to be more distorted than the bulk, with a larger in-plane rotation angle and maybe tilt [28], however, it is not known whether it stabilizes a new ground state. Distorting the RuO_6 octahedra in $Sr_3Ru_2O_7$ either enhances the metamagnetic and nematic behavior by in-plane uniaxial strain [30], or suppresses them by the stabilization of different magnetic orders as seen with doping [19, 29, 213] or out-of-plane uniaxial strain [22]. The aim of this chapter is to determine the low-energy electronic structure of the surface layer of high-purity samples of $Sr_3Ru_2O_7$ and to establish from quasiparticle interference imaging how it evolves with magnetic-field.

STM/STS measurements of the surface layer of $Sr_3Ru_2O_7$ were performed in the temperature range from 80 mK to 9 K and in magnetic fields up to 14 T. The QPI measurements are compared with ARPES measurements [183, 185] and DFT calculations of a free-standing bilayer. Possible interpretations will be discussed, as well as a comparison with the surface layer of Sr_2RuO_4. The experimental data shown in this chapter was collected together with Luke C. Rhodes.

6.1 Surface crystal structure and Brillouin zone

The surface layer of $Sr_3Ru_2O_7$ is a bilayer of RuO_2, with the RuO_6 octahedra joined by one apical oxygen, Figure 6.1(a). In the bulk, the RuO_6 octahedra are rotated in-plane with opposite directions on adjacent lattice sites, as indicated by the arrows in Figure 6.1(a). At the surface, the in-plane rotation of the octahedra is enhanced, from $\sim 8^\circ$ in the bulk to $\sim 12^\circ$ at the surface, as detected by IV/LEED [28].

Due to the octahedral rotation, the two-dimensional unit cell that describes both the bulk and the surface contains two Ru atoms, equivalent to the one used to describe the surface layer of Sr_2RuO_4 (see Figure 5.1). In addition, IV/LEED measurements have found additional diffraction peaks suggesting a small tilt ($\sim 2.5^\circ$) of the surface RuO_6 octahedra [28] towards the Sr atoms, in a staggered fashion between adjacent lattice sites, Figure 6.1(b). This tilting preserves the two-dimensional two-atom unit cell. It is not clear whether the larger distortion at the surface layer of $Sr_3Ru_2O_7$ changes the electronic structure dramatically. ARPES measurements [183, 185] show a Fermi surface and band dispersions consistent with DFT calculations of the bulk $Sr_3Ru_2O_7$, and no additional bands are observed, contrary to Sr_2RuO_4 where clear surface bands are detected [24].

To maintain consistency throughout this work and allow easy comparison with the measurements on the surface layer of Sr_2RuO_4 (chapter 5), the measurements discussed in this chapter will be displayed in relation to the tetragonal unit cell of Sr_2RuO_4, that is, within the Brillouin zone of the two-dimensional one-atom unit cell, black square in Figure 6.1(c). In real space, the features in topographies and differential conductance maps will be given relative to the crystallographic axes [10] and [01], as indicated in Figure 6.1(b). All values corresponding to the reciprocal space will be given in units of $2\pi/a$.

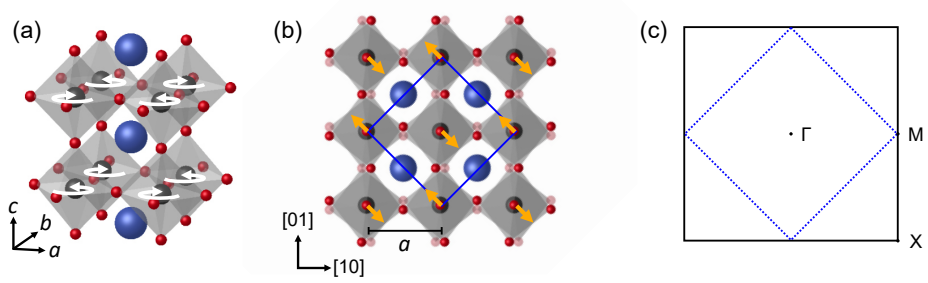

Figure 6.1: **Crystal structure of the surface layer of $Sr_3Ru_2O_7$ and Brillouin zone.** (a) Surface layer of $Sr_3Ru_2O_7$, composed of a bilayer of strontium ruthenate. The arrows indicate the direction of octahedral rotation within the bi-layer. The axes a, b and c correspond to the tetragonal unit cell. (b) Top view of the surface layer of $Sr_3Ru_2O_7$, with the RuO_6 octahedra of the bottom layer of the bilayer shown with transparency. The yellow arrows indicate the directions of tilt as measured by IV/LEED. The blue square indicates the unit cell in two dimensions. The lattice constant of the Sr lattice is $a = 3.89$ Å. The axes indicate the crystallographic directions of a one-atom unit cell square lattice. (c) Sketch of the Brillouin zone corresponding to the one- (black) and two-atom (dotted blue) unit cells.

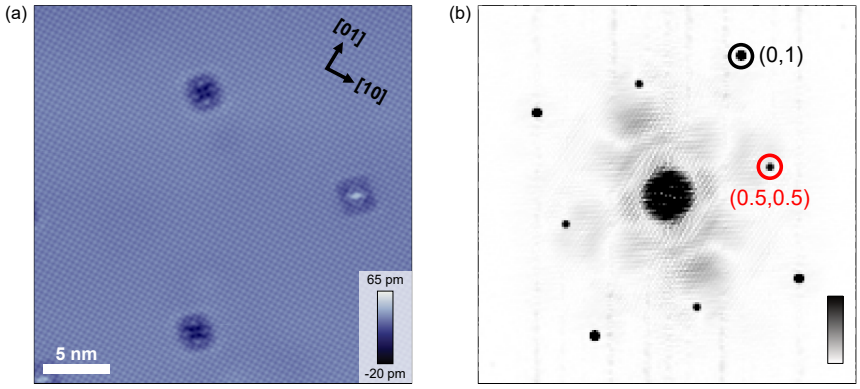

Figure 6.2: **Topography of the surface of $Sr_3Ru_2O_7$.** (a) Typical topography of a SrO-terminated surface of $Sr_3Ru_2O_7$ imaged at $T = 80$ mK (V_{set}= 22 mV, I_{set}= 91 pA). The arrows indicate the crystallographic directions relative to the square unit cell. (b) Fourier transformation of (a). The circles indicate the atomic peaks corresponding to the Sr square lattice (black) and to the checkerboard modulation (red). Units of $2\pi/a$, with $a = 3.89$ Å.

6.2 Topography of the surface of $Sr_3Ru_2O_7$

Single crystals of $Sr_3Ru_2O_7$ cleaved *in-situ* provide surfaces with large and atomically flat terraces, with occasional step edges visible within fields of view larger than 500 nm in lateral size. A typical topography taken at the surface of $Sr_3Ru_2O_7$ is shown in Figure 6.2(a), where a SrO-terminated surface is visible, consistent with a cleave between SrO layers along the $[001]$ plane and in agreement with EBSD measurements (chapter 3 Figure 3.13). The Sr square lattice can be observed. This is confirmed by simulated STM topographic image from DFT calculations on a free-standing bilayer, where the high-intensity spots in the simulated topography correspond to the position of the Sr atoms, shown in Appendix A in Figure A.1. The Sr lattice is superimposed with a bias dependent checkerboard modulation visually identical to the one observed in Sr_2RuO_4 and in agreement with the literature [210, 212]. This is easily seen in the Fourier transformation of the topography, Figure 6.2(b), where two sets of peaks are observed, at $(0, \pm 1)$, $(\pm 1, 0)$ due to the Sr square lattice and at $(\pm 0.5, \pm 0.5)$, $(\pm 0.5, \mp 0.5)$ corresponding to the checkerboard modulation.

Figure 6.2(a) shows the presence of defects. The number of defects constitutes a concentration of $\sim 0.08\%$ deduced from the investigation of large area topographies (> 200 nm). These defects are at the Ru site and show two distinct orientations, in agreement with the rotation of the octahedra in $Sr_3Ru_2O_7$. The FT, Figure 6.2(b), shows clear QPI patterns due to scattering at these defects.

6.2.1 Chiral defects at the Ru sites

Similarly to the defects found in Sr_2RuO_4, the Ru-centered defects in the surface layer of $Sr_3Ru_2O_7$ also exhibit two distinct orientations, confirming the presence of the octahedral rota-

tion. Each orientation can be assigned to one of the Ru sites in the unit cell, Ru(A) and Ru(B). Figures 6.3(a) and (b) show two images of defects of type d^1 with opposite orientations, $d^1_{\mathrm{Ru(A)}}$ and $d^1_{\mathrm{Ru(B)}}$, respectively, while Figures 6.3(c) and (d) show the same but for defects of type d^2, $d^2_{\mathrm{Ru(A)}}$ and $d^2_{\mathrm{Ru(B)}}$. The Fourier transformations (FTs) of the images, Figures 6.3(e-f) for d^1 and (g-h) for d^2, show clear chirality of the intensity of the QPI patterns surrounding these defects, highlighted by the red lines. The different chirality between defects of the same type at different lattice sites is evident by subtracting the FT of their topographies, as shown in Figure 6.3(i) for defects of type d^1 and Figure 6.3(j) for defects of type d^2, where the red follows the chirality of a defect at $\mathrm{Ru(A)}$ and blue at $\mathrm{Ru(B)}$.

The difference between the FTs of defects with opposite chirality, Figures 6.3(i) and (j), show that the chirality of the defects is stronger around the axis that runs along the $[11]$ direction. It

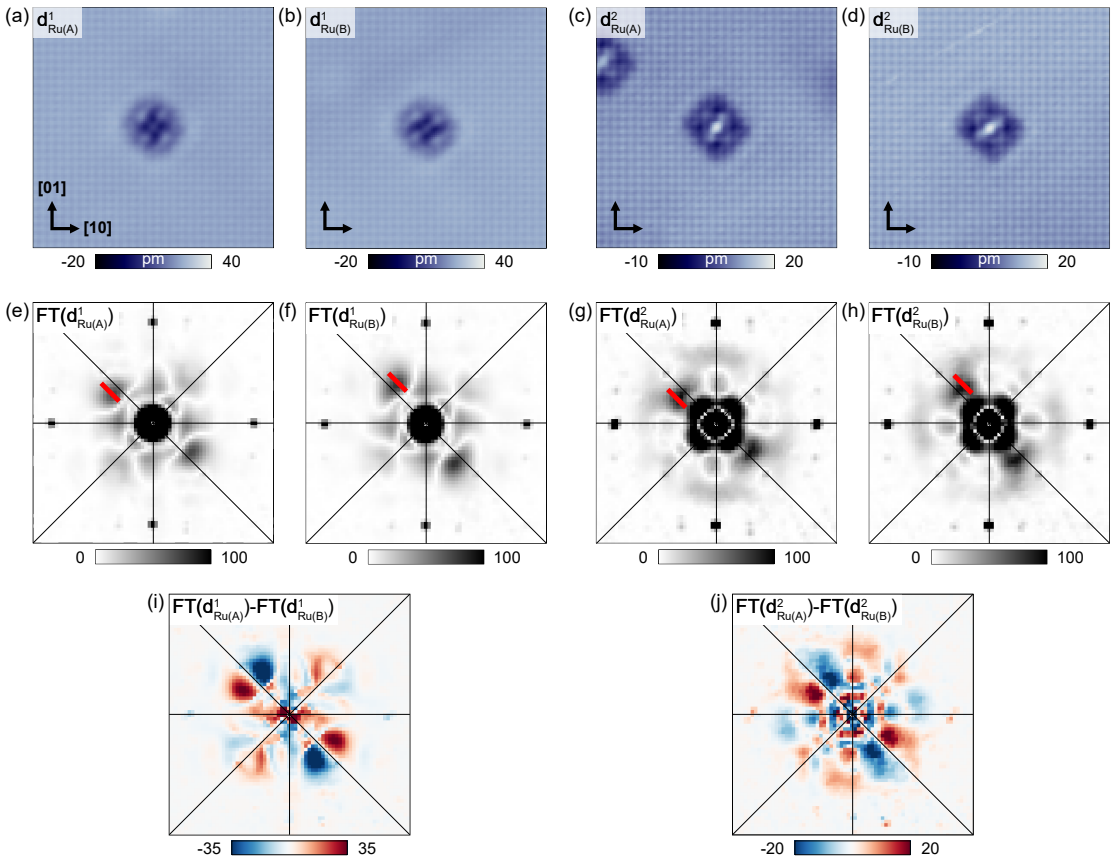

Figure 6.3: **Chiral defects at the Ru sites.** (a) and (b) topographies centered at defects of type d^1 with different orientations, corresponding to sites Ru(A) and Ru(B), respectively. (c) and (d) topographies centered at defects of type d^2 at Ru(A) and Ru(B) sites, respectively (V_{set}= 35 mV, I_{set}= 200 pA). The scanning distortion of the topographies was corrected via the lock-in algorithm (Appendix D). (e) and (f) show the absolute value of the Fourier transformations of (a) and (b). (g) and (h) show the absolute value of the Fourier transformations of (c) and (d).The intensity of the QPI patterns follows the chirality of each defect, evidenced by the red lines. (i-j) Difference between FT of topographies of defects of type d^1 and type d^2 with opposite chirality, respectively.

reflects the anisotropy of the scattering patterns observed in real space surrounding the defects in Figures 6.3(a-d). In addition, the axis of dominant QPI is 45° rotated relative to the axis observed at the surface of Sr_2RuO_4, Figure 5.3, where the axis of dominant QPI was [10], despite both systems being described by the same two-atom unit cell.

6.3 Spectroscopy

A typical tunneling spectrum $g(V)$ is shown in Figure 6.4(a), taken at $T = 80$ mK. It shows a partial gap of width 20 mV (outer arrows) that represents a drop in DOS of $\sim 37\%$ relative to the value at 95 mV. The decrease in DOS is similar to that observed in Sr_2RuO_4, however, the partial gap is four times wider. ARPES measurements [183, 185] do not show evidence for the opening of such a gap and previous theoretical studies of this material [186] do not show such a partial gap around the Fermi level.

Around E_F, two sharp peaks are observed (inner arrows), one at positive and the other at negative bias voltages. A high-resolution tunneling spectrum, Figure 6.4(b), reveals the structure of these peaks. Two peaks can be resolved at positive bias voltages, at 2.3 mV and 4.3 mV, and one peak at negative bias voltages at -3.5 mV (blue arrows).

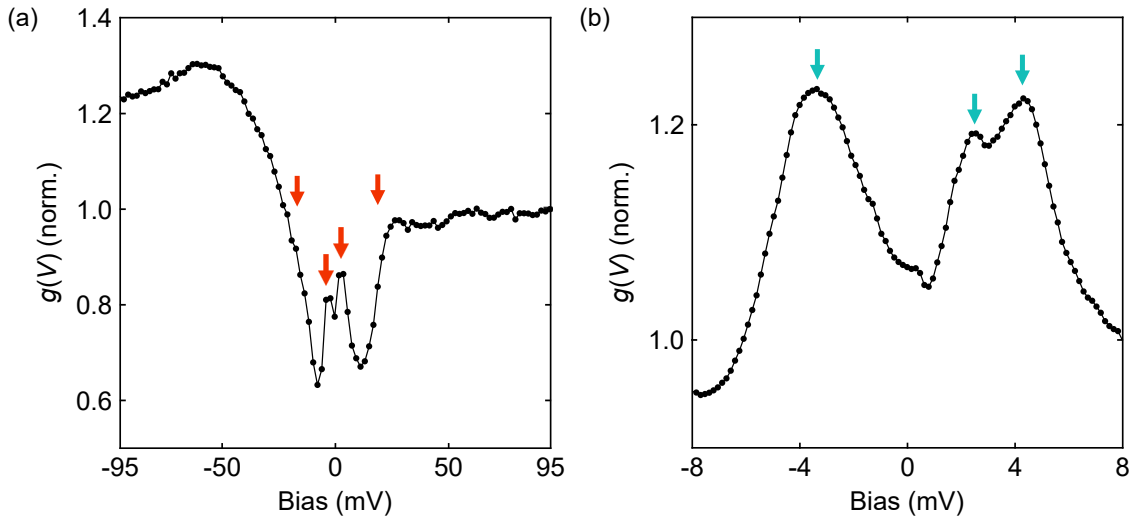

Figure 6.4: **Tunneling spectroscopy at the surface of $Sr_3Ru_2O_7$.** (a) Typical $g(V)$ spectrum measured at $T = 80$mK at the surface of $Sr_3Ru_2O_7$ ($V_{set} = 100$ mV, $I_{set} = 265$ pA, $V_L = 1.90$ mV). (b) High resolution $g(V)$ spectrum around E_F. This was obtained by taking the average spectrum over an area of $(1.48\text{ nm})^2$ on a 16×16 grid ($V_{set} = 8$ mV, $I_{set} = 500$ pA, $V_L = 160\ \mu$V, $T = 80$ mK).

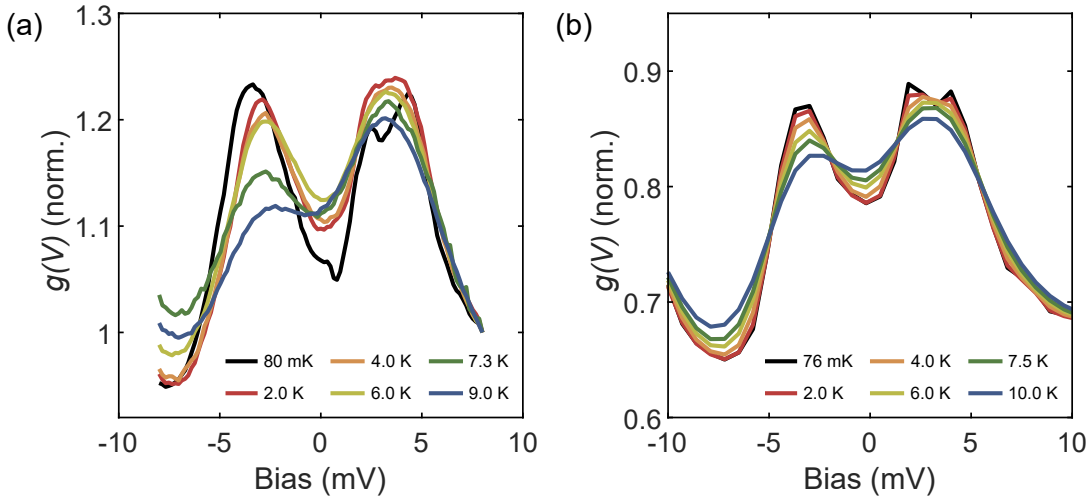

Figure 6.5: **Temperature dependence of the tunneling spectrum.** (a) Differential conductance spectra with increasing temperatures. The curves are the result of the average over an area of $(1.48\ \text{nm})^2$ on a 16×16 grid ($V_{\text{set}} = 8$ mV, $I_{\text{set}} = 500$ pA, $V_{\text{L}} = 160\ \mu$V). The spectra at 7.3 K and 9 K show the peak at negative energies with lower intensity than those at the other temperatures because of a tip change (atomically sharp tips show the peaks at positive and negative energies with similar intensity, less sharp tips show the peak at negative energies with lower intensity). (b) Simulation of thermal broadening at different temperatures, obtained by convoluting a point spectrum taken at 76 mK with the derivative of the Fermi function at each temperature using Eq. (5.1).

6.3.1 Temperature dependence

The evolution of the tunneling spectrum with temperature was studied in the range between 80 mK to 9 K. The measurements at each temperature are shown in Figure 6.5(a), where the peaks are observed at all temperatures, becoming broader with increasing temperature. To compare this broadening to what is expected from the broadening of the Fermi edge in the tip, the $g(V)$ spectrum at 76 mK was convoluted with the derivative of the Fermi function for temperatures up to 10 K, using Eq. (5.1). The result of the convolution is shown in Figure 6.5(b). The peaks become broad, with the peak at negative energies decreasing more in intensity. It confirms that the changes in the spectra shown in Figure 6.5(a) are consistent with the effects of thermal broadening. This suggests that the characteristic energy scales of the phenomena associated with these peaks are significantly larger than 9 K and that they are not due to many-body effects such as the Kondo effect.

6.4 Checkerboard order

The topographies of the surface of $Sr_3Ru_2O_7$ show a checkerboard intensity modulation centered on the Sr lattice, visually identical to the one observed at the surface of Sr_2RuO_4. In $Sr_3Ru_2O_7$, this modulation is also highly dependent on the setpoint bias. Figure 6.6(a) shows two topographies taken at two different bias voltages, but with the same tunneling resistance. The top image

is a topography taken at V_{set}= 50 mV, where the Sr square lattice is resolved. The checkerboard is not easily discernible in the real space image, yet, there is a faint peak at $(0.5, 0.5)$ (top inset). The bottom image shows a topography taken at V_{set}= −4 mV, where a strong checkerboard is clearly visible, reflected in a strong increase in the $(0.5, 0.5)$ peak intensity in the FT (lower inset).

The strength of the checkerboard as a function of energy can be followed by tracking the intensity of the $(0.5, 0.5)$ peak in the Fourier transform as a function of setpoint bias, as introduced in chapter 5. Figure 6.6(b) shows the $(0.5, 0.5)$ peak intensity as a function of bias for three different temperatures. At 80 mK, a sharp asymmetric peak is observed close to the Fermi level. A two-peak Lorentzian fit reveals a strong peak centered at −4.0 mV with a full width at half maximum of 17.9 mV, and a lower peak at 15.6 mV, with a width of 17.4 mV. Their intensity decreases with increasing temperature, consistent with thermal broadening, and it is still visible at 10 K.

To investigate this checkerboard modulation further, and to understand the similarities with the checkerboard found at the surface of Sr_2RuO_4, differential conductance maps were acquired to study the phase-referenced Fourier transform of the $(\pm 0.5, 0.5)$ peaks, using Eq. (5.3). Figure 6.7(a) shows the PR-FT in an energy range from −20 to 40 mV, taken from a map with 57 nm of lateral size. The phase at each energy was referenced at the phase of the energy layer with the strongest modulation, which in this case was at −2.6 mV. As a consequence, a sharp positive peak

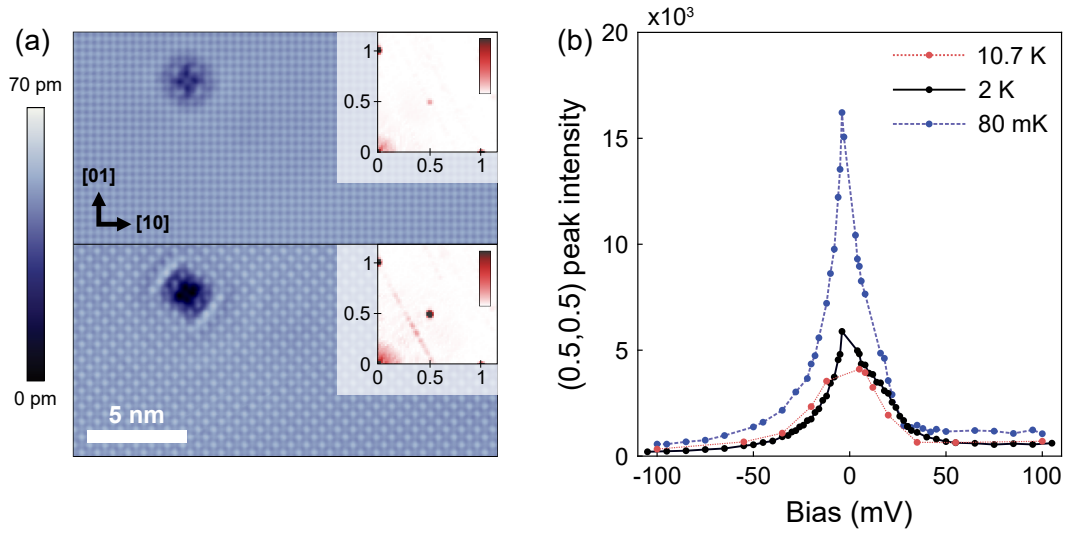

Figure 6.6: **Bias dependence of topographies.** (a) Topographies taken with V_{set}= 50 mV (top) and V_{set}= −4 mV (bottom), measured at 80 mK with the same junction resistance (I_{set}= 909 pA and I_{set}= 72.7 pA, respectively), in the same area. The insets show a quarter of the Fourier transformation at each energy. The scanning distortion was corrected by the Lock-in algorithm (Appendix D) and the images were aligned via a translation transformation estimated using the phase correlation between the two images, from the Registration Estimator of the image processing toolbox in Matlab. (b) Intensity of the $(0.5, 0.5)$ peak in the Fourier transformation as a function of setpoint bias, for measurements taken at constant resistance, $R = 55$ MΩ, and at three different temperatures.

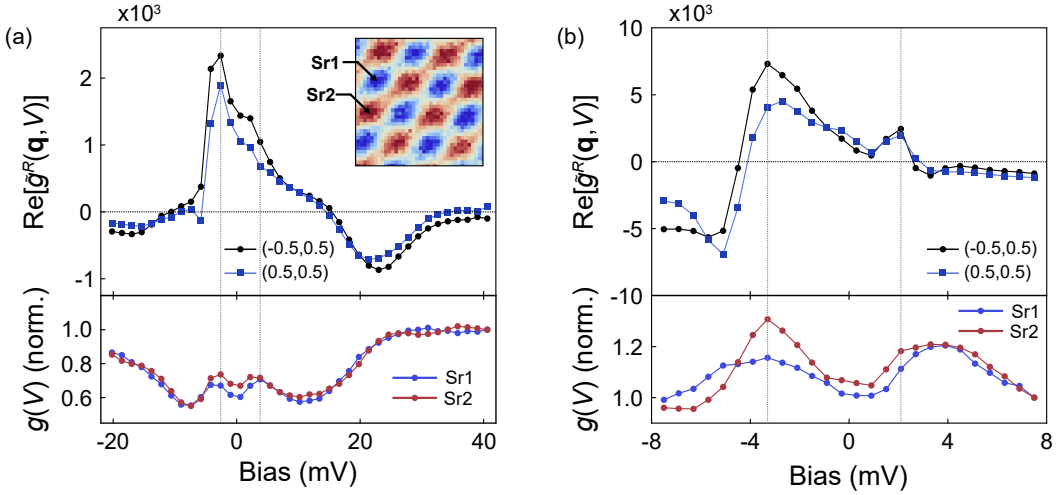

Figure 6.7: **Energy dependence of checkerboard modulation at two energy scales.** (a) Phase-referenced FT, Re $\left[\tilde{g}^{\mathrm{R}}(\mathbf{q},V)\right]$, as a function of energy at the $(0.5,0.5)$ and $(-0.5,0.5)$ peaks in the Fourier transform. The phase at each energy was referenced to the phase at -2.6 mV. The plot at the bottom shows the $g(V)$ spectra at each Sr site (V_{set}= 40 mV, I_{set}= 800 pA, T = 80 mK). The inset shows an atomically resolved $g(V)$ image at -2.6 mV (vused= 40 mV, I_{set}= 450 pA, T = 2 K). (b) PR-FT between ± 8 mV, with the phase at each energy referenced by the phase at -3.3 mV. The bottom plot shows the $g(V)$ spectra at the two inequivalent Sr sites (V_{set}= 8 mV, I_{set}= 700 pA, T = 80 mK).

is observed centered at this energy, and it corresponds to a peak in the $g(V)$ spectrum (see Figure 6.7(a) bottom plot), whose intensity modulates between adjacent Sr sites (Sr1 and Sr2 shown on the inset). A lower intensity peak is observed at positive energies close to E_{F}. The PR-FT intensity becomes negative for bias lower than -10 mV and bias higher than 15 mV. It shows negative peaks at -17 and 23 mV. This phase reversal is an indication of the setpoint effect (see chapter 3). The PR-FT of a higher energy resolution map at the $(0.5,0.5)$ peaks (Figure 6.7(b)) reveals two peaks with the same phase, corresponding to the modulation of the peak at -3.5 mV and the peak at 2.3 mV in the $g(V)$ spectrum between adjacent Sr atoms. Following the discussion in chapter 6 and the identification of a vHs as a peak appearing in the PR-FT, the presence of these two peaks in the PR-FT of $Sr_3Ru_2O_7$ indicates the presence of at least two vHs corresponding to the peaks in the $g(V)$ spectrum at -3.5 mV and 2.30 mV.

6.5 DFT calculations of a bilayer

In $Sr_3Ru_2O_7$, each bilayer, Figure 6.1(a), is well decoupled from its neighbors along the c-axis, demonstrated by highly anisotropic resistivity $\rho_c/\rho_{ab} \sim 300$ [110], and so, the electronic structure of the bulk can be considered quasi-2D. A DFT calculation on a bilayer using LCAO and LDA, neglecting spin-orbit coupling, produces the Fermi surface and band structure shown in Figure 6.8. The overall shape of the Fermi surface, Figure 6.8(a), is consistent with ARPES

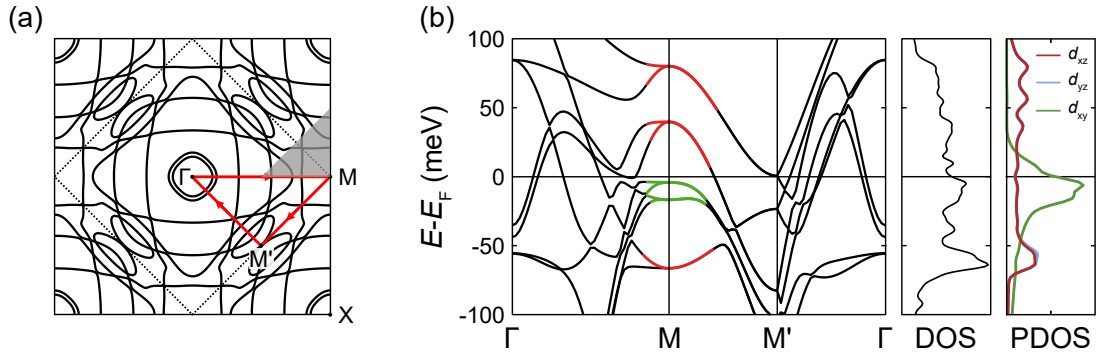

Figure 6.8: **DFT calculation of a free-standing bilayer of $Sr_3Ru_2O_7$.** (a) Fermi surface of a free-standing bilayer, for the supercell shown in Figure 6.1(a). The DFT calculations were performed using GPAW, with LCAO and within LDA. A quarter of the Fermi surface in the two-atom unit cell was calculated on a $41 \times 41 \times 1$ k-grid. (b) Corresponding band structure along the path shown in (a). The calculations were performed over 101 points along the path. The energy of the bands was renormalized by a factor of 4.2 so that the vHs at the M-point right below E_F is at -4 meV, as measured by ARPES [183]. The middle panel shows the total DOS, calculated with an energy broadening of 3.6 meV, where the x-axis goes from 8.6 to 15 eV^{-1}. The panel on the right shows the projected DOS onto the t_{2g} orbitals of the Ru atoms, calculated around the M-point over the shaded area in (a) and with an energy broadening of 4.7 meV. The x-axis goes from 0 to 4 eV^{-1}.

measurements and previous LDA calculations [183, 185]. The δ pocket appears split. while the α_1 and α_2 pockets centered at the Γ-point are well reproduced. The β pocket appears split and the γ_1 pocket has a slightly different shape, as previously reported [95, 183], while the γ_2 band appears at a shorter k_F. Inclusion of spin-orbit coupling would lead to hybridization between the d_{xz}/ d_{yz} and d_{xy} states, resulting in clover-leaf-shaped pockets on the γ_2 band.

The calculated band structure, Figure 6.8(b), taken along the path indicated in red in Figure 6.8(a), captures the energy dispersions around the M-point well, reproducing a vHs a few meV below E_F (highlighted in green). In order for the vHs to appear at the experimentally measured value of -4 meV, all bands were normalized by a factor of 4.2. After renormalization, the Fermi velocities around the M-point are consistent with ARPES [185], but as we move towards the Γ-point the agreement decreases, with the bandwidth of the δ electron-like band highly overestimated. This is consistent with previous reports of band-dependent renormalization [187]. In addition to the above mentioned vHs, the M-point shows at least three more vHs, two at higher energy and one at more negative energies (highlighted in red). The total DOS, middle panel of Figure 6.8(b), shows a complex structure with multiple peaks due to the variety of vHs present in the band structure.

To get an idea of the orbital character of the different vHs at the M-point, the orbitally-projected DOS (PDOS) for the t_{2g} states of the Ru atoms was calculated around the M-point, using a k-point grid with high density in the shaded area in Figure 6.8(a). The result is shown on the right panel of Figure 6.8(b). The PDOS of the d_{xy} states shows two intense peaks correspond-

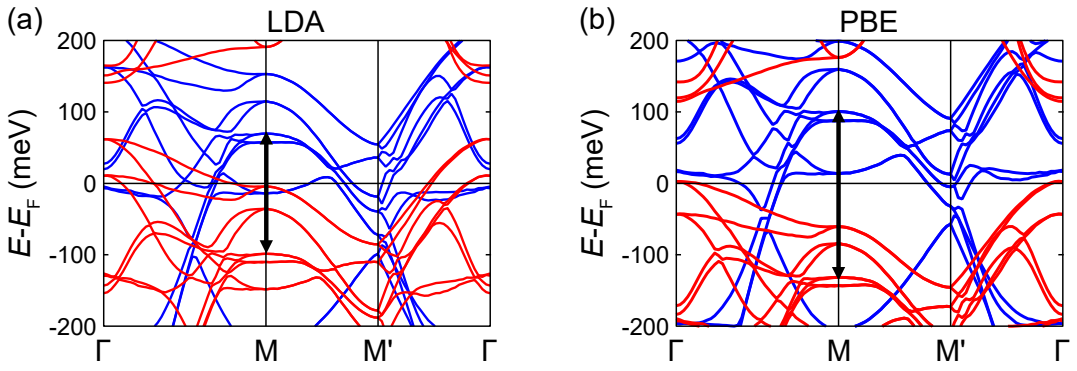

Figure 6.9: **Spin-polarized DFT calculations on a bilayer.** (a) Spin-polarized band structure of a bilayer using plane-waves as basis functions and LDA. The obtained total magnetic moment is $+6.25\ \mu_B$/atom and the magnetic moment of the Ru atoms converged to $1.06\mu_B$/Ru. (b) Spin-polarized band structure of a bilayer calculated using plane-waves as basis functions and PBE. The obtained total magnetic moment is $+7.99\ \mu_B$/atom and the magnetic moment of the Ru atoms converged to $1.39\ \mu_B$/Ru. Red and blue indicate the spin-up and spin down bands, respectively. The black arrows indicate the exchange splitting for each calculation. The calculations were performed over a $4 \times 4 \times 1$ k-grid, including a vacuum layer of 20Å . The magnetic moments of the Ru atoms were initialized as $0.1\ \mu_B$/Ru aligned with the c-axis. The energy of the bands was renormalized by a factor of 4.2. Both band structures were calculated over 101 k-points along the path shown in Figure 6.8(a).

ing to the vHss highlighted in green in Figure 6.8(b). On the other hand, the PDOS of the d_{xz}/ d_{yz} states shows that these states are responsible for the higher energy vHs, highlighted in red in Figure 6.8(b).

$Sr_3Ru_2O_7$ is known to be close to a ferromagnetic instability [110]. To compare the ground state energies of the paramagnetic and ferromagnetic cases and to get an estimate of the exchange splitting on a bilayer, DFT calculations were performed using plane-waves as basis functions and two different exchange-correlation functionals, LDA and PBE. Both calculations were performed on a $4 \times 4 \times 1$ k-grid, including a vacuum layer of 20 Å, with the magnetic moments of the Ru atoms initialized at $0.10\ \mu_B$/Ru. The total magnetic moment obtained from LDA was $+6.25\ \mu_B$/unit cell with $+1.06\ \mu_B$/Ru atom, and from PBE was $+7.99\ \mu_B$/unit cell with $+1.39\ \mu_B$/Ru atom. Both calculations show a small magnetic moment appearing on the oxygen atoms on the RuO_2 plane, as well as on the middle SrO layer, of magnitudes $+0.11\ \mu_B$/atom and $+0.10\ \mu_B$/atom for LDA, and $+0.13\ \mu_B$/atom and $+0.17\ \mu_B$/atom for PBE, respectively. The total energy of these calculations is lower than the corresponding non-magnetic calculation, by 0.24 eV for LDA and 0.55 eV for PBE. These energy differences are significant and suggest that a ferromagnetic ground state is more stable than a non-magnetic one for a free-standing bilayer, in agreement with previous reports for the bulk of $Sr_3Ru_2O_7$ [186].

Figure 6.9 shows the band structures obtained from the LDA (a) and PBE (b) calculations, after renormalization by a factor of 4.2. The exchange splitting obtained from LDA is 0.17 eV. It is such that the top vHs of d_{xz}/ d_{yz} character at the M-point from the majority spin species is pushed down

in energy close to but below E_F, while the bottom d_{xz}/ d_{yz} vHs from the minority spin species is pushed up closer to the Fermi level. In addition, the Γ-point shows a band top slightly above the Fermi level, from the majority spin species, and a heavy band from the minority spin species just below E_F. In contrast, PBE calculations give a larger exchange splitting of 0.24 eV, pushing the vHs at the M-point apart in energy, and putting the top of the band at the Γ-point almost at E_F. These calculations show that, by including ferromagnetism, it is possible to push different vHs to a few meV around the Fermi level, producing peaks in the DOS just above and below E_F. As a consequence, the exchange splitting energy could be introduced in a phenomenological model as a fitting parameter to get a better agreement with the measured tunneling spectrum.

6.6 Quasiparticle interference

Differential conductance maps reveal the presence of strong QPI. Figure 6.10 (a-j) shows a sequence of real-space $g(V)$ layers of an area of $(90.8\text{ nm})^2$ at bias voltages between 6.3 and -4.5 mV, where both long- and short-range modulations are observed surrounding the defects. The inset images show a close up of a defect with clear C_2-symmetric patterns aligned with the $[-11]$ direction (dotted line). The FT of each image is shown in Figure 6.10 **A**-**J**, after anti-aliasing (see Appendix E), drift correction and alignement of the atomic peaks at $(1,0)$ and $(0,1)$ with the x and y axis. To avoid confusion between the aliased and anti-aliased atomic peaks, the FT images are shown in the q-range ± 0.7 (in units of $2\pi/a$). Overall, the FT shows: (1) a prominent four-lobe shaped hole-like scattering vector (orange arrow) with suppressed intensity along the four $\langle 11\rangle$ directions; (2) an electron-like **q**-vector (red arrow); (3) replicas of these two **q**-vectors around the $(0.5,0.5)$ peaks; (4) flat patterns that cross the $q_x = \pm 0.5$ and the $q_y = \pm 0.5$ lines (blue arrows in Figure 6.10**D**) and (5) well-defined **q**-vectors along the $[-11]$ direction that are absent along the $[11]$ direction (light and dark blue and green arrows). While there are QPI features clearly breaking C_4-symmetry, the FT shows that not all scattering vectors break this symmetry.

To study the energy dispersion of the different **q**-vectors, energy-momentum line cuts were taken along the six directions shown in Figure 6.11(a). Figure 6.11(b) shows a line cut along q_x. Three dispersions are observed, two above and one below E_F, with the dispersions reaching $q = 0$ at the energies where peaks are observed in the tunneling spectrum (Figure 6.4(b)), indicated by the colored circles. The top-most hole-like dispersion, $\mathbf{q}_1$, comes from the four-lobe shaped pattern seen in Figure 6.10. It is followed by a second hole-like dispersion with a similar q-vector, $\mathbf{q}_2$. An electron-like dispersion appears below the Fermi level, $\mathbf{q}_3$, which has the same Fermi q_F-vector

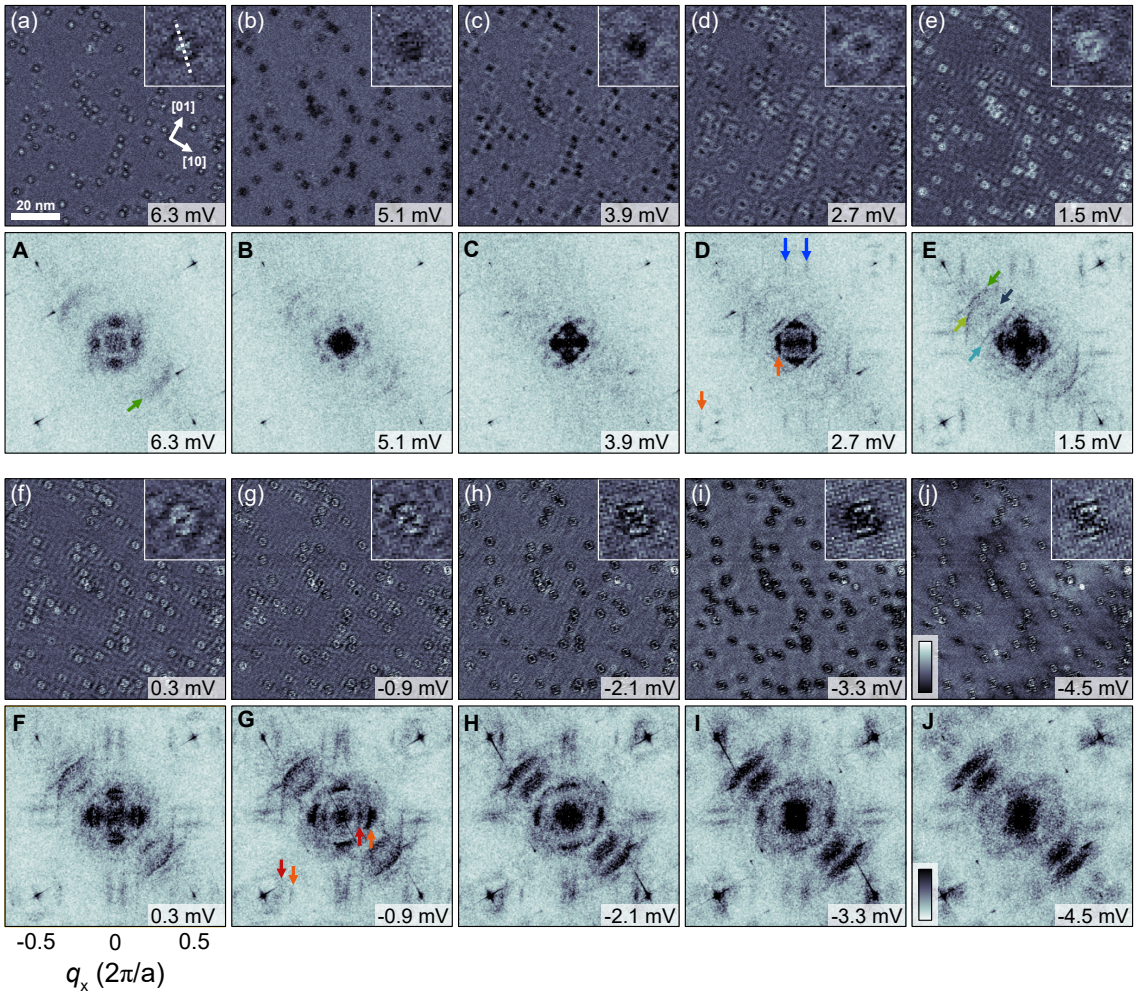

Figure 6.10: **Quasiparticle interference energy layers.** (a)-(j) Real-space $g(V)$ layers at energies within 7 mV of E_F. The insets show the close up of a defect, where clear C_2-symmetric modulations are observed along the $[-11]$ direction (indicated by the dotted white line in the inset of (a)). **A-J** Fourier transforms of (a)-(j), respectively, after anti-aliasing and drift correction (V_{set}= 8 mV, I_{set}= 700 pA, V_L= 0.6 mV, T = 80 mK). The colored arrows indicate the position of different scattering patterns. The edges of the images go from -0.7 to 0.7 in units of $2\pi/a$, so that the reconstruction peaks and the QPI patterns surrounding them are visible, but the atomic peaks (and the aliased/anti-aliased replicas) are not shown.

as $\mathbf{q}_2$. The cut along the perpendicular direction, Figure 6.11(c), shows $\mathbf{q}_2$ and $\mathbf{q}_3$ with opposite dispersions than before: $\mathbf{q}_2$ appears electron-like, and $\mathbf{q}_3$ hole-like. In addition, another dispersion is visible, $\mathbf{q}_4$ with electron-like behavior, which appears faint along q_y.

The cut across $q_y = 0.5$, Figure 6.11(d), shows both $\mathbf{q}_1$ and $\mathbf{q}_3$ dispersions replicated around the $(0.5, 0.5)$ peaks (orange and red arrows). The dispersion associated with $\mathbf{q}_2$ is not observed along this direction. The blue arrows indicate the dispersion of the flat patterns seen in Figure 6.10, which show an hourglass shape, joining together at -2.1 mV. On the other hand, the cut across $q_x = 0.5$, Figure 6.11(e), in addition to the $\mathbf{q}_1$ dispersion, shows a short electron-like dispersion that ends at the same energy as the edge of $\mathbf{q}_2$ (yellow arrows) and a hole-like dispersion at a

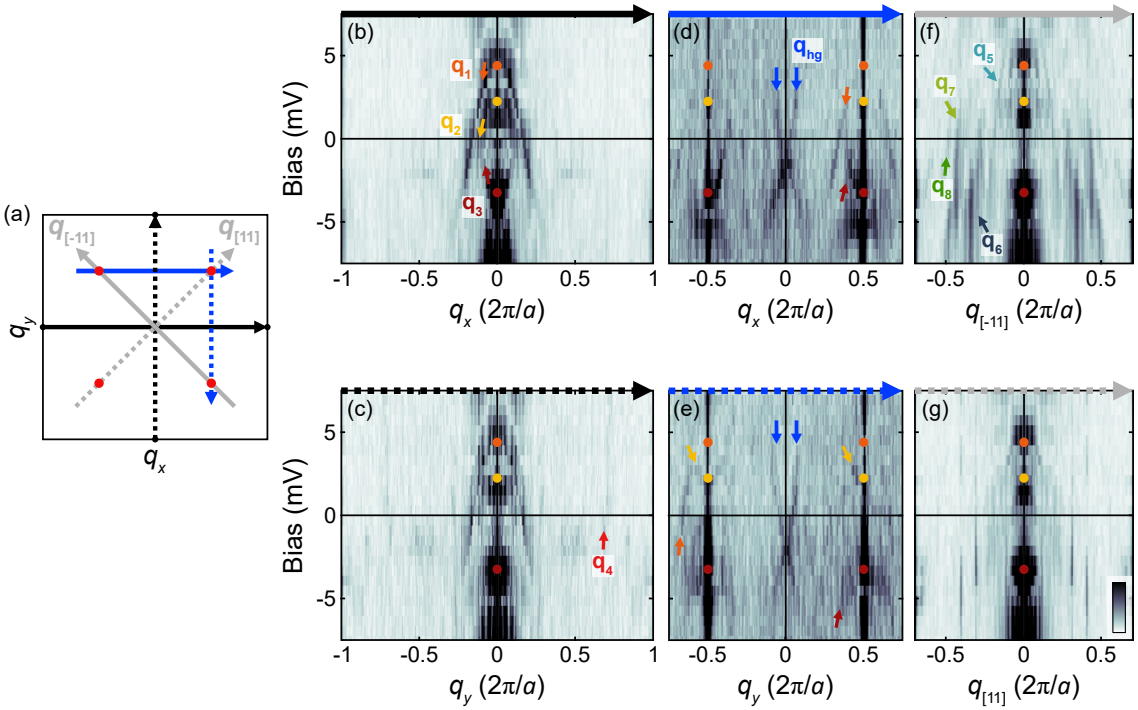

Figure 6.11: **QPI energy dispersions**. (a) Illustration of the directions of the energy cuts shown in panels (b-g). Red circles indicate the positions of the reconstruction peaks. The arrows on top of panels (b-g) make the correspondence with the directions shown in (a). (b) Energy cut across $\mathbf{q} = (0,0)$ along q_x. The circles indicate the peak positions from fitting Lorentzian functions to the high resolution spectrum (Figure 6.4(b)). Three main $\mathbf{q}$-vectors are identified, $\mathbf{q}_1$ (orange), $\mathbf{q}_2$ (yellow) and $\mathbf{q}_3$ (red). (c) Energy cut across $\mathbf{q} = (0,0)$ along q_y. An additional $\mathbf{q}$-vector is identified, $\mathbf{q}_4$. (d) Energy cut at $q_y = (0.5, 0.5)$. Replicas from $\mathbf{q}_1$ and $\mathbf{q}_3$ are observed around $(\pm 0.5, 0.5)$. An hourglass shaped feature, $\mathbf{q}_{hg}$, is observed around $q_x = 0$, indicated by the blue arrows. (e) Energy cut through $q_x = 0.5$. (f) Energy cut along the $[-11]$ direction. Four $\mathbf{q}$-vectors are identified, $\mathbf{q}_5$, $\mathbf{q}_6$, $\mathbf{q}_7$ and $\mathbf{q}_8$. (g) Energy cut along $[11]$. None of the $\mathbf{q}$-vectors $\mathbf{q}_5$ to $\mathbf{q}_8$ are observed. The color intensity in (d) and (e) are 3.2 times lower than the one of panels (b), (c), (f) and (g).

negative bias (red arrow) that terminates at the same energy as $\mathbf{q}_3$. The hourglass shaped patterns follow the same trend as along the perpendicular direction.

The energy cuts along the $[-11]$ and $[11]$ directions are shown in Figure 6.11(f) and (g), respectively. While along $[-11]$ there are four clear hole-like dispersions, $\mathbf{q}_5$ to $\mathbf{q}_8$, these are not visible along $[11]$, clearly showing the high anisotropy of the electronic structure along these directions.

To prove that the dispersions seen around $(0.5, 0.5)$ are replicas of the dispersions seen around $\mathbf{q} = (0,0)$, the energy line profiles were fitted with Lorentzian functions. On the left of Figure 6.12(a), the peak positions obtained from fitting the line profiles parallel to q_X are shown, taken across both $q_y = 0$ (circles) and $q_y = 0.5$ (triangles). The dispersions around $\mathbf{q} = (0.5, 0.5)$ fall on top of the dispersions of $\mathbf{q}_1$ and $\mathbf{q}_3$, demonstrating that they are replicas of these scattering vectors.

In Figure 6.11(a-d), both $\mathbf{q}_2$ and $\mathbf{q}_3$ are observed to change behavior between the q_x and q_y

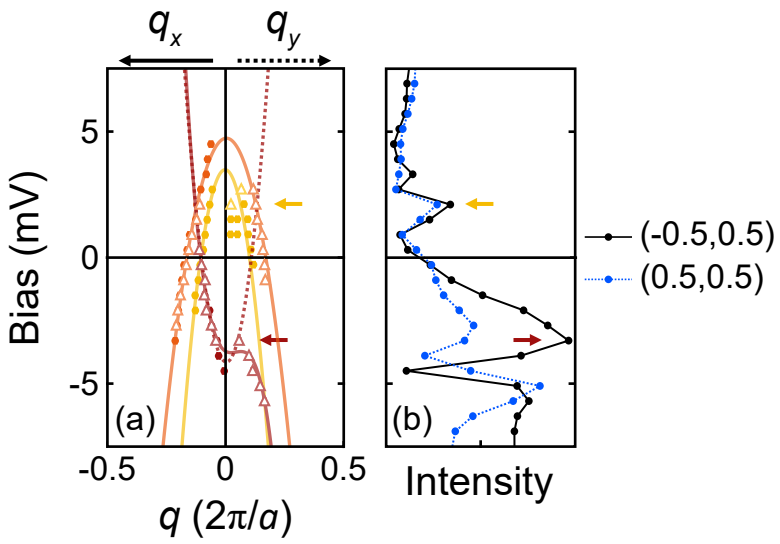

Figure 6.12: **Identification of vHs around the Fermi level.** (a) Peak positions from Lorentzian fits to the line profiles of the energy cuts shown in Figure 6.11. Full circles correspond to fitting features around $\mathbf{q} = (0,0)$ and empty triangles to features around $\mathbf{q} = (\pm 0.5, 0.5)$. The left corresponds to fitting the energy cuts along q_x and the right to cuts along q_y. The size of the symbols is larger than the map resolution. (b) Intensity at $(-0.5, 0.5)$ and $(0.5, 0.5)$ in the Fourier transform. The arrows indicate the energies of the vHs observed in the energy dispersions taken from the fits.

directions. On the right of Figure 6.12(a), the peak positions from Lorentzian fits to the line profiles along $q_x = 0.5$ are shown. While $\mathbf{q}_1$ retains a hole-like dispersion, $\mathbf{q}_2$ shows a short electron-like trend close to $q = 0$, which is easier to fit around $\mathbf{q} = (0.5, 0.5)$ (triangles) than along $\mathbf{q} = (0,0)$ (full circles) where it also shows a hole-like behavior. However, $\mathbf{q}_3$ shows a clear change from hole-like along q_x to electron-like along q_y. This change in behavior is characteristic of a two-fold saddle point in the band structure, resulting in a vHs and a peak in the density of states. Knowing that in this system vHss are expected at the M-point of the BZ and that in chapter 5 we observed signatures of vHss in the intensity of both atomic and reconstruction peaks (see Figures 5.10 and 5.22), the energy at which these vHss occur should appear as peaks in the intensity of the $(0.5, 0.5)$ peaks. Figure 6.12(b) shows the absolute value of the intensity of the FT at the $(-0.5, 0.5)$ and $(0.5, 0.5)$ peaks. Two peaks are observed (arrows), corresponding to the energies at which $\mathbf{q}_2$ and $\mathbf{q}_3$ are seen to collapse onto $\mathbf{q} = (0,0)$ and to the peaks seen in the tunneling spectra. This identifies the presence of two vHs due to saddle points at the surface of $Sr_3Ru_2O_7$, one at 2.3 mV and another below the Fermi level at -3.5 mV. The QPI shows that we have two vHss which are two-fold symmetric: the one corresponding to $\mathbf{q}_2$ is hole-like along q_x and electron-like along q_y, and the one corresponding to $\mathbf{q}_3$ is electron-like along q_x and hole-like along q_y.

Assuming intraband scattering, the Fermi velocity, v_F, the effective mass of the quasiparticles, m^*, and the band edge, E_b, can be estimated by fitting a quadratic function to the energy dispersions

obtained from the Lorentzian fits. Table 6.1 shows the values obtained from such fits, for the scattering vectors identified along the q_x/q_y directions, $\mathbf{q}_1$ to $\mathbf{q}_4$ and $\mathbf{q}_{\text{hg}}$, and along the $[-11]$ direction, $\mathbf{q}_5$ to $\mathbf{q}_8$. It shows that there are two sets of heavy bands: one set with $m^* < 10\,m_e$ ($\mathbf{q}_2$, $\mathbf{q}_3$ and $\mathbf{q}_5$) and another with $m^* > 14\,m_e$ ($\mathbf{q}_1$,$\mathbf{q}_4$, $\mathbf{q}_{\text{hg}}$ and $\mathbf{q}_6$ to $\mathbf{q}_8$). However, all dispersions have low Fermi velocity, $v_F < 0.15$ eVÅ, besides $\mathbf{q}_4$ that has $\hbar v_F \sim 0.2$ eVÅ.

	k_F (Å^{-1})	$\hbar v_F$ (eVÅ)	m^* (m_e)	E_b (meV)
Along q_x/q_y				
$\mathbf{q}_1$	0.13 ± 0.01	-0.07 ± 0.01	-14.4 ± 0.6	4.8 ± 0.3
$\mathbf{q}_2$	0.08 ± 0.01	-0.08 ± 0.01	-7.6 ± 0.6	3.5 ± 0.4
$\mathbf{q}_3$	0.09 ± 0.01	0.10 ± 0.02	6.6 ± 1.3 (-24.8 ± 2.2)	-4.1 ± 1.0
$\mathbf{q}_4$	0.56 ± 0.09	0.21 ± 0.06	20.6 ± 4.8	-56.9 ± 19.0
$\mathbf{q}_{\text{hg}}$ *	0.19 ± 0.13	-0.08 ± 0.02	-17.4 ± 4.4	-
Along $[-11]$				
$\mathbf{q}_5$	0.15 ± 0.01	-0.12 ± 0.01	-9.5 ± 0.7	9.3 ± 1.0
$\mathbf{q}_6$	0.22 ± 0.02	-0.07 ± 0.01	-22.9 ± 2.7	8.3 ± 1.5
$\mathbf{q}_7$	0.31 ± 0.04	-0.07 ± 0.02	-33.3 ± 5.7	11.2 ± 2.9
$\mathbf{q}_8$	0.39 ± 0.02	-0.10 ± 0.01	-31.2 ± 1.9	18.4 ± 1.5

Table 6.1: Fermi wavevector, Fermi velocity and effective masses extracted from the QPI energy dispersions assuming all features originate from intra-band scattering. The values were obtained from a parabolic fit to the data around the Fermi level. The value in the parenthesis on the effective mass of $\mathbf{q}_3$ corresponds to a parabolic fit to the hole-like dispersion along the q_y direction. * Values extracted from a linear fit to the points.

6.7 Magnetic-field dependence

In the above sections, I established the presence of two C_2-symmetric vHs within ~ 4 meV of the Fermi level, one above and one below. Since $Sr_3Ru_2O_7$ has a high Wilson Ratio, $R_W > 10$, the application of a magnetic field is expected to have a large influence on the electronic structure by shifting/splitting bands. Moreover, in $Sr_3Ru_2O_7$, many of the microscopic theories [205–208] developed to describe the metamagnetic phase transitions propose that the mechanism involves a series of vHss crossing the Fermi level with magnetic field, but there is no consensus about which vHss do this. Spectroscopic measurements with micro-volt resolution and in high magnetic fields provide an opportunity to identify the correct microscopic theory or at least provide important benchmark results against which to test them. In this section, the measurements under magnetic

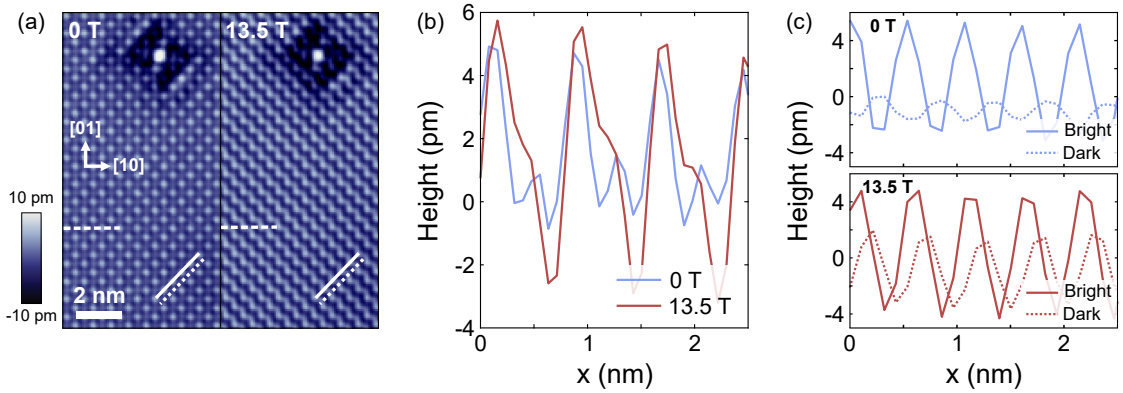

Figure 6.13: **Field-induced stripe pattern.** (a) Topographies taken at 0 T (left) and 13.5 T (right) on the same area ($V_{\text{set}} = -5$mV, $I_{\text{set}} = 91$pA, $T = 80$ mK). The piezo drift was corrected using the Lock-in algorithm (Appendix D) and the images were aligned, see section 3.1.5. (b) Line profile along the $[10]$ direction on the atom row indicated by the dashed white lines in (a) at both fields. (c) Line profiles along the $[11]$ direction on top of a row of bright (solid) and dark (dotted) Sr atoms at 0 T (top) and at 13.5 T (bottom).

field will be presented.

6.7.1 Magnetic field-induced stripes

One of the most unexpected results of this study is a magnetic-field induced charge order in the surface layer of $Sr_3Ru_2O_7$. On the application of a magnetic field aligned with the crystallographic c-axis of the sample, the topographies show a field-induced stripe order. Figure 6.13(a) shows the comparison between topographies of the same area taken at 0 T and 13.5 T, with a bias of -5 mV. At 0 T, only the checkboard charge order is visible, whereas at 13.5 T, a stripe order aligned with the $[11]$ direction is observed. The line profile along the $[10]$ direction, Figure 6.13(b), shows a shift of the positions of the dark Sr stoms towards the bright atoms by ~ 0.08 nm. This is clearly reflected by comparing the line profiles taken along $[11]$ on top of a row of bright and a row of dark Sr atoms, Figure 6.13(c) at each field. While at 0 T the rows of dark Sr atoms have a phase shift of π in relation to the row of bright atoms, as expected for the square lattice, at 13.5 T the phase shift between the rows is smaller, close to $\pi/2$.

The appearance of the stripe order with magnetic field is reflected in the intensity of the $(-0.5, 0.5)$ and $(0.5, 0.5)$ peaks, which become highly inequivalent. Figure 6.14(a) shows the Fourier transform of a topography taken in a magnetic field of 11.8 T, with $V_{\text{set}} = -5$ mV. The intensity of the $(0.5, 0.5)$ peak is enhanced, whereas the $(-0.5, 0.5)$ peak seems to be suppressed. The intensities of these two peaks have strong bias dependence as in the case of the checkerboard at 0 T (see Figure 6.6(b)). At 5.5 T, Figure 6.14(b), the intensity at both $(-0.5, 0.5)$ and $(0.5, 0.5)$ show a peak at -5 mV, with the intensity of the $(0.5, 0.5)$ peak strongly enhanced. With increasing

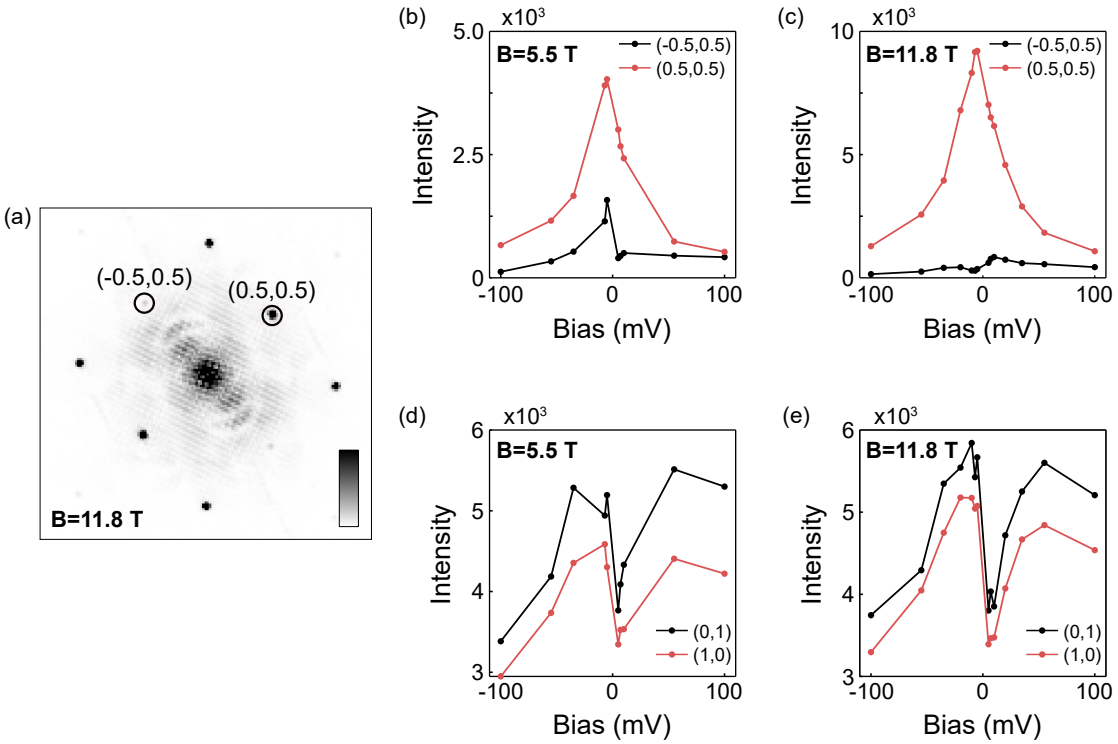

Figure 6.14: **Bias dependence of $(\pm 0.5, 0.5)$ peaks at increasing magnetic fields.**(a) Fourier transformation of a topography taken with $V_{\text{set}} = -5$ mV under a magnetic field of 11.8 T. The positions of the $(-0.5, 0.5)$ and $(0.5, 0.5)$ peaks are indicated by circles. (b) and (c) show the bias dependence of the intensity of the $(-0.5, 0.5)$ and $(0.5, 0.5)$ peaks at 5.5 T and 11.8 T. (d) and (e) show the bias dependence of the atomic peaks at 5.5 T and 11.8 T.

bias voltage, the difference in the intensity of the two peaks decreases becoming almost the same at 100 mV, such that the Sr square lattice is recovered and no stripes are observed. With increasing magnetic field, the inequivalence of the intensity between $(-0.5, 0.5)$ and $(0.5, 0.5)$ increases. Figure 6.14(c) shows the bias dependence at 11.8 T, where the intensity of the $(0.5, 0.5)$ peak doubles in relation to its value at 5.5 T. The intensity of the $(-0.5, 0.5)$ peak does not show a peak at -5 mV and it is suppressed relative to its value at 5.5 T. At 100 mV, the inequivalence between the two peaks is still present, and the stripes are observed in topographies up to higher bias voltages than at lower fields. The bias dependence of the atomic peaks, Figure 6.14(d) and (e), show a slight anisotropy of the intensity between the two spatial directions, however, the intensities at the two different fields show the same trend, following the shape of the spectrum.

Having identified the setpoint bias at which the stripes appear strongest as -5 mV, the intensities of the $(-0.5, 0.5)$ and $(0.5, 0.5)$ peaks can be followed as a function of magnetic field from 0 T to 13.5 T, from topographies taken over the same area and under the same conditions, in particular using the same tip, Figure 6.15(a) blue markers. The two peaks appear with approximately the same intensity up to fields of 3 T, after which their intensity splits. The intensity at $(0.5, 0.5)$

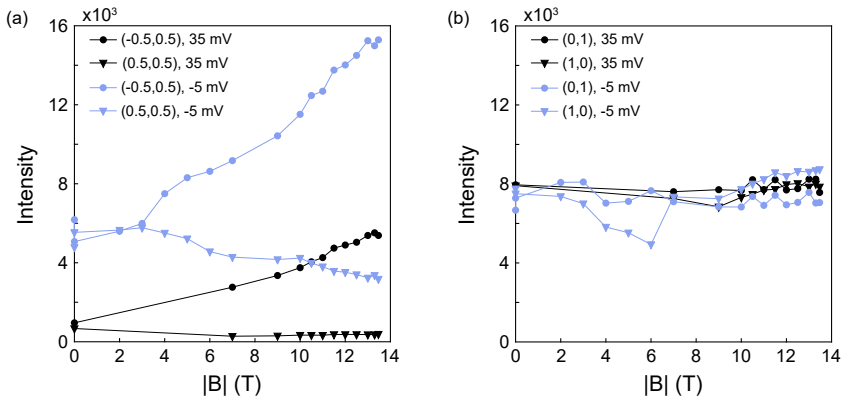

Figure 6.15: **Intensity of FT peaks as a function of magnetic field at two bias voltages.** (a) Intensity of the reconstruction peaks from the FT of topographies at $V_{\text{set}}= 35$ mV and $V_{\text{set}}= -5$ mV as a function of magnetic field. (b) Intensity of the atomic peaks from the same FT of topographies with increasing magnetic field, at $V_{\text{set}}= 35$ mV and $V_{\text{set}}= -5$ mV.

keeps increasing with increasing field, whereas the intensity of the $(-0.5, 0.5)$ peak is seen to be slightly suppressed. For comparison, the same experiment was performed using a setpoint bias of 35 mV, black markers, where the intensity of the $(-0.5, 0.5)$ and $(0.5, 0.5)$ peaks also splits, but as expected from Figure 6.14, their overall intensities are much lower than the ones observed at -5 mV. To confirm that it is not a tip effect, the intensity of the atomic peaks as a function of magnetic field is plotted in Figure 6.15(b). For both bias voltages, the intensity of these peaks remains approximately constant as a function of field, showing that the stripes are not an artifact due to the tip shape. The fact that the $(-0.5, 0.5)$ and $(0.5, 0.5)$ peaks intensities have a strong bias dependence under field, with the stripes disappearing at high bias voltages recovering the undistorted Sr square lattice goes against a structural distortion under magnetic field and in favour of an electronic phenonemon.

6.7.2 Spectroscopy as a function of magnetic field

To follow the changes in the LDOS under magnetic field at the surface of $Sr_3Ru_2O_7$, across the bulk quantum critical end point, we have measured the tunneling spectra up to 13.5 T at a temperature of 80 mK. Figure 6.16(a) shows a color plot of a sequence of $g(V)$ spectra taken over the energy range of ± 8 mV with increasing magnetic field, measured with an energy resolution of 160 μV. With increasing magnetic field, spectral weight is transferred from the peak at 4.3 mV towards low energies, reaching the peak at 2.2 mV at 8 T. Some spectral weight is left behind at 4.3 mV, whose intensity decreases with increasing field. Above 8 T, spectral weight continues to be transferred to lower energies, crossing the Fermi level at $\sim$ 10.5 T and reaching -1.2 mV above 13 T. As it crosses E_{F}, the states at E_{F} keep filling in for higher fields. The peak at 2.2 mV

remains at the same energy position, continuously losing intensity at higher fields. In addition, a small amount of spectral weight is also transferred from the peak at -3.5 mV towards -1.2 mV. The peak at -3.5 mV shifts slightly to higher energies and its intensity is enhanced. These observations are in agreement with the report by Iwaya *et al.* [212].

Looking at the individual $g(V)$ spectra at different fields, Figure 6.16(b), it is possible to follow this trend. Comparing the $g(V)$ spectrum at 0 and 3 T, it appears that the peaks at -3.5 and 4.3 mV are split at 3 T. While the split peaks seem to keep moving towards the Fermi level finally converging at -1.2 mV above 13 T, they leave behind features at 4.3 mV and -3.5 mV. Figure 6.16(b), shows how the intensity of the peak at 4.3 mV decreases with field, changing from a peak-shaped feature to a shoulder, whereas, the peak at -3.5 shifts by ~ 0.3 mV at 13.5 T and its intensity keeps increasing with increasing field. The intensity of the peak at 2.2 mV reaches a maximum at 8 T, decreasing for higher fields.

Although some changes in the spectral weight seem to be connected to 8 T, where the quantum critical end point of bulk $Sr_3Ru_2O_7$ is expected to occur, namely a maximum in the intensity of the peak at 2.2 mV, there is no obvious change at the Fermi level across this particular magnitude of the magnetic field that can be attributed to the metamagnetic phase transitions or the expected quantum critical end point. To investigate if there was a characteristic change to the tunneling spectrum across the magnetic field range of the quantum critical end point of bulk $Sr_3Ru_2O_7$ that could have been missed in the previous data set, we measured the tunneling spectra between 7.5 T and 8.1 T in steps of 0.1 T, Figure 6.17. Besides a small decrease in spectral weight at -2.5 mV,

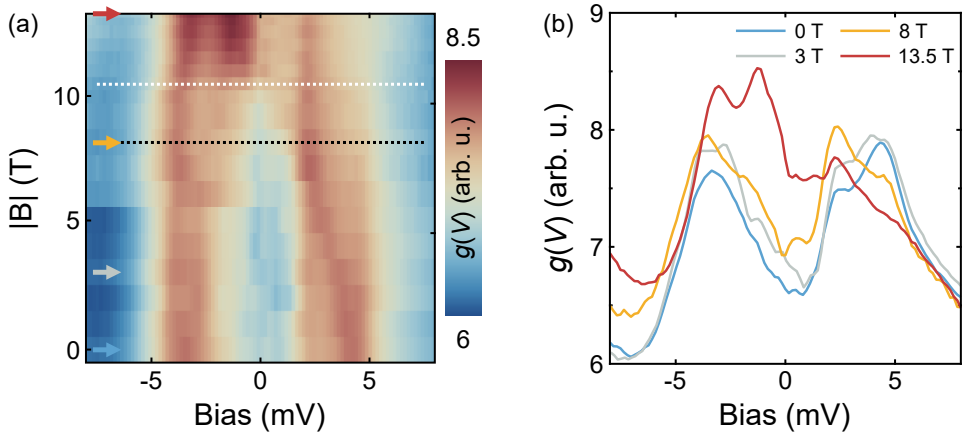

Figure 6.16: **Magnetic field dependence of differential conductance.** (a) Evolution of the $g(V)$ spectrum as a function of magnetic field. The dotted black line indicates 8 T, the field of the quantum critical end point in the bulk, and the dotted white line indicates 10.5 T, the field at which we observe a peak crossing the Fermi level. Each row corresponds to the average spectrum of a 16×16 grid over a $(1.48\text{nm})^2$ area (V_{set}= 8 mV, I_{set}= 500 pm, V_{L}= 160 μV, T = 80 mK). (b) $g(V)$ spectrum at the fields indicated by the colored arrows in (a) at 0 T, 3 T, 8 T and 13.5 T.

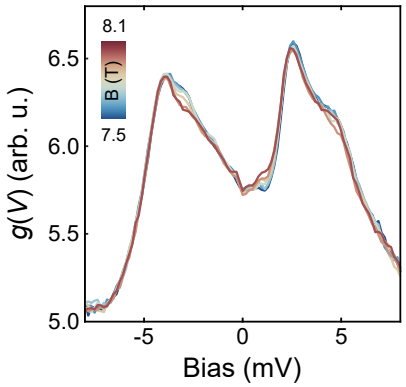

Figure 6.17: **Tunneling spectra across the quantum critical point of bulk $Sr_3Ru_2O_7$.** Tunneling spectra between 7.5 T and 8.1 T in steps of 0.1 T, across the magnetic field range where the quantum critical point and metamagnetic phase transitions of bulk $Sr_3Ru_2O_7$ occur. Each spectrum is the average from a 16×16 pixel grid over a $(1.48\text{nm})^2$ area (V_{set}= 8 mV, I_{set}= 500 pm, V_{L}= 160 μV, T = 80 mK).

and a slight increase in intensity right above E_{F}, there is no drastic change to the LDOS, suggesting that the surface layer does not undergo the same kind of transition as the bulk crystal.

6.7.3 Quasiparticle interference under magnetic field

In Section 6.6 two vHss were identified from quasiparticle interference measurements. The analysis of tunneling spectra under magnetic field, Figure 6.16, suggests that a peak is moving across E_{F} towards negative energies. To confirm this and identify which vHs is most affected by the magnetic field, we measured quasiparticle interference at 8 T and 13 T.

Figure 6.18 shows the Fourier transformations of constant energy QPI layers at 0 T, 8 T and 13 T, at four different energies: (a) at 3.9 mV below the top of the $\mathbf{q}_1$ dispersion, (b) at 1.5 mV just below the top vHs, $\mathbf{q}_2$; (c) at -0.9 mV just below E_{F}; and (d) at -2.7 mV just before the bottom vHs, $\mathbf{q}_3$, according to the energy dispersions at 0 T (Figure 6.11). Clear differences in the scattering patterns are observed between the three applied fields. While at 0 T there is strong spectral weight at $\mathbf{q} = (0,0)$ at 1.5 mV, corresponding to the $\mathbf{q}_2$ vHs, it decreases at 8 T and it is absent from this energy at 13 T. On the other hand, at -0.9 mV, both the maps obtained at 0 T and 8 T show a clear pocket around $\mathbf{q} = (0,0)$, corresponding to $\mathbf{q}_3$, whereas at 13 T, there is an increase in spectral weight consistent with the proximity to a vHs. The QPI layer at -0.9 mV at 13 T looks similar to the QPI layers at -2.7 mV at 0 T and 8 T, suggesting a band shift with magnetic field.

To determine the scattering vectors that are most affected by the magnetic field, energy cuts were taken along the q_x and q_y directions, across both $\mathbf{q} = (0,0)$ and $\mathbf{q} = (\pm 0.5, 0.5)$. Figure 6.19(a) reproduces the line cuts along q_x across $\mathbf{q} = (0,0)$ (left) and $\mathbf{q} = (0.5,0.5)$ (right)

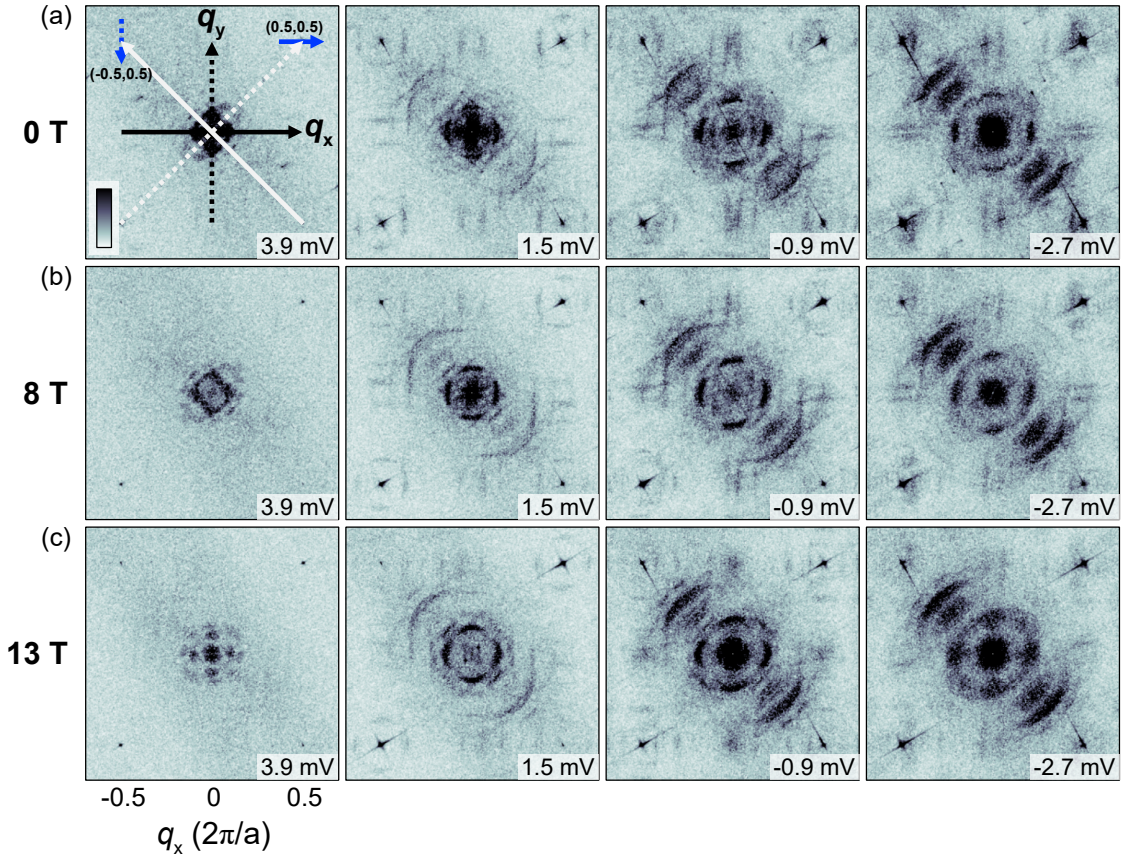

Figure 6.18: **Quasiparticle interference energy layers at different magnetic fields.** (a-c) QPI at 0 T, 8 T and 13 T, respectively, at energies 3.9 mV, 1.5 mV, -0.9 mV and -2.7 mV (V_{set}= 8 mV, I_{set}= 700 pA, V_{L}= 0.6 mV, T = 80 mK). The arrows in the first panel of (a) show the directions of the energy cuts shown in Figure 6.19.

at 0 T. The arrows indicate the positions of the $\mathbf{q}_2$ vHs (yellow) and the $\mathbf{q}_3$ vHs (red), making the correspondence between the dispersions around $\mathbf{q} = (0,0)$ and $\mathbf{q} = (0.5,0.5)$, as before. Along this direction, the $\mathbf{q}_2$ vHs has a hole-like dispersion and the $\mathbf{q}_3$ vHs has an electron-like dispersion. Along the perpendicular direction, q_y, Figure 6.19(b), the $\mathbf{q}_2$ vHs has an electron-like dispersion and the $\mathbf{q}_3$ vHs has a hole-like behavior. Here, the top of the $\mathbf{q}_1$ hole-like dispersion is well defined along both directions and the spectral weight of the $\mathbf{q}_2$ scattering around $\mathbf{q} = (0,0)$ is broad in energy (~ 2 mV).

Increasing the magnetic field to 8 T, Figure 6.19(c) and (d), shows a decrease of spectral weight around $\mathbf{q} = (0,0)$ at the top of the $\mathbf{q}_1$ hole-like dispersion along both directions. In addition, although on average the $\mathbf{q}_2$ vHs is at the same energy, the spectral weight seems to have collapsed onto $\mathbf{q} = (0,0)$, with the hole-like dispersion along q_x appearing slightly heavier than before (Figure 6.19(c)). Along q_y, a clear electron-like dispersion of $\mathbf{q}_2$ is observed, consistent with the interpretation that this is a vHs. Focusing on $\mathbf{q}_3$, around both $(0.5,0.5)$ (Figure 6.19(c), right) and $(-0.5,0.5)$ (Figure 6.19(d), right), the dispersion of $\mathbf{q}_3$ vHs collapses onto these peaks

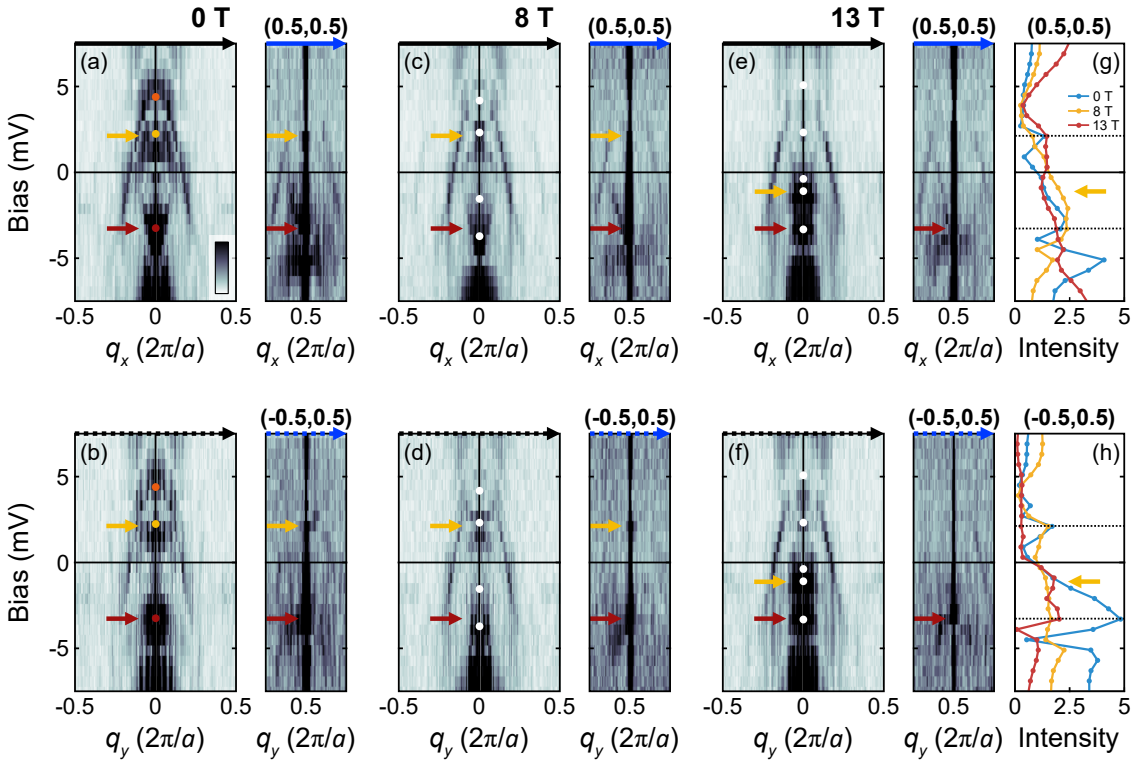

Figure 6.19: **QPI energy dispersion under magnetic field along q_x and q_y.** (a-b) Energy line cuts along q_x and q_y at 0 T. The colored circles indicate the positions of the peaks in the $g(V)$ spectrum at 0 T. (c-d) Same at 8 T. (e-f) Same at 13 T. The white circles indicate the positions of the peaks in the $g(V)$ spectrum at 8 T and 13 T. The yellow and red arrows indicate the position of the top and bottom vHs, respectively, at each field. (V_{set}= 8 mV, I_{set}= 700 pA, V_{L}= 0.6 mV, T = 80 mK). The arrows on top of each panel make the correspondence with the directions indicated in the first panel of Figure 6.18(a). (g) Intensity of the $(0.5,0.5)$ peak in the FT at each field. (h) Intensity of the $(-0.5,0.5)$ peak in the FT at each field. The yellow arrow indicates the energy of the $\mathbf{q}_2$ vHs at 13 T.

(and onto $\mathbf{q} = (0,0)$) at the same energy as at 0 T.

At 13 T, Figure 6.19(e) and (f), spectral weight is absent from the top of the $\mathbf{q}_1$ dispersion, along both directions, with the dispersion becoming straight where the top used to be. There is also no spectral weight at the energy of the vHs associated with $\mathbf{q}_2$. However, an electron-like dispersion is observed with a minimum at -1 meV, connected with a heavier hole-like dispersion (yellow arrow). The cuts across $\mathbf{q} = (0.5,0.5)$ (Figure 6.19(e), right) and $\mathbf{q} = (-0.5,0.5)$ (Figure 6.19(f), right) show the $\mathbf{q}_3$ vHs at the same energy as at 0 T. Therefore, the vHs observed at -1 meV at 13 T corresponds to the $\mathbf{q}_2$ vHs being shifted by the magnetic field.

The intensities of the $(0.5,0.5)$ and $(-0.5,0.5)$ peaks are shown in Figure 6.19(g) and (h), respectively. Due to the formation of the stripe order with increasing magnetic field along the $[-11]$ direction, the intensity of the $(0.5,0.5)$ peak becomes more featureless at higher fields. On the other hand, the intensity of the $(-0.5,0.5)$ peak, Figure 6.19(h), shows a peak at 2.3 mV at 0 T and 8 T, corresponding to the energy of the $\mathbf{q}_2$ vHs, while at 13 T, no peak is observed at that

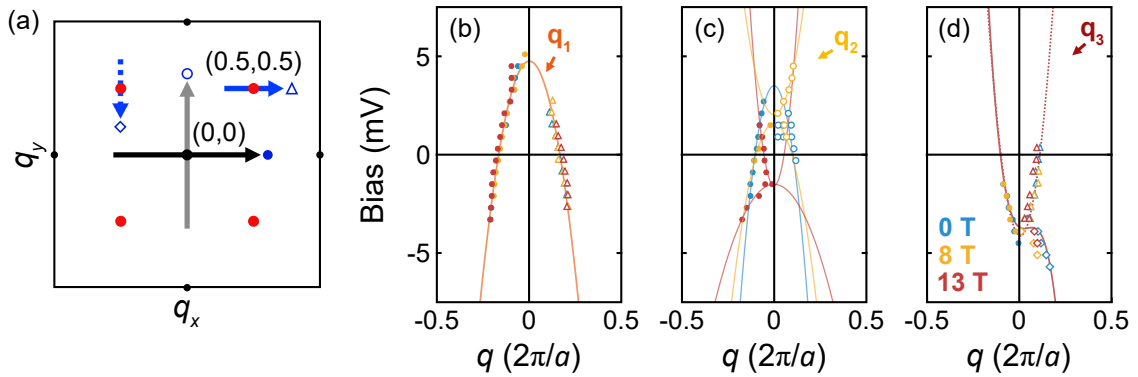

Figure 6.20: **Peak fits to the vHss dispersions under magnetic field.** (a) Sketch of the directions along which the fits were taken. The symbols next to the arrows correspond to the symbols in (b-d), making the assignment to the direction of each fit. (b-d) Peak positions from Lorentzian fits to the line profiles of the energy cuts shown in Figure 6.19 at each field for $\mathbf{q}_1$ (b), $\mathbf{q}_2$ (c) and $\mathbf{q}_3$ (d). The size of the symbols is larger than the map q-resolution.

energy. Instead, there is a peak at ~ -1 mV, confirming the shift of this vHs across the Fermi level under high magnetic fields.

To directly compare the evolution of the q-dispersions $\mathbf{q}_1$, $\mathbf{q}_2$ and $\mathbf{q}_3$ with magnetic field, the peak positions extracted from Lorentzian fits to the energy line cuts for the maps taken at 0 T, 8 T and 13 T are shown in Figure 6.20, along the q_x and q_y directions. Figure 6.20(a) shows the peaks extracted for the $\mathbf{q}_1$ dispersion around $\mathbf{q} = (0,0)$ (circles) and around $\mathbf{q} = (0.5,0.5)$ (triangles), for all fields. It shows that the dispersion is unaffected by the magnetic field at low energies, however the top of the dispersion becomes straight at 13 T, possibly due to a band hybridization. Figure 6.20(b) shows the peak positions for the $\mathbf{q}_2$ dispersion, obtained along q_x (left) and along q_y (right), clearly showing that this vHs moves from 2.3 mV across E_F towards -1 mV at 13 T. This shift occurs together with a broadening of the hole-like dispersion of the band, as evidenced by the parabolic fits. The $\mathbf{q}_2$ dispersion at 13 T along the q_y direction (Figure 6.19(f)) is not shown in Figure 6.20(b) because it was not possible to properly fit Lorentzian functions to the line profiles. Figure 6.20(c) shows the peaks from the $\mathbf{q}_3$ dispersion, obtained across $\mathbf{q} = (0,0)$ (circles) and across $\mathbf{q} = (0.5,0.5)$ along both q_x (triangles) and q_y (diamonds) directions. It shows that this vHs is unaffected by the application of a magnetic field.

Although clear differences are observed along the q_x and q_y directions of maps taken at different magnetic fields, the energy linecuts taken along the $[-11]$ and $[11]$ directions seem largely unaffected. This can be seen in Figure 6.21. While the spectral weight at $\mathbf{q} = (0,0)$ reflects the changes observed along q_x and q_y, the C_2-symmetric scattering vectors remain with the same dispersion at all fields. Figure 6.21(h) shows the peak positions extracted from Lorentzian fits to the dispersions of $\mathbf{q}_6$ and $\mathbf{q}_7$ for all fields, showing that they all fall onto the same dispersion.

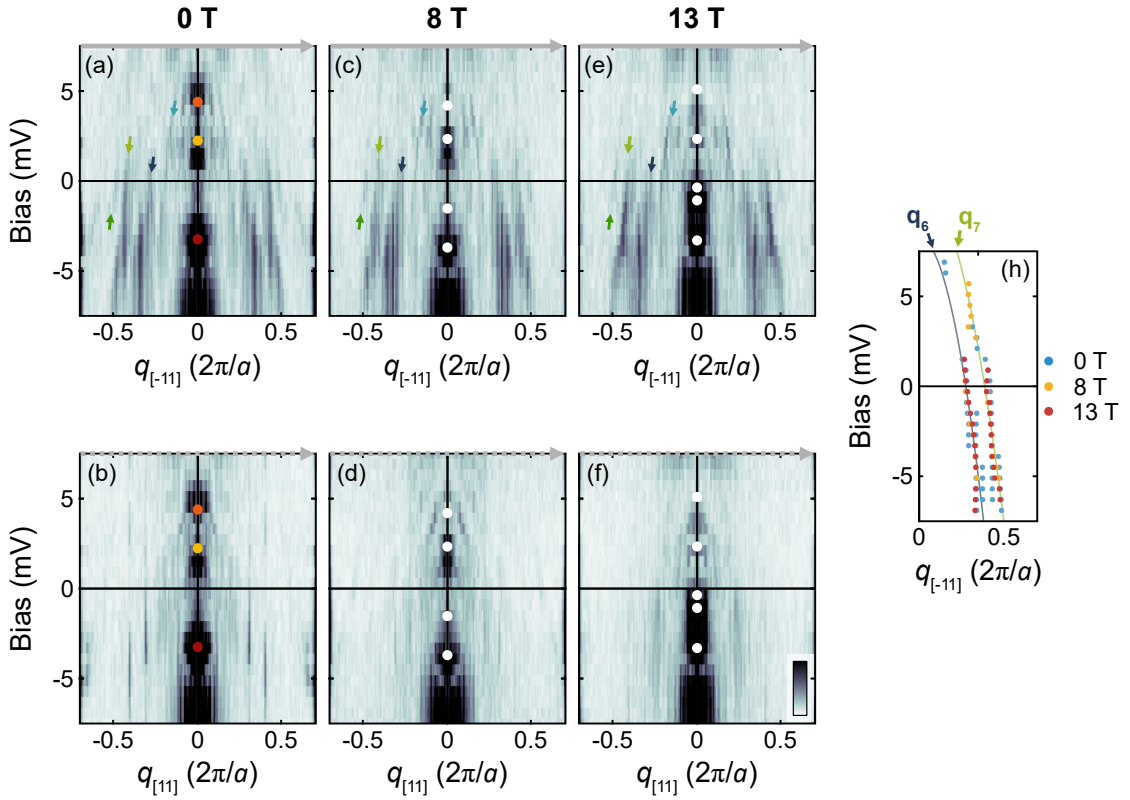

Figure 6.21: **QPI dispersion in magnetic field along $q_{[-11]}$ and $q_{[11]}$.** (a-b) Energy-momentum line cuts along $q_{[-11]}$ and $q_{[11]}$ at 0 T. (c-d) Same at 8 T. (e-f) Same at 13 T (V_{set}= 8 mV, I_{set}= 700 pA, V_L= 0.6 mV, T = 80 mK). (h) Peak positions from Lorentzian fits to the line profiles at 0 T, 8 T and 13 T for $\mathbf{q}_6$ and $\mathbf{q}_7$.

The observations from the QPI measurements are consistent with the evolution of the tunneling spectra with increasing magnetic field, Figure 6.16. The spectral weight transfer from 4.3 mV to 2.3 mV at 8 T can be explained by the transfer of spectral weight from the top of the $\mathbf{q}_1$ dispersion towards lower energies, reaching the energy of the $\mathbf{q}_2$ vHs at 8 T. In addition, the movement of a peak across E_F, reaching -1.2 mV above 13 T is naturally explained by the shift of the $\mathbf{q}_2$ vHs across E_F, between 8 T and 13 T.

In these measurements, no bands are observed to Zeeman-split with increasing magnetic field. It suggests that the surface layer of $Sr_3Ru_2O_7$ already has a magnetic ground state at 0 T.

6.8 Discussion

Using STM and tunneling spectroscopy, the measurements described in this chapter unveil the low-energy electronic structure at the surface of high-purity single crystals of $Sr_3Ru_2O_7$ and its evolution under high magnetic fields. These measurements reveal: (1) direct observation of three vHss, two above and one below E_F at 0 T; (2) bias dependent checkerboard order related to the

vHs at -4 mV; (3) magnetic field applied along the c-axis does not split bands, but pushes the vHs in the unoccupied states across E_F; (4) the electronic structure breaks C_4-symmetry in two ways, via two-fold symmetric vHss along $[10]$ and anisotropic QPI along the $[-11]$ direction; (5) Stripe-order induced by magnetic field with a wave vector $\mathbf{q} = (0.5, 0.5)$, with the same characteristic energy as the checkerboard seen at 0 T.

6.8.1 Comparison with bulk properties

A direct comparison of the electronic properties found in our measurements of the surface layer with the bulk properties of $Sr_3Ru_2O_7$ demonstrates that the surface layer forms a distinct system with its own exciting properties.

A bulk crystal of $Sr_3Ru_2O_7$ shows a large jump in magnetostriction along the c-axis at the metamagnetic phase transition, with three consecutive jumps within the range of fields between 7 and 9 T [194]. In STM, although the tip is only sensitive to the electronic properties at the surface layer, if the bulk crystal is expanding/contracting along the z-direction with increasing applied magnetic field, this will be reflected on the z-position of the tip, since the piezo scanner will have to contract/expand to keep the tunneling current constant. Therefore, it is possible to detect changes in the c-axis of the sample, allowing for a direct measurement of its magnetostriction [289]. Figure 6.22 shows the change in average z height of the tip in tunneling conditions $V_{set}=$ 8 mV and $I_{set}=$ 500 pA. Since to apply each value of magnetic field it was necessary to retract the tip, to guarantee that the measurements were consistent with each other and taken with the same conditions, the z average was obtained by averaging sets of ~ 30 topographies of lateral size 1.48 nm and sampled at 16×16 pixels, taken over the same area within ± 1 nm of uncertainty. A large increase in the z-height of the tip is observed at 7.5 T, confirming that the measured sample undergoes the expected phase transition of bulk $Sr_3Ru_2O_7$. The inset of Figure 6.22 shows the values for the field range of 7.5 to 8.1 T, where the dotted lines indicate the fields at which the magnetostriction measurements from ref. [194] see step increases, however this substructure due to the metamagnetic phases is not observed in our magnetostriction data, likely because of the sample purity ($\rho_{res} > 1\ \mu\Omega$cm).

A key signature of the quantum critical end point in bulk $Sr_3Ru_2O_7$ is a sharp increase in the electronic contribution to the specific heat on approaching the critical magnetic field at constant temperature [197,198]. The electronic contribution to the specific heat is determined by the density of states in the vicinity of the Fermi energy. The differential conductance is proportional to the density of states $n(\varepsilon)$ from Eq. (3.7), thus, we can use the tunneling spectra from Figure 6.4(a) to

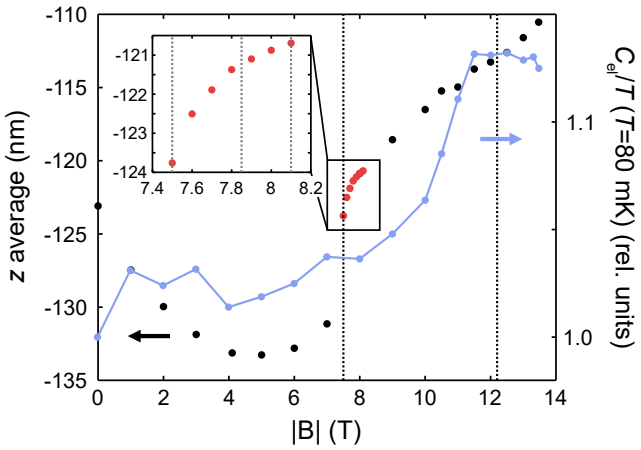

Figure 6.22: **Estimate of magnetostriction and electronic specific heat as a function of magnetic field from STM measurements.** Average tip z-height as a function of magnetic field (black and red circles). Each point is the z average of ~ 30 consecutive topographies taken over an area of 1.48 nm. The data points in red indicate measurements with a different tip and at a different position on the sample. In order for the red points to be compared with the black points, the red data points were multiplied by 0.75 so that the points at 8T from each data set fall onto the same z-average (V_{set}= 8 mV, I_{set}= 500 pA, T = 80 mK). The blue points are the electronic specific heat calculated from Eq. (6.1), plotted relative to the value at 0 T, using the quantity $g(V)/(I(V_{\text{set}})-I(-V_{\text{set}}))$ as an estimation of the density of states $n(\varepsilon)$.

estimate the electronic contribution to the specific heat as a function of magnetic field, using the expression

$$\frac{C_{\text{el}}}{T} = \frac{1}{T}\frac{\partial}{\partial T}\int \varepsilon n(\varepsilon) f(\varepsilon, T) d\varepsilon, \tag{6.1}$$

where $f(\varepsilon, T)$ is the Fermi function. When doing so close to a Lifshitz transition, the setpoint effect due to a van Hove singularity crossing the Fermi energy needs to be accounted for. We do this by normalizing the differential conductance $g(V)$ by the integral of the differential conductance over the whole spectrum, $\int_{-V_{\text{set}}}^{V_{\text{set}}} g(V)dV = I(V_{\text{set}}) - I(-V_{\text{set}})$. In this ratio, the setpoint effect cancels out, providing a more realistic estimate for how the density of states varies with magnetic field. The estimated electronic contribution to the specific heat is plotted in Figure 6.22 as blue circles. Contrary to what is observed for the bulk [197, 198], the specific heat estimated from our tunneling spectra does not diverge at the critical field of ~ 8 T. It rather shows a sharp increase at ~ 11 T, corresponding to the field where the $g(V)$ at 0 mV is seen to increase, that is, the field at which the vHs crosses E_{F}. This direct comparison between a bulk property (magnetostriction) and a surface property (C_{el}/T) measured with the same instrument under the same conditions on the same sample demonstrates that the surface layer does not undergo a metamagnetic transition at ~ 8 T, having a distinct phase diagram from the bulk crystal.

The STM measurements presented in this chapter reveal even more differences between surface and bulk. Both transport [18] and neutron scattering [190] measurements indicate that the

principal axis for the C_2 susceptibility in the metamagnetic phase is along the $\langle 100 \rangle$ directions of the tetragonal unit cell. An in-plane field along the crystallographic a and b axis induces strong resistive anisotropy between [100] and [010] directions, but a field aligned with the [110] direction produces almost no $[110]/[-110]$ anisotropy. In contrast, the QPI measurements shown in Figure 6.10 show clear C_2-symmetric electronic states along the $[-11]$ direction, where the spectral weight is completely absent from [11], whereas the C_4-symmetry breaking between the [10] and [01] directions stems from the presence of two vHS ($\mathbf{q}_2$ and $\mathbf{q}_3$), leaving the rest of the bands with four-fold symmetry.

6.8.2 QPI dispersions versus known electronic structure

Comparing the QPI dispersions with the DFT band structure of a free-standing bilayer, Figure 6.8(b), shows similarity between the two providing that the bands are highly renormalized and some bands are shifted. Figure 6.23(a) shows the DFT band structure of Figure 6.8(b) along the path $\Gamma - M$, superimposed with the dispersions obtained from QPI. The $\mathbf{q}_3$ dispersion seems to be in good agreement with the d_{xy} vHs at ~ -4 meV. The $\mathbf{q}_4$ dispersion seems to be consistent with the dispersions of d_{xz}/ d_{yz} character across the Brillouin zone boundary. However, neither $\mathbf{q}_1$, $\mathbf{q}_2$ or $\mathbf{q}_{hg}$ fall on top of bands, unless the renormalization factor is increased. Figure 6.23(b) shows the DFT band structure renormalized by a factor of 20 and then shifted so that the d_{xy}vHs is at -4 meV. Here, the $\mathbf{q}_1$ dispersion follows the dispersion of the vHs with d_{xz}/ d_{yz} orbital character around the M-point and $\mathbf{q}_{hg}$ falls on top of the dispersion of α_2. The need for different renormalization factors for different bands to have good agreement between experiments and DFT has previously been discussed in the comparison of ARPES data with DFT calculations and reflects the strongly correlated nature of the electronic states in $Sr_3Ru_2O_7$ [187].

The field dependence of the QPI shows a vHs shifting in energy with increasing magnetic field, but no splitting of bands. This suggests that the surface layer of $Sr_3Ru_2O_7$ has a magnetic ground state already in zero field. The magnetic configuration which is most stable according to DFT is a ferromagnetic ground state [290, 291] with out-of-plane magnetic moment, confirmed by the lower energies of the calculations shown in Figure 6.9 compared with their paramagnetic counterparts. However, the comparison with the QPI dispersions shows poor agreement between the two, even with large band renormalizations (> 20). It suggests that the bilayer system does not become ferromagnetic. In addition, no signs of ferromagnetism are observed from the ARPES measurements [183, 185], which should be able to detect evidence for the exchange splitting.

ARPES is sensitive to both bulk and surface bands. In the case of Sr_2RuO_4, the distinction

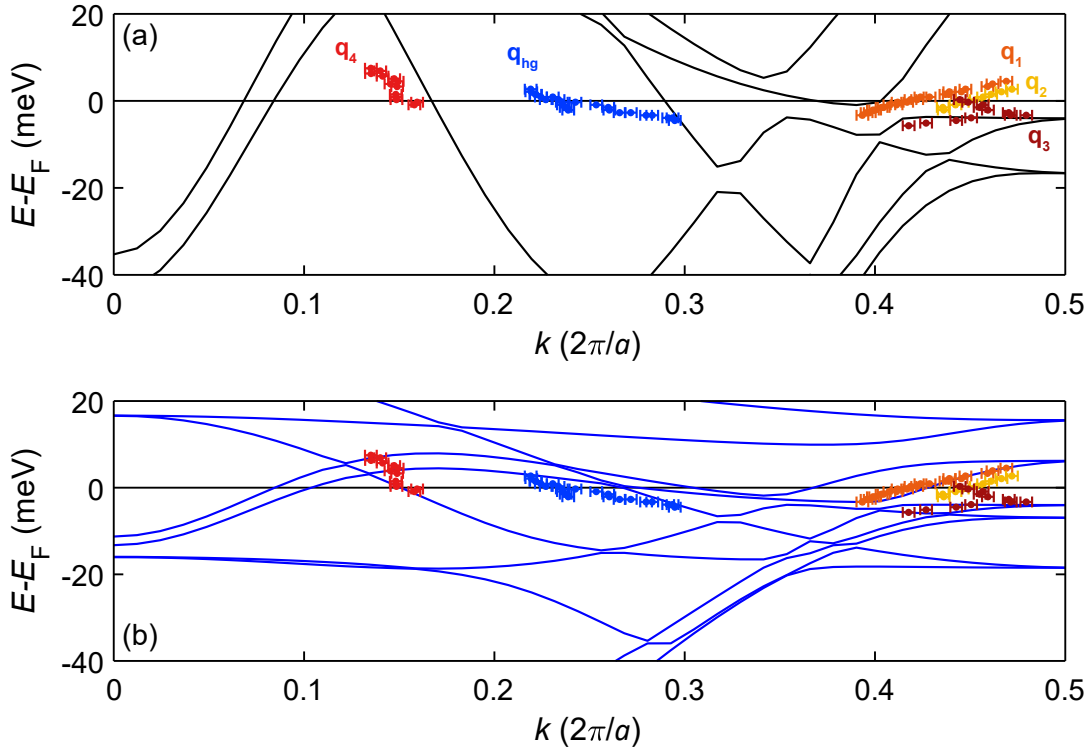

Figure 6.23: **QPI versus DFT calculations with different renormalizations.** (a) Band structure from DFT calculations on a free-standing bilayer, superimposed with the dispersions from QPI for $\mathbf{q}_1$, $\mathbf{q}_2$, $\mathbf{q}_3$, $\mathbf{q}_4$ and $\mathbf{q}_{\mathrm{hg}}$. Here the bands were renormalized by a factor of 4.2. (b) Same as in (a), but the bands were renormalized by a factor of 20, and shifted so that the vHs below E_{F} is at -4 meV.

from bulk and surface bands is clear due to the surface reconstruction that doubles the unit cell, doubling the number of bands that appear at the Fermi surface [24]. The comparison between the QPI $\mathbf{q}$-vector dispersion corresponding to the β-band and the ARPES energy dispersion of the surface β-band are in excellent agreement with each other [117], where the Fermi velocity and k_F measured in chapter 5 from QPI agree with the ones reported in ref. [27]. In $Sr_3Ru_2O_7$, the surface relaxation consists of an increase in octahedral rotation angle and potentially a tiny tilt of the RuO_6 octahedra [28], see Figure 6.1(b). These distortions preserve the unit cell of the bulk and are not expected to have such a drastic effect on the band structure, according to DFT and assuming a paramagnetic ground state [292]. This could imply that the bands from both bulk and surface are not discernible in current ARPES measurements, where the effect of the surface bands might appear as a larger apparent broadening of the bulk bands. In addition, surface degradation can not be excluded, which suppresses the surface bands.

Figure 6.24(a) shows the QPI layer at -0.3 mV from the differential conductance map in Figure 6.10, with the extracted contours shown as open circles for some of the scattering vectors identified in section 6.6, namely $\mathbf{q}_1$, $\mathbf{q}_4$, $\mathbf{q}_6$, $\mathbf{q}_7$ and $\mathbf{q}_{\mathrm{hg}}$. The $\mathbf{q}$-vectors $\mathbf{q}_2$ and $\mathbf{q}_3$ are not shown because they have the same magnitude at this energy and are too close to $\mathbf{q}_1$, and both $\mathbf{q}_5$ and $\mathbf{q}_8$

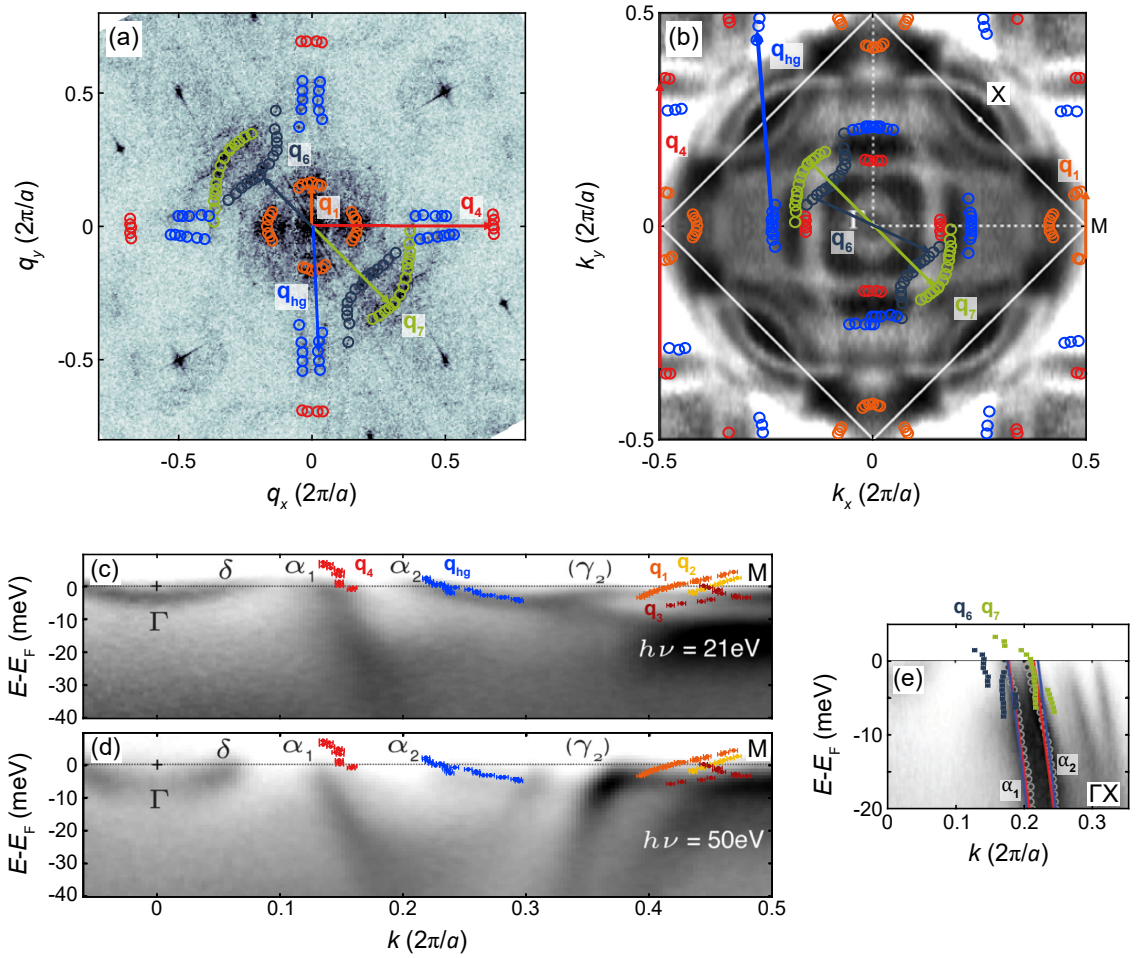

Figure 6.24: **Comparison of QPI with ARPES measurements.** (a) QPI layer at -0.3 mV from the map shown in Figure 6.10. The extracted QPI contours are shown for the features identified as $\mathbf{q}_1$ (orange), $\mathbf{q}_4$ (red), $\mathbf{q}_6$ (dark blue), $\mathbf{q}_7$ (green) and $\mathbf{q}_{\rm hg}$ (blue). (b) ARPES fermi surface, reproduced with permission from A. Tamai *et al.* [183]. The QPI patterns extracted from the map layer in (a) are superimposed on the image. Both $\mathbf{q}_1$ and $\mathbf{q}_4$ are shown centered around the M-point, and the features corresponding to $\mathbf{q}_{\rm hg}$ were shifted by $1/4$. (c-d) ARPES energy cuts along the $\Gamma - M$ direction, measured with photon energies of $h\nu = 21$ eV and $h\nu = 50$, respectively. The $\mathbf{q}_1$, $\mathbf{q}_2$, $\mathbf{q}_3$, $\mathbf{q}_4$ and $\mathbf{q}_{\rm hg}$ dispersions are shown on top of the ARPES data. (f) ARPES energy line cut along the $\Gamma - X$ direction. The q-dispersions of $\mathbf{q}_6$ and $\mathbf{q}_7$ are superimposed. ARPES data in panels (d-f) are reproduced from M. P. Allan *et al.* [185].

are neglected because they have magnitudes close to $\mathbf{q}_6$ and $\mathbf{q}_7$, respectively. Figure 6.24(b) shows the ARPES Fermi surface reproduced from A. Tamai *et al.* [183], with the scattering patterns corresponding to $\mathbf{q}_1$, $\mathbf{q}_4$, $\mathbf{q}_6$, $\mathbf{q}_7$ and $\mathbf{q}_{\rm hg}$ superimposed, extracted from the QPI layer in Figure 6.24(a). The first obvious difference is that the Fermi surface from ARPES is C_4-symmetric, whereas there are clearly C_2-symmetric QPI patterns. The symmetry breaking scattering vectors, $\mathbf{q}_6$ and $\mathbf{q}_7$ fall on top of the intersection between the α_1 and α_2 pockets. When plotted centered around the M-point, $\mathbf{q}_4$ falls on top of the edges of the α_1 pocket, corresponding to inter-BZ scattering. The scattering vector corresponding to the hourglass patterns of Figure 6.11(d-e), $\mathbf{q}_{\rm hg}$, corresponds to inter-BZ scattering between the flat edges of the α_2 pocket. The scattering vector $\mathbf{q}_1$, being identi-

fied as a vHs of d_{xz}/ d_{yz} orbital character around the M-point from the comparison with DFT, falls close to the edge of the γ_2 pocket.

Figure 6.24(c) and (d) show the ARPES energy cuts along $\Gamma - M$, across the vHs, reproduced from Allan *et al.* [185]. Superimposing the dispersions of $\mathbf{q}_1$ to $\mathbf{q}_4$ around the M-point shows quite a good agreement between our QPI and ARPES. The $\mathbf{q}_3$ dispersion is in very good agreement with the vHs found at -4 meV in ARPES. The dispersions of $\mathbf{q}_1$ and $\mathbf{q}_2$ finish right below the Fermi level, and so are difficult to compare. The $\mathbf{q}_4$ dispersion seems to agree with the α_1 dispersion and the $\mathbf{q}_{hg}$ dispersion, after shifting by $1/4$, falls on top of the dispersion of the α_2 pocket.

Along the $\Gamma - X$ direction, Figure 6.24(e), there is also good agreement between the dispersions of $\mathbf{q}_6$ and $\mathbf{q}_7$ with the α_1 and α_2 bands, respectively, although the effective masses estimated from the parabolic fits to the QPI data give effective masses an order of magnitude larger than the cyclotron masses extracted from the ARPES.

Overall, the measured QPI is in agreement with the ARPES band structure. The most significant difference is the C_4-symmetry breaking of the QPI patterns, which is clearly not reflected in the ARPES Fermi surface. A model of the surface electronic structure has to be able to reproduce the C_4-symmetry breaking while keeping good agreement with ARPES measurements. The above comparison suggests that the α_1 and α_2 pockets are C_2-symmetric at the surface along the $\Gamma - X$ direction.

Better agreement between ARPES, DFT and QPI can be obtained by energy- and moment-dependent band renormalizations. If the Fermi level is in the middle of a band, it is trivial to assume that the renormalization factor of that band will be the same at all energies. However, if the Fermi level is close to a vHs, the effects of strong electronic correlations could result in a larger renormalization close to the vHs-point than at energies far away from it. In $Sr_3Ru_2O_7$, since there is a plethora of vHs at the M-point, it is conceivable that all these are subjected to strong renormalizations due to strong correlations, resulting in a larger normalization factor at positive energies, which pushes the d_{xz}/ d_{yz} vHs down in energy to ~ 4 meV above E_F, originating the scattering vector $\mathbf{q}_1$.

For a tetragonal unit cell, the d_{xy} vHs in $Sr_3Ru_2O_7$ at -4 meV is four-fold at the M-point, however, due to the orthorhombic distortion, even though almost negligible, this vHs is expected to be slightly split into two vHss with two-fold symmetry [211]. The QPI data suggests that the vHss corresponding to $\mathbf{q}_2$ and $\mathbf{q}_3$ could be two-fold vHss due to the splitting of a four-fold vHs, since they are observed to have opposite behavior to each other: while $\mathbf{q}_2$ has a hole-like dispersion along q_x and an electron-like dispersion along q_y, $\mathbf{q}_3$ has an electron-like dispersion

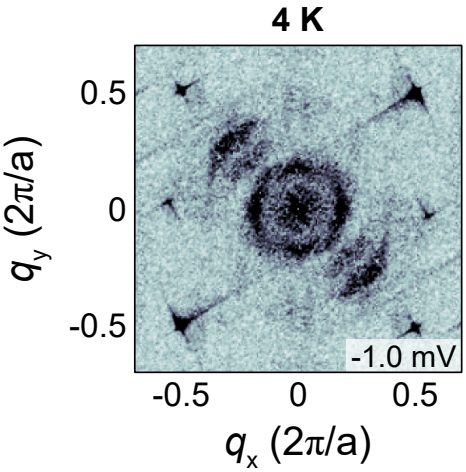

Figure 6.25: **Quasiparticle interference at $T = 4$ K.** Fourier transform of a differential conductance map at -1 mV, taken at $T = 4$ K (V_{set}= 15 mV, I_{set}= 800 pA, V_{L}= 1 mV).

along q_x and a hole-like dispersion along q_y. They are split by ~ 6 meV, suggesting that the effect of the orthorhombic distortion on the band structure is amplified by correlation effects. In addition, it is difficult to explain the C_2-symmetric states along $[-11]$ solely based on the orthorhombicity, which seem to correspond to highly distorted α_1 and α_2 bands. At the surface, the increased structural distortions, namely a larger octahedral rotation and possibility of tilt [28], together with strong electronic correlations could result in such a large splitting of the vHss, moving one of the vHs above the Fermi level, and could be responsible for the strong C_4-symmetry breaking of the α_1 and α_2 bands.

The QPI measurements reported in this thesis show striking differences from previous QPI measurements on Ti-doped $Sr_3Ru_2O_7$ crystals (1% doping) by Lee *et al.* [210], measured at 4 K. While we observe clear C_4-symmetry breaking QPI patterns along the $[-11]$ direction, the QPI patterns observed by Lee *et al.* are four-fold symmetric. To check if it was due to the temperature, we took QPI maps at 4 K. Figure 6.25 shows the Fourier transform of a differential conductance map taken at 4 K at an energy of -1 meV. The QPI patterns remain C_2-symmetric. The difference might be attributed to the Ti-doping, which is known to change the electronic structure, potentially restoring C_4-symmetry. In addition, the model to describe the observed QPI by coming only from scattering from the α_2 band is not consistent with our data, where we observe more diversity of q-vectors that can be explained by scattering between other bands, namely the different vHs at the M-point of the Brillouin zone. The QPI simulations from Lee *et al.* [209] also do not reflect our measurements, showing patterns closer to the ones observed at the surface of Sr_2RuO_4. The dominant C_2-symmetry in our measurements is in a different direction than the one expected from transport measurements, and so the nematic order parameter introduced in ref. [209] is not the

correct one to describe the QPI at the surface of $Sr_3Ru_2O_7$. As suggested, STM measurements should be able to distinguish which band is responsible for the nematic order, where the prediction is that if the d_{xy} band is the dominant band for the nematic phase then the QPI pattern should be C_4-symmetric. We observe both cases, C_4-symmetry breaking from the d_{xz}/d_{yz} states, along $[-11]$, and two vHs with two-fold symmetry along $[10]$, one above and one below E_F, implying that the nematic order parameter at the surface of $Sr_3Ru_2O_7$ is not trivial. It is also discussed that the contribution of the d_{xy} states is largely suppressed, however, we observe clear signatures from the d_{xy} vHs in our QPI. This does not come as a surprise after the conclusions of chapter 5, where I showed that the octahedral rotations promote the mixture of the d_{xy} and d_{z^2} states at the M-point of the Brillouin zone resulting in stronger coupling to the tip, which also happens in $Sr_3Ru_2O_7$.

6.8.3 Magnetic-field induced Lifshitz transition

Our results demonstrate a magnetic-field induced Lifshitz transition at the surface of $Sr_3Ru_2O_7$. The QPI measurements under magnetic field show a vHs at positive energies at 0 T and 8 T, which moves below the Fermi level to ~ -1 meV at 13 T. The shift of the vHs across the Fermi level naturally explains the observed evolution of the tunneling spectra with increasing field, Figure 6.16, where a spectral weight shift is detected from positive to negative energies consistent with a peak moving across E_F. In a Fermi liquid picture, the spectroscopic signature of a vHs approaching the Fermi level should be a peak getting sharper as E_F is approached, due to infinite lifetime and increased coherence of the quasiparticles. However, this is not observed in our measurements, instead, the observed changes to the tunneling spectra under magnetic field seem more consistent with a peak that becomes incoherent as it approaches E_F, which could be a signature of quantum fluctuations becoming dominant. This is similar to what has been observed in twisted bilayer graphene, in which as the vHs is pushed across E_F, tuned by gate voltage, its peak in the tunneling spectra appears to lose coherence before emerging on the other side of E_F [293]. Our observations are in agreement with the report by Iwaya *et al.* [212], however here, by being able to go to magnetic fields beyond 11 T, we could demonstrate that the surface layer of $Sr_3Ru_2O_7$ undergoes a Lifshitz transition at higher fields than the bulk, with a critical field of $\sim$ 11 T, as illustrated by the behavior of the electronic specific heat as a function of magnetic field calculated from the tunneling spectra, Figure 6.22.

The QPI measurements show the vHs moving down in energy with magnetic field without a spin-split partner. In addition, the rest of the bands seem not to be affected by the magnetic field, with the most noticeable change being the loss of spectral weight of the top of the $\mathbf{q}_1$ hole-like

band. It suggests that the surface layer of $Sr_3Ru_2O_7$ is already in a magnetic ground state at 0 T.

The topographies show a magnetic field-induced stripe order aligned with the $[-11]$ direction, parallel to the direction of the C_2-symmetric QPI patterns. Its strength is reflected in the intensity of the $(0.5, 0.5)$ peak in the Fourier transformations of the topographies, which increases with magnetic field at a higher rate than the decrease in the intensity of the $(-0.5, 0.5)$ peak. The intensity of the $(0.5, 0.5)$ peak retains a bias dependence similar to the checkerboard at 0 T, with a peak at -5 mV, demonstrating an electronic origin. The appearance of such a stripe order is intimately linked with the C_2-symmetric states and the movement of the vHs towards negative energies, but the exact mechanism behind its formation is not known. A similar stripe order has been observed in La-doped $Sr_3Ir_2O_7$ at zero field [294], which was ascribed to be a consequence of the electronic density wave present in this material together with the octahedral tilt, identical to the one illustrated in Figure 6.1(b).

The field-induced stripe order could in principle result in anisotropic transport behavior, as it is observed around the quantum critical end point of bulk $Sr_3Ru_2O_7$ [18]. However, it occurs in a different direction. While the stripe order and C_2-symmetric QPI occur between the $[-11]$ and $[11]$ directions, the anisotropic transport behavior and the spin density wave order found in neutron scattering measurements occur along the $[10]$ and $[01]$ directions of the tetragonal unit cell [18, 190, 295].

6.8.4 Possible mechanisms

From our STM/STS measurements and the above discussion, a model of the surface layer of $Sr_3Ru_2O_7$ has to: (1) have bands that break C_4-symmetry between the $[-11]$ and $[11]$ directions; (2) be consistent with the ARPES band structure; (3) have a four-fold vHs split at the M-point and (4) have a magnetic ground state. The comparison with ARPES measurements in section 6.8.2, suggests that both α_1 and α_2 bands become highly C_2-symmetric at the surface. The fact that we do not observe signal along $[11]$, shows that the symmetry breaking cannot be accounted for by considering a small perturbative term. Possible scenarios include the formation of magnetic order, Fermi surface reconstruction due to strong spin-orbit coupling effects, a combination of the two or spin-fluctuations.

A magnetic order consistent with our measurements has to be able to explain the anisotropy along the $\langle 11 \rangle$ directions and the field-induced stripes. DFT calculations, using both LDA and PBE exchange-correlation functionals, show that different magnetic orders give lower energies than the paramagnetic case, with the ferromagnetic ground state being the lowest energy state [290].

A ferromagnetic order does not seem to be consistent with our data and ARPES measurements because one would expect all bands to be exchange split, as shown by the band structure of a ferromagnetic free-standing bilayer in Figure 6.9. The order with the second-lowest energy, with only a small energy difference from the ferromagnetic case, is an E-type antiferromagnetic ground state [291], illustrated in Figure 2.16(b). In $Sr_3Ru_2O_7$, this magnetic order is observed upon doping with small amounts of Mn [20], Fe [21] and Ti [296]. This order has a characteristic wave vector $\mathbf{q} = (0.25, 0.25)$, in the same direction as we observe the C_2-symmetry. For out-of-plane spins, the application of the magnetic field parallel to the c-axis should push the spin up bands down in energy, increasing its density of states. As a result, since the STM topographies are proportional to the integrated DOS, the positions of spin-up should appear with high intensity, resulting in a stripe order with characteristic wavevector $\mathbf{q} = (0.25, 0.25)$, inconsistent with our observations, where the stripe order appears with $\mathbf{q} = (0.5, 0.5)$. One way to obtain the $\mathbf{q} = (0.5, 0.5)$ stripe order would be if the spins were oriented in-plane, and the out-of-plane magnetic field, together with spin-orbit coupling, would introduce out-of-plane canting to the spins. In this way, both spin directions would appear with the same intensity in the STM topographies. However, the Fermi surface from this ground state is significantly different from the one observed here, with a lower number of bands crossing the Fermi level [292], which is not consistent with the observation that our measurements are in good agreement with the ARPES band structure and that obtained from a paramagnetic DFT calculation.

The microscopic theories proposed to describe the metamagnetic transitions in $Sr_3Ru_2O_7$ need a vHs which is split and crosses the Fermi level, either of d_{xz}/d_{yz} or of d_{xy} orbital character, where the region where the bands are split results in an increase in magnetization [205, 208]. The increased octahedral rotation at the surface together with high susceptibility towards magnetic ordering and strong correlations in $Sr_3Ru_2O_7$, could result in the splitting of a vHs with one of the split partners moving above E_F, locking the surface layer in a state with high polarization. Our QPI measurements show two vHs that seem consistent with the d_{xy} vHs split at the surface of $Sr_3Ru_2O_7$, and since we do not see bands splitting under magnetic field, it suggests that the surface layer is already in a high polarization state. This high polarization state together with spin-orbit coupling [205, 208] could result in the observed anisotropy of the electronic states and would be expected to follow the orientation of the magnetic field. Another possibility that cannot be excluded from our measurements is the formation of an additional spin density wave on top of the itinerant electron system, as was found for the bulk from neutron scattering measurements [190].

6.8.5 Comparison with the surface of Sr_2RuO_4

The surface layer of $Sr_3Ru_2O_7$ is essentially two surface layers of Sr_2RuO_4 on top of each other coupled together via the apical oxygen, with an opposite orientation of the octahedral rotation between the layers. Apart from this bilayer coupling, their electronic structure is very similar, as evidenced by comparing the ARPES Fermi surfaces of both systems (Figure 2.12 and Figure 2.14) and the presence of vHs within 5 meV of the Fermi level. It is thus relevant to compare our observations on both systems.

Tunneling spectra at both the surface layer of Sr_2RuO_4 and of $Sr_3Ru_2O_7$ show a partial gap around the Fermi level, which represents a suppression of the density of states of about 35% relative to the value at bias voltages outside of the gap (20 mV in the case of Sr_2RuO_4 and 95 mV in the case of $Sr_3Ru_2O_7$). While the width of the partial gap in Sr_2RuO_4 is ~ 5 meV, in $Sr_3Ru_2O_7$ it is four times larger. In Sr_2RuO_4, some of the partial gap can be accounted for by the gapping of the d_{xy} band at the M-point of the Brillouin zone, when a checkerboard charge and nematic order parameters are introduced phenomenologically into a tight-binding model. In the case of $Sr_3Ru_2O_7$, a gapping of the d_{xy} band would not be sufficient to produce a partial gap with a width of 20 mV, and it is inconsistent with our measurements that suggest that the d_{xy} vHs is split by significantly less than would be necessary to explain this gap. The fact that we do not observe QPI patterns corresponding to scattering from the β and γ_1 bands in $Sr_3Ru_2O_7$ might be an indication that these are gapped out at the surface layer, however, our measurements cannot definitively confirm or refute this possibility. Nevertheless, it is the presence of such partial gaps that allow us to detect the vHs peaks in the tunneling spectrum so clearly and to follow their movement under magnetic field.

The low energy tunneling spectra in both systems show multiple vHs within 5 mV of the Fermi level. In Sr_2RuO_4, four vHss are detected, two above and two below E_F, whereas in $Sr_3Ru_2O_7$, two vHss are observed above E_F and one below. In both cases, a visually identical checkerboard charge modulation is observed in the topographies, which is pinned to the energy of the vHss at -4 mV in each system, at 0 T. In the case of Sr_2RuO_4, the phase-referenced Fourier transformation reveals two peaks at ± 3.5 mV with opposite phase, consistent with a charge density wave, whereas in $Sr_3Ru_2O_7$, the PR-FT shows a strong peak at -3.5 mV and a second peak with the same phase at 2.3 mV, corresponding to the position of the vHss. As a consequence, the range of bias voltages over which the checkerboard is visible is wider than in Sr_2RuO_4. Upon the application of magnetic field, the vHs in Sr_2RuO_4 is observed to Zeeman-split, with one of the branches expected to reach the Fermi level at ~ 32 T, whereas in $Sr_3Ru_2O_7$ no splitting of the bands is

observed, and the measurements are consistent with a vHs crossing the Fermi level at ~ 11 T. In differential conductance maps, the checkerboard in Sr_2RuO_4 follows the Zeeman-split vHs under magnetic field, whereas in $Sr_3Ru_2O_7$ a stripe order appears in field, whose strength increases with the magnitude of the magnetic field.

The QPI measurements show C_4-symmetry breaking in both systems. In Sr_2RuO_4, both short-range atomic-scale modulations and long-range QPI modulations break C_4-symmetry along the $[10]$ and $[01]$ directions of the tetragonal unit cell. This C_2-symmetry is naturally explained by the d_{xy} vHss becoming anisotropic along the $[10]$ and $[01]$ directions. The remaining QPI patterns, corresponding to the d_{xz}/d_{yz}states, remain C_4-symmetric. In $Sr_3Ru_2O_7$, we observe two vHss which are C_2-symmetric along the $[10]$ and $[01]$ directions of the tetragonal unit cell, but the strong anisotropy in the QPI measurements is seen between the $[-11]$ and $[11]$ directions , together with the appearance of the stripe order along the $[-11]$ direction under magnetic field. In contrast to Sr_2RuO_4, a perturbative nematic order parameter is not sufficient to explain the C_2-symmetric bands observed in $Sr_3Ru_2O_7$.

The comparison between the two systems highlights how seemingly tiny structural differences result in dramatically different ground states. It suggests that both increased octahedral rotation expected of $Sr_3Ru_2O_7$ and possible tilt and bilayer coupling are necessary to understand the differences between the two systems.

6.9 Conclusion

The results presented in this chapter establish the surface layer of $Sr_3Ru_2O_7$ as a distinct system from the bulk. We find that the surface layer undergoes a Lifshitz transition at ~ 11 T, from the tunneling spectra and the QPI measurements, which is higher than the field at which the metamagnetic transition of the bulk is observed. The evolution of the tunneling spectra in increasing magnetic field further suggests that the vHs becomes incoherent as it crosses the Fermi energy, pointing towards the importance of quantum fluctuations in the Lifshitz transition. The QPI measurements at 0 T reveal the presence of three vHs within 5 meV of the Fermi level, two above and one below E_F, as well as states that strongly break C_4-symmetry. Applying a magnetic field pushes one of the vHs across the Fermi level, from positive to negative energies, making the system go through a Lifshitz transition. No splitting of the bands is observed, suggesting that the surface already has a magnetic ground state at zero field. Most surprisingly, we find a striped order developing with magnetic field, whose strength increased with the magnitude of the applied field,

which is intimately related with the C_4-symmetry breaking states and the movement of the vHs to lower energies. These results show, for the first time, atomic-scale real space images of magnetic field induced nematic states, promising key insights into the microscopic mechanism of the field-induced nematicity and metamagnetic quantum critical end point in $Sr_3Ru_2O_7$ and provide an opportunity to validate the theories aimed at describing the physics close to a metamagnetic quantum critical end point.

Chapter 7

Conclusion and outlook

The STM/STS measurements presented in this thesis reveal the rich physics of the ruthenate systems by unveiling the low-energy electronic states at the surface of Sr_2RuO_4 and $Sr_3Ru_2O_7$, where I have found emergent ordered phases that are distinct from the bulk. This work has implications on the mechanism for unconventional superconductivity in Sr_2RuO_4 and the physics behind the quantum critical end point and nematicity in $Sr_3Ru_2O_7$, as well as on the interplay between structural and electronic degrees of freedom in these materials. It demonstrates how the surface of Sr_2RuO_4 and $Sr_3Ru_2O_7$ provide ideal platforms for testing microscopic theories aimed at describing the effect of strong electron correlations on the electronic structure in general, and specifically the role of quantum fluctuations in magnetic-field driven Lifshitz transitions.

At the surface of Sr_2RuO_4, I found that the surface reconstruction, involving octahedral rotations, results in a dramatically different ground state from that of the bulk, stabilizing a checkerboard charge order intertwined with nematicity. The tunneling spectrum shows a partial gap of width ~ 5 meV around the Fermi level, which encloses four van Hove singularities. We find that both the checkerboard charge order and the nematicity are intimately linked to these van Hove singularities. Including a weak intraband hybridization and a nematic order parameter phenomenologically into a tight-binding model, we achieved excellent agreement with experiment. Continuum LDOS calculations using this tight-binding model qualitatively reproduce the experimental quasiparticle interference measurements. By applying a magnetic field along the c-axis, we observed one of the van Hove singularities to Zeeman-split, with one of the spin branches moving towards the Fermi level. Extrapolating our data predicts that the van Hove singularity will reach the Fermi level at 32 T. Our results demonstrate that the surface layer of Sr_2RuO_4 is a clean two-dimensional system that provides a textbook example of tuning towards a magnetic field-driven Lifshitz transition.

To determine the effects of quantum fluctuations on a Zeeman-driven Lifshitz transition, and ascertain if it leads to a quantum phase transition, it is necessary to have the van Hove singularity closer to the Fermi level. Uniaxial strain on single crystals of Sr_2RuO_4 has been shown to push the vHs in the direction normal to the applied strain across the Fermi level [7]. Therefore, it is expected that by applying uniaxial strain to the surface layer of Sr_2RuO_4, one of the vHs will be pushed closer to the Fermi energy, so that an applied magnetic field of accessible magnitude in the laboratory ($\sim$ 22 T) would be sufficient to push one of the Zeeman-split partners across the Fermi level, allowing to track the shape of the peak in the local density of states associated with the vHs as it crosses the Fermi level. If quantum fluctuations become important, the peak is expected to broaden significantly when approaching the Fermi energy, potentially providing direct insights into their importance when traversing the Lifshitz transition.

Due to the splitting of the vHs under magnetic field, the system becomes spin-polarized, and when the vHs approaches the Fermi energy, it might be expected that the system forms a spin-density wave with a possible quantum phase transition. In addition, our results show the appearance of a field-induced feature at $(0, 1/3)$ in differential conductance maps, Figure 5.26. To determine if there is an underlying magnetic order, spin-polarized STM measurements would be needed. These measurements would also allow us to investigate if the checkerboard pinned to the split vHs becomes magnetically ordered. By doing in-plane magnetic field measurements in a vector magnet, it would be possible to determine if these orders have an in-plane easy axis anisotropy due to spin-orbit coupling, where if so, they should follow the in-plane component of the magnetic field.

One of the remaining questions is the absence of the superconducting gap in the tunneling spectra measured below 100 mK. Our results suggest that the octahedral rotation at the surface and stabilization of the checkerboard charge and nematic orders suppress the superconducting state present in the bulk of the sample. For phonon-mediated superconductivity, and if the dominant phonon is linked to the rotational mode of the octahedra, superconductivity might be expected to be suppressed once the rotational mode freezes out as happens in the surface layer of Sr_2RuO_4. Whether superconductivity is suppressed because the rotational mode is frozen at the surface or because the checkerboard charge order and nematicity compete with the superconducting order parameter is an open question. The seemingly contradictory reports in the literature [158,159,165], call for a more controlled way to observe the superconducting gap since if it was possible to reliably detect it, STM would be the ideal technique to aid in the quest of identifying the symmetry of the superconducting order parameter of Sr_2RuO_4. Possibilities include measuring on a room-

temperature cleave, remove a flake of the surface with the tip at low temperatures or covering the surface with different adatoms [286], in an attempt to suppress the octahedral rotation of the surface layer.

The measurements at the surface of $Sr_3Ru_2O_7$ reveal the presence of a partial gap 4 times wider than the one found at the surface of Sr_2RuO_4, and three vHs within 5 meV of the Fermi level, two above and one below, plus a checkerboard charge order reminiscent of that in Sr_2RuO_4. Quasiparticle interference measurements reveal strong anisotropy of the scattering patterns, with C_4 symmetry breaking between the $[-11]$ and $[11]$ directions of the tetragonal unit cell, as well as two van Hove singularities that are two-fold along the $[10]$ and $[01]$ directions. The tunneling spectra in magnetic field along the c-axis show spectral weight shifting from the unoccupied states to the occupied states, crossing the Fermi level at a field of ~ 11 T. Field-dependent QPI measurements show that this shift of spectral weight is connected with a vHs crossing the Fermi energy, associated with a Lifshitz transition of the surface layer. No splitting of the bands was observed, suggesting that the ground state of the surface layer of $Sr_3Ru_2O_7$ is already magnetic. The changes to the tunneling spectra as the vHs is pushed across E_F are distinct from the ones expected from a vHs shift in a Fermi liquid picture, suggesting that quantum fluctuations play a role in this transition. Our measurements establish the surface layer of $Sr_3Ru_2O_7$ as having a distinct ground state from the bulk, undergoing a Lifshitz transition at a higher critical field than the bulk of ~ 11 T.

To determine if the strong C_2 symmetry observed in the QPI along the $[-11]$ direction is related to spin-orbit coupling, measurements with an in-plane magnetic field are necessary. In analogy to theories proposed for the field-induced nematicity for bulk $Sr_3Ru_2O_7$ [205, 208], spin-orbit coupling in a polarized state can explain the C_2 symmetric features. In this case, the C_2 symmetric features should follow the direction of the in-plane component of the magnetic field. The quantum critical end point in an out-of-plane magnetic field appears due to the suppression of the temperature of a critical end point of the metamagnetic transition observed with an in-plane magnetic field [15]. By doing a series of measurements with increasing out-of-plane component it might be possible to track the suppression of a critical end point and determine the onset of quantum fluctuations for the surface layer of $Sr_3Ru_2O_7$. To further investigate the magnetic ground state found at the surface layer of $Sr_3Ru_2O_7$ and the field-induced stripe order, spin-polarized STM measurements are necessary. Such measurements will allow us to distinguish between different possible magnetic ground states such as the E-type antiferromagnetic order and ferromagnetism.

The measurements discussed in this thesis on both the surfaces of Sr_2RuO_4 and $Sr_3Ru_2O_7$ show that instabilities present in the bulk are stabilized at the surface layer: checkerboard charge

order and nematicity in Sr_2RuO_4 and a magnetic ground state in $Sr_3Ru_2O_7$. Studies on single crystals of Sr_2RuO_4 with increasing Ca doping show that the surface layer usually has an increased structural distortion compared to the bulk [254, 297], hindering the access to the bulk ground state with STM. However, by acquiring the distortions of the next doping concentration, it seems that by studying the low-energy electronic structure of the surface layer it is possible to probe the ground state of the next doped compound, allowing access to the ordered phases stabilized with that structural distortion. The implication is that by measuring the surface of, for example, $Ca_{1.5}Sr_{0.5}RuO_4$, it is possible to study the glassy magnetic metallic phase found in the bulk of $Ca_{1.7}Sr_{0.3}RuO_4$, which would otherwise be hidden by the increased distortion of its surface layer. Another example would be the evolution of the ground state with Ca doping in $Sr_3Ru_2O_7$, where one could find a concentration of Ca at which the surface layer would stabilize the ground state of $Ca_3Ru_2O_7$.

In a wider context, performing both high-resolution tunneling spectroscopy and QPI measurements at temperatures below 100 mK while tuning the magnetic field across the metamagnetic transitions of other strongly correlated electron materials, such as $CeRu_2Si_2$ [103, 298] and $YbRh_2Si_2$ [105, 299, 300], would help to disentangle the underlying changes to their electronic structures as a quantum critical point is traversed. This will give insight into the mechanisms behind such transitions with the determination of the role of quantum fluctuations and Kondo-breakdown in driving them. Due to the high diversity of phases found in strongly correlated electron materials and their sensitivity to external stimuli, studying their surfaces opens up the opportunity to find new emergent ordered states and study the materials in parameter regimes not accessible in the bulk, as we found at the surfaces of Sr_2RuO_4 and $Sr_3Ru_2O_7$.

Bibliography

[1] Z. F. Weng, M. Smidman, L. Jiao, X. Lu, and H. Q. Yuan. Multiple quantum phase transitions and superconductivity in Ce-based heavy fermions. *Reports on Progress in Physics*, 79(9):094503, 2016.

[2] Y. Tokura, M. Kawasaki, and N. Nagaosa. Emergent functions of quantum materials. *Nature Physics*, 13(11):1056–1068, 2017.

[3] P. Coleman and A. J. Schofield. Quantum criticality. *Nature*, 433(7023):226–229, 2005.

[4] B. Binz and M. Sigrist. Metamagnetism of itinerant electrons in multi-layer ruthenates. *Europhysics Letters*, 65(6):816–822, 2004.

[5] M. Malvestuto, E. Carleschi, R. Fittipaldi, E. Gorelov, E. Pavarini, M. Cuoco, Y. Maeno, F. Parmigiani, and A. Vecchione. Electronic structure trends in the $Sr_{n+1}Ru_nO_{3n+1}$ family ($n = 1,2,3$). *Physical Review B*, 83(16):165121, 2011.

[6] K. M. Shen, N. Kikugawa, C. Bergemann, L. Balicas, F. Baumberger, W. Meevasana, N. J. C. Ingle, Y. Maeno, Z.-X. Shen, and A. P. Mackenzie. Evolution of the fermi surface and quasiparticle renormalization through a van hove singularity in $Sr_{2-y}La_yRuO_4$. *Physical Review Letters*, 99(18):187001, 2007.

[7] V. Sunko, E. Abarca Morales, I. Marković, M. E. Barber, D. Milosavljević, F. Mazzola, D. A. Sokolov, N. Kikugawa, C. Cacho, P. Dudin, H. Rosner, C. W. Hicks, P. D. C. King, and A. P. Mackenzie. Direct observation of a uniaxial stress-driven Lifshitz transition in Sr_2RuO_4. *npj Quantum Materials*, 4(1):46, 2019.

[8] Y. Maeno, H. Hashimoto, K. Yoshida, S. Nishizaki, T. Fujita, J. G. Bednorz, and F. Lichtenberg. Superconductivity in a layered perovskite without copper. *Nature*, 372(6506):532–534, 1994.

[9] A. Pustogow, Yongkang Luo, A. Chronister, Y.-S. Su, D. A. Sokolov, F. Jerzembeck, A. P. Mackenzie, C. W. Hicks, N. Kikugawa, S. Raghu, E. D. Bauer, and S. E. Brown. Constraints on the superconducting order parameter in Sr_2RuO_4 from oxygen-17 nuclear magnetic resonance. *Nature*, 574(7776):72–75, 2019.

[10] S. A. Kivelson, A. C. Yuan, B. Ramshaw, and R. Thomale. A proposal for reconciling diverse experiments on the superconducting state in Sr_2RuO_4. *npj Quantum Materials*, 5(1):1–8, 2020.

[11] V. Grinenko, S. Ghosh, R. Sarkar, J.-C. Orain, A. Nikitin, M. Elender, D. Das, Z. Guguchia, F. Brückner, M. E. Barber, J. Park, N. Kikugawa, D. A. Sokolov, J. S. Bobowski, T. Miyoshi, Y. Maeno, A. P. Mackenzie, H. Luetkens, C. W. Hicks, and H.-H. Klauss. Split superconducting and time-reversal symmetry-breaking transitions in Sr_2RuO_4 under stress. *Nature Physics*, 17(6):748–754, 2021.

[12] A. P. Mackenzie, R. K. W. Haselwimmer, A. W. Tyler, G. G. Lonzarich, Y. Mori, S. Nishizaki, and Y. Maeno. Extremely Strong Dependence of Superconductivity on Disorder in Sr_2RuO_4. *Physical Review Letters*, 80(1):161–164, 1998.

[13] J. P. Carlo, T. Goko, I. M. Gat-Malureanu, P. L. Russo, A. T. Savici, A. A. Aczel, G. J. MacDougall, J. A. Rodriguez, T. J. Williams, G. M. Luke, C. R. Wiebe, Y. Yoshida, S. Nakatsuji, Y. Maeno, T. Taniguchi, and Y. J. Uemura. New magnetic phase diagram of $(Sr,Ca)_2RuO_4$. *Nature Materials*, 11(4):323–328, 2012.

[14] S. J. Yuan, S. Aswartham, J. Terzic, H. Zheng, H. D. Zhao, P. Schlottmann, and G. Cao. From $J_{eff} = 1/2$ insulator top-wave superconductor in single-crystal $Sr_2Ir_{1-x}Ru_xO_4$ ($0 \leq x \leq 1$). *Physical Review B*, 92(24):245103, 2015.

[15] R. S. Perry, L. M. Galvin, S. A. Grigera, L. Capogna, A. J. Schofield, A. P. Mackenzie, M. Chiao, S. R. Julian, S. I. Ikeda, S. Nakatsuji, Y. Maeno, and C. Pfleiderer. Metamagnetism and Critical Fluctuations in High Quality Single Crystals of the Bilayer Ruthenate $Sr_3Ru_2O_7$. *Physical Review Letters*, 86(12):2661–2664, 2001.

[16] S. A. Grigera, R. S. Perry, A. J. Schofield, M. Chiao, S. R. Julian, G. G. Lonzarich, S. I. Ikeda, Y. Maeno, A. J. Millis, and A. P. Mackenzie. Magnetic field-tuned quantum criticality in the metallic ruthenate $Sr_3Ru_2O_7$. *Science*, 294(5541):329–332, 2001.

[17] S. A. Grigera, P. Gegenwart, R. A. Borzi, F. Weickert, A. J. Schofield, R. S. Perry, T. Tayama, T. Sakakibara, Y. Maeno, A. G. Green, and A. P. Mackenzie. Disorder-Sensitive Phase Formation Linked to Metamagnetic Quantum Criticality. *Science*, 306(5699):1154–1157, 2004.

[18] R. A. Borzi, S. A. Grigera, J. Farrell, R. S. Perry, S. J. S. Lister, S. L. Lee, D. A. Tennant, Y. Maeno, and A. P. Mackenzie. Formation of a nematic fluid at high fields in $Sr_3Ru_2O_7$. *Science*, 315(5809):214–217, 2006.

[19] J. Peng, Z. Qu, B. Qian, D. Fobes, T. Liu, X. Wu, H. M. Pham, L. Spinu, and Z. Q. Mao. Interplay between the lattice and spin degrees of freedom in$(Sr_{1-x}Ca_x)_3Ru_2O_7$. *Physical Review B*, 82(2), 2010.

[20] D. Mesa, F. Ye, S. Chi, J. A. Fernandez-Baca, W. Tian, B. Hu, R. Jin, E. W. Plummer, and J. Zhang. Single-bilayer E -type antiferromagnetism in Mn-substituted $Sr_3Ru_2O_7$: Neutron scattering study. *Physical Review B*, 85(18):180410, 2012.

[21] M. Zhu, Y. Wang, P. G. Li, J. J. Ge, W. Tian, D. Keavney, Z. Q. Mao, and X. Ke. Tipping the magnetic instability in paramagnetic $Sr_3Ru_2O_7$ by Fe impurities. *Physical Review B*, 95(17):174430, 2017.

[22] S.-I. Ikeda, N. Shirakawa, T. Yanagisawa, Y. Yoshida, S. Koikegami, S. Koike, M. Kosaka, and Y. Uwatoko. Uniaxial-pressure induced ferromagnetism of enhanced paramagnetic $Sr_3Ru_2O_7$. *Journal of the Physical Society of Japan*, 73(5):1322–1325, 2004.

[23] E. Ko, B. J. Kim, C. Kim, and H. J. Choi. Strong Orbital-Dependentd-Band Hybridization and Fermi-Surface Reconstruction in Metallic $Ca_{2-x}Sr_xRuO_4$. *Physical Review Letters*, 98(22):226401, 2007.

[24] A. Damascelli, D. H. Lu, K. M. Shen, N. P. Armitage, F. Ronning, D. L. Feng, C. Kim, Z.-X. Shen, T. Kimura, Y. Tokura, Z. Q. Mao, and Y. Maeno. Fermi Surface, Surface States, and Surface Reconstruction in Sr_2RuO_4. *Physical Review Letters*, 85(24):5194, 2000.

[25] R. Matzdorf. Ferromagnetism stabilized by lattice distortion at the surface of the p-wave superconductor Sr_2RuO_4. *Science*, 289(5480):746–748, 2000.

[26] K. M. Shen, A. Damascelli, D. H. Lu, N. P. Armitage, F. Ronning, D. L. Feng, C. Kim, Z.-X. Shen, D. J. Singh, I. I. Mazin, S. Nakatsuji, Z. Q. Mao, Y. Maeno, T. Kimura, and

Y. Tokura. Surface electronic structure of Sr_2RuO_4. *Physical Review B*, 64(18):180502(R), 2001.

[27] C. N. Veenstra, Z.-H. Zhu, B. Ludbrook, M. Capsoni, G. Levy, A. Nicolaou, J. A. Rosen, R. Comin, S. Kittaka, Y. Maeno, I. S. Elfimov, and A. Damascelli. Determining the Surface-To-Bulk Progression in the Normal-State Electronic Structure of Sr_2RuO_4 by Angle-Resolved Photoemission and Density Functional Theory. *Physical Review Letters*, 110(9):097004, 2013.

[28] B. Hu, G. T. McCandless, M. Menard, V. B. Nascimento, J. Y. Chan, E. W. Plummer, and R. Jin. Surface and bulk structural properties of single-crystalline $Sr_3Ru_2O_7$. *Physical Review B*, 81(18):184104, 2010.

[29] Z. Qu, J. Peng, T. Liu, D. Fobes, L. Spinu, and Z. Mao. Complex electronic states in double-layered ruthenates $(Sr_{1-x}Ca_x)_3Ru_2O_7$. *Physical Review B*, 80(11):115130, 2009.

[30] D. O. Brodsky, M. E. Barber, J. A. N. Bruin, R. A. Borzi, S. A. Grigera, R. S. Perry, A. P. Mackenzie, and C. W. Hicks. Strain and vector magnetic field tuning of the anomalous phase in $Sr_3Ru_2O_7$. *Science Advances*, 3(2):e1501804, 2017.

[31] E. Morosan, D. Natelson, A. H. Nevidomskyy, and Q. Si. Strongly Correlated Materials. *Advanced Materials*, 24(36):4896–4923, 2012.

[32] L. D. Landau. On the Theory of Fermi Liquid. In D. Ter Haar, editor, *Collected Papers of L. D. Landau*, pages 752–760. Pergamon, 1965.

[33] A. Damascelli, Z. Hussain, and Z.-X. Shen. Angle-resolved photoemission studies of the cuprate superconductors. *Reviews of Modern Physics*, 75(2):473–541, 2003.

[34] L. D. Landau, E. M. Lifshits, and L. P. Pitaevskii. *Statistical Physics, part 2*. Number pt. 2 in Course of theoretical physics. Butterworth-Heinemann, 1980.

[35] J. Mravlje, M. Aichhorn, T. Miyake, K. Haule, G. Kotliar, and A. Georges. Coherence-incoherence crossover and the mass-renormalization puzzles in Sr_2RuO_4. *Physical Review Letters*, 106(9):096401, 2011.

[36] L. D. Landau and I. Pomeranchuk. On the properties of metals at very low temperatures. *Zhurnal Experimental'noi i Teoreticheskoi Fiziki*, 7:379, 1937.

[37] T. Valla, A. V. Fedorov, P. D. Johnson, B. O. Wells, S. L. Hulbert, Q. Li, G. D. Gu, and N. Koshizuka. Evidence for quantum critical behavior in the optimally doped cuprate $Bi_2Sr_2CaCu_2O_{8+\delta}$. *Science*, 285(5436):2110–2113, 1999.

[38] B. Keimer, S. A. Kivelson, M. R. Norman, S. Uchida, and J. Zaanen. From quantum matter to high-temperature superconductivity in copper oxides. *Nature*, 518(7538):179–186, 2015.

[39] L. Taillefer. Scattering and pairing in cuprate superconductors. *Annual Review of Condensed Matter Physics*, 1(1):51–70, 2010.

[40] H. K. Onnes. Investigations into the properties of substances at low temperatures, which have led, amongst other things, to the preparation of liquid helium. *Nobel lecture*, 4:306–336, 1913.

[41] J. Bardeen, L. N. Cooper, and J. R. Schrieffer. Theory of Superconductivity. *Physical Review*, 108(5):1175–1204, 1957.

[42] J. F. Cochran and D. E. Mapother. Superconducting Transition in Aluminum. *Physical Review*, 111(1):132–142, 1958.

[43] B. T. Matthias, T. H. Geballe, S. Geller, and E. Corenzwit. Superconductivity of Nb_3Sn. *Physical Review*, 95(6):1435–1435, 1954.

[44] A. P. Drozdov, M. I. Eremets, I. A. Troyan, V. Ksenofontov, and S. I. Shylin. Conventional superconductivity at 203 kelvin at high pressures in the sulfur hydride system. *Nature*, 525(7567):73–76, 2015.

[45] M. Somayazulu, M. Ahart, A. K. Mishra, Z. M. Geballe, M.Baldini, Y. Meng, V. V. Struzhkin, and R. J. Hemley. Evidence for Superconductivity above 260 K in Lanthanum Superhydride at Megabar Pressures. *Physical Review Letters*, 122(2):027001, 2019.

[46] H. Ding, M. R. Norman, J. C. Campuzano, M. Randeria, A. F. Bellman, T. Yokoya, T. Takahashi, T. Mochiku, and K. Kadowaki. Angle-resolved photoemission spectroscopy study of the superconducting gap anisotropy in $Bi_2Sr_2CaCu_2O_{8+x}$. *Physical Review B*, 54(14):R9678–R9681, 1996.

[47] J. E. Hoffman, K. McElroy, D.-H. Lee, K. M. Lang, H. Eisaki, S. Uchida, and J. C. Davis. Imaging quasiparticle interference in $Bi_2Sr_2CaCu_2O_{8+\delta}$. *Science*, 297(5584):1148–1151, 2002.

[48] D. J. Scalapino, E. Loh, and J. E. Hirsch. d-wave pairing near a spin-density-wave instability. *Physical Review B*, 34(11):8190–8192, 1986.

[49] T. Dahm, V. Hinkov, S. V. Borisenko, A. A. Kordyuk, V. B. Zabolotnyy, J. Fink, B. Büchner, D. J. Scalapino, W. Hanke, and B. Keimer. Strength of the spin-fluctuation-mediated pairing interaction in a high-temperature superconductor. *Nature Physics*, 5(3):217–221, 2009.

[50] P. W. Anderson, P. A. Lee, M. Randeria, T. M. Rice, N. Trivedi, and F. C. Zhang. The physics behind high-temperature superconducting cuprates: the plain vanilla version of RVB. *Journal of Physics: Condensed Matter*, 16(24):R755–R769, 2004.

[51] M. K. Wu, J. R. Ashburn, C. J. Torng, P. H. Hor, R. L. Meng, L. Gao, Z. J. Huang, Y. Q. Wang, and C. W. Chu. Superconductivity at 93 K in a new mixed-phase Y-Ba-Cu-O compound system at ambient pressure. *Physical Review Letters*, 58(9):908–910, 1987.

[52] A. Schilling, M. Cantoni, J. D. Guo, and H. R. Ott. Superconductivity above 130 K in the Hg–Ba–Ca–Cu–O system. *Nature*, 363(6424):56–58, 1993.

[53] B. Michon, C. Girod, S. Badoux, J. Kačmarčík, Q. Ma, M. Dragomir, H. A. Dabkowska, B. D. Gaulin, J.-S. Zhou, S. Pyon, T. Takayama, H. Takagi, S. Verret, N. Doiron-Leyraud, C. Marcenat, L. Taillefer, and T. Klein. Thermodynamic signatures of quantum criticality in cuprate superconductors. *Nature*, 567(7747):218–222, 2019.

[54] P. J. Hirschfeld. Using gap symmetry and structure to reveal the pairing mechanism in Fe-based superconductors. *Comptes Rendus Physique*, 17(1-2):197–231, 2016.

[55] R. M. Fernandes, A. V. Chubukov, and J. Schmalian. What drives nematic order in iron-based superconductors? *Nature Physics*, 10(2):97–104, 2014.

[56] T. Shibauchi, A. Carrington, and Y. Matsuda. A Quantum Critical Point Lying Beneath the Superconducting Dome in Iron Pnictides. *Annual Review of Condensed Matter Physics*, 5(1):113–135, 2014.

[57] Y. Kamihara, T. Watanabe, M. Hirano, and H. Hosono. Iron-Based Layered Superconductor $La[O_{1-x}F_x]FeAs$ ($x = 0.05 - 0.12$) with T_c= 26 k. *Journal of the American Chemical Society*, 130(11):3296–3297, 2008.

[58] S. Jiang, H. Xing, G. Xuan, C. Wang, Z. Ren, C. Feng, J. Dai, Z. Xu, and G. Cao. Superconductivity up to 30 K in the vicinity of the quantum critical point in $BaFe_2(As_{1-x}P_x)_2$. *Journal of Physics: Condensed Matter*, 21(38):382203, 2009.

[59] G. R. Stewart. Heavy-fermion systems. *Reviews of Modern Physics*, 56(4):755–787, 1984.

[60] T. Park, F. Ronning, H. Q. Yuan, M. B. Salamon, R. Movshovich, J. L. Sarrao, and J. D. Thompson. Hidden magnetism and quantum criticality in the heavy fermion superconductor $CeRhIn_5$. *Nature*, 440(7080):65–68, 2006.

[61] C. Grenzebach, F. B. Anders, G. Czycholl, and T. Pruschke. Transport properties of heavy-fermion systems. *Physical Review B*, 74(19):195119, 2006.

[62] B. D. White, J. D. Thompson, and M. B. Maple. Unconventional superconductivity in heavy-fermion compounds. *Physica C: Superconductivity and its Applications*, 514:246–278, 2015.

[63] H. Hegger, C. Petrovic, E. G. Moshopoulou, M. F. Hundley, J. L. Sarrao, Z. Fisk, and J. D. Thompson. Pressure-Induced Superconductivity in Quasi-2D $CeRhIn_5$. *Physical Review Letters*, 84(21):4986–4989, 2000.

[64] N. D. Mathur, F. M. Grosche, S. R. Julian, I. R. Walker, D. M. Freye, R. K. W. Haselwimmer, and G. G. Lonzarich. Magnetically mediated superconductivity in heavy fermion compounds. *Nature*, 394(6688):39–43, 1998.

[65] F. M. Grosche, I. R. Walker, S. R. Julian, N. D. Mathur, D. M. Freye, M. J. Steiner, and G. G. Lonzarich. Superconductivity on the threshold of magnetism in $CePd_2Si_2$ and $CeIn_3$. *Journal of Physics: Condensed Matter*, 13(12):2845–2860, 2001.

[66] D. J. Scalapino. A common thread: The pairing interaction for unconventional superconductors. *Reviews of Modern Physics*, 84(4):1383–1417, 2012.

[67] A. J. Leggett. A theoretical description of the new phases of liquid ^{3}He. *Reviews of Modern Physics*, 47(2):331–414, 1975.

[68] J. C. Wheatley. Experimental properties of superfluid ^{3}He. *Reviews of Modern Physics*, 47(2):415–470, 1975.

[69] A. M. Gulian and K. S. Wood. Triplet superconductors from the viewpoint of basic elements for quantum computers. *IEEE Transactions on Appiled Superconductivity*, 13(2):944–947, 2003.

[70] A. P. Mackenzie and Y. Maeno. The superconductivity of Sr_2RuO_4 and the physics of spin-triplet pairing. *Reviews of Modern Physics*, 75(2):657–712, 2003.

[71] K. Ishida, H. Mukuda, Y. Kitaoka, K. Asayama, Z. Q. Mao, Y. Mori, and Y. Maeno. Spin-triplet superconductivity in Sr_2RuO_4 identified by ^{17}O knight shift. *Nature*, 396(6712):658–660, 1998.

[72] A. P. Mackenzie, T. Scaffidi, C. W. Hicks, and Y. Maeno. Even odder after twenty-three years: the superconducting order parameter puzzle of Sr_2RuO_4. *npj Quantum Materials*, 2(1):1–9, 2017.

[73] K. Ishida, M. Manago, K. Kinjo, and Y. Maeno. Reduction of the ^{17}O knight shift in the superconducting state and the heat-up effect by NMR pulses on Sr_2RuO_4. *Journal of the Physical Society of Japan*, 89(3):034712, 2020.

[74] H. Tou, Y. Kitaoka, K. Asayama, N. Kimura, Y. Ōnuki, E. Yamamoto, and K. Maezawa. Odd-Parity Superconductivity with Parallel Spin Pairing in UPt_3: Evidence from ^{195}Pt Knight Shift Study. *Physical Review Letters*, 77(7):1374–1377, 1996.

[75] H. Tou, Y. Kitaoka, K. Ishida, K. Asayama, N. Kimura, Y. O¯nuki, E. Yamamoto, Y. Haga, and K. Maezawa. Nonunitary spin-triplet superconductivity in UPt_3: Evidence from ^{195}Pt knight shift study. *Physical Review Letters*, 80(14):3129–3132, 1998.

[76] G. P. Felcher and R. Kleb. Antiferromagnetic domains and the spin-flop transition of MnF_2. *Europhysics Letters*, 36(6):455–460, 1996.

[77] R. Z. Levitin and A. S. Markosyan. Itinerant metamagnetism. *Soviet Physics Uspekhi*, 31(8):730–749, 1988.

[78] T. Goto, K. Fukamichi, T. Sakakibara, and H. Komatsu. Itinerant electron metamagnetism in YCo_2. *Solid State Communications*, 72(9):945–947, 1989.

[79] C. Pfleiderer, G. J. McMullan, S. R. Julian, and G. G. Lonzarich. Magnetic quantum phase transition in MnSi under hydrostatic pressure. *Physical Review B*, 55(13):8330–8338, 1997.

[80] C. Pfleiderer, S. R. Julian, and G. G. Lonzarich. Non-Fermi-liquid nature of the normal state of itinerant-electron ferromagnets. *Nature*, 414(6862):427–430, 2001.

[81] A. McCollam, M. Fu, and S. R. Julian. Lifshitz transition underlying the metamagnetic transition of UPt_3. *Journal of Physics: Condensed Matter*, 33(7):075804, 2020.

[82] H. P. van der Meulen, A. de Visser, J. J. M. Franse, T. T. J. M. Berendschot, J. A. A. J. Perenboom, H. van Kempen, A. Lacerda, P. Lejay, and J. Flouquet. Field suppression of the heavy-fermion state in $CeRu_2Si_2$. *Physical Review B*, 44(2):814–818, 1991.

[83] H. Aoki, S. Uji, A. K. Albessard, and Y. Ōnuki. Transition of f electron nature from itinerant to localized: Metamagnetic transition in $CeRu_2Si_2$ studied via the de Haas-van Alphen effect. *Physical Review Letters*, 71(13):2110–2113, 1993.

[84] S. Blundell. *Magnetism in Condensed Matter*. Oxford Master Series in Condensed Matter Physics. Oxford University Press, 2001.

[85] H. Yamada. Metamagnetic transition and susceptibility maximum in an itinerant-electron system. *Physical Review B*, 47(17):11211–11219, 1993.

[86] D. Meyer and W. Nolting. Strong-coupling scenario of a metamagnetic transition. *Physical Review B*, 64(5):052402, 2001.

[87] H-Y. Kee and Y. B. Kim. Itinerant metamagnetism induced by electronic nematic order. *Physical Review B*, 71(18):184402, 2005.

[88] S. L. Sondhi, S. M. Girvin, J. P. Carini, and D. Shahar. Continuous quantum phase transitions. *Reviews of Modern Physics*, 69(1):315–333, 1997.

[89] H. v. Löhneysen, T. Pietrus, G. Portisch, H. G. Schlager, A. Schröder, M. Sieck, and T. Trappmann. Non-Fermi-liquid behavior in a heavy-fermion alloy at a magnetic instability. *Physical Review Letters*, 72(20):3262–3265, 1994.

[90] S. A. Grigera, A. P. Mackenzie, A. J. Schofield, S. R. Julian, and G. G. Lonzarich. A Metamagnetic Quantum Critical Endpoint in $Sr_3Ru_2O_7$. *International Journal of Modern Physics B*, 16(20n22):3258–3264, 2002.

[91] A. J. Millis, A. J. Schofield, G. G. Lonzarich, and S. A. Grigera. Metamagnetic Quantum Criticality in Metals. *Physical Review Letters*, 88(21):217204, 2002.

[92] W. Wu, A. McCollam, S. A. Grigera, R. S. Perry, A. P. Mackenzie, and S. R. Julian. Quantum critical metamagnetism of $Sr_3Ru_2O_7$ under hydrostatic pressure. *Physical Review B*, 83(4):045106, 2011.

[93] L. Van Hove. The Occurrence of Singularities in the Elastic Frequency Distribution of a Crystal. *Physical Review*, 89(6):1189–1193, 1953.

[94] I. M. Lifshitz. Anomalies of electron characteristics of a metal in the high pressure region. *Soviet Physics JETP*, 11(5):1130–1135, 1960.

[95] D. V. Efremov, A. Shtyk, A. W. Rost, C. Chamon, A. P. Mackenzie, and J. J. Betouras. Multicritical Fermi Surface Topological Transitions. *Physical Review Letters*, 123(20):207202, 2019.

[96] A. Steppke, L. Zhao, M. E. Barber, T. Scaffidi, F. Jerzembeck, H. Rosner, A. S. Gibbs, Y. Maeno, S. H. Simon, A. P. Mackenzie, and C. W. Hicks. Strong peak in T_c of Sr_2RuO_4 under uniaxial pressure. *Science*, 355(6321):eaaf9398, 2017.

[97] G. Li, A. Luican, J. M. B. Lopes dos Santos, A. H. Castro Neto, A. Reina, J. Kong, and E. Y. Andrei. Observation of Van Hove singularities in twisted graphene layers. *Nature Physics*, 6(2):109–113, 2009.

[98] A. Kerelsky, L. J. McGilly, D. M. Kennes, L. Xian, M.Yankowitz, S. Chen, K. Watanabe, T. Taniguchi, J. Hone, C. Dean, A. Rubio, and A. N. Pasupathy. Maximized electron interactions at the magic angle in twisted bilayer graphene. *Nature*, 572(7767):95–100, 2019.

[99] Y. Jiang, X. Lai, K. Watanabe, T. Taniguchi, K. Haule, J. Mao, and E. Y. Andrei. Charge order and broken rotational symmetry in magic-angle twisted bilayer graphene. *Nature*, 573(7772):91–95, 2019.

[100] Y. Xie, B. Lian, B. Jäck, X. Liu, C. L. Chiu, K. Watanabe, T. Taniguchi, B. A. Bernevig, and A. Yazdani. Spectroscopic signatures of many-body correlations in magic-angle twisted bilayer graphene. *Nature*, 572(7767):101–105, 2019.

[101] M. Bercx and F. F. Assaad. Metamagnetism and Lifshitz transitions in models for heavy fermions. *Physical Review B*, 86(7):075108, 2012.

[102] D. Aoki, G. Seyfarth, A. Pourret, A. Gourgout, A. McCollam, J. A. N. Bruin, Y. Krupko, and I. Sheikin. Field-Induced Lifshitz Transition without Metamagnetism in $CeIrIn_5$. *Physical Review Letters*, 116(3):037202, 2016.

[103] R. Daou, C. Bergemann, and S. R. Julian. Continuous Evolution of the Fermi Surface of $CeRu_2Si_2$ across the Metamagnetic Transition. *Physical Review Letters*, 96(2):026401, 2006.

[104] H. R. Naren, S. Friedemann, G. Zwicknagl, C. Krellner, C. Geibel, F. Steglich, and S. Wirth. Lifshitz transitions and quasiparticle de-renormalization in $YbRh_2Si_2$. *New Journal of Physics*, 15(9):093032, 2013.

[105] A. Hackl and M. Vojta. Zeeman-Driven Lifshitz Transition: A Model for the Experimentally Observed Fermi-Surface Reconstruction in $YbRh_2Si_2$. *Physical Review Letters*, 106(13):137002, 2011.

[106] D. Fobes, M. H. Yu, M. Zhou, J. Hooper, C. J. O'Connor, M. Rosario, and Z. Q. Mao. Phase diagram of the electronic states of trilayered ruthenate $Sr_4Ru_3O_{10}$. *Physical Review B*, 75(9):094429, 2007.

[107] A. Callaghan, C. W. Moeller, and R. Ward. Magnetic Interactions in Ternary Ruthenium Oxides. *Inorganic Chemistry*, 5(9):1572–1576, 1966.

[108] B. Dabrowski, M. Avdeev, O. Chmaissem, S. Kolesnik, P. W. Klamut, M. Maxwell, and J. D. Jorgensen. Freezing of octahedral tilts below the Curie temperature in $SrRu_{1-v}O_3$ perovskites. *Physical Review B*, 71(10):104411, 2005.

[109] Y. Maeno, K. Yoshida, H. Hashimoto, S. Nishizaki, S. Ikeda, M. Nohara, T. Fujita, A. P. Mackenzie, N. E. Hussey, J. G. Bednorz, and F. Lichtenberg. Two-Dimensional Fermi Liquid Behavior of the Superconductor Sr_2RuO_4. *Journal of the Physical Society of Japan*, 66(5):1405–1408, 1997.

[110] S.-I. Ikeda, Y. Maeno, S. Nakatsuji, M. Kosaka, and Y. Uwatoko. Ground state in $Sr_3Ru_2O_7$: Fermi liquid close to a ferromagnetic instability. *Physical Review B*, 62(10):R6089–R6092, 2000.

[111] M. Zhou, J. Hooper, D. Fobes, Z. Q. Mao, V. Golub, and C. J. O'Connor. Electronic and magnetic properties of triple-layered ruthenate $Sr_4Ru_3O_{10}$ single crystals grown by a floating-zone method. *Materials Research Bulletin*, 40(6):942–950, 2005.

[112] N. Kikugawa, R. Baumbach, J. S. Brooks, T. Terashima, S. Uji, and Y. Maeno. Single-crystal growth of a perovskite ruthenate $SrRuO_3$ by the Floating-Zone Method. *Crystal Growth & Design*, 15(11):5573–5577, 2015.

[113] F. Lichtenberg, A. Catana, J. Mannhart, and D. G. Schlom. Sr_2RuO_4: A metallic substrate for the epitaxial growth of $YBa_2Cu_3O_{7-\delta}$. *Applied Physics Letters*, 60(9):1138–1140, 1992.

[114] M. Braden, A.H. Moudden, S. Nishizaki, Y. Maeno, and T. Fujita. Structural analysis of Sr_2RuO_4. *Physica C: Superconductivity*, 273(3-4):248–254, 1997.

[115] N. E. Hussey, A. P. Mackenzie, J. R. Cooper, Y. Maeno, S. Nishizaki, and T. Fujita. Normal-state magnetoresistance of Sr_2RuO_4. *Physical Review B*, 57(9):5505–5511, 1998.

[116] Y. Pennec, N. J. C. Ingle, I. S. Elfimov, E. Varene, Y. Maeno, A. Damascelli, and J. V. Barth. Cleaving-Temperature Dependence of Layered-Oxide Surfaces. *Physical Review Letters*, 101(21):216103, 2008.

[117] A. Tamai, M. Zingl, E. Rozbicki, E. Cappelli, S. Riccò, A. de la Torre, S. McKeown Walker, F. Y. Bruno, P. D. C. King, W. Meevasana, M. Shi, M. Radović, N. C. Plumb, A. S. Gibbs, A. P. Mackenzie, C. Berthod, H. U. R. Strand, M. Kim, A. Georges, and F. Baumberger. High-Resolution Photoemission on Sr_2RuO_4 Reveals Correlation-Enhanced Effective Spin-Orbit Coupling and Dominantly Local Self-Energies. *Physical Review X*, 9(2):021048, 2019.

[118] T. Scaffidi, J. C. Romers, and S. H. Simon. Pairing symmetry and dominant band in Sr_2RuO_4. *Physical Review B*, 89(22), 2014.

[119] A. P. Mackenzie, S. R. Julian, A. J. Diver, G. J. McMullan, M. P. Ray, G. G. Lonzarich, Y. Maeno, S. Nishizaki, and T. Fujita. Quantum Oscillations in the Layered Perovskite Superconductor Sr_2RuO_4. *Physical Review Letters*, 76(20):3786–3789, 1996.

[120] K. K. Ng and M. Sigrist. The role of spin-orbit coupling for the superconducting state in Sr_2RuO_4. *Europhysics Letters*, 49(4):473–479, 2000.

[121] H. Kontani, T. Tanaka, D. S. Hirashima, K. Yamada, and J. Inoue. Giant intrinsic spin and orbital Hall effects in Sr_2MO_4 ($m = ru$, rh, mo). *Physical Review Letters*, 100(9):096601, 2008.

[122] V. B. Zabolotnyy, D. V. Evtushinsky, A. A. Kordyuk, T. K. Kim, E. Carleschi, B. P. Doyle, R. Fittipaldi, M. Cuoco, A. Vecchione, and S. V. Borisenko. Renormalized band structure of Sr_2RuO_4: A quasiparticle tight-binding approach. *Journal of Electron Spectroscopy and Related Phenomena*, 191:48–53, 2013.

[123] T. Oguchi. Electronic band structure of the superconductor Sr_2RuO_4. *Physical Review B*, 51(2):1385–1388, 1995.

[124] D. J. Singh. Relationship of Sr_2RuO_4 to the superconducting layered cuprates. *Physical Review B*, 52(2):1358–1361, 1995.

[125] E. J. Rozbicki, J. F. Annett, J. R. Souquet, and A. P. Mackenzie. Spin–orbit coupling and k-dependent Zeeman splitting in strontium ruthenate. *Journal of Physics: Condensed Matter*, 23(9):094201, 2011.

[126] P. K. de Boer and R. A. de Groot. Electronic structure of magnetic Sr_2RuO_4. *Physical Review B*, 59(15):9894–9897, 1999.

[127] T. Mizokawa, L. H. Tjeng, G. A. Sawatzky, G. Ghiringhelli, O. Tjernberg, N. B. Brookes, H. Fukazawa, S. Nakatsuji, and Y. Maeno. Spin-Orbit Coupling in the Mott Insulator Ca_2RuO_4. *Physical Review Letters*, 87(7):077202, 2001.

[128] M. W. Haverkort, I. S. Elfimov, L. H. Tjeng, G. A. Sawatzky, and A. Damascelli. Strong spin-orbit coupling effects on the fermi surface of Sr_2RuO_4 and Sr_2RhO_4. *Physical Review Letters*, 101(2):026406, 2008.

[129] H. Iwasawa, Y. Yoshida, I. Hase, S. Koikegami, H. Hayashi, J. Jiang, K. Shimada, H. Namatame, M. Taniguchi, and Y. Aiura. Interplay among Coulomb Interaction, Spin-Orbit Interaction, and Multiple Electron-Boson Interactions in Sr_2RuO_4. *Physical Review Letters*, 105(22):226406, 2010.

[130] C. N. Veenstra, Z.-H. Zhu, M. Raichle, B. M. Ludbrook, A. Nicolaou, B. Slomski, G. Landolt, S. Kittaka, Y. Maeno, J. H. Dil, I. S. Elfimov, M. W. Haverkort, and A. Damascelli. Spin-Orbital Entanglement and the Breakdown of Singlets and Triplets in Sr_2RuO_4 Revealed by Spin- and Angle-Resolved Photoemission Spectroscopy. *Physical Review Letters*, 112(12):127002, 2014.

[131] C. Bergemann, A. P. Mackenzie, S. R. Julian, D. Forsythe, and E. Ohmichi. Quasi-two-dimensional Fermi liquid properties of the unconventional superconductor Sr_2RuO_4. *Advances in Physics*, 52(7):639–725, 2003.

[132] D. Stricker, J. Mravlje, C. Berthod, R. Fittipaldi, A. Vecchione, A. Georges, and D. van der Marel. Optical Response of Sr_2RuO_4 Reveals Universal Fermi-Liquid Scaling and Quasiparticles Beyond Landau Theory. *Physical Review Letters*, 113(8):087404, 2014.

[133] K. Yoshida, F. Nakamura, T. Goko, T. Fujita, Y. Maeno, Y. Mori, and S. NishiZaki. Electronic crossover in the highly anisotropic normal state of Sr_2RuO_4 from pressure effects on electrical resistivity. *Physical Review B*, 58(22):15062–15066, 1998.

[134] R. H. McKenzie. Wilson's ratio and the spin splitting of magnetic oscillations in quasi-two-dimensional metals. *arXiv:cond-mat/9905044*, 1999. arXiv: cond-mat/9905044.

[135] T. Imai, A. W. Hunt, K. R. Thurber, and F. C. Chou. ^{17}O NMR Evidence for Orbital Dependent Ferromagnetic Correlations in Sr_2RuO_4. *Physical Review Letters*, 81(14):3006–3009, 1998.

[136] Y. Sidis, M. Braden, P. Bourges, B. Hennion, S. NishiZaki, Y. Maeno, and Y. Mori. Evidence for incommensurate spin fluctuations in Sr_2RuO_4. *Physical Review Letters*, 83(16):3320–3323, 1999.

[137] F. Servant, B. Fåk, S. Raymond, J. P. Brison, P. Lejay, and J. Flouquet. Magnetic excitations in the normal and superconducting states of Sr_2RuO_4. *Physical Review B*, 65(18):184511, 2002.

[138] P. Steffens, Y. Sidis, J. Kulda, Z. Q. Mao, Y. Maeno, I. I. Mazin, and M. Braden. Spin Fluctuations in Sr_2RuO_4 from Polarized Neutron Scattering: Implications for Superconductivity. *Physical Review Letters*, 122(4):047004, 2019.

[139] Z. Q. Mao, Y. Mori, and Y. Maeno. Suppression of superconductivity in Sr_2RuO_4 caused by defects. *Physical Review B*, 60(1):610–614, 1999.

[140] N. Kikugawa, A. P. Mackenzie, C. Bergemann, R. A. Borzi, S. A. Grigera, and Y. Maeno. Rigid-band shift of the Fermi level in the strongly correlated metal: $Sr_{2-y}La_yRuO_4$. *Physical Review B*, 70(6):060508(R), 2004.

[141] J. A. Duffy, S. M. Hayden, Y. Maeno, Z. Mao, J. Kulda, and G. J. McIntyre. Polarized-Neutron Scattering Study of the Cooper-Pair Moment in Sr_2RuO_4. *Physical Review Letters*, 85(25):5412–5415, 2000.

[142] G. M. Luke, Y. Fudamoto, K. M. Kojima, M. I. Larkin, J. Merrin, B. Nachumi, Y. J. Uemura, Y. Maeno, Z. Q. Mao, Y. Mori, H. Nakamura, and M. Sigrist. Time-reversal symmetry-breaking superconductivity in Sr_2RuO_4. *Nature*, 394(6693):558–561, 1998.

[143] J. Xia, Y Maeno, P. T. Beyersdorf, M. M. Fejer, and A. Kapitulnik. High Resolution Polar Kerr Effect Measurements of Sr_2RuO_4: Evidence for Broken Time-Reversal Symmetry in the Superconducting State. *Physical Review Letters*, 97(16):167002, 2006.

[144] C. Lupien, W. MacFarlane, Cyril Proust, Louis Taillefer, Z. Mao, and Y. Maeno. Ultrasound Attenuation in Sr_2RuO_4: An Angle-Resolved Study of the Superconducting Gap Function. *Physical Review Letters*, 86(26):5986–5989, 2001.

[145] E. Hassinger, P. Bourgeois-Hope, H. Taniguchi, S. René de Cotret, G. Grissonnanche, M. S. Anwar, Y. Maeno, N. Doiron-Leyraud, and L. Taillefer. Vertical Line Nodes in the Superconducting Gap Structure of Sr_2RuO_4. *Physical Review X*, 7(1):011032, 2017.

[146] K. Deguchi, Z. Q. Mao, H. Yaguchi, and Y. Maeno. Gap Structure of the Spin-Triplet Superconductor Sr_2RuO_4 Determined from the Field-Orientation Dependence of the Specific Heat. *Physical Review Letters*, 92(4):047002, 2004.

[147] S. Kittaka, S. Nakamura, T. Sakakibara, N. Kikugawa, T. Terashima, S. Uji, D. A. Sokolov, A. P. Mackenzie, K. Irie, Y. Tsutsumi, K. Suzuki, and K. Machida. Searching for Gap Zeros in Sr_2RuO_4 via Field-Angle-Dependent Specific-Heat Measurement. *Journal of the Physical Society of Japan*, 87(9):093703, 2018.

[148] P. G. Björnsson, Y. Maeno, M. E. Huber, and K. A. Moler. Scanning magnetic imaging of Sr_2RuO_4. *Physical Review B*, 72(1):012504, 2005.

[149] C. W. Hicks, J. R. Kirtley, T. M. Lippman, N. C. Koshnick, M. E. Huber, Y. Maeno, W. M. Yuhasz, M. Brian Maple, and K. A. Moler. Limits on superconductivity-related magnetization in Sr_2RuO_4 and $PrOs_4Sb_{12}$ from scanning SQUID microscopy. *Physical Review B*, 81(21):214501, 2010.

[150] C. A. Watson, A. S. Gibbs, A. P. Mackenzie, C. W. Hicks, and K. A. Moler. Micron-scale measurements of low anisotropic strain response of local T_c in Sr_2RuO_4. *Physical Review B*, 98(9):094521, 2018.

[151] C. W. Hicks, D. O. Brodsky, E. A. Yelland, A. S. Gibbs, J. A. N. Bruin, M. E. Barber, S. D. Edkins, K. Nishimura, S. Yonezawa, Y. Maeno, and A. P. Mackenzie. Strong Increase of T_c of Sr_2RuO_4 Under Both Tensile and Compressive Strain. *Science*, 344(6181):283–285, 2014.

[152] A. Chronister, A. Pustogow, N. Kikugawa, D. A. Sokolov, F. Jerzembeck, C. W. Hicks, A. P. Mackenzie, E. D. Bauer, and S. E. Brown. Evidence for even parity unconventional superconductivity in Sr_2RuO_4. *Proceedings of the National Academy of Sciences*, 118(25):e2025313118, 2021.

[153] A. N. Petsch, M. Zhu, Mechthild Enderle, Z. Q. Mao, Y. Maeno, I. I. Mazin, and S. M. Hayden. Reduction of the Spin Susceptibility in the Superconducting State of Sr_2RuO_4 Observed by Polarized Neutron Scattering. *Physical Review Letters*, 125(21):217004, 2020.

[154] S. Ghosh, A. Shekhter, F. Jerzembeck, N. Kikugawa, D. A. Sokolov, M. Brando, A. P. Mackenzie, C. W. Hicks, and B. J. Ramshaw. Thermodynamic evidence for a two-component superconducting order parameter in Sr_2RuO_4. *Nature Physics*, 17(2):199–204, 2020.

[155] S. Benhabib, C. Lupien, I. Paul, L. Berges, M. Dion, M. Nardone, A. Zitouni, Z. Q. Mao, Y. Maeno, A. Georges, L. Taillefer, and C. Proust. Ultrasound evidence for a two-component superconducting order parameter in Sr_2RuO_4. *Nature Physics*, 17(2):194–198, 2020.

[156] Y.-S. Li, N. Kikugawa, D. A. Sokolov, F. Jerzembeck, A. S. Gibbs, Y. Maeno, C. W. Hicks, J. Schmalian, M. Nicklas, and A. P. Mackenzie. High-sensitivity heat-capacity measurements on Sr_2RuO_4 under uniaxial pressure. *Proceedings of the National Academy of Sciences*, 118(10):e2020492118, 2021.

[157] V. Grinenko, D. Das, R. Gupta, B. Zinkl, N. Kikugawa, Y. Maeno, C. W. Hicks, H.-H. Klauss, M. Sigrist, and R. Khasanov. Unsplit superconducting and time reversal symmetry breaking transitions in Sr_2RuO_4 under hydrostatic pressure and disorder. *Nature Communications*, 12(1):3920, 2021.

[158] B. I. Barker, S. K. Dutta, C. Lupien, P. L. McEuen, N. Kikugawa, Y. Maeno, and J. C. Davis. STM studies of individual Ti impurity atoms in Sr_2RuO_4. *Physica B: Condensed Matter*, 329-333:1334–1335, 2003.

[159] C. Lupien, S. K. Dutta, B. I. Barker, Y. Maeno, and J. C. Davis. mK-STM Studies of the Temperature- and Field-dependence of the Quasiparticle Spectrum of Sr_2RuO_4. *arXiv:cond-mat/0503317*, 2005.

[160] H. Kambara, Y. Niimi, K. Takizawa, H. Yaguchi, Y. Maeno, and H. Fukuyama. Scanning tunneling microscopy and spectroscopy of Sr_2RuO_4. *AIP Conference Proceedings*, 850(1):539–540, 2006.

[161] C. A. Marques, L. C. Rhodes, R. Fittipaldi, V. Granata, C. M. Yim, R. Buzio, A. Gerbi, A. Vecchione, A. W. Rost, and P. Wahl. Magnetic-Field Tunable Intertwined Checkerboard Charge Order and Nematicity in the Surface Layer of Sr_2RuO_4. *Advanced Materials*, 33(32):2100593, 2021.

[162] I. A. Firmo, S. Lederer, C. Lupien, A. P. Mackenzie, J. C. Davis, and S. A. Kivelson. Evidence from tunneling spectroscopy for a quasi-one-dimensional origin of superconductivity in Sr_2RuO_4. *Physical Review B*, 88(13):134521, 2013.

[163] M. D. Upward, L. P. Kouwenhoven, A. F. Morpurgo, N. Kikugawa, Z. Q. Mao, and Y. Maeno. Direct observation of the superconducting gap of Sr_2RuO_4. *Physical Review B*, 65(22):220512(R), 2002.

[164] H. Suderow, V. Crespo, I. Guillamon, S. Vieira, F. Servant, P. Lejay, J. P. Brison, and J. Flouquet. A nodeless superconducting gap in Sr_2RuO_4 from tunneling spectroscopy. *New Journal of Physics*, 11(9):093004, 2009.

[165] R. Sharma, S. D. Edkins, Z. Wang, A. Kostin, C. Sow, Y. Maeno, A. P. Mackenzie, J. C. S. Davis, and V. Madhavan. Momentum-resolved superconducting energy gaps of Sr_2RuO_4 from quasiparticle interference imaging. *Proceedings of the National Academy of Sciences*, 117(10):5222–5227, 2020.

[166] S. Nakatsuji and Y. Maeno. Switching of magnetic coupling by a structural symmetry change near the mott transition in $Ca_{2-x}Sr_xRuO_4$. *Physical Review B*, 62(10):6458–6466, 2000.

[167] O. Friedt, M. Braden, G. André, P. Adelmann, S. Nakatsuji, and Y. Maeno. Structural and magnetic aspects of the metal-insulator transition in $Ca_{2-x}Sr_xRuO_4$. *Physical Review B*, 63(17):174432, 2001.

[168] Z. Fang and K. Terakura. Magnetic phase diagram of $Ca_{2-x}Sr_xRuO_4$ governed by structural distortions. *Physical Review B*, 64(2):020509(R), 2001.

[169] S. Nakatsuji, D. Hall, L. Balicas, Z. Fisk, K. Sugahara, M. Yoshioka, and Y. Maeno. Heavy-Mass Fermi Liquid near a Ferromagnetic Instability in Layered Ruthenates. *Physical Review Letters*, 90(13):137202, 2003.

[170] N. Kikugawa, C. Bergemann, A. P. Mackenzie, and Y. Maeno. Band-selective modification of the magnetic fluctuations in Sr_2RuO_4: A study of substitution effects. *Physical Review B*, 70(13):134520, 2004.

[171] H. Taniguchi, K. Nishimura, S. K. Goh, S. Yonezawa, and Y. Maeno. Higher-T_c Superconducting Phase in Sr_2RuO_4 Induced by In-Plane Uniaxial Pressure. *Journal of the Physical Society of Japan*, 84(1):014707, 2015.

[172] M. E. Barber, A. S. Gibbs, Y. Maeno, A. P. Mackenzie, and C. W. Hicks. Resistivity in the Vicinity of a van Hove Singularity: Sr_2RuO_4 under Uniaxial Pressure. *Physical Review Letters*, 120(7):076602, 2018.

[173] B. Burganov, C. Adamo, A. Mulder, M. Uchida, P. D. C. King, J. W. Harter, D. E. Shai, A. S. Gibbs, A. P. Mackenzie, R. Uecker, M. Bruetzam, M. R. Beasley, C. J. Fennie, D. G. Schlom, and K. M. Shen. Strain Control of Fermiology and Many-Body Interactions in Two-Dimensional Ruthenates. *Physical Review Letters*, 116(19):197003, 2016.

[174] M. Braden, W. Reichardt, S. Nishizaki, Y. Mori, and Y. Maeno. Structural stability of Sr_2RuO_4. *Physical Review B*, 57(2):1236, 1998.

[175] M. Braden, W. Reichardt, Y. Sidis, Z. Mao, and Y. Maeno. Lattice dynamics and electron-phonon coupling in Sr_2RuO_4: Inelastic neutron scattering and shell-model calculations. *Physical Review B*, 76(1):014505, 2007.

[176] R. Matzdorf, Ismail, T. Kimura, Y. Tokura, and E. W. Plummer. Surface structural analysis of the layered perovskite Sr_2RuO_4 by LEED *I(V)*. *Physical Review B*, 65(8):085404, 2002.

[177] T. Kondo, M. Ochi, M. Nakayama, H. Taniguchi, S. Akebi, K. Kuroda, M. Arita, S. Sakai, H. Namatame, M. Taniguchi, Y. Maeno, R. Arita, and S. Shin. Orbital-Dependent Band Narrowing Revealed in an Extremely Correlated Hund's Metal Emerging on the Topmost Layer of Sr_2RuO_4. *Physical Review Letters*, 117(24):247001, 2016.

[178] S. Akebi, T. Kondo, M. Nakayama, K. Kuroda, S. Kunisada, H. Taniguchi, Y. Maeno, and S. Shin. Low-energy electron-mode couplings in the surface bands of Sr_2RuO_4 re-

vealed by laser-based angle-resolved photoemission spectroscopy. *Physical Review B*, 99(8):081108(R), 2019.

[179] Z. Wang, D. Walkup, P. Derry, T. Scaffidi, M. Rak, S. Vig, A. Kogar, I. Zeljkovic, A. Husain, L. H. Santos, Y. Wang, A. Damascelli, Y. Maeno, P. Abbamonte, E. Fradkin, and V. Madhavan. Quasiparticle interference and strong electron–mode coupling in the quasi-one-dimensional bands of Sr_2RuO_4. *Nature Physics*, 13(8):799–805, 2017.

[180] R. Kiyanagi, K. Tsuda, N. Aso, Hiroyuki K., Y. Noda, Y. Yoshida, S.-I. Ikeda, and Y. Uwatoko. Investigation of the Structure of Single Crystal $Sr_3Ru_2O_7$ by Neutron and Convergent Beam Electron Diffractions. *Journal of the Physical Society of Japan*, 73(3):639–642, 2004.

[181] H. Shaked, J.D. Jorgensen, O. Chmaissem, S. Ikeda, and Y. Maeno. Neutron diffraction study of the structural distortions in $Sr_3Ru_2O_7$. *Journal of Solid State Chemistry*, 154(2):361–367, 2000.

[182] J.-F. Mercure, A. W. Rost, E. C. T. O'Farrell, S. K. Goh, R. S. Perry, M. L. Sutherland, S. A. Grigera, R. A. Borzi, P. Gegenwart, A. S. Gibbs, and A. P. Mackenzie. Quantum oscillations near the metamagnetic transition in $Sr_3Ru_2O_7$. *Physical Review B*, 81(23):235103, 2010.

[183] A. Tamai, M. P. Allan, J. F. Mercure, W. Meevasana, R. Dunkel, D. H. Lu, R. S. Perry, A. P. Mackenzie, D. J. Singh, Z.-X. Shen, and F. Baumberger. Fermi surface and van hove singularities in the itinerant metamagnet $Sr_3Ru_2O_7$. *Physical Review Letters*, 101(2):026407, 2008.

[184] R. A. Borzi, S. A. Grigera, R. S. Perry, N. Kikugawa, K. Kitagawa, Y. Maeno, and A. P. Mackenzie. de Haas–van Alphen Effect Across the Metamagnetic Transition in $Sr_3Ru_2O_7$. *Physical Review Letters*, 92(21):216403, 2004.

[185] M. P. Allan, A. Tamai, E. Rozbicki, M. H. Fischer, J. Voss, P. D. C. King, W. Meevasana, S. Thirupathaiah, E. Rienks, J. Fink, D. A. Tennant, R. S. Perry, J. F. Mercure, M. A. Wang, J. Lee, C. J. Fennie, E.-A. Kim, M. J. Lawler, K. M. Shen, A. P. Mackenzie, Z.-X. Shen, and F. Baumberger. Formation of heavy d-electron quasiparticles in $Sr_3Ru_2O_7$. *New Journal of Physics*, 15(6):063029, 2013.

[186] D. J. Singh and I. I. Mazin. Electronic structure and magnetism of $Sr_3Ru_2O_7$. *Physical Review B*, 63(16):165101, 2001.

[187] M. P. Allan. *The electronic structure of the nematic materials $Sr_3Ru_2O_7$ and Ca $(Co_xFe_{1-x})_2As_2$*. PhD thesis, University of St Andrews, 2010.

[188] S. A. Grigera, R. A. Borzi, A. P. Mackenzie, S. R. Julian, R. S. Perry, and Y. Maeno. Angular dependence of the magnetic susceptibility in the itinerant metamagnet $Sr_3Ru_2O_7$. *Physical Review B*, 67(21):214427, 2003.

[189] R. S. Perry, K. Kitagawa, S. A. Grigera, R. A. Borzi, A. P. Mackenzie, K. Ishida, and Y. Maeno. Multiple first-order metamagnetic transitions and quantum oscillations in ultrapure $Sr_3Ru_2O_7$. *Physical Review Letters*, 92(16):166602, 2004.

[190] C. Lester, S. Ramos, R. S. Perry, T. P. Croft, R. I. Bewley, T. Guidi, P. Manuel, D. D. Khalyavin, E. M. Forgan, and S. M. Hayden. Field-tunable spin-density-wave phases in $Sr_3Ru_2O_7$. *Nature Materials*, 14(4):373–378, 2015.

[191] Y. Tokiwa, M. Mchalwat, R. S. Perry, and P. Gegenwart. Multiple metamagnetic quantum criticality in $Sr_3Ru_2O_7$. *Physical Review Letters*, 116(22):226402, 2016.

[192] D. Sun, A. W. Rost, R. S. Perry, A. P. Mackenzie, and M. Brando. Low temperature thermodynamic investigation of the phase diagram of $Sr_3Ru_2O_7$. *Physical Review B*, 97(11):115101, 2018.

[193] J. A. N. Bruin, R. A. Borzi, S. A. Grigera, A. W. Rost, R. S. Perry, and A. P. Mackenzie. Study of the electronic nematic phase of $Sr_3Ru_2O_7$ with precise control of the applied magnetic field vector. *Physical Review B*, 87(16):161106, 2013.

[194] P. Gegenwart, F. Weickert, R. S. Perry, and Y. Maeno. Low-temperature magnetostriction of $Sr_3Ru_2O_7$. *Physica B: Condensed Matter*, 378-380:117–118, 2006.

[195] C. Stingl, R. S. Perry, Y. Maeno, and P. Gegenwart. Anisotropy of the low-temperature magnetostriction of $Sr_3Ru_2O_7$. *physica status solidi (b)*, 247(3):574–576, 2010.

[196] F. Obermair, C. Pfleiderer, P. Raychaudhuri, R. S. Perry, and Y. Maeno. Magnetic field dependence of the specific heat of $Sr_3Ru_2O_7$. *Physica B: Condensed Matter*, 359-361:1273–1275, 2005.

[197] A. W. Rost, R. S. Perry, J.-F. Mercure, A. P. Mackenzie, and S. A. Grigera. Entropy Landscape of Phase Formation Associated with Quantum Criticality in $Sr_3Ru_2O_7$. *Science*, 325(5946):1360–1363, 2009.

[198] A. W. Rost, S. A. Grigera, J. A. N. Bruin, R. S. Perry, D. Tian, S. Raghu, S. A. Kivelson, and A. P. Mackenzie. Thermodynamics of phase formation in the quantum critical metal $Sr_3Ru_2O_7$. *Proceedings of the National Academy of Sciences*, 108(40):16549–16553, 2011.

[199] L. Capogna, E. M. Forgan, S. M. Hayden, A. Wildes, J. A. Duffy, A. P. Mackenzie, R. S. Perry, S. Ikeda, Y. Maeno, and S. P. Brown. Observation of two-dimensional spin fluctuations in the bilayer ruthenate $Sr_3Ru_2O_7$ by inelastic neutron scattering. *Physical Review B*, 67(1):012504, 2003.

[200] S. Ramos, E.M. Forgan, C. Bowell, S.M. Hayden, A.J. Schofield, A. Wildes, E.A. Yelland, S.P. Brown, M. Laver, R.S. Perry, and Y. Maeno. Spin dynamics in near the metamagnetic transition by inelastic neutron scattering. *Physica B: Condensed Matter*, 403(5-9):1270–1272, 2008.

[201] P. Rivero, V. Meunier, and W. Shelton. Half-metallic ferromagnetism in $Sr_3Ru_2O_7$. *Physical Review B*, 95(19):195106, 2017.

[202] A. Putatunda, G. Qin, W. Ren, and D. J. Singh. Competing magnetic orders in quantum critical $Sr_3Ru_2O_7$. *Physical Review B*, 102(1):014442, 2020.

[203] A. M. Berridge, A. G. Green, S. A. Grigera, and B. D. Simons. Inhomogeneous Magnetic Phases: A Fulde-Ferrell-Larkin-Ovchinnikov-Like Phase in $Sr_3Ru_2O_7$. *Physical Review Letters*, 102(13):136404, 2009.

[204] A. M. Berridge, S. A. Grigera, B. D. Simons, and A. G. Green. Magnetic analog of the Fulde-Ferrell-Larkin-Ovchinnikov phase in $Sr_3Ru_2O_7$. *Physical Review B*, 81(5):054429, 2010.

[205] C. M. Puetter, J. G. Rau, and H.-Y. Kee. Microscopic route to nematicity in $Sr_3Ru_2O_7$. *Physical Review B*, 81(8):081105(R), 2010.

[206] C. H. Mousatov, E. Berg, and S. A. Hartnoll. Theory of the strange metal $Sr_3Ru_2O_7$. *Proceedings of the National Academy of Sciences*, 117(6):2852–2857, 2020.

[207] W.-C. Lee and C. Wu. Theory of unconventional metamagnetic electron states in orbital band systems. *Physical Review B*, 80(10):104438, 2009.

[208] S. Raghu, A. Paramekanti, E. A. Kim, R. A. Borzi, S. A. Grigera, A. P. Mackenzie, and S. A. Kivelson. Microscopic theory of the nematic phase in $Sr_3Ru_2O_7$. *Physical Review B*, 79(21):214402, 2009.

[209] W.-C. Lee, D. P. Arovas, and C. Wu. Quasiparticle interference in the unconventional metamagnetic compound $Sr_3Ru_2O_7$. *Physical Review B*, 81(18):184403, 2010.

[210] J. Lee, M. P. Allan, M. A. Wang, J. Farrell, S. A. Grigera, F. Baumberger, J. C. Davis, and A. P. Mackenzie. Heavy d-electron quasiparticle interference and real-space electronic structure of $Sr_3Ru_2O_7$. *Nature Physics*, 5(11):800–804, 2009.

[211] M. Behrmann, C. Piefke, and F. Lechermann. Multiorbital physics in Fermi liquids prone to magnetic order. *Physical Review B*, 86(4):045130, 2012.

[212] K. Iwaya, S. Satow, T. Hanaguri, N. Shannon, Y. Yoshida, S. I. Ikeda, J. P. He, Y. Kaneko, Y. Tokura, T. Yamada, and H. Takagi. Local tunneling spectroscopy across a metamagnetic critical point in the bilayer ruthenate $Sr_3Ru_2O_7$. *Physical Review Letters*, 99(5):057208, 2007.

[213] B. Hu, G. T. McCandless, V. O. Garlea, S. Stadler, Y. Xiong, J. Y. Chan, E. W. Plummer, and R. Jin. Structure-property coupling in $Sr_3(Ru_{1-x}Mn_x)_2O_7$. *Physical Review B*, 84(17):174411, 2011.

[214] R. Mathieu, A. Asamitsu, Y. Kaneko, J. P. He, X. Z. Yu, R. Kumai, Y. Onose, N. Takeshita, T. Arima, H. Takagi, and Y. Tokura. Impurity-induced transition to a Mott insulator in $Sr_3Ru_2O_7$. *Physical Review B*, 72(9):092404, 2005.

[215] M. A. Hossain, B. Bohnenbuck, Y. D. Chuang, M. W. Haverkort, I. S. Elfimov, A. Tanaka, A. G. Cruz Gonzalez, Z. Hu, H.-J. Lin, C. T. Chen, R. Mathieu, Y. Tokura, Y. Yoshida, L. H. Tjeng, Z. Hussain, B. Keimer, G. A. Sawatzky, and A. Damascelli. Mott versus Slater-type metal-insulator transition in Mn-substituted $Sr_3Ru_2O_7$. *Physical Review B*, 86(4):041102, 2012.

[216] C. Julian Chen. *Introduction to Scanning Tunneling Microscopy*. Oxford University Press, 2007.

[217] B. Voigtländer. *Scanning Probe Microscopy*. Springer Berlin Heidelberg, 2015.

[218] G. Binnig, H. Rohrer, Ch. Gerber, and E. Weibel. Tunneling through a controllable vacuum gap. *Applied Physics Letters*, 40(2):178–180, 1982.

[219] P. K. Hansma and J. Tersoff. Scanning tunneling microscopy. *Journal of Applied Physics*, 61(2):R1–R24, 1987.

[220] R. Young, J. Ward, and F. Scire. The Topografiner: An Instrument for Measuring Surface Microtopography. *Review of Scientific Instruments*, 43(7):999–1011, 1972.

[221] G. Binnig, H. Rohrer, Ch. Gerber, and E. Weibel. Surface Studies by Scanning Tunneling Microscopy. *Physical Review Letters*, 49(1):57–61, 1982.

[222] G. Binnig, H. Rohrer, Ch. Gerber, and E. Weibel. 7×7 reconstruction on Si (111) resolved in real space. *Physical Review Letters*, 50(2):120–123, 1983.

[223] D. M. Eigler and E. K. Schweizer. Positioning single atoms with a scanning tunnelling microscope. *Nature*, 344(6266):524–526, 1990.

[224] F. E. Kalff, M. P. Rebergen, E. Fahrenfort, J. Girovsky, R. Toskovic, J. L. Lado, J. Fernández-Rossier, and A. F. Otte. A kilobyte rewritable atomic memory. *Nature Nanotechnology*, 11(11):926–929, 2016.

[225] M. F. Crommie, C. P. Lutz, and D. M. Eigler. Confinement of Electrons to Quantum Corrals on a Metal Surface. *Science*, 262(5131):218–220, 1993.

[226] M. F. Crommie, C. P. Lutz, and D. M. Eigler. Imaging standing waves in a two-dimensional electron gas. *Nature*, 363(6429):524–527, 1993.

[227] Y. Hasegawa and Ph. Avouris. Direct observation of standing wave formation at surface steps using scanning tunneling spectroscopy. *Physical Review Letters*, 71(7):1071–1074, 1993.

[228] P. T. Sprunger, L. Petersen, E. W. Plummer, E. Lægsgaard, and F. Besenbacher. Giant Friedel Oscillations on the Beryllium(0001) Surface. *Science*, 275(5307):1764–1767, 1997.

[229] P. O. Sprau, A. Kostin, A. Kreisel, A. E. Böhmer, V. Taufour, P. C. Canfield, S. Mukherjee, P. J. Hirschfeld, B. M. Andersen, and J. C. Séamus Davis. Discovery of orbital-selective cooper pairing in FeSe. *Science*, 357(6346):75–80, 2017.

[230] V. Madhavan, W. Chen, T. Jamneala, M. F. Crommie, and Ned S. Wingreen. Local spectroscopy of a Kondo impurity: Co on Au(111). *Physical Review B*, 64(16):165412, 2001.

[231] Y. H. Zhang, S. Kahle, T. Herden, C. Stroh, M. Mayor, U. Schlickum, M. Ternes, P. Wahl, and K. Kern. Temperature and magnetic field dependence of a kondo system in the weak coupling regime. *Nature Communications*, 4(1):2110, 2013.

[232] M. Enayat. *Construction and Operation of a milli-Kelvin Spectroscopic Imaging STM for the study of correlated electron materials*. PhD thesis, École Polytechnique Fédérale de Lausanne, May 2014.

[233] N. Romming, A. Kubetzka, C. Hanneken, K. von Bergmann, and R. Wiesendanger. Field-Dependent Size and Shape of Single Magnetic Skyrmions. *Physical Review Letters*, 114(17):177203, 2015.

[234] J. Bardeen. Tunnelling from a Many-Particle Point of View. *Physical Review Letters*, 6(2):57–59, 1961.

[235] J. Tersoff and D. R. Hamann. Theory of the scanning tunneling microscope. *Physical Review B*, 31(2):805–813, 1985.

[236] N. D. Lang. Spectroscopy of single atoms in the scanning tunneling microscope. *Physical Review B*, 34(8):5947–5950, 1986.

[237] R. M. Feenstra, J. A. Stroscio, and A. P. Fein. Tunneling spectroscopy of the Si(111)2×1 surface. *Surface Science*, 181(1-2):295–306, 1987.

[238] S. K. Khanna and J. Lambe. Inelastic Electron Tunneling Spectroscopy. *Science*, 220(4604):1345–1351, 1983.

[239] U. R. Singh, M. Enayat, S. C. White, and P. Wahl. Construction and performance of a dilution-refrigerator based spectroscopic-imaging scanning tunneling microscope. *Review of Scientific Instruments*, 84(1):013708, 2013.

[240] L. Petersen, Ph. Hofmann, E. W. Plummer, and F. Besenbacher. Fourier transform–STM: determining the surface Fermi contour. *Journal of Electron Spectroscopy and Related Phenomena*, 109(1-2):97–115, 2000.

[241] J. E. Hoffman. Spectroscopic scanning tunneling microscopy insights into Fe-based superconductors. *Reports on Progress in Physics*, 74(12):124513, 2011.

[242] A. J. Macdonald, Y.-S. Tremblay-Johnston, S. Grothe, S. Chi, P. Dosanjh, S. Johnston, and S. A. Burke. Dispersing artifacts in FT-STS: a comparison of set point effects across acquisition modes. *Nanotechnology*, 27(41):414004, 2016.

[243] T. Hanaguri, Y. Kohsaka, J. C. Davis, C. Lupien, I. Yamada, M. Azuma, M. Takano, K. Ohishi, M. Ono, and H. Takagi. Quasiparticle interference and superconducting gap in $Ca_{2-x}Na_xCuO_2Cl_2$. *Nature Physics*, 3(12):865–871, 2007.

[244] M. P. Allan, A. W. Rost, A. P. Mackenzie, Y. Xie, J. C. Davis, K. Kihou, C. H. Lee, A. Iyo, H. Eisaki, and T.-M. Chuang. Anisotropic energy gaps of iron-based superconductivity from intraband quasiparticle interference in LiFeAs. *Science*, 336(6081):563–567, 2012.

[245] H. Inoue, A. Gyenis, Z. Wang, J. Li, S. Woo Oh, S. Jiang, N. Ni, B. Andrei Bernevig, and A. Yazdani. Quasiparticle interference of the Fermi arcs and surface-bulk connectivity of a Weyl semimetal. *Science*, 351(6278):1184–1187, 2016.

[246] Z. Zhu, T. R. Chang, C. Y. Huang, H. Pan, X. A. Nie, X. Z. Wang, Z. T. Jin, S. Y. Xu, S. M. Huang, D. Guan, S. Wang, Y. Li, C. Liu, D. Qian, W. Ku, F. Song, H. Lin, H. Zheng, and J.-F. Jia. Quasiparticle interference and nonsymmorphic effect on a floating band surface state of ZrSiSe. *Nature Communications*, 9(1):4153, 2018.

[247] L. Petersen, P. Laitenberger, E. Lægsgaard, and F. Besenbacher. Screening waves from steps and defects on Cu(111) and Au(111) imaged with STM: Contribution from bulk electrons. *Physical Review B*, 58(11):7361–7366, 1998.

[248] A. Weismann, M. Wenderoth, S. Lounis, P. Zahn, N. Quaas, R. G. Ulbrich, P. H. Dederichs, and S. Blugel. Seeing the Fermi Surface in Real Space by Nanoscale Electron Focusing. *Science*, 323(5918):1190–1193, 2009.

[249] S. Lounis, P. Zahn, A. Weismann, M. Wenderoth, R. G. Ulbrich, I. Mertig, P. H. Dederichs, and S. Blügel. Theory of real space imaging of fermi surface parts. *Physical Review B*, 83(3):035427, 2011.

[250] T. Hanaguri, K. Iwaya, Y. Kohsaka, T. Machida, T. Watashige, S. Kasahara, T. Shibauchi, and Y. Matsuda. Two distinct superconducting pairing states divided by the nematic end point in $FeSe_{1-x}S_x$. *Science Advances*, 4(5):eaar6419, 2018.

[251] L. C. Rhodes, M. D. Watson, T. K. Kim, and M. Eschrig. k_z selective scattering within quasiparticle interference measurements of FeSe. *Physical Review Letters*, 123(21):216404, 2019.

[252] C. A. Marques, M. S. Bahramy, C. Trainer, I. Marković, M. D. Watson, F. Mazzola, A. Rajan, T. D. Raub, P. D. C. King, and P. Wahl. Tomographic mapping of the hidden dimension in quasi-particle interference. *Nature communications*, 12(1):1–8, 2021.

[253] Y. Hasegawa and Ph. Avouris. Manipulation of the Reconstruction of the Au(111) Surface with the STM. *Science*, 258(5089):1763–1765, 1992.

[254] R. G. Moore, V. B. Nascimento, Jiandi Zhang, J. Rundgren, R. Jin, D. Mandrus, and E. W. Plummer. Manifestations of Broken Symmetry: The Surface Phases of $Ca_{2-x}Sr_xRuO_4$. *Physical Review Letters*, 100(6):066102, 2008.

[255] C. Trainer, C. M. Yim, M. McLaren, and P. Wahl. Cryogenic STM in 3D vector magnetic fields realized through a rotatable insert. *Review of scientific instruments*, 88(9):093705, 2017.

[256] C. M. Yim, C. Trainer, R. Aluru, S. Chi, W. N. Hardy, R. Liang, D. Bonn, and P. Wahl. Discovery of a strain-stabilised smectic electronic order in LiFeAs. *Nature Communications*, 9(1):2602, 2018.

[257] C. Enss and S. Hunklinger. *Low-Temperature Physics*. SpringerLink: Springer e-Books. Springer-Verlag Berlin Heidelberg, 2005.

[258] C. A. Marques, M. J. Neat, C. M. Yim, M. D. Watson, L. C. Rhodes, C. Heil, K. S. Pervakov, V. A. Vlasenko, V. M. Pudalov, A. V. Muratov, T. K. Kim, and P. Wahl. Electronic structure and superconductivity of the non-centrosymmetric Sn_4As_3. *New Journal of Physics*, 22(6):063049, 2020.

[259] T. Machida, Y. Kohsaka, K. Iwaya, R. Arita, T. Hanaguri, R. Suzuki, M. Ochi, and Y. Iwasa. Orbital-dependent quasiparticle scattering interference in 3R-NbS_2. *Physical Review B*, 96(7):075206, 2017.

[260] P. Hohenberg and W. Kohn. Inhomogeneous Electron Gas. *Physical Review*, 136(3B):B864–B871, 1964.

[261] W. Kohn and L. J. Sham. Self-Consistent Equations Including Exchange and Correlation Effects. *Physical Review*, 140(4A):A1133–A1138, 1965.

[262] J. P. Perdew, K. Burke, and M. Ernzerhof. Generalized Gradient Approximation Made Simple. *Physical Review Letters*, 77(18):3865–3868, 1996.

[263] J. J. Mortensen, L. B. Hansen, and K. W. Jacobsen. Real-space grid implementation of the projector augmented wave method. *Physical Review B*, 71(3):035109, 2005.

[264] J. Enkovaara, C. Rostgaard, J. J. Mortensen, J. Chen, M. Dułak, L. Ferrighi, J. Gavnholt, C. Glinsvad, V. Haikola, H. A. Hansen, H. H. Kristoffersen, M. Kuisma, A. H. Larsen, L. Lehtovaara, M. Ljungberg, O. Lopez-Acevedo, P. G. Moses, J. Ojanen, T. Olsen, V. Petzold, N. A. Romero, J. Stausholm-Møller, M. Strange, G. A. Tritsaris, M. Vanin, M. Walter, B. Hammer, H. Häkkinen, G. K. H. Madsen, R. M. Nieminen, J. K. Nørskov, M. Puska, T. T. Rantala, J. Schiøtz, K. S. Thygesen, and K. W. Jacobsen. Electronic structure calculations with GPAW: a real-space implementation of the projector augmented-wave method. *Journal of Physics: Condensed Matter*, 22(25):253202, 2010.

[265] S. R. Bahn and K. W. Jacobsen. An object-oriented scripting interface to a legacy electronic structure code. *Computing in Science & Engineering*, 4(3):56–66, 2002.

[266] A. Hjorth Larsen, J. Jørgen Mortensen, J. Blomqvist, I.E Castelli, R. Christensen, M. Dułak, J. Friis, M. N Groves, B. Hammer, C. Hargus, E. D Hermes, P. C Jennings, P. Bjerre Jensen, J. Kermode, J. R Kitchin, E. Leonhard Kolsbjerg, J. Kubal, K. Kaasbjerg, S. Lysgaard, J. Bergmann Maronsson, T. Maxson, T. Olsen, L. Pastewka, A. Peterson, C. Rostgaard, J. Schiøtz, O. Schütt, M. Strange, K. S Thygesen, T. Vegge, L. Vilhelmsen, M. Walter, Z. Zeng, and K. W Jacobsen. The atomic simulation environment—a Python library for working with atoms. *Journal of Physics: Condensed Matter*, 29(27):273002, 2017.

[267] G. A. Fiete and E. J. Heller. Colloquium: Theory of quantum corrals and quantum mirages. *Reviews of Modern Physics*, 75(3):933–948, 2003.

[268] P. Choubey, T. Berlijn, A. Kreisel, C. Cao, and P. J. Hirschfeld. Visualization of atomic-scale phenomena in superconductors: Application to FeSe. *Physical Review B*, 90(13):134520, 2014.

[269] A. Kreisel, P. Choubey, T. Berlijn, W. Ku, B. M. Andersen, and P. J. Hirschfeld. Interpretation of Scanning Tunneling Quasiparticle Interference and Impurity States in Cuprates. *Physical Review Letters*, 114(21):217002, 2015.

[270] A. Kreisel, R. Nelson, T. Berlijn, W. Ku, R. Aluru, S. Chi, H. Zhou, U. R. Singh, P. Wahl, R. Liang, W. N. Hardy, D. A. Bonn, P. J. Hirschfeld, and B. M. Andersen. Towards a quantitative description of tunneling conductance of superconductors: Application to LiFeAs. *Physical Review B*, 94(22):224518, 2016.

[271] P. Choubey, A. Kreisel, T. Berlijn, B. M. Andersen, and P. J. Hirschfeld. Universality of scanning tunneling microscopy in cuprate superconductors. *Physical Review B*, 96(17):174523, 2017.

[272] A. Kreisel, C. A. Marques, L. C. Rhodes, X. Kong, T. Berlijn, R. Fittipaldi, V. Granata, A. Vecchione, P. Wahl, and P. J. Hirschfeld. Quasi-particle interference of the van hove singularity in Sr_2RuO_4. *npj Quantum Materials*, 6(1):1–9, 2021.

[273] N. W. Ashcroft and N. D. Mermin. *Solid State Physics*. HRW international editions. Holt, Rinehart and Winston, 1976.

[274] K. Iyakutti, M. Thiagarajan, and K. Kumarasamy. Transforming gaussians into wannier functions using inversion of cyclic matrix. *International Journal of Quantum Chemistry*, 40(5):703–708, 1991.

[275] D. Halwidl, B. Stöger, W. Mayr-Schmölzer, J. Pavelec, D. Fobes, J. Peng, Z. Mao, G. S. Parkinson, M. Schmid, F. Mittendorfer, J. Redinger, and U. Diebold. Adsorption of water at the SrO surface of ruthenates. *Nature Materials*, 15(4):450–455, 2015.

[276] Ismail, J. Zhang, R. Matzdorf, T. Kimura, Y. Tokura, and E. W. Plummer. Surface lattice dynamics of layered transition metal oxides: Sr_2RuO_4 and $La_{0.5}Sr_{1.5}MnO_4$. *Physical Review B*, 67(3):035407, 2003.

[277] S. Chi, W. N. Hardy, R. Liang, P. Dosanjh, P. Wahl, S. A. Burke, and D. A. Bonn. Extracting phase information about the superconducting order parameter from defect bound states. *arXiv:1710.09088*, 2017.

[278] W. Sacks, D. Roditchev, and J. Klein. Voltage-dependent STM image of a charge density wave. *Physical Review B*, 57(20):13118–13131, 1998.

[279] J. M. Carpinelli, H. H. Weitering, E. W. Plummer, and R. Stumpf. Direct observation of a surface charge density wave. *Nature*, 381(6581):398–400, 1996.

[280] M. M. Ugeda, A. J. Bradley, Y. Zhang, S. Onishi, Y. Chen, W. Ruan, C. Ojeda-Aristizabal, H. Ryu, M. T. Edmonds, H.-Z. Tsai, A. Riss, S. K. Mo, D. Lee, A. Zettl, Z. Hussain, Z. X. Shen, and M. F. Crommie. Characterization of collective ground states in single-layer $NbSe_2$. *Nature Physics*, 12(1):92–97, 2015.

[281] Á. Pásztor, A. Scarfato, M. Spera, F. Flicker, C. Barreteau, E. Giannini, J. van Wezel, and C. Multiband charge density wave exposed in a transition metal dichalcogenide. *Nature Communications*, 12(1), 2021.

[282] E. J. Rozbicki. *Effects of spin-orbit coupling and many-body interactions on the electronic structure of Sr_2RuO_4*. PhD thesis, University of St Andrews, 2011.

[283] K. Rossnagel. On the origin of charge-density waves in select layered transition-metal dichalcogenides. *Journal of Physics: Condensed Matter*, 23(21):213001, 2011.

[284] A. Chubukov and P. J. Hirschfeld. Iron-based superconductors, seven years later. *Physics Today*, 68(6):46–52, 2015.

[285] D. C. Johnston. The puzzle of high temperature superconductivity in layered iron pnictides and chalcogenides. *Advances in Physics*, 59(6):803–1061, 2010.

[286] W. Kyung, C. H. Kim, Y. K. Kim, B. Kim, C. Kim, W. Jung, J. Kwon, M. Kim, A. Bostwick, J. D. Denlinger, Y. Yoshida, and C. Kim. Electric-field-driven octahedral rotation in perovskite. *npj Quantum Materials*, 6(1):5, 2021.

[287] A. Chubukov. Pairing Mechanism in Fe-Based Superconductors. *Annual Review of Condensed Matter Physics*, 3(1):57–92, 2012.

[288] C. Lester, S. Ramos, R. S. Perry, T. P. Croft, M. Laver, R. I. Bewley, T. Guidi, A. Hiess, A. Wildes, E. M. Forgan, and S. M. Hayden. Magnetic-field-controlled spin fluctuations and quantum criticality in $Sr_3Ru_2O_7$. *Nature Communications*, 12(1):1–6, 2021.

[289] C. Trainer, C. Abel, S. L. Bud'ko, P. C. Canfield, and P. Wahl. Phase diagram of $CeSb_2$ from magnetostriction and magnetization measurements: Evidence for ferrimagnetic and antiferromagnetic states. *Physical Review B*, 104(20):205134, 2021.

[290] D. J. Singh and I. I. Mazin. Electronic structure and magnetism of $Sr_3Ru_2O_7$. *Physical Review B*, 63(16):165101, 2001.

[291] A. Putatunda, G. Qin, W. Ren, and D. J. Singh. Competing magnetic orders in quantum critical $Sr_3Ru_2O_7$. *Physical Review B*, 102(1):014442, 2020.

[292] L. C. Rhodes. Private communication.

[293] Y. Choi, J. Kemmer, Y. Peng, A. Thomson, H. Arora, R. Polski, Y. Zhang, H. Ren, J. Alicea, G. Refael, F. von Oppen, K. Watanabe, T. Taniguchi, and S. Nadj-Perge. Electronic correlations in twisted bilayer graphene near the magic angle. *Nature Physics*, 15(11):1174–1180, 2019.

[294] Z. Wang, D. Walkup, Y. Maximenko, W. Zhou, T. Hogan, Z. Wang, S. D. Wilson, and V. Madhavan. Doping induced mott collapse and possible density wave instabilities in $(Sr_{1-x}La_x)_3Ir_2O_7$. *npj Quantum Materials*, 4(1):43, 2019.

[295] C. Stingl, R. S. Perry, Y. Maeno, and P. Gegenwart. Electronic nematicity and its relation to quantum criticality in $Sr_3Ru_2O_7$ studied by thermal expansion. *Phys. Status Solidi B*, 250(3):450–456, 2013.

[296] P. Steffens, J. Farrell, S. Price, A. P. Mackenzie, Y. Sidis, K. Schmalzl, and M. Braden. Incommensurate magnetic ordering in Ti-doped $Sr_3Ru_2O_7$. *Physical Review B*, 79(5):054422, 2009.

[297] R. G. Moore, Jiandi Zhang, V. B. Nascimento, R. Jin, Jiandong Guo, G.T. Wang, Z. Fang, D. Mandrus, and E. W. Plummer. A Surface-Tailored, Purely Electronic, Mott Metal-to-Insulator Transition. *Science*, 318(5850):615–619, 2007.

[298] A. Maldonado, H. Suderow, S. Vieira, D. Aoki, and J. Flouquet. Temperature dependent tunneling spectroscopy in the heavy fermion $CeRu_2Si_2$ and in the antiferromagnet $CeRh_2Si_2$. *Journal of Physics: Condensed Matter*, 24(47):475602, 2012.

[299] S. Ernst, S. Kirchner, C. Krellner, C. Geibel, G. Zwicknagl, F. Steglich, and S. Wirth. Emerging local Kondo screening and spatial coherence in the heavy-fermion metal $YbRh_2Si_2$. *Nature*, 474(7351):362–366, 2011.

[300] S. Seiro, L. Jiao, S. Kirchner, S. Hartmann, S. Friedemann, C. Krellner, C. Geibel, Q. Si, F. Steglich, and S. Wirth. Evolution of the Kondo lattice and non-Fermi liquid excitations in a heavy-fermion metal. *Nature Communications*, 9(3324):3324, 2018.

[301] M. J. Lawler, K. Fujita, Jhinhwan Lee, A. R. Schmidt, Y. Kohsaka, Chung Koo Kim, H. Eisaki, S. Uchida, J. C. Davis, J. P. Sethna, and Eun-Ah Kim. Intra-unit-cell electronic nematicity of the high-T_c copper-oxide pseudogap states. *Nature*, 466(7304):347–351, 2010.

Appendix A

STM simulated images from DFT calculations

The ASE package implemented in GPAW includes a module for generating STM topographies using the Tersoff-Hamann formulation (Eq. (3.6)), with the explicit formula

$$I = \int_{E_F}^{E_F+eV} \sum_{kn} w_{\mathbf{k}} |\Psi_{\mathbf{k}n}(\mathbf{r})|^2 \delta(\varepsilon - \varepsilon_{\mathbf{k}n}) d\varepsilon, \tag{A.1}$$

where $w_{\mathbf{k}}$ is the $\mathbf{k}$-point weight, $\Psi_{\mathbf{k}n}(\mathbf{r})$ the wave function and V the bias voltage. The STM topographs in Figure A.1 were calculated using this module, for constant current 2D scan. The simulated STM images of the surface of Sr_2RuO_4, Figure A.1 (a), and $Sr_3Ru_2O_7$, Figure A.1 (b), show that the high intensity of the charge density at 5 Å above the surface occurs at the Sr positions. It confirms that the lattice imaged in the STM measurements is the Sr lattice, Figure 5.2 (a) and Figure 6.2 (and all the topographies shown in this work).

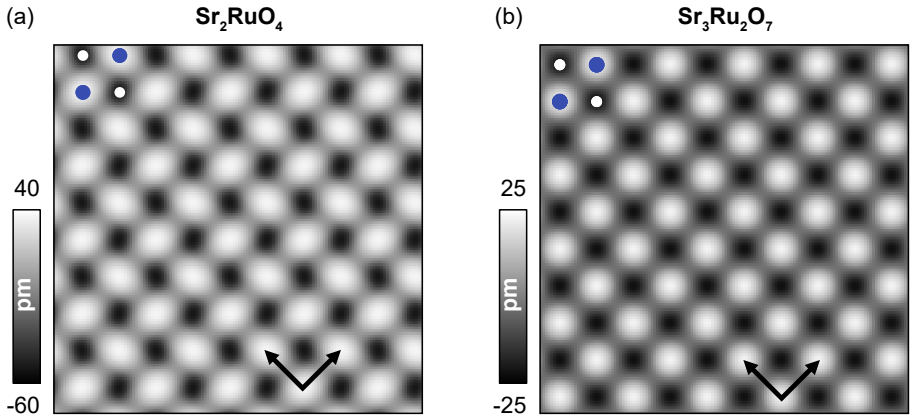

Figure A.1: **STM simulated images from DFT calculations of Sr_2RuO_4 and $Sr_3Ru_2O_7$.** (a) Simulated STM topographic image at 200 meV, taken 5 Å above the surface of a single layer of Sr_2RuO_4, with 6° of octahedral rotation. (b) Simulated STM topographic image at 200 meV, taken 5 Å above the surface of a single layer of $Sr_3Ru_2O_7$, with the octahedral distortions of the bulk crystal structure. For both cases, the ground state was calculated within LDA and using LCAO as the basis fucntions, for a slab composed of a single layer of $Sr_2RuO_4/Sr_3Ru_2O_7$, on a $40 \times 40 \times 1$ k-grid, with 20 Å of vacuum. The blue and white circles indicate the position of the Sr and Ru atoms, respectively, in the unit cell.

Appendix B

Sr vertical corrugation

A structural distortion on a surface, such as a step edge, appears in STM topographies with a height change that is essentially bias independent. If the checkerboard modulation discussed in section 6.4 is due to a structural reconstruction of the Sr atoms, with a staggered vertical displacement of the Sr atoms, the checkerboard should be visible at all bias voltages. Figure B.1 shows the height difference between adjacent Sr atoms, $h_{Sr1} - h_{Sr2}$, as a function of bias voltage, extracted from the unit cell averaged image of each topography taken with each bias voltage. It shows a sharp peak at -5 mV and it becomes largely bias independent for bias voltages of $|V| > 20$ mV. The bias independent part of Figure B.1 will be most representative of a possible atomic displacement, giving an upper bound of ~ 130 fm for the vertical displacement of the Sr atoms.

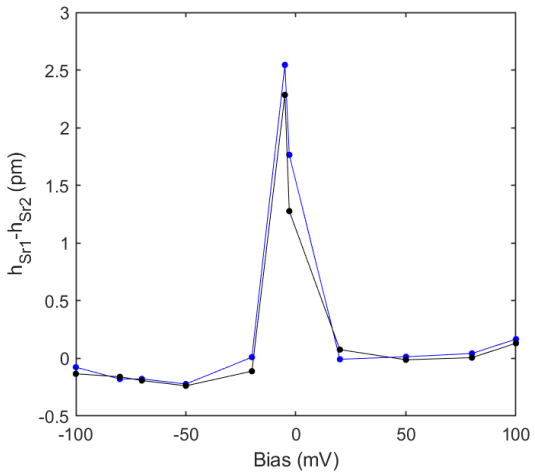

Figure B.1: **Sr lattice corugation as a function of bias voltage.** Height difference between Sr1 and Sr2 from topographies taken at bias voltages between ± 100 mV. The height difference was extracted after performing an unit cell average of the topographies. The blue and black lines indicate the difference between Sr1 and Sr2 on two Sr rows on the unit cell.

Appendix C

Gaussian-type orbitals

To calculate the continuum LDOS in section 5.8.2 using the tight-binding model described in section 5.8, gaussian-type orbitals were used to perform the continuum transformation. Figure C.1 shows gaussian-type orbitals with the symmetries of the d_{xz}, d_{yz} and d_{xy} orbitals, centered on Ru positions A (top) and B (bottom). The gaussian-type orbitals show staggered rotation between positions A and B with an angle of $\theta_{rot} = 6^\circ$ to simulate the octahedral rotation at the surface layer of Sr_2RuO_4.

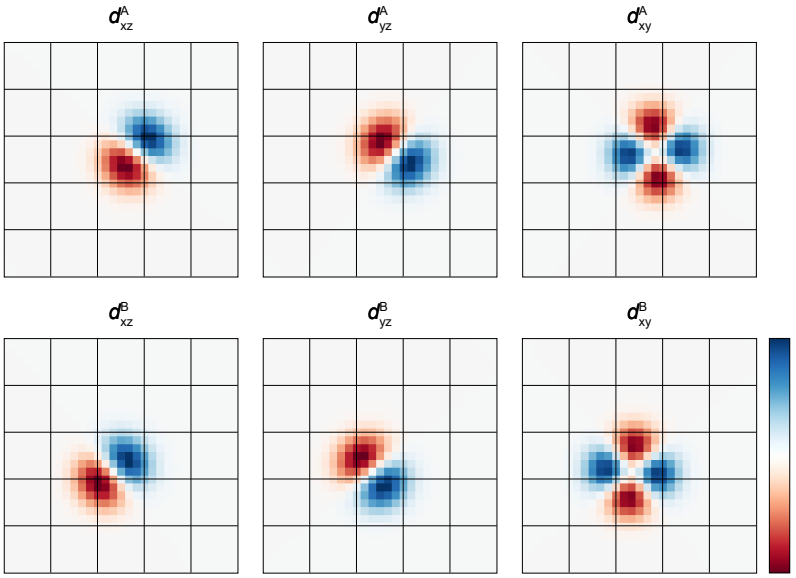

Figure C.1: **Gaussian-type orbitals used in cLDOS calculations.** Intensity plots of the gaussian-type orbitals used in the continuum transformation in section 5.8.2, with the symmetries of the d_{xz} (left), d_{yz} (middle) and d_{xy} (right) orbitals, for an angle of rotation of $\theta_{rot} = 6^\circ$ and a spread of $\phi = 2$. The top and bottom rows show the gaussian-type orbitals centered on Ru positions A and B in the unit cell, respectively. The lines are the edges of the unit cells considered for the summation.

The spread of the gaussian-type orbitals is a free parameter that is set phenomenologically.

Figure C.2 shows cLDOS calculations using gaussian-type orbitals with spreads of $\phi = 1$, 2 and 4. Using $\phi = 2$ results in a well-resolved atomic lattice with maxima between the Ru positions. With $\phi = 1$, the lateral extent of the gaussian-type orbitals is too large to show a well-resolved atomic lattice, and with $\phi = 4$ it becomes too small, making the rotation of the gaussian-type orbitals visible.

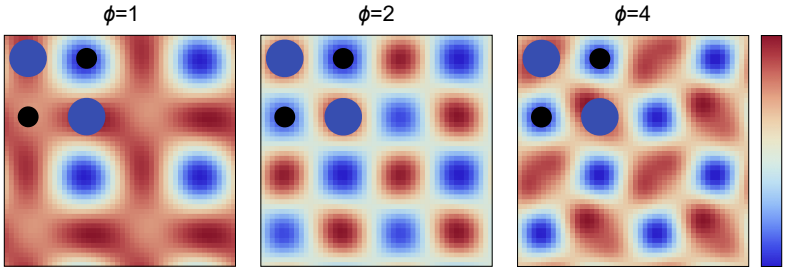

Figure C.2: **Homogeneous cLDOS calculations with different gaussian spreads ϕ.** Calculations performed with the same parameters as Table 5.3, but with $n_{pixel} = 24$ and $V_{imp} = 0$, for different spreads ϕ of the gaussian-type orbitals, at an energy of -10 meV. Purple and black circles indicate the Sr and Ru positions.

Appendix D

Implementation of the Lock-in algorithm

A typical differential conductance map of 256 pixels over an area of 20 nm takes about three days to complete, for a spectrum with several dozens of layers. During this time, as a result of the fast and slow scanning directions, piezo creep and thermal fluctuations, the images will have picometer size distortions, which render the imaged lattice non-perfect. Let us take the example of a square lattice. The consequences are more obvious in the Fourier transform: the two sets of equivalent Bragg peaks are not in an 90° angle from each other, and the distance between them and the center is not the same. Due to the picometer change, these Bragg peaks will not show up as delta-functions, they will have an intrinsic width due to variations of the periodicity along the image. These artifacts can be corrected so that the Bragg peaks occupy only one pixel in the Fourier transform. To this end, we need to apply a transformation to our image that makes our lattice perfect. This can be done by implementing the Lawler-Fujita algorithm [301], also called the Lock-in algorithm.

Here, we will implement a 'lock-in method' to obtain the map phase between the imaged lattice and a perfect lattice. The perfect lattice is given by

$$T(\mathbf{r}) = \cos(\mathbf{q_{br1}}.\mathbf{r} + \phi) + \cos(\mathbf{q_{br2}}.\mathbf{r} + \phi) \tag{D.1}$$

where $\mathbf{q_{br1}}$ and $\mathbf{q_{br2}}$ are the $\mathbf{q}$-vectors corresponding to the Bragg peaks ($2\pi/a_{sr}$, where a_{sr} is the lattice contant of the Sr square lattice), and ϕ is just a phase. For simplicity, we can consider $\mathbf{q_{br1}}$ and $\mathbf{q_{br2}}$ to be aligned with the x and y directions. For this, we rotate our image in order for one of the Bragg peaks to be aligned with the y-axis. We take ϕ as being the phase of the Bragg

peak taken from the FFT of the topography of the map. We now implement the lock-in method: we implement two phase-sensitive detections for each spatial direction. The modulation due to the drift has a characteristic length which is larger than the atomic modulation (there is, it has a smaller $\mathbf{q}$-vector than the Bragg peaks). Thus, to extract this slow variation, we implement a low-pass filter with width in Fourier space $\Lambda_u \leq 0.5 q_{br}$. By doing this, we now have the quantities $X1$ and $Y1$ (for the other direction $X2$ and $Y2$) which can be seen as the real and imaginary part of a complex number. Thus, we can extract the slow varying phase by computing the quantity

$$\Theta_i(\mathbf{r}) = \arctan 2(Yi, Xi) \tag{D.2}$$

with $i = 1, 2$, the phase along each spatial direction. These phase maps will have jumps of order 2π, each time it matches a lattice constant. We need to eliminate those jumps from the images, to make the phasemap single-valued. This is done by implementing a cycle that runs from the center of the image towards the egdes, and each time it finds a jump it adds 2π.

The last step is to obtain the distortion displacement field. This phase is equal to

$$\Theta_i(\mathbf{r}) = \mathbf{q_{bri}}.\mathbf{u}(\mathbf{r}) \tag{D.3}$$

and thus, the displacement field can be obtained. Here, the $\mathbf{q_{bri}}$ corresponds to the $\mathbf{q}$-vectors of the perfect lattice. This allows to map the distorted lattice of the map to the perfect lattice.

Appendix E

Anti-aliasing

When a differential conductance map is taken on a grid with a number of pixels lower than the necessary to resolve the atomic lattice, the atomic peaks will appear aliased in the Fourier transform, that is, at a lower **q**-vector, Figure E.1(a). To recover the **q**-vector at which they would appear if the map had been taken with enough pixels to resolve the atomic lattice, the image of the Fourier transform is unfolded as shown in Figure E.1(b) so that the aliased atomic peaks are mapped onto their original positions. To correct for the drift distortion, a geometrical transformation is used to map the anti-aliased atomic peaks onto a perfect square lattice Figure E.1(c). The aliased maps were used in section 5.9 in Figure 5.19(a), section 6.6 in Figures 6.10 and 6.11, and in section 6.7.3 in Figures 6.18, 6.19 and 6.21.

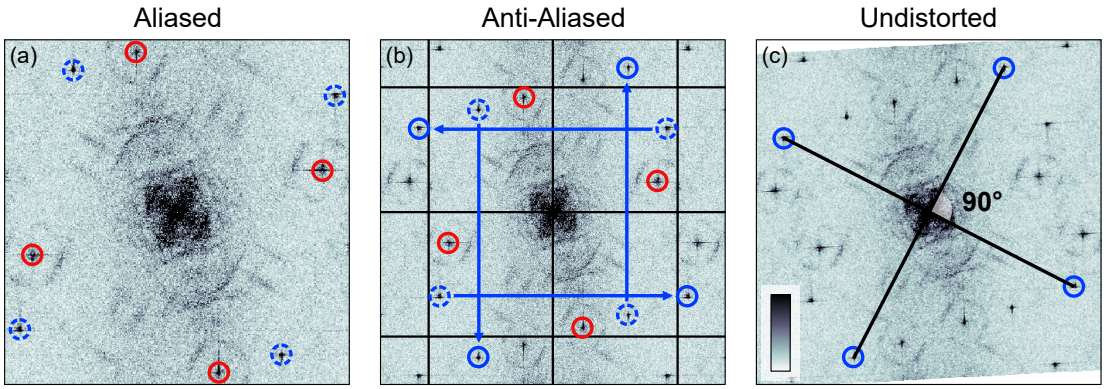

Figure E.1: **QPI data processing of aliased maps.** (a) Fourier transform of a differential conductance map layer taken on a grid of pixels smaller than the necessary to resolve the atomic lattice. The atomic peaks (dashed blue circles) are aliased and thus appear at a lower **q**-vector. The number of pixels used was enough to resolve the checkerboard so that the reconstruction peaks at $(0.5, 0.5)$ (red circles) appear in their correct positions. (b) Anti-aliased version of (a), where the atomic peaks (dashed blue circles) were unfolded to their original positions. (c) After the distortion correction algorithm, where a geometrical transformation is used to map the anti-aliased atomic peaks (blue circles) onto the positions expected from a square lattice.